Spectra of High-Energy Neutrinos and AGN Population Evolution inferred by X-ray/γ-ray Surveys

Idunn Blindheim Jacobsen

Thesis submitted for the degree of

Doctor of Philosophy

of

University College London

Mullard Space Science Laboratory

Department of Space and Climate Physics

University College London

2015

I, Idunn Blindheim Jacobsen, confirm that the work presented in this thesis is my own. Where information has been derived from other sources, I confirm that this has been indicated in the thesis.

_____

_____

Abstract

In this thesis I investigate the evolution of high-energy neutrinos, and their ability to diagnose the environment of their origin. AGN are identified as candidates for high-energy neutrino production, and the radio-loud population is particularly attractive due to observed energetic regions in the jet features. I derive source populations at different redshifts and brightness using data obtained from AGN surveys detecting X-ray and γ-ray bright sources. These trace the accretion disc and beamed jet luminosities, respectively, and reflect AGN populations varying in observable properties.

Two hadronic interaction models are considered to determine neutrino production efficiencies in AGN. The region of high-energy particle production is located at the base of the AGN jet, where relevant interactions are expected to occur. The diffuse neutrino emission on Earth is calculated as the sum of the contributions from various cosmological epochs, and X-ray luminosities.

I find that the bulk of AGN sources would produce a neutrino flux far exceeding the current upper limits set on the received neutrino emission. The only neutrino energy spectra consistent with these limits are due to neutrino production in blazars. Additionally, the importance of a reliable luminosity scaling model is demonstrated, and hence the need for an improved understanding of the radiative processes in jets.

To further investigate the physical processes relevant to neutrino production, I construct a neutrino luminosity function for blazar sources. The expected neutrino energy distribution is produced by assuming typical parameters, such as luminosity and Lorentz factor, for each class along the blazar sequence. This will establish constraints on possible AGN sources, the relative neutrino duty cycle, and production efficiencies across the sequence.

Acknowledgements

First of all I extend my sincere gratitude to my supervisor Prof. Kinwah Wu. His lectures introduced me to high-energy astrophysics, and I have been fortunate to immerse myself further in the field under his supervision. He has generously devoted his time to guide me through the PhD, and his sessions have taught me how to understand complex physical concepts in a simple manner, about life in academia, and so much more. I thank him for sharing his passion for science, for his patience and steady hand throughout my time here at MSSL.

I would like to thank Dr. Ignacio Ferreras for assuming the role of my second supervisor in my first year, and for always being available to help and share his expertise. I thank Prof. Ofer Lahav for kind advice and direction. As my secondary supervisor he has provided a balance to the supervisory team with discussions on my project, as well as on cosmic neutrinos and philosophy. I especially acknowledge and thank Dr. Kumiko Kotera for her time devoted to mentoring me. Her generous help and supervision has been invaluable. I will always be grateful for my London meetings with Drs. Kotera and Fotini Oikonomou, for their kind insights and discussions.

I thank Dr. Curtis Saxton and Alvina On for discussions on the astrophysics of AGN, in particular the AGN luminosity functions, and neutrino astrophysics in general. I thank Dr. Ziri Younsi for discussions on AGN jet structures and his help in advanced mathematics and numerical methods. I thank all three of them for the collaborations. I am also thankful for helpful advice I have received from others at MSSL. In particular Drs. Missagh Mehdipour and David Barnes for inspiring conversations and extensive technical help. I thank the students of the Astrophysics group for their support,

comments and discussions; Megan Whewell, Ellis Owen, and Jennifer Chan. To my friends, and particularly my flatmates, the good Drs. Yudish Ramanjooloo and Rob Grand, for their support and friendship. I thank Simon for providing the artistic balance. I wish you all the best for the future.

I acknowledge the support from Lånekassen, Norway, whose financial help has let me spend over ten wonderful years at UCL, studying a subject that never seizes to amaze me. The research has made use of NASAs Astrophysics Data Systems.

Finally, I am forever indebted to my family for always encouraging and inspiring me, and for their unconditional support. Burak, words cannot express how thankful I am for having you in my life.

Last, but not least, Alexandria and Axel, the brightest stars in our lives. Remember to always look for the beauty in the world.

Contents

List of Figures

List of Tables

Chapter 1

Introduction

The study of astrophysical neutrinos on all energy scales provides a window through which we may begin to understand powerful astrophysical objects and the earliest moments of the Universe. These, either extremely dense or distant, regions in space are currently unavailable to us, and the advancements in neutrino astronomy highlight the efforts to continue to push detection boundaries. As neutrinos escape the densest environments nearly unhindered, and are practically unabsorbed and unscattered over large distances, they can be used to diagnose astrophysical environments that traditional photonic studies cannot reach.

Neutrinos and photons are therefore complementary messengers, probing violent astrophysical processes and structural evolution of the Universe. High-energy neutrinos may be generated in cosmic accelerators, such as active galactic nuclei (AGN) and associated jet structures, as well as in gamma-ray bursters, supernovae and magnetars. Other messenger particles emitted in the same processes are high-energy cosmic rays and γ-rays. The neutrino production process sheds light on the physics governing the inner regions of the sources – regions that often are opaque to other sources of emission.

AGN are persistent over cosmological epochs, and are among the most luminous X-ray sources in the Universe. A super-massive black hole resides at their core, and the accretion of matter onto the black hole is often accompanied by large-scale relativistic jets. These structures have the potential to accelerate particles to ultra-high energies, which in turn will interact with radiation or

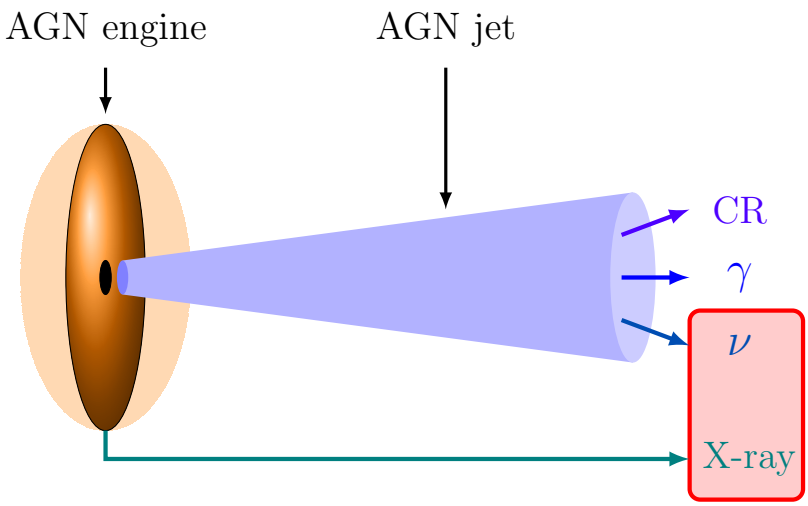

Fig. 1.1: Neutrino production linked to AGN accretion power. X-ray emission is a telltale sign of AGN accretion activity. Associated jet structures are often seen, which may generate high-energy cosmic rays (CR), γ-rays (γ) and neutrinos (ν). A correlation between neutrinos and either cosmic rays or γ-rays tests the hadronic models in a particle physics context; however, by directly linking neutrino production to the accretion power, we test the production scenarios in an astrophysical context.

matter fields within the jets. Interactions involving energetic protons will lead to the production of neutrinos, which may be observed in current dedicated neutrino observatories, such as the *IceCube*.

This work aims to verify if all AGN are neutrino sources, and look at how the production efficiency varies across the family of AGN types. Conventionally, neutrino fluxes are correlated with the emission of cosmic rays or γ-rays. This approach will however only test the hadronic models and neutrino production scenarios in the context of particle physics. Here we aim to investigate how neutrino production in jets is scaled with the accretion power of the central AGN engine. We therefore use solid astrophysical data obtained by state-of-the-art X-ray observations. In this way we look directly at the link between AGN power and high-energy production in AGN jets, illustrated in Fig. 1.1. In light of these all-sky X-ray surveys of AGN, we furthermore verify if two commonly accepted scenarios of neutrino production in AGN jets, where energetic protons interact with radiation fields close to the AGN core, are applicable.

The cumulative neutrino flux spectrum is calculated by considering the cosmic distribution of AGN based on solid astrophysical data. Using the X-ray luminosity functions, which are constructed from three comprehensive X-ray studies carried out recently, we derive the number density of AGN at different epochs of the Universe.

As AGN are an inhomogeneous family of objects, we cannot claim that all are equally efficient in producing neutrinos. We therefore derive population sizes for a variety of AGN types in order to test their production potential. This enables a comparison between types, distributed both over cosmological epochs and X-ray luminosity.

This work is the first to relate survey X-ray observations of AGN to neutrino production in this manner, and to comprehensively compute neutrino fluxes across AGN populations over the history of the Universe, and the first results of the thesis are published in Jacobsen et al. (2015). This method paves a new way of multi-messenger astrophysics, and connects astrophysics and astroparticle physics in a quantitative manner.

1.1 Neutrino Physics

The physical concept of the neutrino has been in continuous development over the past hundred years, and the first clue to the existence of this particle appeared already in 1896 with the discovery of radioactivity by Henri Becquerel, observing ionising energy spontaneously emitted from uranium. Three types of radioactive decay were identified, namely those leading to the emission of α- (helium nuclei), β- (electron), and γ- (photon) particles. The decays were studied by observing their energy spectra, and here the first clue to the neutrino is found.

The energy spectra observed from α- and γ-rays were quantised in energy. That of the electrons emitted in β-decays was on the other hand seen to be continuous. The obvious explanation was that additional energy to that carried away by electrons was lost in the decay. The idea of a new particle developed to explain this missing energy.

In 1930 Wolfgang Pauli wrote a letter to a conference in Tübingen, Ger-

many (Riesselmann 2007) where he proposed that, in addition to protons and electrons, there was an extremely light and neutral particle within the nuclei. This particle would be emitted in β-decays along with the electron (see Sec. 1.1.4). The name of Pauli's particle was given its name by Enrico Fermi, the *neutrino*, to distinguish it from the neutral, but significantly heavier, nucleon discovered by James Chadwick (Chadwick 1932), the *neutron*.

He formulated a theory of β-decay in 1934 (Fermi 1934a,b; Wilson 1968) which further solidified the prediction of the neutrino's existence. In Fermi's theory, the neutrino is massless and chargeless, and the β-decay, i.e. the decay of a neutron to a proton and electron antineutrino,

$$\mathrm{n} \rightarrow \mathrm{p} + \mathrm{e}^{-} + \bar{\nu}_{\mathrm{e}} \ , \tag{1.1}$$

is understood as a transition probability known as Fermi's Golden Rule. It depends on coupling strength of the initial and final states, as well as the final density of states that determines the number of ways this transition can occur. The nature of the weak interaction enabling β-decays was still unknown to Fermi, and it took another twenty years to refine the model to fit observations.

The lightest of the neutrinos, the electron neutrino, which is associated with electron emission in β-decays, was finally observed in a nuclear reactor experiment, led by Clyde L. Cowan and Frederick Reines in 1956 (Cowan et al. 1956; Reines and Cowan 1956) (see details of the experiment in Sec. B.4).

A concept of the fundamental particle generations began to emerge with the discovery of the muon in 1937 (Street and Stevenson 1937; Neddermeyer and Anderson 1937). Further support of this concept came in 1962, when the muon neutrino was discovered by L. M. Lederman, M. Schwartz and J. Steinberger at Brookhaven National Laboratory (BNL, Danby et al. 1962, see also Sec. B.4).

By the 1970s, the known fundamental particles were grouped in pairs of two generations of two leptons each: the electron (e) and electron neutrino (ν_{e}); and the muon (μ) and muon neutrino (ν_{μ}). The second generation of particles followed the pattern of the first generation, but were more massive, hence

more unstable. This apparently structured arrangement motivated the idea for further generations, and was confirmed by the discovery of the tau lepton (τ) in 1975 (Perl et al. 1975). This signalled the existence of the third generation neutrino; the tau neutrino (ν_τ) (Perl 1980). It was finally detected by the DONUT collaboration (DONUT Collaboration et al. 2001; Kodama et al. 2008) in 2000, thus completing the picture of the three generations of fermionic particles.

1.1.1 The Neutrino and the Weak interaction

The existence of a particle explaining the concept of the missing energy in the β-decay process is a physical manifestation of the weak interaction.

The 1960s saw the development of a formal theory of weak interactions by S. Weinberg and A. Salam (Weinberg 1967; Salam and Ward 1964), basing their work on a gauge model proposed by S. L. Glashow (Glashow 1961). This theory is now known as the Glashow-Weinberg-Salam (GWS) Standard Model of particle physics, and was refined by proving renormalisability of the theory by G. 't Hooft and M. J. G. Veltman in 1971 ('t Hooft 1971; 't Hooft and Veltman 1972).

The GWS model predicts the existence of the W boson from the usual charged current events seen in weak interactions, complementary neutral currents, and the associated Z boson (see Sec. 1.1.5). The first of the neutral current events were seen in 1973 by the Gargamelle experiment at CERN (Hasert et al. 1973, 1974), and confirmed by the Fermi National Accelerator Laboratory (Fermilab) in the same year (Benvenuti et al. 1974). However, it took another ten years to detect the mediating weak bosons, and in 1983 CERN reported detections of the $W^\pm$ bosons (Arnison et al. 1983a; Banner et al. 1983) and the Z^0 boson (Arnison et al. 1983b; Bagnaia et al. 1983), establishing this model as the recognised description for the (electro-) weak interactions in the Standard Model of particle physics (see Sec. 1.1.2).

The electroweak theory, quantum chromodynamics (QCD) and quantum electrodynamics (QED) are three dynamical theories of the weak, strong and electromagnetic interactions, respectively. These three local gauge theories are collectively the recognised Standard Model of Particle Physics, and are

formulated on the framework of Quantum Field Theory. The Standard Model describes the quantum mechanical behaviour of these three fundamental forces of nature, and explain all phenomena of particle physics in terms of the properties and interactions of a set of fundamental particles. The fourth fundamental force of nature, gravity, has negligible strength at nuclear length scales relative to other three forces.

1.1.2 The Neutrino and the Standard Model

The collection of fundamental particles are considered point-like and without any internal structure or excited states in the Standard Model, shown in Fig. 1.2. Their measured properties are mass, spin and charge, and are categorised in two main groups; fermions, which have half-integer spin; and bosons, which carry integer spin.

Fermions are the building blocks of matter, each with an associated antiparticle with opposite charge. They are classified according to their properties of interaction. The quarks interact via the strong force and are bound to form hadrons; three quarks make up baryonic matter (e.g. protons and neutrons), and two quarks make up mesonic matter (e.g. pions and kaons). Leptons interact via the electomagnetic and weak forces, and consist of three electrically charged particles, and three associated neutral particles – the neutrinos.

Pairs of each fermionic family form a generation depending on their properties. The first generation (up, down; electron, electron neutrino) consists of stable matter (i.e. matter that does not decay) that are the building blocks of all ordinary matter. The second and third generations are more exotic matter, for which the charged counterparts are highly unstable with very short half-lives, and only found in high-energy environments. Furthermore, the particles of later generations are more massive than their corresponding particles of earlier generations.

Bosons in the standard model are force carriers exchanged when fermionic matter particles interact via one of the fundamental forces of nature. When quarks interact via the strong force, due to their colour charge, the mediating force carrier is called a gluon. The QCD theory in the Standard Model

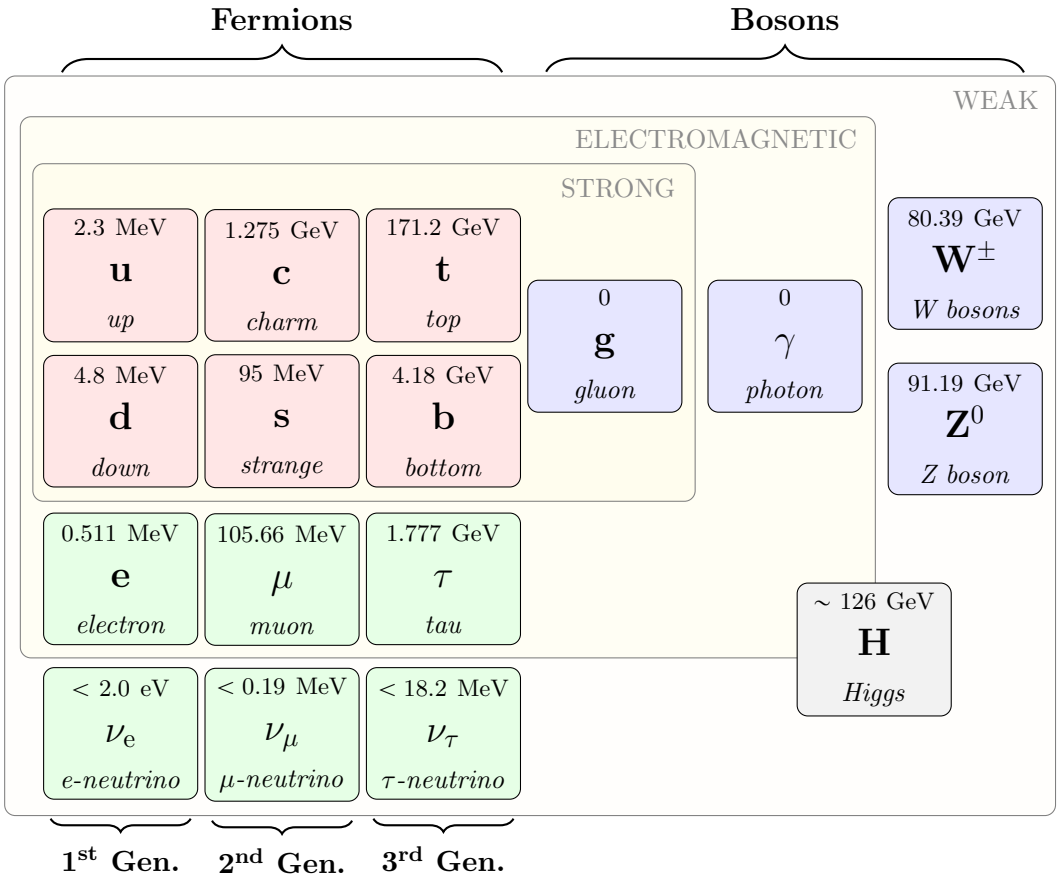

Fig. 1.2: The fundamental particles in the Standard Model: the quarks (red) and leptons (green) form the three generations of fermionic matter. The bosons (blue) are the mediators of respective forces and the fermions. The Higgs boson (grey) is the mediator of the Higgs field which caused the electro-weak symmetry breaking. Masses (Beringer et al. 2012) are quoted above the symbol of each particle, and their given name is quoted below.

describes eight massless, but electrically charged, gluons. Along with charged leptons, they can interact with one another via the electric and magnetic fields due to the electromagnetic force, which is mediated by the photon. This massless particle and the interactions it is involved in, is also described in the QED theory.

Neutrinos are the lightest particles in the fermionic family. They do not decay, and interact only through the weak force. The weak force is mediated by three force carriers: the charged W^- and W^+, that, due to their charge also couple to the electromagnetic interaction; and the neutral Z^0. The interactions governed by this force are described in the Standard Model in the

electroweak theory, which is a unified description of the electromagnetic and weak interactions. The GWS model describes the two forces as two aspects of the same force, unified at energies reached moments after the Big Bang. As the Universe cooled below a characteristic energy, the electroweak force split into the two separate forces we observe today.

The need for spontaneous symmetry breaking in the formulation of the Standard Model is therefore necessary, and provided by the Higgs mechanism. The Higgs mechanism makes massless bosons massive in the formulation of the local gauge model of Glashow, and was independently proposed by F. Englert and R. Brout (Englert and Brout 1964), P. Higgs (Higgs 1964), and G. S. Guralnik, C. R. Hagen and T. W. Kibble (Guralnik et al. 1964) in 1964. This model has now gained further recognition with the recent reports of the discovery of the Higgs boson. CERN reported the detection of a new particle in 2012 (ATLAS Collaboration Aad et al. 2012; CMS Collaboration Chatrchyan et al. 2012) found to be consistent with the Standard Model Higgs particle (Aad et al. 2013), thus completing the picture of the Standard Model fundamental particles.

Particles that interact with the Higgs field through the exchange of the Higgs boson find that the coupling allows a transfer of potential energy to the particles, thus, they acquire some intrinsic mass. The observation of the Higgs scalar particle, a very unstable boson of spin-0, confirms the existence of the Higgs field. It explains why some fundamental particles are massive, such as the very massive weak force carriers ($m_{\mathrm{W}} \approx 80.4$ GeV, $m_{\mathrm{Z}} \approx 91.2$ GeV). This results in a very short interaction range of only 10^{-16} cm, which is 10^{13} times weaker than the strong interaction and 10^{11} times weaker than the electromagnetic interaction.

The strength of the interactions comes out of quantum field theory, for which a dimensionless coupling constant g is either much less than one, leading to a weakly coupled theory; or of order one or larger, leading to a strongly coupled theory. The weak coupling constant, g_{w} is determined by the mass of the mediating boson and the Fermi constant, G_{F}, which gives the strength of

the interaction

$$\frac{g_{\mathrm{w}}^2}{8m_{\mathrm{W}}^2} = \frac{G_{\mathrm{F}}}{\sqrt{2}} \,. \tag{1.2}$$

The value of the Fermi constant is $G_{\mathrm{F}} \approx 1.166 \times 10^{-5}$ GeV^{-2}, experimentally found from measurements of the muon lifetime, which is inversely proportional to G_{F}^2. It is worth noting, that although the Higgs boson has been discovered, a more cautious description of it is rather *a* Higgs boson, since it is not known if it is the only of its kind, or if there are more of them.

Although the Standard Model describes most phenomena of particle physics accurately, there are some issues that must be solved for it to be a complete and fully predictive model. Of the four fundamental forces, the gravitational force is not included, as no known prescription of quantum gravity exists. As such, the hypothesised graviton, the gravitational force carrier, is not included in the collection of fundamental particles of the Standard Model (Fig. 1.2).

The Standard Model also has short-comings with regards to neutrinos. In the original formulation of the model, dating back to Fermi's derivation of the β-decay, the neutrino is considered massless. However, early hints of a neutrino mass came with the so-called Solar Neutrino Problem, first identified in the Davis and Bahcall neutrino experiment, and the Atmospheric Neutrino Anomaly first observed in the late 1980s. The solution to these problems was the concept of neutrino oscillations, which explains how a neutrino of definite flavour will morph to another flavour as it travels form the source to the point of detection, observed in the late 1990s by, among others, Super-Kamiokande (see Secs. 1.1.3 and B.4).

The confirmation of the oscillation phenomenon in neutrinos led to the necessity of a neutrino mass term in the Standard Model formulation. This has major implications for particle physics, astrophysics and cosmology.

1.1.3 Neutrino Oscillations and Flavour Mixing

The concept of neutrino oscillation was proposed by V. Gribov and B. Pontecorvo in 1969 as a solution to the solar neutrino deficit observed by Davis and Bahcall (Gribov and Pontecorvo 1969). It is a quantum mechanical con-

cept, for which the observed oscillation from one flavour to another is a consequence of the mixing of neutrino eigenstates. This was already conceptualised by Pontecorvo in 1957, after observing the mixing of neutral kaons, and the foundation was further developed by Z. Maki, M. Nakagawa and S. Sakata in 1962 as a two-flavour scenario (Maki et al. 1962).

Flavour is a property of the weak interaction, through the coupling to the associated charged lepton. A neutrino of a specific flavour ν_ℓ, where $\ell = \{e, \mu, \tau\}$, is defined as a linear combination of three mass eigenstates $\mid \nu_i\rangle$, where $i = \{1, 2, 3\}$, having definite masses m_i. The mass eigenstates are properties of the Higgs interaction, as the mass of the particles is directly linked through the coupling between the particles and the Higgs field (Yukawa couplings). Thus, the flavour eigenstate determines how the neutrino interacts with matter, and mass determines how the particle propagates through space.

In standard oscillation theory (see e.g. Giunti and Kim 2007), a neutrino that is produced with flavour ℓ and momentum $\mathbf{p}$ through charged-current processes from a charged (anti-)lepton can be described in its flavour state as

$$\mid \nu_\ell\rangle = \sum_i U^*_{\ell i} \mid \nu_i\rangle \ , \tag{1.3}$$

where $U_{\ell i}$ is the Pontecorvo-Maki-Nakagawa-Sakata (PMNS) unitary transformation matrix. It is specified in terms of mixing angles, expressed by $s_{ij} = \sin\theta_{ij}$ and $c_{ij} = \cos\theta_{ij}$, that are determined from experiment. The angle θ_{12} is measured from solar neutrino experiments to be $\sin^2(2\theta_{12}) = 0.857$. The θ_{23} is measured from atmospheric neutrino experiments, measured to be $\sin^2(2\theta_{23}) > 0.95$. The smallest angle, θ_{13} is measured from reactor experiments, and it is found from $\sin^2(2\theta_{13}) = 0.098$ (Beringer et al. 2012).

The matrix describes the probability of a neutrino of a specific flavour ℓ being found in a mass eigenstate i. Similarly, the mass state can be described in terms of its flavour state

$$\mid \nu_i\rangle = \sum_\ell U_{\ell i} \mid \nu_\ell\rangle \ . \tag{1.4}$$

The PMNS transformation matrix is expressed as

$$
\begin{aligned}
U_{\ell i} &= \begin{bmatrix} U_{e1} & U_{e2} & U_{e3} \\ U_{\mu 1} & U_{\mu 2} & U_{\mu 3} \\ U_{\tau 1} & U_{\tau 2} & U_{\tau 3} \end{bmatrix} \\
&= \begin{bmatrix} 1 & 0 & 0 \\ 0 & c_{23} & s_{23} \\ 0 & -s_{23} & c_{23} \end{bmatrix} \begin{bmatrix} c_{13} & 0 & s_{13}e^{-i\delta_{13}} \\ 0 & 1 & 0 \\ -s_{13}e^{i\delta_{13}} & 0 & c_{13} \end{bmatrix} \begin{bmatrix} c_{12} & s_{12} & 0 \\ -s_{12} & c_{12} & 0 \\ 0 & 0 & 1 \end{bmatrix} \\
&= \begin{bmatrix} c_{12}c_{13} & s_{12}c_{13} & s_{13}e^{-i\delta_{13}} \\ -s_{12}c_{23} - c_{12}s_{23}s_{13}e^{i\delta_{13}} & c_{12}c_{23} - s_{12}s_{23}s_{13}e^{i\delta_{13}} & s_{23}c_{13} \\ s_{12}s_{23} - c_{12}c_{23}s_{13}e^{i\delta_{13}} & -c_{12}s_{23} - s_{12}c_{23}s_{13}e^{i\delta_{13}} & c_{23}c_{13} \end{bmatrix} .
\end{aligned} \tag{1.5}
$$

The term in the PMNS matrix denoted δ_{ij} is the CP-violating phase factor, which is zero in the case of neutrino oscillation obeying CP-symmetry.

Another useful quantity to measure is the difference in the mass eigenvalues, $\Delta m^2_{ji} = m^2_j - m^2_i$. The measured values are $\Delta m^2_{21} = 7.50 \times 10^{-5}$ eV^2, $\Delta m^2_{32} = 2.32 \times 10^{-3}$ eV^2, $\Delta m^2_{31} \sim \Delta m^2_{32}$ (Beringer et al. 2012).

Mixing of Two Generations. The neutrino oscillation probability is needed by experiments and detectors in order to calculate the composition of the neutrino emission and thus deduce the composition at source. For a simplified treatment (see e.g. Perkins 2000; Giunti and Kim 2007), consider the case of two neutrino flavours, ℓ_1 and ℓ_2, where each is a linear combination of the two mass states, i and j, through a 2×2 mixing matrix and a non-zero mixing angle θ,

$$
\begin{bmatrix} \nu_{\ell_1} \\ \nu_{\ell_2} \end{bmatrix} = \begin{bmatrix} \cos\theta & \sin\theta \\ -\sin\theta & \cos\theta \end{bmatrix} \begin{bmatrix} \nu_i \\ \nu_j \end{bmatrix} . \tag{1.6}
$$

Although the neutrino is produced in one definite flavour state, it will not remain in that flavour eigenstate as it propagates through space. If vacuum propagation is assumed, the mass eigenstates can be expressed as stationary states in terms of the vacuum Hamiltonian, $\hat{H}_{\rm v}$:

$$
\hat{H}_{\rm v} \mid \nu_i \rangle = E_i \mid \nu_i \rangle , \tag{1.7}
$$

with energy eigenvalues $E_i = \sqrt{\mid \mathbf{p}_i \mid^2 + m_i^2}$. Introducing this stationary state to the time-dependent Schrödinger equation,

$$i\frac{d}{dt} \mid \nu_i(t)\rangle = \hat{H}_v \mid \nu_i(t)\rangle \ , \tag{1.8}$$

implies that the neutrino mass states evolve in time as plane waves. Due to the difference in mass of the states, they propagate as waves of slightly different frequencies, thus it will not be in a specific mass state, but rather propagate as a mix between the states. Due to the different frequency, the waves of the mass states will therefore become misaligned periodically, and this mixing of mass states causes the neutrino oscillation between flavours.

Hence, at time $t = 0$, the flavour eigenstate of the neutrino is a linear combination of two mass eigenstates,

$$\mid \nu_\ell(t=0)\rangle = \cos\theta \mid \nu_i\rangle + \sin\theta \mid \nu_j\rangle \ . \tag{1.9}$$

When acted upon by the the time evolution operator, $\hat{U}(t) = e^{-i\hat{H}_v t}$, the wavefunction evolves to

$$\mid \nu_\ell(t)\rangle = \cos\theta e^{-iE_i t} \mid \nu_i\rangle + \sin\theta e^{-iE_j t} \mid \nu_j\rangle \tag{1.10}$$

at time t.

The mass states have fixed momentum, $\mathbf{p}$, so for ultra-relativistic neutrinos, the masses are $m_i \ll E_i$ with $E_\nu = \mid \mathbf{p} \mid$. The dispersion relation above can be approximated to $E_i \simeq E_\nu + m_i^2/2E_\nu$. Introducing the square mass differences, $\Delta m_{ji}^2 \equiv m_j^2 - m_i^2$, gives the energy difference between the two mass states due to the slightly varying mass eigenstates,

$$E_j - E_i \simeq \frac{\Delta m_{ji}^2}{2E_\nu} \ , \tag{1.11}$$

The associated wavefunctions evolve with slightly different frequencies, and as a result, the neutrino that was created with an ℓ_2 flavour state will develop a ℓ_2 flavour component. The intensity of the ℓ_2 component will increase along the propagation, whereas the ℓ_1 component will correspondingly be reduced. The probability of measuring a particular flavour will therefore vary periodically with propagation as the particles travel as superpositions of the mass eigenstates while they are created and annihilated as flavour states.

Measuring the probability that a neutrino is in either flavour state after a time t, can be calculated by assuming that the distance between source and detector, $d = t$. This is possible because ultrarelativistic neutrinos travel close to the speed of light. The probability that the neutrino will remain in its original flavour state is found by the survival probability by

$$P_{\nu_{\ell_1}\to\nu_{\ell_1}}(d) = \mid A_{\nu_{\ell_1}\to\nu_{\ell_1}}(d) \mid^2 = 1 - \sin^2(2\theta)\sin^2\left(\frac{\Delta m^2_{ji} d}{4E_\nu}\right) . \tag{1.12}$$

where $A_{\nu_{\ell_1}\to\nu_{\ell_1}}(d) \equiv \langle \nu_{\ell_1} \mid \nu_{\ell_1}(d) \rangle$. The probability then oscillates back and forth between 1 and $1 - \sin^2(2\theta)$ over a vacuum oscillation length, $d^{\rm osc}_{ji} = 4E_\nu/\Delta m^2_{ji}$. The probability of measuring a neutrino of flavour ℓ_2 is then

$$P_{\nu_{\ell_1}\to\nu_{\ell_2}}(d) = \sin^2(2\theta)\sin^2\left(\frac{2d}{d^{\rm osc}_{ji}}\right) . \tag{1.13}$$

For the mixing of three flavours, a 3×3 matrix is required and the probability of measuring the oscillation of a neutrino to a different flavour from origin becomes more complicated (see e.g. Giunti and Kim 2007). The probability of detecting a different flavoured neutrino after propagating a distance d is in this case

$$\begin{aligned} P_{\nu_{\ell_1}\to\nu_{\ell_2}}(d, E) = \delta_{\ell_1\ell_2} &- 4\sum_{j>i} \mathfrak{Re}[U^*_{\ell_1 j} U_{\ell_2 j} U_{\ell_1 i} U^*_{\ell_2 i}] \sin^2\left(\frac{\Delta m^2_{ji} d}{4E_\nu}\right) \\ &- 2\sum_{j>i} \mathfrak{Im}[U_{\ell_1 j} U_{\ell_2 i} U^*_{\ell_1 i} U^*_{\_2 j}] \sin^2\left(\frac{\Delta m^2_{ji} d}{2E_\nu}\right) , \end{aligned} \tag{1.14}$$

using the PMNS mixing matrix (Giunti and Studenikin 2009).

The above formalism assumes neutrinos travel in a vacuum, however this is not necessarily the case in a physical scenario. Experiments need to take into consideration neutrinos traversing matter, thus need to account for the Mikheyev-Smirnov-Wolfenstein (MSW) effect when determining oscillation probabilities.

Mikheyev-Smirnov-Wolfenstein Effect. When neutrinos travel through matter, an additional effect which modifies the evolution of the neutrino is important. This is particularly important for Solar neutrinos, as they are created in the dense interior of the Sun, and propagate through layers of varying density en route to detectors on Earth. The potential generated from coherent elastic

forward weak scattering of neutrinos on electrons and nuclei of the ambient matter changes the effective neutrino mass. This modifies the oscillation and mixing, as these are dependent on the square mass difference, e.g. Eqns. 1.12 and 1.13.

When neutrinos travels from high density regions to low density regions, they become heavier than the surrounding matter, and in environments of varying densities, a resonant flavour transition may occur. This is known as the Mikheyev-Smirnov-Wolfenstein (MSW) effect (Wolfenstein 1978; Mikheev and Smirnov 1986). In vacuum the oscillations occur due to a mass-related difference in frequency of the mass wavefunctions, however in matter the misalignment of the phases is due to the total energy of the mass eigenstate.

Although all neutrino flavours undergo neutral scattering via the Z^0 exchange on electrons and nucleons, only electron neutrinos undergo charged scattering on electrons via the exchange of $W^{\pm}$ (see Sec. 1.1.5). If only the charged-current potential affects the electron neutrinos, the effective potential for an ultra-relativistic neutrino ν_ℓ travelling through matter is

$$V_\ell = V_{\rm CC}\delta_{\ell \rm e} + V_{\rm NC} = \sqrt{2}G_{\rm F}(n_{\rm e}\delta_{\ell \rm e} - \frac{1}{2}n_{\rm n}) \ , \tag{1.15}$$

where $n_{\rm e}$ and $n_{\rm n}$ are the electron and neutron densities in the ambient medium, respectively, and $G_{\rm F}$ is Fermi's constant. The charged-current (CC) and neutral-current (NC) potentials are given by

$$V_{\rm CC} = \sqrt{2}G_{\rm F}n_{\rm e} \tag{1.16}$$

$$V_{\rm NC} = -\frac{\sqrt{2}}{2}G_{\rm F}n_{\rm n} \ . \tag{1.17}$$

The two-neutrino mixing scenario can then be applied to the propagation of a $\nu_{\rm e}$ through an ambient electron field. The evolution of the neutrino is found using the effective mixing matrix,

$$U_{\rm M} = \begin{bmatrix} \cos\theta_{\rm M} & \sin\theta_{\rm M} \\ -\sin\theta_{\rm M} & \cos\theta_{\rm M} \end{bmatrix} \ . \tag{1.18}$$

The matter mixing angle $\theta_{\rm M}$ is given by

$$\tan(2\theta_{\rm M}) = \tan(2\theta)\left[1 - \frac{A_{\rm CC}}{\Delta m^2\cos(2\theta)}\right]^{-1} \ , \tag{1.19}$$

and the effective square-mass difference is

$$\Delta m^2_{\rm M} = \sqrt{[\Delta^2\cos(2\theta) - A_{\rm CC}]^2 + [\Delta m^2 \sin(2\theta)]^2}\ . \tag{1.20}$$

Here, $A_{\rm CC} = 2E_\nu V_{\rm CC} = 2\sqrt{2}E_\nu G_{\rm F} N_{\rm e}$. The resonance transition occurs when $A_{\rm CC} \to A^{\rm R}_{\rm CC} = \Delta m^2 \cos(2\theta)$, which corresponds to an electron density of $n_{\rm e} = \Delta m^2 \cos(2\theta)/2\sqrt{2}E_\nu G_{\rm F}$. At the resonance, the mixing angle $\theta_{\rm M}$ is maximal, thus if the resonance region is wide enough, there can be a total transition between flavours.

The transition probability of the oscillation in constant matter density is

$$P_{\nu_{\rm e}\to\nu_\mu}(d_{\rm M}) = \sin^2(2\theta_{\rm M})\sin^2\left(\frac{\Delta m^2_{\rm M} d_{\rm M}}{4E}\right)\ , \tag{1.21}$$

where $d_{\rm M}$ is the distance travelled from the source. The form of this transition probability is similar to that of the vacuum probability in Eqn. 1.13. If the matter density is not constant the effect of $d\theta_{\rm M}/d(d_{\rm M})$ must be taken into account by

$$\frac{d\theta_{\rm M}}{d(d_{\rm M})} = \frac{1}{2}\frac{\sin(2\theta_{\rm M})}{\Delta^2_{\rm M}}\frac{dA_{\rm CC}}{d(d_{\rm M})}\ . \tag{1.22}$$

The MSW effect is important to account for not only in studying the oscillation phenomenon, but also in studying astrophysical neutrinos, which are created in the dense interior of stars, as well as other environments, e.g. supernovae and astrophysical jets.

1.1.4 Neutrino Production

Neutrino Production in β-decays. The production of neutrinos is highly energy dependent, due to the decay of hadrons. The prototypical weak interaction producing a neutrino, the β^--decay (see Fig. 1.3), is of the form

$$\mathrm{n} \to \mathrm{p} + \mathrm{e}^- + \bar{\nu}_{\rm e}\ , \tag{1.23}$$

and usually occurs in neutron rich nuclei.

The process of electron capture produces a neutrino through the interaction of a proton and electron,

$$\mathrm{p} + \mathrm{e}^- \to \mathrm{n} + \nu_{\rm e}\ . \tag{1.24}$$

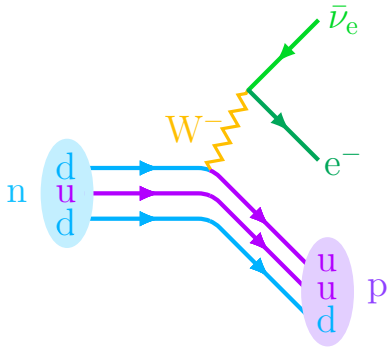

Fig. 1.3: Illustration of the neutron (β^-) decay, for which a proton, electron, and anti-electron neutrino are produced. This is a weak interaction mediated by the W$^-$ boson, indicated by the resultant neutrino product.

The decay of a proton, however, only occurs in nuclei. It is known as β^+-decay, i.e.

$$\mathrm{p} \rightarrow \mathrm{n} + \mathrm{e}^+ + \nu_\mathrm{e} \ , \tag{1.25}$$

and is the decay path of nuclei with proton excess. Due to the mass difference between a proton and neutron, it requires additional energy to occur – the nuclear binding energy. This binding energy is the potential energy released from the constituent nucleons in a fusion reaction. It is given by the energy difference between the sum of the nucleons (and electrons) and the measured mass of the atom $N(A, Z)$,

$$B(A, Z) = [Zm_\mathrm{p} + (A - Z)m_\mathrm{n}] - m_{N(A,Z)} \ , \tag{1.26}$$

where A is the atomic mass number (the sum of protons and neutrons in the nucleus) and Z is the number of protons.

The energy released in nuclear reactions is represented by the Q-value, which is the difference between the kinetic energy of the initial and final states of the system. Accounting for the rest masses of the reactants and products of the process,

$$Q = (m_\mathrm{before} - m_\mathrm{after})\mathrm{c}^2 \ , \tag{1.27}$$

gives the energy released as photons and neutrinos. In the case of positron production in a plasma, the positron will annihilate with ambient free electrons, and produce heat following $e^+ + e^- \rightarrow 2\gamma$. Because the Q-value is the

total energy released in a given nuclear decay, this heat is added to express the effective Q-value. As it is determined from the binding energy of the nucleus, the kinetic energy of an emitted neutrino will never exceed nuclear energies, i.e. $\sim$ MeV.

In an astrophysical context, β-decays are the dominant reaction in stellar sources, with energy releases from a few keV in low-energy thermonuclear interactions in stars, to a few tens of MeV in supernova explosions.

Neutrino production in HE proton interactions. The production of ultra-high energy (UHE) neutrinos is possible through hadronic decays in highly energetic environments (see Sec. 1.2). The inelastic interaction (see discussion on cross sections in Sec. 5.3) between energetic protons and ambient matter fields produce neutrinos through the decay of the secondary neutrons and pions (see below). The dominant reactions leading to the production of pions are

$$\mathrm{p} + \mathrm{p} \rightarrow \begin{cases} \mathrm{n} + \mathrm{p} + \pi^+ \\ \mathrm{p} + \mathrm{p} + \pi^+ + \pi^- \\ \mathrm{p} + \mathrm{p} + \pi^0 \end{cases} . \tag{1.28}$$

The threshold energy for neutral pion production from pp interactions is

$$E_{\mathrm{th},\pi^0}/\mathrm{c}^2 = m_\mathrm{p} + 2m_\pi \left(1 + \frac{m_\pi}{4m_\mathrm{p}}\right) = 1.218 \text{ GeV/c}^2 , \tag{1.29}$$

where $m_{\pi^0} = 134.98$ MeV/c^2. For the production of a charged pion, the threshold energy of the proton field (with observer frame energy E_cp) is given by

$$E_{\mathrm{th},\pi^+}/\mathrm{c}^2 = \frac{m_\mathrm{p}}{2}(\chi - 2) + \chi m_\mathrm{p} + \chi m_\pi \left(1 + \frac{m_\pi}{2\chi m_\mathrm{p}}\right) = 1.220 \text{ GeV/c}^2 , \tag{1.30}$$

where

$$\chi = \frac{m_\mathrm{n}}{m_\mathrm{p}} + 1 , \tag{1.31}$$

and $m_{\pi^+} = 139.57$ MeV/c^2. The incident proton then requires a Lorentz factor of

$$\gamma_\mathrm{p} \gtrsim \begin{cases} \dfrac{609 \text{ MeV}}{E_\mathrm{cp}} & (\mathrm{pp} \rightarrow \mathrm{pp}\pi^0) \\ \dfrac{610 \text{ MeV}}{E_\mathrm{cp}} & (\mathrm{pp} \rightarrow \mathrm{n}\mathrm{p}\pi^+) \end{cases} \tag{1.32}$$

to produce a neutral or charged pion.

The third reaction produces both π^+ and π^- particles, and the threshold energy is

$$E_{\mathrm{th},\pi^+\pi^-}/\mathrm{c}^2 = m_\mathrm{p} + 2N_\pi m_\pi \left(1 + \frac{N_\pi m_\pi}{4m_\mathrm{p}}\right) = 1.538\ \mathrm{GeV/c}^2\ , \tag{1.33}$$

for $N_\pi = 2$, giving a Lorentz factor of the incident proton

$$\gamma_\mathrm{p} \gtrsim \frac{769\ \mathrm{MeV}}{E_\mathrm{cp}}\ . \tag{1.34}$$

With increasing energy of the incident proton, the number of possible decay channels increase, as does the pion multiplicity. This is due to the production and subsequent decay of the resonances (see Fig. 1.4), as each decay can produce more than one pion.

Below $\sim$ 2, GeV the pp-interaction is dominated by the single-pion production channel, and the dominant resonance is the Δ-baryon. These interactions are studied in several ground-based experiments. Towards higher energies, however, the experimental data is increasingly lacking, and the details of the interactions are scarce. Above $\sim$ 2 GeV, intermediate resonances may form, leading to numerous decay channels.

Generalising the pp-interactions to include multiplicity gives

$$\mathrm{p} + \mathrm{p} \rightarrow \begin{cases} \mathrm{p} + \Delta^+ \rightarrow \begin{cases} \mathrm{p} + \mathrm{n} + \pi^+ + \xi_0(\pi^0) + \xi_\pm(\pi^+ + \pi^-) \\ \mathrm{p} + \mathrm{p} + \pi^0 + \xi_0(\pi^0) + \xi_\pm(\pi^+ + \pi^-) \end{cases} \\ \mathrm{n} + \Delta^{++} \rightarrow \begin{cases} \mathrm{n} + \mathrm{p} + \pi^+ + \xi_0(\pi^0) + \xi_\pm(\pi^+ + \pi^-) \\ \mathrm{n} + \mathrm{n} + 2(\pi^+) + \xi_0(\pi^0) + \xi_\pm(\pi^+ + \pi^-) \end{cases} \end{cases}\ , \tag{1.35}$$

where ξ_0 and $\xi_\pm$ are the multiplicities for neutral and charged pions, respectively, and the Δ^+ and Δ^{++} baryons are the resonances (Fig. 1.4). The pp-interactions are particularly efficient at lower energies in astrophysical systems. However, at higher energies ($\sim$GeV, see Begelman et al. 1990) other processes begin to dominate the proton cooling, such as proton-photon interactions.

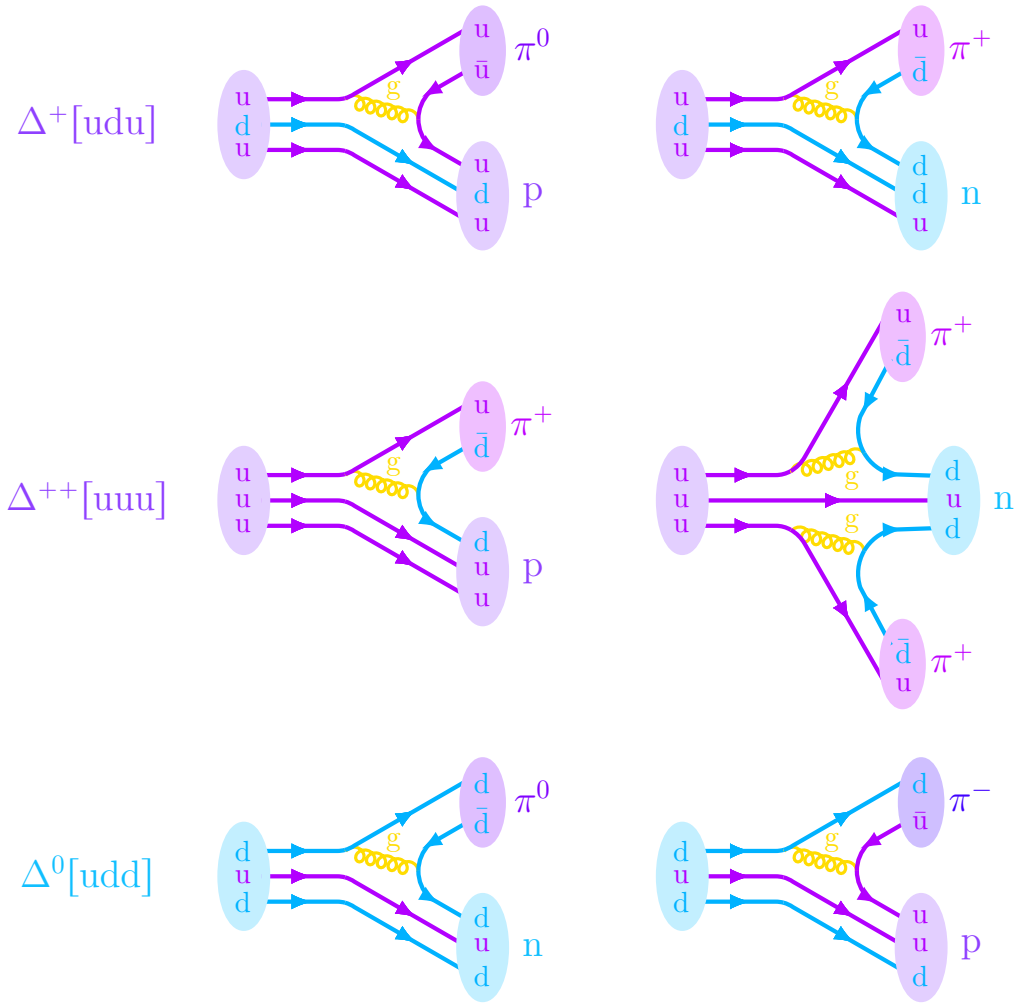

Fig. 1.4: The interaction between a baryon and a secondary photon or baryon leads to meson production through the Δ-resonance. *Top:* The decay of the Δ^+ decay, which is produced in pp- or pγ interactions (Eqns. 1.35 and 1.36). *Middle:* The Δ^{++}-decay produced in pp-interactions (Eqn. 1.35). *Bottom:* The Δ^0-baryon is produced in nγ-interactions (Eqn. 1.44).

An energetic proton interacting with ambient radiation fields leads to photomeson production, through the decay of the Δ^+-resonance (Fig. 1.4),

$$\mathrm{p} + \gamma \rightarrow \Delta^+ \rightarrow \begin{cases} \mathrm{p} + \pi^0 + \xi_0(\pi^0) + \xi_\pm(\pi^+ + \pi^-) \\ \mathrm{n} + \pi^+ + \xi_0(\pi^0) + \xi_\pm(\pi^+ + \pi^-) \end{cases} . \tag{1.36}$$

The pions will subsequently decay to neutrinos, among other particles. Similar to the pp-interactions of Eqn. 1.35, the single-pion production (i.e. when $\xi_0 = \xi_\pm = 0$) is dominant at lower energies. The branching ratio is $\mathrm{Br}(\Delta^+ \rightarrow \mathrm{p} + \pi^0) = 2/3$, and $\mathrm{Br}(\Delta^+ \rightarrow \mathrm{n} + \pi^+) = 1/3$. Measured in the pro-

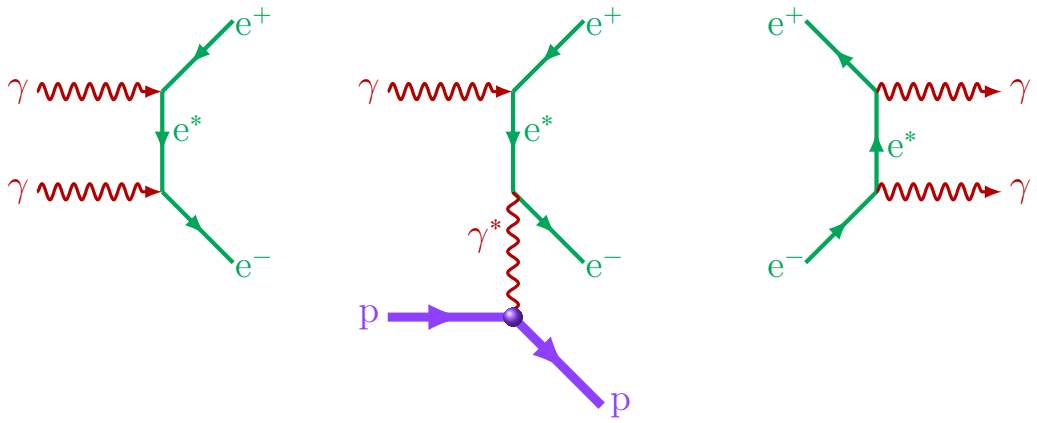

Fig. 1.5: Illustration of interactions with electron-positron pairs. *Left:* Breit-Wheeler pair production, described in Eqn. 1.42. *Centre:* Pair production due to the interaction of a photon with a baryon, known as Bethe-Heitler pair production (Eqn. 1.41). *Right:* Pair annihilation producing a pair of photons (Eqn. 1.43).

ton rest frame, the threshold energy of the photon for the interaction to produce a neutral pion is

$$\varepsilon^*_{\mathrm{th},\pi^0}/\mathrm{c}^2 = m_\pi \left(1 + \frac{m_\pi}{2m_\mathrm{p}}\right) = 144.69\ \mathrm{MeV/c^2}\ . \tag{1.37}$$

In the proton rest frame, the photon energy is $\varepsilon^* = \varepsilon\gamma_\mathrm{p}(1 - \beta_\mathrm{p}\cos\theta)$, where ε is the photon energy in the observer frame. A commonly assumed head-on collision gives the collision angle $\theta = \pi$, hence $\varepsilon^* = 2\varepsilon\gamma_\mathrm{p}$. The incident proton must therefore have a Lorentz factor of

$$\gamma_\mathrm{p} \gtrsim \frac{72.3\ \mathrm{MeV}}{\varepsilon}\ . \tag{1.38}$$

Similarly, the threshold energy for charged pion production is

$$\varepsilon^*_{\mathrm{th},\pi^+}/\mathrm{c}^2 = \frac{m_\mathrm{p}}{2}(\chi - 1) + \chi m_\pi \left(1 + \frac{m_\pi}{2\chi m_\mathrm{p}}\right) = 151.44\ \mathrm{MeV/c^2}\ , \tag{1.39}$$

where $\chi = m_\mathrm{n}/m_\mathrm{p}$. The incident proton Lorentz factor therefore needs to be

$$\gamma_\mathrm{p} \gtrsim \frac{75.7\ \mathrm{MeV}}{\varepsilon} \tag{1.40}$$

for the interaction to produce a charged pion.

The photomeson channel competes with Bethe-Heitler pair production, which is illustrated in Fig. 1.5. It follows

$$\mathrm{p} + \gamma \rightarrow \mathrm{p} + \mathrm{e}^- + \mathrm{e}^+\ , \tag{1.41}$$

and is triggered at a lower energy threshold ($\varepsilon^*_{\mathrm{th,e^\pm}} \approx 1.02$ MeV). This interaction channel becomes important in the high-energy emission from astrophysical environments, as the production rate increases monotonically with the energy of the photon-target (Begelman et al. 1990). Pair-production can however also occur in the interaction of two γ-rays,

$$\gamma + \gamma \rightarrow \mathrm{e}^- + \mathrm{e}^+ \ , \tag{1.42}$$

known as Breit-Wheeler pair production (Fig. 1.5). Electron-positron pairs may suffer annihilation, producing γ-rays by

$$e^- + e^+ \rightarrow \gamma + \gamma \ , \tag{1.43}$$

also shown in Fig. 1.5. These leptonic and photonic products must be considered when studying emission from hadronic interactions in astrophysical environments, e.g. when assuming a scaling relations between γ-ray, cosmic ray, and neutrino emissions.

Products of proton interactions. The secondaries of the pγ- and pp-interactions are predominantly neutrons, protons and pions, as seen in Eqns. 1.35 and 1.36. Other more exotic mesons, such as kaons and eta mesons, are also possible products. However, due to their masses ($\gtrsim 500$ MeV) they require significantly higher primary energies to be produced. Their production rates are therefore quite low, and the emission from neutrinos produced in the decay of these mesons is not detectable by current instruments (e.g. Asano and Nagataki 2006)

Secondary protons in astrophysical systems will either continue to suffer energy losses through repeated hadronic interactions, such as those described in Eqns. 1.35 and 1.36, until their energies are too low for these interactions to occur (e.g. Eqns. 1.38 and 1.40) – or escape the confinement of the source as cosmic rays (see Sec. 1.2). Secondary neutrons can also lose energy through photomeson production similar to that of Eqn 1.36, in the photo-induced conversion to protons

$$\mathrm{n} + \gamma \rightarrow \Delta^0 \rightarrow \begin{cases} p + \pi^- + \xi_0(\pi^0) + \xi_\pm(\pi^+ + \pi^-) \\ n + \pi^0 + \xi_0(\pi^0) + \xi_\pm(\pi^+ + \pi^-) \end{cases} \ . \tag{1.44}$$

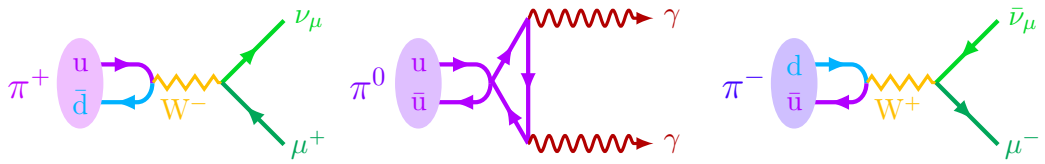

Fig. 1.6: Illustration of the decay of pions. The charged pions decay to muonic leptons, whereas the neutral pion decays to photons, described in Eqns. 1.45 - 1.47. *Left:* The decay of a π^+-meson, mediated by the positive W-boson. *Centre:* The decay of a neutral pion results in the production of 2γ. *Right:* The decay of a π^--meson via the negative W-boson.

If the neutron escapes its confinement, it can also decay directly to neutrinos through the beta decay reaction given in Eqn. 1.23. Neutrons are therefore a source of both cosmic ray and neutrino emission from astrophysical systems.

As illustrated in Fig. 1.6, the pions will decay as

$$\pi^+ \rightarrow \mu^+ + \nu_\mu \tag{1.45}$$

$$\pi^- \rightarrow \mu^- + \bar{\nu}_\mu \tag{1.46}$$

$$\pi^0 \rightarrow \gamma + \gamma \ , \tag{1.47}$$

hence, the charged pions contribute to the cosmic neutrino content, and the decay of neutral pions adds to the extragalactic γ-ray background (EBL).

The subsequent decay of muons (Fig. 1.7) leads to additional neutrinos through

$$\mu^+ \rightarrow \mathrm{e}^+ + \nu_\mathrm{e} + \bar{\nu}_\mu \tag{1.48}$$

$$\mu^- \rightarrow \mathrm{e}^- + \bar{\nu}_\mathrm{e} + \nu_\mu \ , \tag{1.49}$$

and thus contribute to the diffuse neutrino flux. If the synchrotron energy losses are low or negligible, the neutrino fluxes may be at observable energies.

1.1.5 Neutrino Interactions

A neutrino interacts weakly with matter through the exchange of the weak force carriers, the $W^\pm$ and Z^0 bosons, illustrated in Fig. 1.8. These are dependent on the energy range and neutrino flavour. In charged-current (CC) interactions a neutrino of flavour $\ell = \{\mathrm{e}, \mu, \tau\}$ interacts with a nucleon X, through the exchange of the $W^\pm$ bosons. It is thus a neutrino capture process

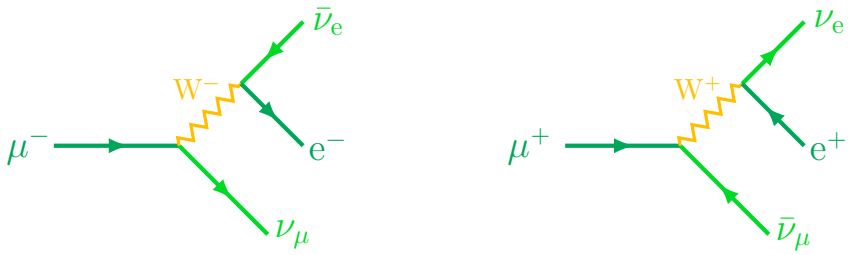

Fig. 1.7: Illustration of the decay of muons, which results in a muon neutrino, and an electron and electron neutrino mediated by the W-boson. *Left:* The decay of a negative muon. *Right:* The decay of a positive muon.

following

$$\nu_\ell + X \rightarrow \ell^- + X' \ , \tag{1.50}$$

producing a lepton, $\ell = \{e, \mu, \tau\}$, and a hadron X' that will produce a jet (e.g. $\nu_\ell + n \rightarrow \ell^- + p$).

A CC interaction which occurs in proton rich nuclei is known as inverse β-decay, and is dominant in stellar sources. It is commonly used in nuclear reactors, in the interaction

$$p + \nu_e \rightarrow n + e^- \ , \tag{1.51}$$

whereby the escaping electron goes through electron capture (Eqn. 1.24, i.e. the reverse of the inverse β-decay process).

Nuclear reactors and stellar environments have an energy threshold only allowing ν_e to participate in CC interactions, whereas particle accelerators can produce 2nd generation and a few 3rd generation leptons (see Sec. 1.3).

Neutral current (NC) interactions occur through the exchange of the Z^0 boson, for which all flavours can participate,

$$\nu_\ell + X \rightarrow \nu_\ell + X' \ . \tag{1.52}$$

This also leads to a hadronic cascade, e.g. $\nu_\ell + n(p) \rightarrow \nu_\ell + n(p)$.

The elastic scattering (ES) process is a third reaction by which the neutrino interacts with matter. The neutrino scatters off an electron mediated by one of the weak force carriers, following

$$\nu_\ell + e^- \rightarrow \nu_\ell + e^- \ . \tag{1.53}$$

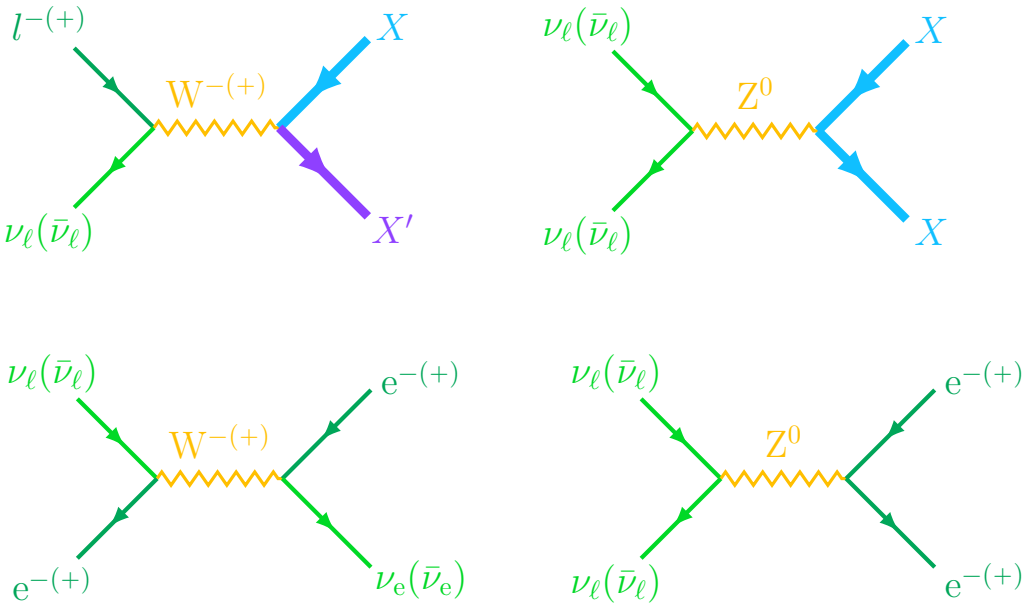

Fig. 1.8: Illustration of possible interactions between neutrinos and matter. The top left figure shows the CC interaction between a neutrino ν_ℓ and a nucleon X, producing a lepton and nucleon X'; top right shows the neutral interaction scattering the two incoming particles without a charge transfer. The bottom left figure illustrates the ES process mediated by a W-boson; and the bottom right figure illustrates ES scattering mediated by a neutral Z-boson. See text for details.

These three ways for neutrinos to interact with matter are sensitive to energy and flavour. Neutrino experiment and observatories can therefore probe a variety of phenomena within particle physics and astrophysics by looking at the details of the interactions. This is elaborated on in Sec. 1.3.

1.2 Neutrino Astrophysics

Detection of naturally occurring (extra-terrestrial) neutrinos has been an ongoing endeavour since the late 1960s, when R. Davis Jr. and J. N. Bahcall offered a direct test for stellar evolution models involving nuclear fusion (see e.g. Bahcall 1969; Bahcall and Davis 2000). They made the first detection of Solar neutrinos (ν_e), thus solidifying the importance of studying neutrinos produced through astrophysical phenomena. This momentous discovery was the first step towards bridging neutrino physics with astronomy.

Astrophysical neutrinos are produced over a wide range of energies, depending on the processes they emerge from (Fig. 1.9). Neutrinos from the

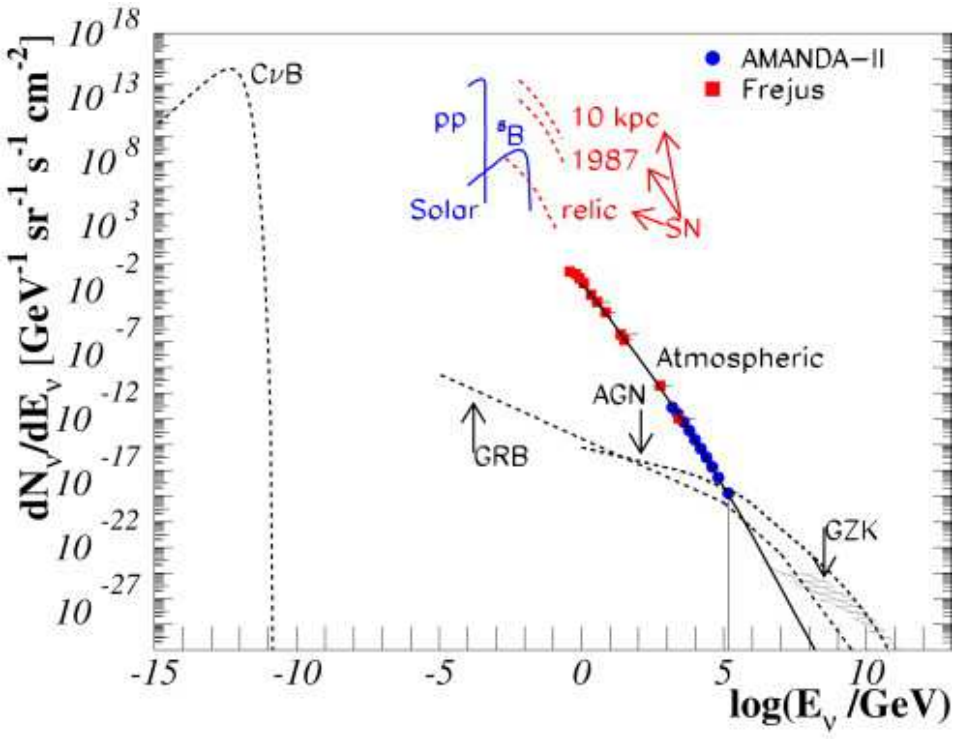

Fig. 1.9: Expected source contributions to the SED of astrophysical neutrinos, supported by neutrino detections by *AMANDA-II* and *Frejus* (see Sec. 1.3). The component at the lowest energies is the cosmic neutrino background (CνB). Solar neutrinos are produced at MeV-energies, with SN neutrinos dominating at energies of a few tens of MeV. At energies $\gtrsim$ GeV, the atmospheric background is prominent. Neutrinos at the highest energies ($\gtrsim 10^5$ GeV) are presumably produced in the brightest and most energetic sources known, e.g. GRBs and AGN. Figure is taken from Becker (2008).

Sun and other stellar objects are produced in thermonuclear reactions, and therefore have energies of order MeV. Supernova neutrinos can reach up to a few tens of MeV, as they are produced in the most energetic phase of a stellar source. The atmospheric neutrino background is a consequence of interactions of ultrahigh-energy cosmic ray (UHECR) particles with the upper atmosphere. These cascade down as a shower of secondary particles, including a measured neutrino flux at energies $\gtrsim$ GeV. This background is heavily influenced by the primary CR spectrum and composition.

As UHECR particles propagate through space from their source of origin, they will produce a population of so-called cosmogenic neutrinos in their interaction with ambient matter and radiation fields. The Galactic sources

responsible for the production of UHECRs are pulsars, supernova remnants (SNRs) and merging neutron stars.

The origin of extra-galactic UHECR flux, on the other hand, has not yet been identified. There are, however, a number of source populations that are observed to fulfil the requirements for the production of particles to UHEs, such as the ability to generate large-scale shocks. These cosmic accelerators include sources with a supermassive black hole (SMBH) core, such as active galactic nuclei (AGN), and extremely bright gamma-ray burst (GRB) events produced by either particularly massive supernovae or merging neutron stars. They are among the most luminous point sources in the Universe, and can therefore be observed at distances far beyond our Galaxy. AGN are particularly interesting, due to their persistent existence throughout the history of large-scale structures in the Universe, and are also abundant in the local Universe. Other extra-galactic candidate sources are starburst galaxies and bright galactic centres; and, as large-scale shocks are capable of accelerating particles to observed energies, shocks in the intergalactic medium (IGM) are also possible source candidates.

The neutrino spectral energy distribution is a superposition of the flux emitted from the various source populations, shown in Fig. 1.9. The diffuse emission from various Galactic source populations dominates at MeV-energies. Above GeV-energies, neutrinos are produced by UHECRs interacting with the atmosphere or within extra-galactic point sources.

As discussed in Sec. 1.1.5, neutrinos are produced in hadronic processes, hence, the production path for UHECR protons in a given source will inevitably produce neutrinos as well. The UHECR composition is found to be largely made up of high-energy protons, α-particles and some heavier nuclei. Interactions with radiation or matter fields within the source environment will therefore produce a population of astrophysical UHE neutrinos. The fluxes of HE neutrinos of atmospheric or cosmogenic origin, or generated within the source, can in principle be told apart due to the steepness of their spectra (see Fig. 1.10, see also e.g. Gaisser et al. 1995).

At the very lowest energies of the neutrino content of the Universe, is the

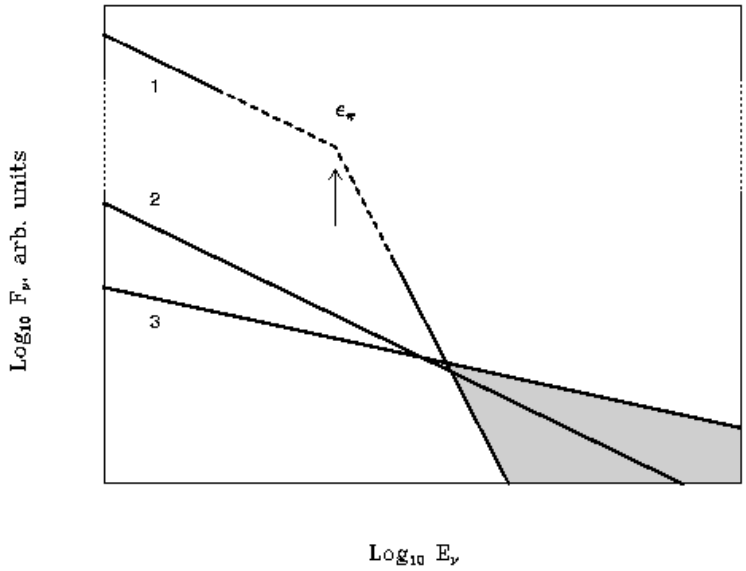

Fig. 1.10: Schematic representation of neutrino fluxes originating from atmospheric processes (indicated on the figure with 1); produced by Galactic CRs interacting with the interstellar medium (2); or within the source itself (3). The arrow is pointing at the neutrino energy at the atmospheric spectral break. Figure is taken from Gaisser et al. (1995).

cosmic neutrino background (CνB) that is a relic neutrino population from the first two seconds after the Big Bang, when neutrinos decoupled from matter. It peaks at energies of $\sim 10^{-4}$ eV (or a temperature of 1.945 K), which is far below the energy threshold of current neutrino detectors.

A brief summary of the production of neutrinos below GeV-energies, i.e. stellar neutrinos, including Solar and SN neutrinos, and the CνB is given in Appendix B.

1.2.1 The Atmospheric Neutrino Background

When extra-terrestrial charged UHECRs impinge on the Earth, the first interactions occur in the upper atmosphere. The atmosphere consists of atomic nuclei, mostly oxygen and nitrogen, and the interactions produce secondary showers of pions ($\pi^+\pi^-$), kaons ($K^+K^-K^0$) and muons ($\mu^+\mu^-$). These are unstable particles, and consequently decay weakly into observable neutrinos.

The spectrum of the atmospheric neutrino background follows the energy spectrum of UHECRs, thus spans over many magnitudes in energy. It covers a detectable flux across the energy range of $1 \lesssim E_\nu[\mathrm{GeV}] \lesssim 10^5$. The uniform

background is valuable as a test for experiments, and is an important source of neutrinos for particle physics studies, such as for oscillation experiments (see Sec. 1.3). It also provides a normalisation of the flux from astrophysical neutrinos.

1.2.2 Cosmogenic Neutrinos

A central area of astroparticle physics is the study of UHECRs (see e.g. review by Kotera and Olinto 2011). These particles are messengers from, in some cases, distant sources, and are prime candidates to diagnose the environments in which they are produced. Additionally, as they propagate through space, interactions with ambient radiation and matter fields will produce a population of cosmogenic neutrinos.

The composition of UHECRs is debated, but observations lean towards a mix of predominantly protons, α-particles and possibly a component of heavier nuclei, such as iron (Kotera and Olinto 2011). A consequence of the charged composition of UHECRs is that the path they follow travelling through space is affected by cosmic magnetic fields. The degree of deflection is dependent on the UHECR energy; i.e. composition and properties of the production region within the source; and the strength of the magnetic fields they traverse. Furthermore, as they propagate through space, the UHECR particles interact with radiation and matter fields in the intergalactic and Galactic medium (IGM and GM, respectively), resulting in the attenuation of the emission.

Cosmic radiation fields are particularly important target fields; one of which is the ubiquitous cosmic microwave background (CMB), consisting of a thermal photon population with energies $\sim 10^{-4}$ eV (or a temperature of 2.725 K). This background is the emission from when the Universe became transparent, allowing photons to travel freely through space, and took place 380 000 years after the Big Bang. Cosmogenic neutrinos are in this case produced by

$$\mathrm{p_{UHECR}} + \gamma_{\mathrm{CMB}} \rightarrow \pi^{+} \rightarrow \nu_{\mu} \mathrm{e}^{+} \nu_{\mathrm{e}} \bar{\nu}_{\mathrm{e}} \ . \tag{1.54}$$

requiring the primary proton to have a Lorentz factor of $\gamma_{\mathrm{p}} \gtrsim 10^{11}$ (see Eqn. 1.40).

The extragalactic background light (EBL) is the diffuse photon background consisting of radiation from star formation and AGN emission throughout the history of the Universe. It extends several decades of energy, with an observed spectrum covering the infrared (IR) to ultraviolet (UV) wavebands (i.e. $10^{-3} \lesssim E_{\rm EBL}$ [eV] $\lesssim 10^{2}$). These pγ-interactions between UHECRs and these radiation fields are described in Eqn. 1.36 in Sec. 1.1.4.

Similarly, UHECRs participate in hadronic interactions pp-interactions (see Eqn. 1.35 in Sec. 1.1.4) when they propagate through the IGM or the interstellar medium (ISM). The pγ- and pp-interaction channels will both lead to the production of UHE neutrinos, and a comparable emission of γ-rays; the former due to the decay of charged pions; and the latter due to the decay of the neutral pion (see Eqns. 1.45-1.47). The energy spectra of these products therefore follows that of the UHECRs. The origin and energy distribution of cosmogenic neutrinos has been widely discussed since the 1970s (e.g. Beresinsky and Zatsepin 1969; Stecker 1973; Berezinskii and Ozernoi 1981; Learned and Mannheim 2000; Engel et al. 2001; Anchordoqui et al. 2007; Becker 2008; Kotera et al. 2010; Berezinsky et al. 2011; Ahlers and Halzen 2012; Sigl and van Vliet 2014).

The observed cosmic ray energy spectrum is remarkably detailed, ranging several orders of magnitude. It follows a broken power law, $\propto E^{-\alpha}$, with spectral index α, as shown in Fig. 1.11 and has well-defined spectral breaks (see e.g. Hillas 2006; Kotera and Olinto 2011). Below the knee (spectral break at $E_{\rm UHECR} \sim 10^{6}$ GeV), the spectral slope is $\alpha \approx 2.7$.

At energies around $10^{6}-10^{9}$ GeV, a transition in the spectrum from Galactic to extra-galactic CRs, is expected to occur. The transition to extragalactic sources is determined by the limits of acceleration feasible in known Galactic objects; such as SNRs, pulsars and merging neutron stars. A second knee is observed at $E_{\rm UHECR} \sim 3 \times 10^{8}$ GeV, and the slope between the two knee-features is $\alpha \approx 3$. Between the second knee and the ankle ($E_{\rm UHECR} \sim 4 \times 10^{9}$ GeV), the slope is $\alpha \approx 3.3$.

Above the ankle, the slope is $\alpha \approx 2.6$, up to an observed suppression in the spectrum at $E_{\rm UHECR} \gtrsim 3 \times 10^{10}$ GeV (see e.g. Abbasi et al. 2008;

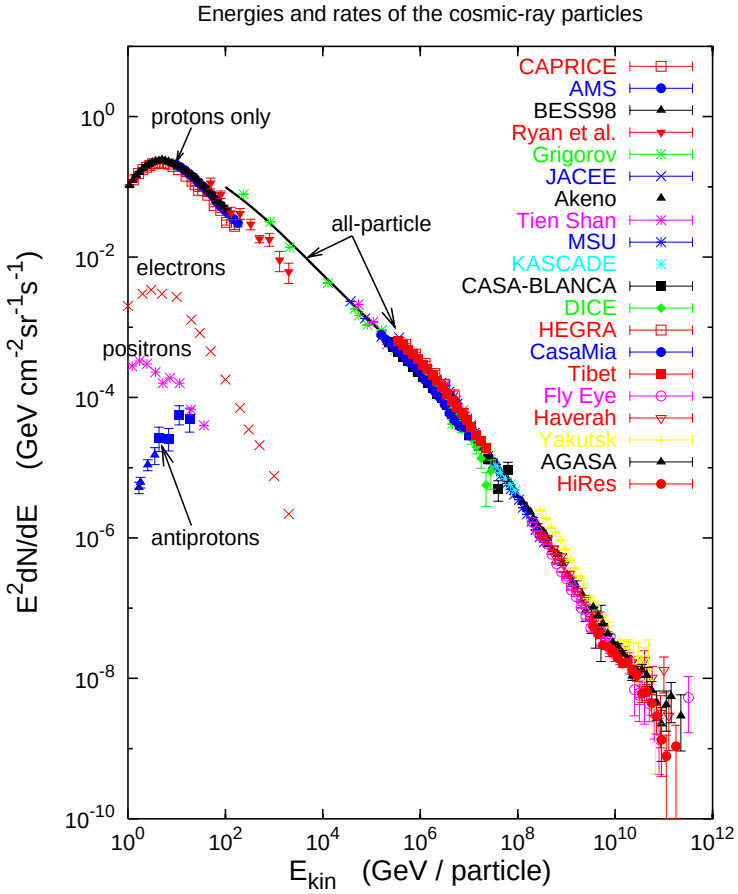

Fig. 1.11: The observed UHECR spectrum is exceptionally detailed, with three identifiable breaks, in an otherwise uniform distribution. Figure is taken from Hillas (2006).

Abraham et al. 2008). This spectral feature is consistent with the Greisen-Zatsepin-Kuzmin (GZK) cut-off (Greisen 1966; Zatsepin and Kuz'min 1966), which limits the maximum energy of UHECRs due to energy losses in pγ-interactions between propagating UHECRs and extragalactic radiation fields. It may, however, also be a consequence of the maximum particle energy that the sources are capable of generating. UHECRs are observed at energies $\sim 10^{11}$ GeV (see e.g. Linsley 1963; Pierre Auger Collaboration et al. 2007; Kotera and Olinto 2011), which sets a lower limit to the Lorentz factor of the primary particle (see Eqn. 1.40). The highest energy UHECR was detected at an energy of 3×10^{11} GeV (Bird et al. 1993).

Photomeson production is a particularly efficient proton energy loss mechanism, and limits the distances that observed UHECRs have travelled. This is known as the GZK horizon, and refers to the pγ-interaction between UHECRs

and CMB photons. The interaction limits the maximum energy that UHECRs can have if travelling across distances beyond $50 - 100$ Mpc, as protons are attenuated in the pγ-interactions (see Eqns. 1.36 and 1.41). In comparison, the diameter of the Virgo Supercluster is about 30 Mpc.

The GZK mechanism implies that UHECRs with energies above about $\approx 3 \times 10^{11}$ GeV must have been produced within the GZK horizon. The detection of UHECRs exceeding the GZK energy threshold indicates that within the GZK horizon, there exist cosmic accelerators. These populations are also expected to produce a population of so-called GZK neutrinos. The sources are, however, not yet confirmed.

1.2.3 Neutrinos from Cosmic Accelerators

Interactions between charged UHECRs and ambient radiation and matter fields will naturally lead to the production of cosmogenic neutrinos. In addition to the neutrino signal from propagating UHECRs, it is therefore expected that neutrino production also takes place within the same sources that are responsible for the production of UHECR particles. As UHECRs have been observed at energies up to $\sim 10^{11}$ GeV, their production requires highly violent astrophysical source environments. Candidate sources must be cosmic accelerators with strong magnetic fields and strong radiative emission, thus capable of generating a population of highly energetic protons (e.g. Rachen 2000; Kotera and Olinto 2011). Assuming that the primary energetic proton population is larger than that escaping as UHECRs, neutrinos will consequently be produced in the interactions between these primary protons and ambient matter or radiation fields in the source.

The maximum energy that primary interacting particles can attain in a powerful accelerator can be estimated from a relation between the size of the source and its magnetic field strength, as the source must be able to confine and accelerate particles to the required energies. This implies that the radius of the circular motion of a charged particle i travelling in a uniform magnetic field B within the source (the Larmor radius, $r_{\rm L} = E_i/(q_{\rm e}B)$) must be smaller than the size of the acceleration region, r. This is known as the Hillas criterion

(Hillas 1984), given by

$$E_{\rm max}({\rm erg}) = Zq_{\rm e}({\rm esu})\ B({\rm G})\ r({\rm cm})\ , \tag{1.55}$$

where $Zq_{\rm e}$ is the charge of the particle, and $q_{\rm e}$ is the elementary charge magnitude in electrostatic units (esu); B is the strength of the magnetic field in units of Gauss, and r is the size of the accelerating source in units of centimetres. For a primary proton population ($Z = 1$), the maximum energy in units of GeV is

$$E_{\rm p,max}({\rm GeV}) \approx 3 \times 10^{-7}\ B({\rm G})\ r({\rm cm})\ . \tag{1.56}$$

The associated Hillas diagram summarises powerful sources capable of producing the highest energy cosmic rays, seen in Fig. 1.12. Candidate sources of UHECRs include AGN, GRBs, SNRs, and neutron stars. Within the AGN system, energetically suitable environments include the AGN core, jets, and the terminal shock region of the outer lobe.

The Hillas criterion is however purely an upper limit, as there are other considerations which determine the maximum energy of the particles. Energy losses due various radiative processes within the sources must be taken into account. The acceleration mechanism is not well understood, though observations indicate shock acceleration as a strong possibility, through e.g. Fermi processes (see Sec. 5.2.2). For significant energy gain, the acceleration timescale must be shorter than the timescale for the particles to escape the confinement region. Accounting for processes of energy gain and losses imparts a second constraint, ensuring there is sufficient time to reach the required energies. This means that for sufficient energy gain, the timescale of acceleration $t_{\rm acc} < t_{\rm loss}$, where the cooling timescale $t_{\rm loss}$ includes losses due to synchrotron emission ($t_{\rm synch}$), adiabatic expansion ($t_{\rm ad}$), and energy losses due to interactions with ambient radiative or hadronic media, given by the timescales $t_{\rm p\gamma}$ and $t_{\rm pp}$ (see Sec. 5.3).

A third constraint, the GZK limit, is imposed by the observation of UHECRs (with energies $E_{\rm p} \gtrsim 3 \times 10^{10}$ GeV) so that the acceleration is required to be faster than the attenuation of UHECR upon interaction with the CMB. This implies that the sources must be found within the GZK horizon, with

radius $r_{\rm GZK} \sim 50 - 100$ Mpc), depending on the energy and composition of the cosmic rays. The implications for UHE neutrino sources is that a source population should exist both locally and at larger distances. A UHECR signal should therefore be expected to correlate with the UHE neutrino signal within the GZK horizon. At larger distances, however, only the neutrino population is expected to reach us with negligible attenuation. If these criteria are fulfilled, neutrino production also requires that matter or radiation fields in the source are opaque to protons so that interactions may occur. Neutrino production will therefore set constraints on the strength of the source magnetic field and the optical depth of the ambient fields that allow interactions to occur.

Neutrino production is intimately connected to the production of UHECRs and γ-rays, as shown in Eqns. 1.36 and 1.35. Despite the evident link to these high-energy messenger particles, the neutrino emission may deviate significantly from a correlation to the UHECR and γ-ray signals derived from the production channels. If the source environment is significantly opaque, it would effectively absorb these particles whereas neutrinos would escape freely (Berezinsky and Dokuchaev 2006). Additionally, the intensity of the escaping UHECR and γ-ray emission would suffer losses when travelling through the extragalactic background (e.g. the CMB), and CRs are deflected in cosmological magnetic fields. It is, however, a good indicator of possible sources of neutrinos, due to this primary connection of these three high-energy messengers.

A number of candidate sources have been suggested and discussed over the years, summarised in the Hillas plot shown in Fig. 1.12. These range from galactic to extragalactic systems, e.g. Eichler and Schramm (1978); Schramm (1980); Berezinskiĭ (1981); Gaisser et al. (1995); Learned and Mannheim (2000); Becker (2008); Chiarusi and Spurio (2010); Katz and Spiering (2012); Anchordoqui et al. (2013). Galactic sources include SNRs, young pulsars surrounded by opaque supernova shells, and binary systems such as X-ray binaries and microquasars (Kolb et al. 1985; Alvarez-Muñiz and Halzen 2002; Beall and Bednarek 2002; Zhang et al. 2003; Nagataki 2004; Christiansen et al. 2006; Razzaque et al. 2010; Baerwald and Guetta 2013). These sources are

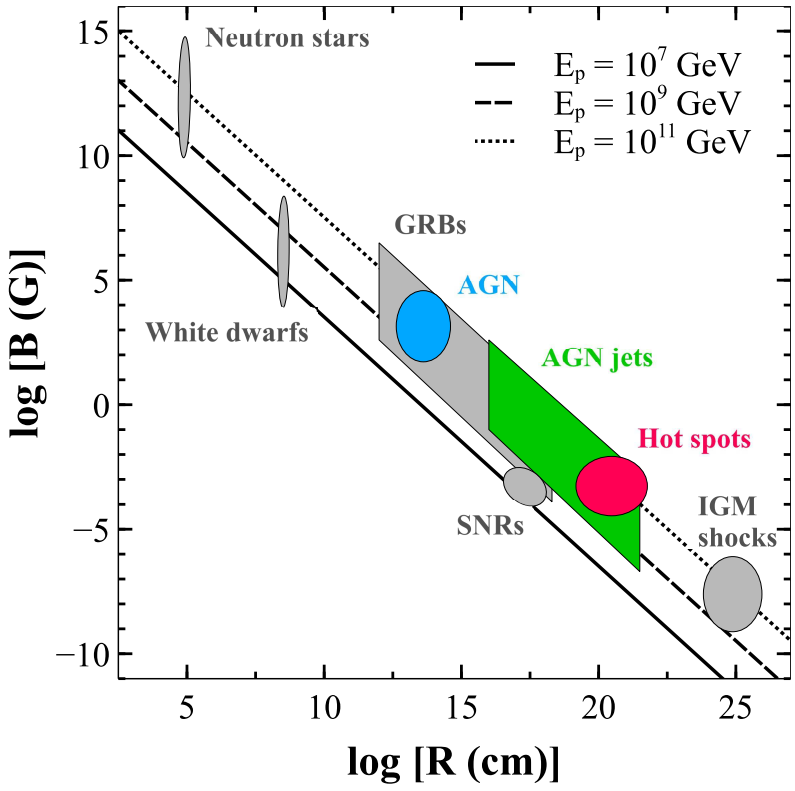

Fig. 1.12: Adaptation of the Hillas diagram for maximum proton energies from Kotera and Olinto (2011), where the source parameter uncertainties for each candidate population is taken into account. The lines denote the maximum proton energy possible for a given source: above 10^7, 10^9 and 10^{11} GeV. At the highest energies AGN, including jets and hotspots, are seen as strong candidate sources for UHECR production, hence also sources of the accompanying HE neutrino emission. We assume that the composition of UHECRs is purely made up of protons, but note that this is debated, in particular for energies above 10^9 GeV where a heavier composition is likely (Kotera and Olinto 2011).

expected to produce neutrinos through pp-interactions, where the acceleration of protons occurs in the core of SNRs due to a central neutron star (pulsar). The energetic protons collide with the remnant shell surrounding the central object after escaping the confinement region. In binary systems the neutrino production occurs through the interaction of the energetic protons with matter in the stellar companion (e.g. red giant) star. In microquasar/pulsar jets, neutrino production is also modelled through pγ-interactions with ambient radiation fields in or around the jet. Clearly these sources would also be found in other normal galaxies, however, if the flux of cosmic rays can be assumed

to be of similar order to that of our own galaxy, the emission in the Milky Way will dominate due to attenuation on larger distances.

The observed transition from galactic to extragalactic sources in the UHECR spectrum (Fig. 1.11, see also Kotera and Olinto 2011) means that a population of powerful extragalactic sources must be considered. The most powerful sources known are AGN, quasars, and GRBs, that have all been studied extensively as possible cosmic accelerators. Quasars and GRBs are not only the brightest point sources on the sky, but also those identified at the largest cosmological distances – at about $z \sim 7$ and $z \sim 8$, respectively (Mortlock et al. 2011; Tanvir et al. 2009). In addition, starburst galaxies have been given attention as neutrino producers as they are expected to have a high supernova rate, implying a source capable of accelerating CR protons and a dense ISM to act as target field for pp-interactions (Loeb and Waxman 2006; Stecker 2007; Lacki et al. 2011).

GRBs have been central to high-energy emission and neutrino production studies. The emission from GRBs have also been studied considering the precursor, such as colliding neutron stars (Ruffert et al. 1997; Ruffert and Janka 1998), core-collapse supernovae and collapsars (Linke et al. 2001; Razzaque et al. 2004), and population-III progenitors (Schneider et al. 2002; Iocco et al. 2008). Two variations of the phenomenon are identified; short and long flashes of gamma rays, on timescales shorter or longer than two seconds, respectively. The origin of these extremely energetic bursts - among the brightest in the Universe - is still debated. The short and long bursts are thought to be caused by different processes because the two events are found to occur in different physical environments. Short GRBs are found in low star formation regions, and are thought to originate from neutron star mergers – either a binary system of neutron stars, or the merging of a neutron star with a black hole. Long bursts are associated with galaxies exhibiting rapid star formation, and so are strongly linked with the death of massive stars and core-collapse SNe. The long GRBs account for about 70% of GRB events. High energy emission from GRBs is observed, however, the exact mechanisms of the conversion of energy to radiation is not fully understood.

Neutrino production in GRBs is a possibility due to this high-energy component. The attempt to identify GRBs as UHECR sources has motivated models that predict an associated observed HE neutrino flux since the mid 1990s (the fireball model of Waxman and Bahcall 1997, see also recent review of Gehrels and Razzaque 2013). Although the *IceCube* Collaboration reported strong constraints on GRB neutrinos (Abbasi et al. 2012), excluding certain features of the fireball model, modifications and new models have since been proposed with the expectation of further detections.

The most promising candidates are AGN due to their very compact and energetic regions in the centre of their host galaxies. These objects are among the most luminous in the Universe, involving the gravitational infall of matter onto a super-massive black hole (SMBH) of masses typically in the range $10^7 - 10^9\ M_\odot$. The accreting matter is attracted by the SMBH from the host galaxy stars and gas, which forms an accretion disc surrounding the black hole. Emission is observed over a wide range of wavebands, from radio to gamma ray, as gravitational potential energy is efficiently converted to radiative emission.

In some cases, the radiation is released as two oppositely directed collimated relativistic jets, aligned perpendicular to the accretion disc – and it is here that the answer to the origin of high-energy astroparticles may lie. Along the relativistic jets, energy and particles are transported from the inner parts of the accretion disc to regions on kpc and Mpc scales away from the nucleus. The creation mechanisms of these jets (including the launching region) and their composition is still unknown. If it has a hadronic component, this may be where the charged high-energy particles are accelerated to observed energies. UHECRs are observed at energies beyond 10^{11} GeV and, if created in AGN jets, there will be an accompanying emission of neutrinos (see Ch. 2).

1.3 Neutrino Experiments and Observatories

From standard oscillation theory, the flux of neutrinos produced in pion decay, $(\nu_e : \nu_\mu : \nu_\tau)_{\text{source}} = (1 : 2 : 0)$, will give the observed flux ratio $(\nu_e : \nu_\mu : \nu_\tau)_{\text{Earth}} = (1 : 1 : 1)$ (see e.g. Learned and Pakvasa 1995). Deviations from this ratio is however possible, such as in a muon-damped case, in which $(\nu_e :$

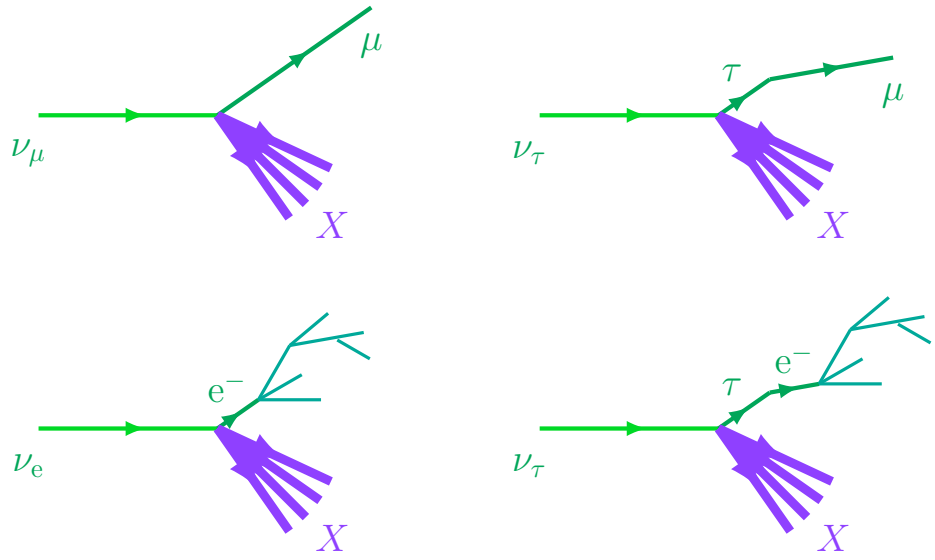

Fig. 1.13: CC tracks of neutrino interactions. *Left:* the interaction of a ν_μ with matter will produce a long muon track and a shower of hadrons (X), whereas that of an ν_e will lead to a short electron track, followed by a shower. *Right:* the interactions of ν_τ has a more complicated event signature. The branching ratio for either a decay to a muon (i.e. a long event) and neutrinos, or electrons (short event) and neutrinos is 18%. However, 86% of τ decays leads to a single charged particle. The neutrino experiments are looking for these signatures when studying neutrino interactions.

$\nu_\mu : \nu_\tau)_{\text{source}} = (0 : 1 : 0)$ becomes $(\nu_e : \nu_\mu : \nu_\tau)_{\text{Earth}} = (4 : 7 : 7)$ (e.g. Winter 2012).

Neutrinos may only be observed through their associated charged leptons. As neutrinos interact with nuclei in the detector medium, the secondary leptonic and hadronic showers show the signatures of the incoming neutrino. The interactions described in Sec. 1.1.5 are therefore of particular interest, as the trails and cascades detected are unique to the particles involved in the interactions, as seen in Fig. 1.13.

The interactions are only kinematically allowed if there is sufficient energy in the centre of mass of the particle. Hence, for interactions of nuclear and astrophysical origin, the energy considerations are particularly important. For example, nuclear interactions in reactors, accelerators or stellar environments (see Sec. B.4) involve neutrinos with energies of order $\sim$ 1 MeV, so only ν_e are able to interact through CC scattering, as there is not sufficient energy available for the other flavours to produce their associated charged leptons.

The energy of neutrinos of atmospheric and cosmic accelerator origin is of order ~ 1 GeV or higher, meaning CC scattering of later generation leptons is possible.

A Cherenkov detector takes advantage of the observed effect of a charged particle travelling through a dielectric medium (e.g. water) at speeds faster than the speed of light in that medium; a cone of electromagnetic radiation known as Cherenkov light, is emitted around the direction of motion. It appears as a blue glow, and its shape is used to distinguish incoming particles, and allows for the tracks to be reconstructed, as illustrated in Fig. 1.14. Due to the difference in tracks of the charged leptons, shown in Fig. 1.13, the Cherenkov cone produced will vary with the type of lepton. As the muon track is a long event, the observed Cherenkov cone is detected as a well-defined circle by photomultiplier tubes (PMTs). As the electron track is short, and produces a shower, the observed Cherenkov light is a superposition of several cones, thus producing a more diffuse ring in the detector. The half-angle of the Cherenkov cone, θ_{C} is found by

$$\cos(\theta_{\mathrm{C}}) = \frac{1}{n\beta} \ , \tag{1.57}$$

where n is the refractive index of the medium (for water at $20^{\circ}\mathrm{C}, n = 1.33$), and the speed of the charged particle i is expressed as $\beta = v_i/c$. The speed of the Cherenkov light waves is $v_{\mathrm{em}} = c/n$. The use of Cherenkov detectors was invaluable to the development of neutrino astrophysics, as the Cherenkov effect provides directional, temporal, and spectral information.

The detection of UHE ($\gtrsim 10^3$ GeV) neutrinos was highlighted as a problem of special importance and interest by Ginzburg (1971) at the very advent of neutrino astronomy, when the experiments to detect Solar neutrinos kept physicists puzzled by the discrepancy between theory and observation (see Sec. B.4). Already observed at this time were UHECRs reaching energies up to 10^{11} GeV (Linsley 1963), although their sources were then, as now, debated. The success of Cherenkov detectors in the study of low ($E_\nu \sim$ MeV) to intermediate ($E_\nu <$ GeV) energy neutrinos launched a new generation of large-scale dedicated neutrino observatories constructed to detect the highest-

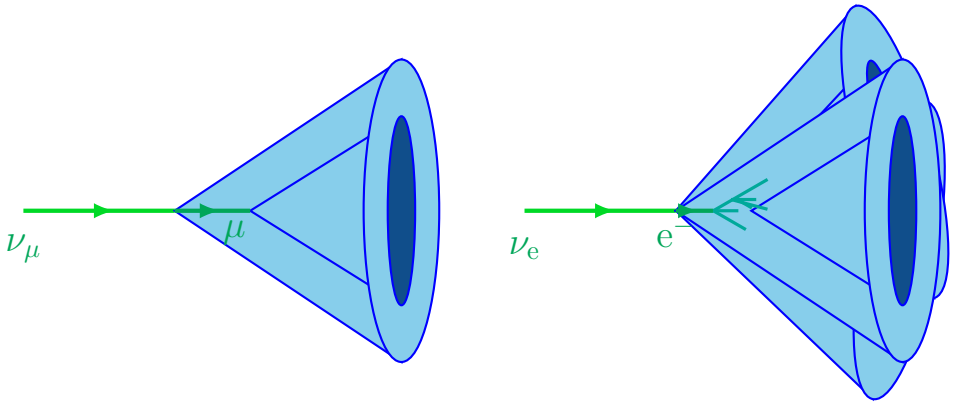

Fig. 1.14: Cherenkov radiation. *Left:* the signature of a muon in a Cherenkov detector is a well-defined circle. *Right:* the electron leaves a short trail followed by an electron shower, hence the detector will see a diffuse circle left by multiple Cherenkov cones.

energy neutrinos.

Due to the elusive nature of the neutrino, hence low interaction rates with matter, the detection of the highest-energy neutrinos requires large volumes of target material for interaction statistics to be significant. The target medium must be both dense to increase interactions, but also transparent to allow Cherenkov light to travel to the optical sensors of the detector. A naturally available target is polar ice and sea water, which allows the detection of considerably higher-energy neutrinos than is possible by detectors with man-made tanks. The Deep Underwater Muon and Neutrino Detection (DUMAND) project, located in the Pacific Ocean off the coast of Hawaii, pioneered this type of high-energy neutrino detector. Although it was never completed, research and development (R&D) carried out while active (1976-1995, see e.g. Markov and Zheleznykh 1986; Chiarusi and Spurio 2010), established the field of UHE neutrino astrophysics. The large-scale neutrino observatory concept developed by DUMAND involves cables lowered into the target medium, spread over a squared-kilometre area, as demonstrated in Fig. 1.15. Each cable have a number of optical modules with PMTs attached, which record the Cherenkov light emitted when a neutrino-induced lepton travels in the medium. Both CC and NC interactions are observed, giving a unique detection signature, as described above. To get an astrophysical neutrino signal larger than that from downwards-moving muon tracks (from the interaction

of cosmic rays with the atmosphere), neutrino detectors cover a large volume, and are located far below the surface, to detect upward-going neutrinos, such that the Earth is used as a shield from background radiation.

1.3.1 Cherenkov detectors with Water and Ice

Cherenkov detectors with a water or ice target have the potential of detecting astrophysical neutrinos with energies up to about 10^8 GeV. The first generation of neutrino telescopes based on the DUMAND-design was the NT200 detector, 1.1 km beneath Lake Baikal in Russia (Aynutdinov et al. 2009); and the Antarctic Muon And Neutrino Detector Array (AMANDA), at depths between 1.5 and 2 km at the South Pole (Andrés et al. 2001).

The Baikal detector began operating in 1998, covering an effective volume of $0.1 - 5$ m^3, for an incoming neutrino of energy 10^4 GeV to 10^7 GeV, respectively. In 2005, the detector was upgraded, increasing the effective volume by an order of magnitude. An analysis of data taken from 1038 days between 1998 to 2003 resulted in a diffuse flux limit for astrophysical UHE neutrinos, shown in Fig. 1.16 (Aynutdinov et al. 2006; Avrorin et al. 2009, see also Table 1.1). The Baikal collaboration is currently constructing a km^3-scale neutrino observatory – the Gigaton Volume Detector (GVD, Avrorin et al. 2013) – which will be able to detect (upward-going) UHE astrophysical neutrinos from the Southern Hemisphere.

The AMANDA-B10 detector was a proof-of-concept detector that began to record data in 1997. It used the Antarctic ice as target material, following the proposition of Halzen and Learned; that ice would be a suitable Cherenkov medium, similar to the water target proposed by the DUMAND project (Halzen and ICnumu 1988). The detector was upgraded to AMANDA-II, completed in 1999, with an effective volume of $10^4 - 10^6$ m^3 for neutrinos in the energy range $10^4 < E_\nu[\text{GeV}] < 10^6$. Both detector configurations were used to set diffuse neutrino flux limits (Ahrens et al. 2003; Achterberg et al. 2007), summarised in Table 1.1. The latter is shown in Fig. 1.16. AMANDA ran for nine years, and has now been integrated into the largest neutrino observatory to date – the *IceCube Neutrino Observatory* – finally realising the km^3-scaled neutrino observatory envisioned by the DUMAND science group. *Ice-*

	Diffuse ν_μ-flux limit	Energy range	Years (live days)
Baikal[a]	9.7×10^{-8}	$2 \times 10^4 - 2 \times 10^7$	1998 – 2003 (1038)
AMANDA-B10	8.4×10^{-7}	$6 \times 10^3 - 10^6$	1997 (138)
AMANDA-II	7.4×10^{-8}	$1.6 \times 10^4 - 2.5 \times 10^6$	2000 – 2003 (807)
IC-59	1.44×10^{-8}	$3.45 \times 10^4 - 3.66 \times 10^7$	2009 – 2010 (348.1)
IC-79 + IC-86[b]	1.2×10^{-8}	$3 \times 10^4 - 1.2 \times 10^7$	2010 – 2012 (615.9)
IC-3yr[b]	0.95×10^{-8}	$3 \times 10^4 - 2 \times 10^7$	2010 – 2013 (988)
ANTARES-2yr	5.3×10^{-8}	$2 \times 10^4 - 2.5 \times 10^6$	2007 – 2009 (334)
ANTARES-4yr	5.1×10^{-8}	$4.5 \times 10^4 - 10^6$	2007 – 2011 (855)
AUGER-6yr[b]	1.74×10^{-7}	$10^8 - 10^{11}$	2004 – 2010 ($\sim$ 730)
AUGER-9yr[b]	6.4×10^{-9}	$10^8 - 2.5 \times 10^{10}$	2004 – 2013 ($\sim$ 2336)
RICE[a]	1.67×10^{-7}	$10^8 - 10^{11}$	1999 – 2010 (1751)
ANITA-II[a]	4.7×10^{-8}	$10^{9.5} - 10^{14.5}$	2008 – 2009 (28.5)

Table 1.1: Experimental diffuse ν_μ-flux limits measured by high-energy neutrino observatories. The neutrino flux limits are given as $E_\nu^2 \Phi_\nu$ [GeV cm^{-2} s^{-1} sr^{-1}]; neutrino energy ranges are given in units of GeV. a) a third of the all-flavour limit reported in the relevant publication is quoted. b) quoted is the single-flavour limit, which, due to equal mixing ratio on Earth, applies to ν_μ-neutrinos. Comparable limits are plotted in Fig. 1.16. See text for details.

Cube detects astrophysical neutrinos coming from the Northern Hemisphere.

The design of *IceCube* is shown in Fig. 1.15. A total of 86 cables are immersed in the polar ice, and each of these hold 60 digital optical modules

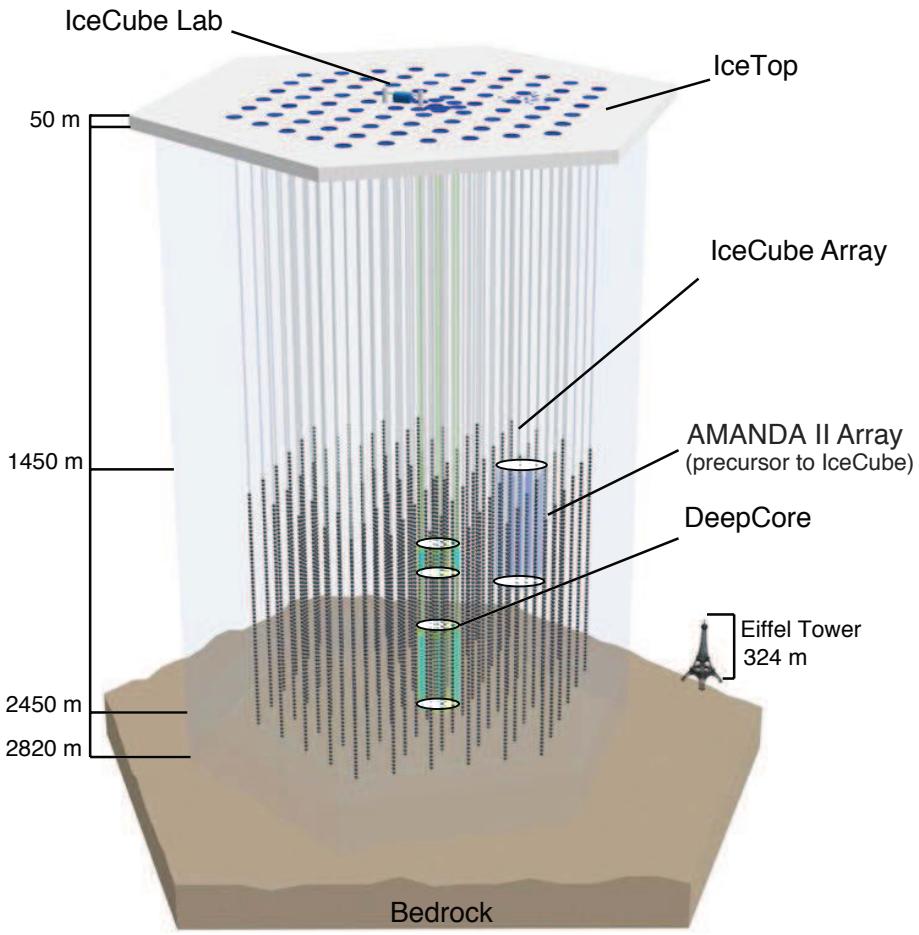

Fig. 1.15: Schematic of the IceCube neutrino detector. The 86 cables are immersed in the ice, each with 60 optical sensors with PMTs. Built around the proof-of-concept detector AMANDA, it covers a cubic kilometre-sized volume, 1450 metres under the polar ice. Figure taken from Anchordoqui et al. (2013).

containing PMTs. The cables are located at depths between 2450 and 1450 metres beneath the ice, surrounding the retired AMANDA detector. The final configuration was completed at the end of 2010, and it has since then consistently lowered the experimental flux limits, and most importantly, confirmed the existence of astrophysical neutrinos. The first reports of detections came out in 2013 (Aartsen et al. 2013; IceCube Collaboration 2013), with the observation of two PeV-neutrinos (with energies of 1.07×10^6 and 1.24×10^6 GeV, Halzen 2014), and an additional 26 neutrino-induced events between 3×10^3 and 1.2×10^3 GeV – thus, it has definitively opened a new window to the Universe.

Table 1.1 summarises the latest flux limits, set by the *IceCube*, at 90% confidence level, from analyses of data taken during its partial configurations with 59 cables (IC-59, Aartsen et al. 2014a); combined 2-year (IC-79+IC-86, IceCube Collaboration 2013); and 3-year (IC-3yr, Aartsen et al. 2014b) 79- and 86-cable configurations. Full configuration is 86 cables, so the *IceCube* observatory has been running at full capacity since late 2010. The 3-year analysis resulted in the detection of 37 astrophysical neutrinos in total, for which nine were detected in the third year – including a third PeV-neutrino, depositing 2×10^6 GeV into the detector. A best-fit power-law for the astrophysical neutrino flux was determined from a two-year (2010-2012; 641 live days) analysis, giving a best-fit flux spectrum for astrophysical neutrinos of

$$\Phi_\nu = 2.06 \times 10^{-18} \left(\frac{E_\nu}{10^5 \text{ GeV}} \right)^{-2.46} \text{GeV}^{-1} \text{ cm}^{-2} \text{ s}^{-1} \text{ sr}^{-1} \tag{1.58}$$

in the energy range of $2.5 \times 10^4 < E_\nu[\text{GeV}] < 1.4 \times 10^6$ (Aartsen et al. 2015b). After 659.5 live days, in the same two-year period, an updated flux spectrum was found to be

$$\Phi_\nu = 9.9 \times 10^{-19} \left(\frac{E_\nu}{10^5 \text{ GeV}} \right)^{-2} \text{GeV}^{-1} \text{ cm}^{-2} \text{ s}^{-1} \text{ sr}^{-1} \text{ ,} \tag{1.59}$$

with a spectral index fixed at $\alpha = 2$. A sample of 35 000 muon neutrinos from the Northern hemisphere was included in this analysis (Aartsen et al. 2015a).

These *IceCube* flux measurements can be found in Fig. 1.16. The analysis of the confirmed astrophysical neutrino events has concluded that these are not of an atmospheric origin, confirming the existence of HE neutrinos from powerful sources – either from within our galaxy (e.g. pulsars) or beyond (e.g. AGN, GRBs). The statistics are yet too low to derive any significant information on the origin of these events. The detections are however consistent with an extra-galactic origin, as some of the highest-energy events are detected at high Galactic latitudes, and has a large isotropic component (Aartsen et al. 2015a).

Whereas the *IceCube* observatory is looking at the Northern Hemisphere, the Southern Hemisphere is yet to be covered by a large-scale neutrino observatory. The Baikal-GVD is under development, however, construction of a

multi-kilometre-scaled observatory in the Mediterranean, named *KM3NeT*, is also underway. The *KM3NeT* will incorporate three prototype first-generation neutrino observatories that demonstrate the concept of a large neutrino observatory deep underwater; NESTOR (Neutrino Extended Submarine Telescope with Oceanographic Research, Rapidis and NESTOR Collaboration 2009), which is located off the Greek coast; NEMO (Neutrino Mediterranean Observatory, Capone et al. 2009), which is under development off the Italian coast; and ANTARES (Astronomy with a Neutrino Telescope and Abyss environmental REsearch, Ageron et al. 2011), which is located off the French coast. NESTOR and NEMO are in the R&D phase, with first deployment of detector structures in 2003 and 2006, respectively.

ANTARES, on the other hand began taking data in 2007, with five of twelve cables deployed. The construction completed in 2008, and it has already set some limits on the diffuse neutrino flux. The first limit set by ANTARES covered the first two years of operation (Aguilar et al. 2011), which was later reduced in an updated limit, covering four years of data (Schnabel 2015), summarised in 1.1.

The Pierre Auger Observatory (PAO) is a hybrid UHECR detector, combining water Cherenkov detection with fluorescence detectors to detect air showers (Watson 2008; The Pierre Auger Collaboration 2015). The observatory consists of 1660 Cherenkov detectors filled with 12 000 litres of ultra-pure water; each with three PMTs detecting the secondary particles from air showers. The Cherenkov array covers an area of 3000 km^2. 27 fluorescence detectors observe the developments of the air showers above the water tanks. It is located in western Argentina, and began taking data in 2004. In 2008 its construction was completed.

Apart from the detection of UHECRs, its design enables the observatory to differentiate between showers initiated by neutrinos and protons, and is therefore able to set limits on the diffuse astrophysical flux as well. Neutrino showers occur deeper in the atmosphere than hadronic showers, and by identifying highly inclined showers, PAO determined diffuse limit, covering the first 6 years of operation (Abreu et al. 2011), and recently reported an updated

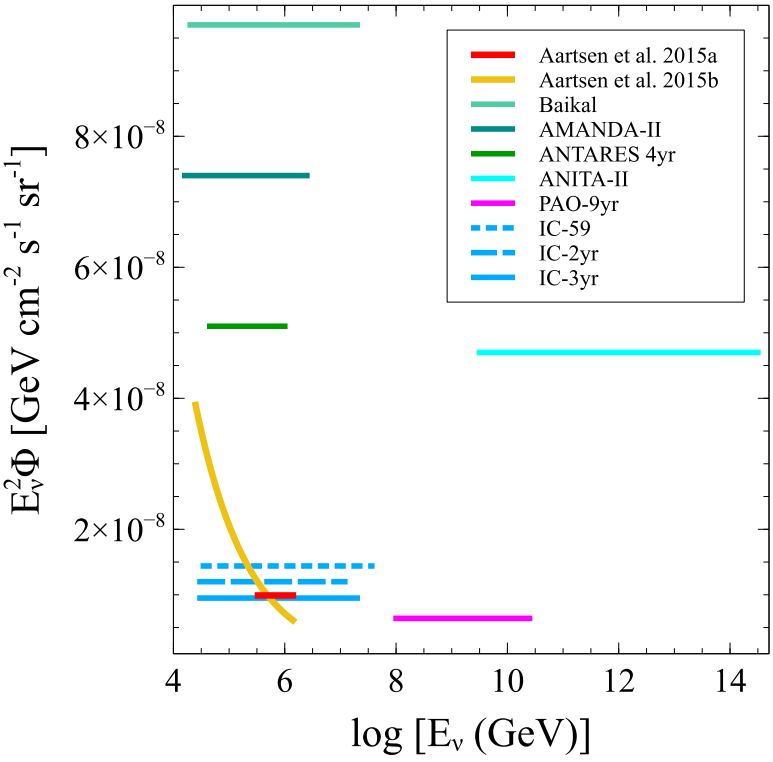

Fig. 1.16: Experimental diffuse ν_μ-flux limits. The limits are given from; Baikal: (Avrorin et al. 2009); AMANDA-II (Achterberg et al. 2007); the ANTARES 4-year analysis (Schnabel 2015); ANITA-II (Gorham et al. 2012); nine years of data from PAO (Aab et al. 2015); and *IceCube* limits from the 59-string (Aartsen et al. 2014a), combined 79- and 86-string configurations after 2 years (IceCube Collaboration 2013) and 3 years (Aartsen et al. 2014b). The derived power-law spectrum given in (Aartsen et al. 2015a) is shown in red; the yellow curve gives spectrum given in (Aartsen et al. 2015b). See text for details.

limit (Aab et al. 2015), both which are shown in Table 1.1. In Fig. 1.16 we plot the most recent limit.

The PAO design is currently expanding to include radio arrays, which will complement the Cherenkov and fluorescence detectors (see e.g. Berat and Pierre Auger Collaboration 2013; Maller and Pierre Auger Collaboration 2014). The radio arrays will constrain the nature of the air showers, such as properties of the primary particle, arrival direction and energies.

1.3.2 Radio Cherenkov detectors

Water and ice Cherenkov detectors have a discovery potential of neutrinos up to about 100 PeV, but fluxes above these energies are expected to be too low

any valuable detection probabilities. In an effort to detect extremely high-energy neutrinos (EHE, $E_\nu \gtrsim 10^8$ GeV), experiments using radio signatures from the Cherenkov radiation are developed (e.g. Becker 2008). The method was originally proposed by G. A. Askaryan (e.g. Jelley 1996, and references therein), showing that a radio-frequency signal from Cherenkov radiation can be detected by antennae near a dielectric target medium of e.g. ice, salt or sand.

The signal arises from the neutrino induced electron-positron showers; due to electrons in the medium becoming part of the shower and pair-annihilation, there is a 20% charge asymmetry. This negative charge excess leads to a coherent Cherenkov radiation signal at wavelengths longer than the transverse size of the shower ($\sim$ 10 cm), and is therefore observed at radio frequencies (see e.g. Connolly 2008).

The Radio Ice Cherenkov Experiment (RICE) was co-deployed with AMANDA, collecting data since 1999. Using the Askaryan effect, it detects neutrino-induced radio signals with an array of 18 radio receivers submerged deep in the Antarctic ice (Kravchenko et al. 2003). The first receivers were depolyed in holes drilled in the ice for the AMANDA experiment, and it was later expanded to additional holes drilled specifically for the RICE experiment. From data collected between 1999 and 2010, they reported a non-detection of astrophysical neutrinos; hence, determining an upper limit for the diffuse flux (Kravchenko et al. 2012).

Another experiment observing neutrino-induced cascades in the Antarctic ice is the Antarctic Impulsive Transient Antenna (ANITA). The radio antenna has had two Long Duration Balloon flights; the first, called ANITA-I was done over 35 days, in 2006-2007 (Gorham et al. 2009). The second flight, ANITA-II, was done two years later, and improved the diffuse limit by 4 times that of ANITA-I (Gorham et al. 2010, 2012), shown in Table 1.1 and Fig. 1.16.

The Askaryan method has proven successful for the detection of UHE neutrinos. The RICE experiment has recently been absorbed into a larger-scale detector array named the Askaryan Radio Array (ARA), which is expected to improve the results of RICE by two orders of magnitude by 2017

(Kravchenko et al. 2012). Furthermore, the experimental efforts of ANITA and RICE have led to a planned 10-100 kilometre-scale array, using the infrastructure of *IceCube*, named the Askaryan Under-ice Radio Array (AURA) (Landsman and AURA Collaboration 2007; Landsman et al. 2009).

Finally, the Moon can be used as the target medium for UHE neutrino events using the radio Cherenkov method (Ekers et al. 2009). Radio telescopes on Earth may detect radio pulses produced when the neutrino interacts with the lunar regolith, and the subsequent particle cascades. This concept has already been investigated – for instance through the LUNASKA (Lunar Ultra-high energy Neutrino Astrophysics with the SKA) project (James et al. 2011; Bray et al. 2013). The non-detection of these radio-pulses has recently set a limit on the neutrino flux, which is expected to be improved when SKA becomes operational (Bray et al. 2015).

The future for the study of neutrinos through dedicated observatories is full of promise, a number of larger-scale observatories are underway. The recent detection of astrophysical neutrinos at energies of order PeV by *IceCube* confirms the need for larger observatories to enable the detection of neutrinos at comparable energies to observed ultra high energy cosmic rays (UHECR).

Neutrinos are not deflected by intervening magnetic fields, unlike charged cosmic rays, nor are they attenuated by the CMB and EBL (as both CRs and γ-rays are). Therefore, using neutrinos to diagnose the dense cores of cosmic accelerators and high-energy environments is advantageous, and is well-supported by recent detections from *IceCube*. Furthermore, the expectation of increased statistics will enable additional constraints on neutrino source models, and hence narrow down the source class responsible for the highest-energy particles observed.

Chapter 2

AGN as Neutrino Sources

Active galactic nuclei (AGN) are a population of compact, dense and very energetic non-stellar objects, identified by the core emission being comparable to, or even outshining, the stellar emission of their host galaxies. They are among the most luminous systems observed in the Universe, thought to be due to matter accreting onto a central SMBH with typical mass of $10^7 - 10^9$ $M_\odot$. Gravitational potential and kinetic energy are converted efficiently to radiative emission through accretion, and the energy release is in some cases seen as two oppositely directed, highly collimated relativistic jets, perpendicular to the accretion disc surrounding the black hole.

Their prominent position as possible cosmic accelerators responsible of producing ultra-high energy (UHE) neutrinos comes from the immense power an AGN can generate in the compact central regions. The observation of UHECRs imply the existence of UHE neutrinos, as hadronic interactions lead to the production of both high-energy messengers, as discussed in Sec. 1.1.4.

The recent detection of astrophysical neutrinos with PeV-energies confirm their existence (Aartsen et al. 2013; IceCube Collaboration 2013; Aartsen et al. 2014b), and even though the source population is yet to be identified, the events are consistent with an extragalactic origin. As AGN are persistent over several cosmological epochs they are prime candidates for the production of these UHE neutrinos. Furthermore, a number of locations in the AGN system, such as the cores and radio jets are possible confinement regions for the production of highly energetic particles, as they fulfil the Hillas

criterion, seen in Sec. 1.2.3.

As AGN are observed with a variety of observed properties, these sources are particularly interesting in light of high-energy particle production. Morphology, orientation and emissions are seen to vary across different types of AGN, which implies that conditions within the confinement regions may vary as well. This requires a classification scheme, which separates observable differences of AGN into different types of AGN. For example, some AGN are observed with jets, others without; some AGN jets are brightest at the tip of the lobes, at the very edge of their jets (*edge-brightened*). Others are brightest in regions of the jets close to the central nucleus (*edge-darkened*). Energetic regions along the jet features, known as knots, are often observed. The structure of the jet is therefore crucial, and acceleration processes are highly dependent on the properties of the accelerating region. Emission observed over various wavebands is another important observable, as these imply a variation of radiative processes occurring in AGN; from the very central regions of the accretion disc to the jets.

Sec. 2.1 outlines the classification scheme of AGN, in particular radio-loud AGN and the radio-loud unification model. Sec. 2.2 describes various important processes that lead to observable HE emission in AGN systems. In the event of AGN being the dominant source population of the high-energy neutrino flux, we require an estimate of the distribution of AGN populations to study the overall evolution of the neutrino spectrum over cosmic time. AGN have been surveyed extensively over the entire electromagnetic spectrum, so we focus on X-ray and γ-ray surveys as these trace the accretion disc emission and the beamed jet emission, respectively, ensuring a wide selection of AGN properties. The AGN evolutionary tracks are derived from luminosity function (LF) models, that give the number of sources as a function of luminosity and comoving volume. This is described in Secs. 2.3 and 2.4. In Sec. 2.5 the beaming of blazar emission is discussed.

2.1 AGN Classification and Unification

As with all astrophysical systems, particularly those at large distances, we can only rely on observable features to distinguish and classify the various objects. AGN are no different, and the classification of this diverse population is based on decades of photonic studies. Since AGN emission is observed at wavelengths ranging from radio to γ-ray, independent AGN studies in different wavebands have led to overlapping classification schemes.

Here we use the simple classification commonly applied, based on optical studies, with further distinctions due to radio power of the AGN system and its nuclear luminosity (see e.g. Tadhunter 2008). Though the AGN population in reality proves more complex, the following serves as a reasonable first approach for the study of physical processes within AGN systems.

From studies in optical wavelengths, three broad types of AGN emerge. Both broad and narrow emission lines are prominent in the optical spectra of Type-I AGN, whereas Type-II AGN spectra only show narrow lines. Type-0 AGN show in some cases weak or no emission lines, however the defining feature of a Type-0 is the rapid variability at optical wavelengths.

A second broad distinction is that of radio emission which leads to the radio-loud and radio-quiet AGN classifications. The dividing line between the two classes is normally defined in terms of the ratio of the radio flux to that of the optical/ultraviolet (UV) (Kellermann et al. 1989). Radio-quiet AGN in the optical Type-I and Type-II scheme are known as Seyfert 1 (Sy1) and Seyfert 2 (Sy2) AGN, respectively. They are preferentially found in spiral and irregular galaxies. Radio-quiet quasars (RQQ, historically known as QSOs) show similar spectra to Sy1 AGN, but have a much higher nuclear luminosity and are often found in ellipticals.

Radio-loud AGN are optically identified as broad-line radio galaxies (BLRG) or narrow-line radio galaxies (NLRG) as the radio-loud equivalent to Sy1 and Sy2 AGN. These can be further distinguished based on their extended radio jet structures, such that the morphology of an edge-darkened radio-structure is classified as a Fanaroff-Riley I (FR-I) radio galaxy, and a radio galaxy with edge-brightened radio-structures is known as a FR-II type.

	Radio-quiet	Radio-loud	
Type-0		Blazar	BL Lac OVV (FSRQ)
Type-I	RQQ	RLQ	FSRQ SSRQ
	Sy1	BLRG	
Type-II	Sy2	NLRG	FR-I FR-II

Table 2.1: Optical emission line classification of AGN, see e.g. Urry and Padovani (1995); Tadhunter (2008). The three types are classified in terms of presence or absence of broad emission lines, in addition to narrow emission lines in the optical spectra of AGN without (radio-quiet) or with (radio-loud) prominent radio structures. Type-II radio-loud AGN (NLRGs) are sub-classified in terms of radio-power as FR-I and FR-II; radio-loud quasars (RLQ) are further classified in terms of their radio spectra, and Type-0 blazar sub-classes are classified in terms of optical variability and presence of emission lines. See text for details.

This is apparent in imaging of radio-structures of the two types, where the former is brightest in knots (bright regions) along the jet close to the core, and the jet extends into fading plume structures. The latter is relatively weak in radio close to the central core, but very bright in regions called hotspots at the end of the jets, where the jet lobes interact with the intergalactic medium (see Fig. 2.1, but also e.g. Figs. 1.4 and 1.5 in Peterson 1997). FR-Is show on average a lower radio-power than FR-IIs, with a defined dividing line in luminosity between the two of 2×10^{32} erg s^{-1} Hz^{-1} sr^{-1} measured at 178 MHz (for a cosmology with the Hubble constant $H_0 = 50$ km s^{-1} Mpc^{-1}, Fanaroff and Riley 1974; Ghisellini and Celotti 2001).

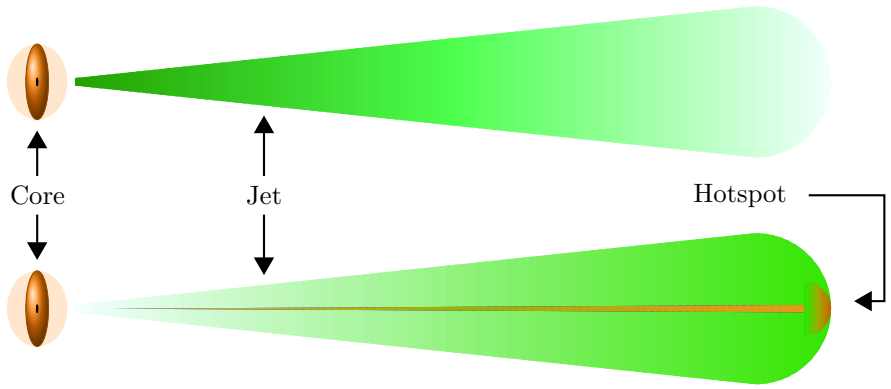

Fig. 2.1: Schematic illustration of possible neutrino production sites in AGN systems. *Top:* FR-I jet (limb-darkened), which is brightest in radio towards the core. Suitable high-energy production sites are the core and the inner jet. *Bottom:* FR-II jet (limb-brightened), which is brightest in radio at the outer lobes, with a bright hotspot at the end.

The more luminous Type-I radio sources are known as radio-loud quasars (RLQ; historically called quasars), and can be further classified based on their radio emission spectra. The shape of the radio spectrum defines the steep spectrum radio quasar (SSRQ) and the flat spectrum radio quasar (FSRQ), and the morphology of the radio structure determines core dominated or lobe dominated quasars. It is found that SSRQs are often lobe-dominated radio structures, whereas FSRQs tend to be core-dominated, and also show high variability in their optical spectra (as opposed to the less variable SSRQs).

Type-0 AGN of the optical classification scheme are known as blazars. The blazars are radio-loud sources known for high variability in their optical spectra. There are two identified members of this class; the BL Lacs that have weak or no emission lines in their optical spectra, and the optical violent variables (OVV) which show broad spectral lines. Radio-loud quasars are predominantly hosted by massive elliptical galaxies (Best 2009, and references therein).

The optical classification scheme is summarised in Table 2.1. The ability to classify these (in many cases very distant) sources reflect years spent and remarkable efforts to learn of the composition of these sources and what physical processes lie at the foundation of their existence. AGN (quasars/QSOs) are among the oldest sources detected to date, and the most luminous. A

consistent picture of AGN structure has emerged from decades of studies at all wavelengths, illustrated in Figs. 2.2 and 4.1.

The AGN is located at the centre of its host galaxy with an accreting SMBH at the very centre, hence the *active nucleus*. The SMBH is surrounded by an accretion disc and corona, and a region of relatively dense clouds orbiting at high velocities called the broad line region (BLR) at distances less than 0.1 pc from the core. The BLR is the origin of the broad lines observed in the optical spectra. The width of the emission lines provides information on the properties of the emitting regions, and in the Doppler broadening interpretation, the broadness (FWHM $\sim 10^3 - 10^4$ km s^{-1}) of the emission lines is due to high velocities in the presence of the gravitational field of the nucleus.

These central components of the AGN (SMBH, accretion disc, corona, and BLR) are surrounded by an optically thick torus of dense molecular gas and dust. The central nucleus is too small to be imaged and spatially resolved by current telescopes, thus the structure and physical processes governing the nucleus are studied through other means, such as spectroscopy and variability analyses. At distances up to $\sim$ 1 kpc from the nucleus less dense regions of clouds than that of the BLR, are found (with measured FWHM $\lesssim 10^3$ km s^{-1}) called the narrow line region (NLR). Finally, in radio-loud sources a prominent radio jet (and an oppositely-directed counter jet) is observed whose morphology will differ for various radio-loud types.

From the classification of AGN, patterns of physical properties have become clear across the types which highlights the possibility of AGN evolving from one type to another, e.g. from radio-quiet to radio-loud in the course of its lifetime, or driven by fundamentally different processes. Furthermore, the continuous sequence from, for example, Type-I to Type-II AGN have become evident giving intermediate Seyfert AGN an additional identifier based on the ratio of the broad to narrow line strengths.

The lack of a static classification has also opened the possibility for AGN unification models, (e.g. Antonucci 1993; Urry and Padovani 1995; Urry 2004; Tadhunter 2008). The currently accepted model for radio-loud AGN unification, outlined in Urry and Padovani (1995), is based on the inclination angle

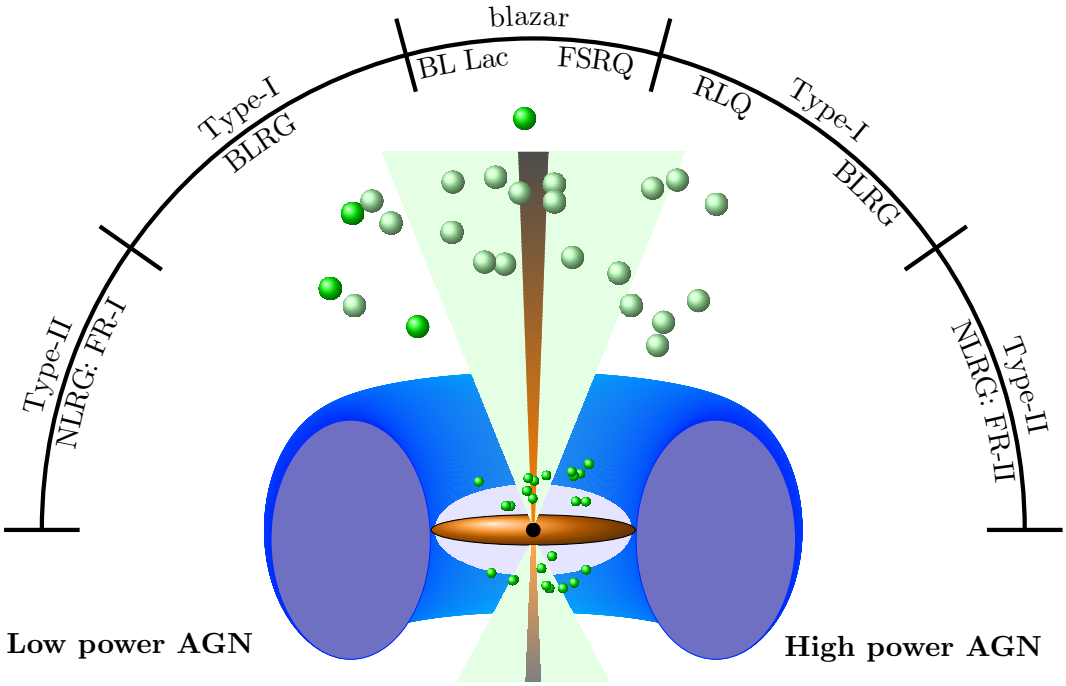

Fig. 2.2: Schematic representation of the structure and unification of radio-loud AGN. At the centre, the SMBH is surrounded by an accretion disc (orange) and a hot corona (blue), and the BLR (small green spheres). Around these features is the optically thick torus that blocks the view of the central regions, thus a Type-II AGN is observed. Further out (large green spheres) is the NLR, which produces emission lines seen in these AGN. For a decreasing viewing angle, the BLR region is seen for Type-I radio galaxies, and closer to the jet axis are quasars, and the blazars when the jet is seen head-on. Left-hand side are low-power AGN, and the right-hand side shows the high-power AGN unification.

of the jet axis to our line of sight, commonly known as the viewing angle. If the jet is pointed in our line of sight, i.e. a viewing angle $\theta_{\rm v} = 0°$, we are looking at a blazar. At larger viewing angles we see quasars and Type-I AGN, and at viewing angles approaching 90° we observe Type-II radio galaxies. This concept of AGN unification, illustrated in Fig. 2.2, is based on two supporting ideas. First, that of optical depth and geometry of the obscuring torus; namely, if seen edge-on, the AGN centre and emission from the BLR will be obscured by the surrounding torus, hence only narrow lines will be seen in the optical AGN spectrum. At a smaller viewing angles the central regions will be increasingly more visible, hence the emission from the BLR will be visible along with the narrow emission lines, and a Type-I AGN will be observed.

At even smaller viewing angles, the beaming of the bulk motion of the

jet plasma will lead to anisotropic radiation, causing an observable change in the appearance of the AGN/quasar (Blandford and Königl 1979). From these considerations, SSRQs, being lobe-dominated and lacking variability, and FSRQs, which are core-dominated and in some cases highly variable, are seen at decreasing viewing angles, respectively (Orr and Browne 1982). Whether a quasar is core- or lobe-dominated is determined as a ratio of the emission from the core to the emission from the extended radio structures. Furthermore, in the cases of high variability FSRQ, these are classified as OVVs (Tadhunter 2008) (hence, in this work we will call the blazar constituents BL Lacs and FSRQs from here on).

The unification of the radiogalaxy types FR-I and FR-II with radio-loud quasars/blazars are also a part of the generally accepted unification (Blandford and Rees 1978; Antonucci and Ulvestad 1985; Barthel 1989). Here the FR-II radio galaxies are seen as the unbeamed counterparts of FSRQs, whereas luminous FR-I radio galaxies are the possible parent population of (X-ray selected) BL Lacs. Selection effects show that the parent population of radio-selected BL Lacs is a mixture of both FR-I and FR-II radio galaxies (Antonucci 1993).

The unification model for radio-loud AGN sources is shown in Fig. 2.2, where the central parts of the AGN structure are shown along with the emission of a (not to scale) radio jet. Depending on the viewing angle and the radio power of the sources (on the left are low-power sources, FR-I and BL Lacs; on the right are high-power sources, FR-II and FSRQs), the AGN sources have essentially the same physical nature.

A unifying sequence for γ-ray bright blazars has also been proposed (Padovani and Giommi 1995; Fossati et al. 1998; Ghisellini et al. 1998), consisting of BL Lac sources with a low-energy (LBL), intermediate-energy (IBL), and high-energy (HBL) synchrotron peak. The unification is motivated by broad-band studies of blazars, where the spectral energy distributions (SEDs, see Fig. 2.4) highlight observable differences within the BL Lac population, as well as between BL Lacs and FSRQs.

Properties of sources identified as LBL and FSRQ are in some cases seen

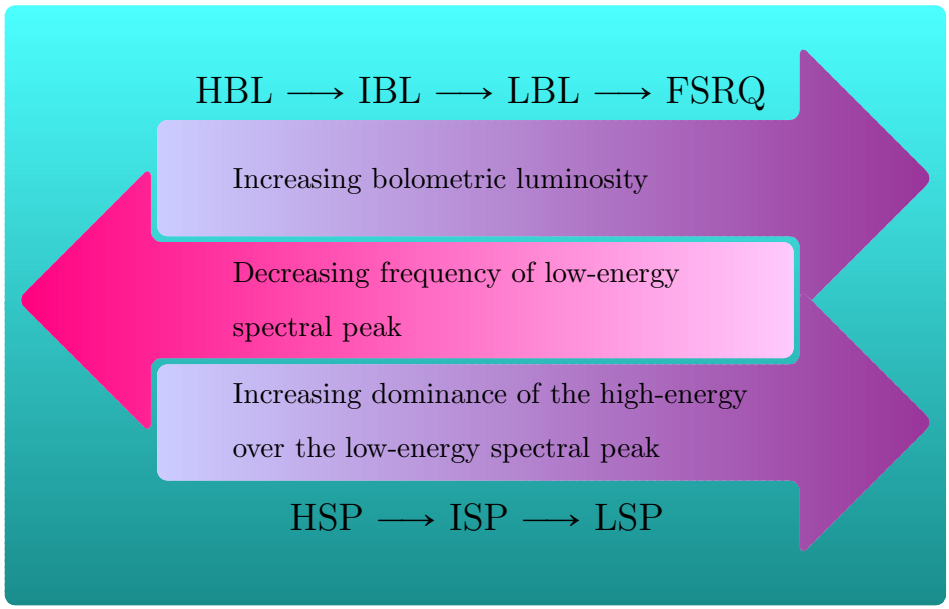

Table 2.2: Continuous blazar sequence. Along the sequence from high-frequency BL Lacs to FSRQs (or, equally, HSP to LSP), the bolometric (and γ-ray) luminosity increases; similarly does the dominance of the high-energy to the low-energy peak. The low-energy peak decreases in frequency along the sequence. See text for details.

to overlap. An extension to the sequence is therefore proposed (Abdo et al. 2010a), assuming that all non-thermally dominated AGN follow a sequence from high synchrotron peaked blazars (HSP), through intermediate synchrotron peaked blazars (ISP), to low synchrotron peaked blazars (LSP). The sequence shows the trend of a decreasing synchrotron peak, thus corresponds to the sequence of HBL, IBL and LBL/FSRQ classes, respectively. FSRQs may additionally be classified as high-polarisation (HPQ) and low-polarisation (LPQ) core-dominated flat spectrum quasars.

Furthermore, the trend from high to low energy in the SED shows the shift of the low-energy peak along the sequence, from low-luminosity high-frequency BL Lacs (HBL) to high-luminosity low-frequency BL Lacs (LBL) and FSRQs. The bolometric luminosity increases as the synchrotron peak shifts to lower energies, and the dominance of the high-energy peak over the low-energy peak is also shown to increase. The trends of the blazar sequence are summarised in Table 2.2.

The processes leading to the observed emission in AGN is briefly described

in the following section. A more detailed description on processes related to jet emission is found in Ch. 5.

2.2 Emission from AGN

The SED is a useful tool to deduce the strength of emission across the entire electromagnetic spectrum. A common representation is a logarithmic $f - f\phi_f$ plot, where f is the frequency and ϕ_f the flux at a given frequency, or equivalently in terms of luminosity as a function of frequency, $f - fL_f$. The observed AGN emission forms a broadband spectrum ranging from radio to γ-rays.

The SED has both thermal and non-thermal components, and there is a clear distinction between blazar (i.e. beamed sources, see Fig. 2.4) and non-blazar AGN spectra (Fig. 2.3). For blazars, the spectrum is dominated by beamed emission from non-thermal processes in the jet, whereas unbeamed sources have a larger thermal component. The thermal emission originates from the central engine, and is observed over several spectral bands, as the emission is either direct or reprocessed by various AGN components.

For unbeamed sources, the SED is approximately flat between the far infra-red (IR) and X-rays, seen in Fig. 2.3. In this region the spectral features remain similar for AGN over many orders of magnitude in luminosity. Hence there should exist a scaling relation with luminosity which is strongly tied to the central engine of the AGN, the SMBH (i.e. the accretion power, see Ch. 5).

Towards radio frequencies there is a decline in flux of about two orders of magnitude for radio-loud sources, and about three times that for radio-quiet sources. For a radio-loud AGN, the radio is dominated by the emission of synchrotron photons as relativistic electrons in the jet travel in a magnetic field. The radio spectrum can be well approximated by a power-law such that the flux varies as $\phi_{\rm f} \propto f^{-\alpha_{\rm r}}$, where $\alpha_{\rm r}$ is the radio spectral index. The index is usually flat ($\alpha_{\rm r} \lesssim 0.5$) in the core, and steep ($\alpha_{\rm r} \gtrsim 0.5$) in the outer lobes. This divides the flat-spectrum from the steep-spectrum quasar sources.

The power-law of the radio spectrum follows the distribution of electrons

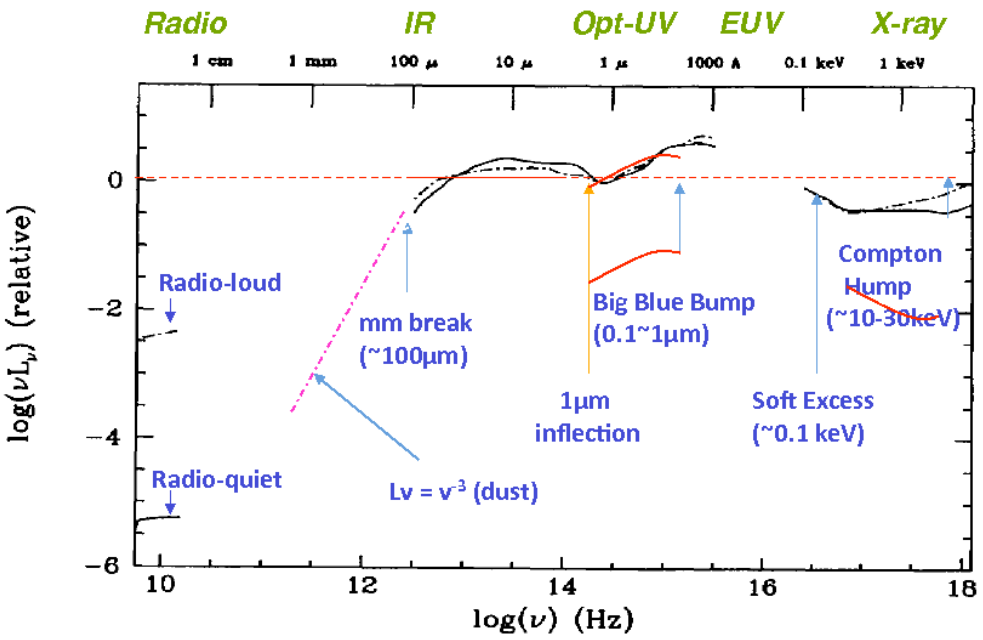

Fig. 2.3: Broadband SED of quasars In the radio the spectrum clearly distinguishes radio-loud (dashed lines) from radio-quiet (solid lines) AGN. From IR to X-rays, the SED is approximately flat. Direct emission from the accretion peaks in the UV, and in the X-rays the inverse Compton emission results in a flat power-law (see text). Figure taken from http://hea-www.harvard.edu/~elvis/, see also Elvis et al. (1994).

producing the synchrotron radiation (see Sec. 5.3). The electron energy distribution is assumed as a power-law with the particle energy index ρ, such that $N(E_e) \propto E_e^{-\rho}$, and the particle index is related to the spectral index through $\alpha_r = (\rho - 1)/2$. For blazars, the radio emission is highly beamed, so for these sources a rather different SED is observed, seen in Fig. 2.4.

The SED peaks in the IR band due to reprocessed emission from the accretion disc in the dusty torus. A local minimum in the near IR (at about 1 eV) is followed by direct thermal emission from the accretion disc emission in the optical/UV. It peaks in the UV, in what is known as the *big blue bump*.

Absorption in the interstellar medium leaves the region between the extreme UV and soft X-rays unobservable. In the X-ray band, the emission can be approximated by a flat power-law which is the result of inverse Compton scattering of the disc photons with electrons in the corona surrounding the accretion disc. In the soft X-rays there is an observed excess emission in addi-

tion to the power-law. Its origin is debated, but may be the high energy tail of the big blue bump peaking in the extreme UV, or Comptonisation of the disc photons by a corona surrounding the inner disc. This inner corona is believed to be optically thick, whereas the X-ray power-law emission originates from an optically thinner corona further out (see e.g. Mehdipour et al. 2011, and references therein for a detailed discussion on the soft X-ray excess).

For radio-quiet sources, there is also an apparent hump above 10 keV due to the Compton reflection from cold material, and associated fluorescence Fe Kα emission lines, the strongest at $\sim$ 6 keV. For radio-loud sources, these lines are weaker and there is no reflection hump. Unbeamed AGN, i.e. not blazars, are not strong emitters in the γ-ray.

The SEDs of blazars reflect variations in the dominance of the radiative processes within the sources classified as high-frequency (HBL), intermediate-frequency (IBL), and low-frequency (LBL) BL Lacs, followed by FSRQs, and are shown in Fig. 2.4. The blazar SEDs are dominated by beamed emission, and so the decline towards the radio band is not seen and the radio spectrum rather smoothly joins the IR part. This reflects a non-thermal continuum which dominates over the thermal continuum seen in non-beamed sources.

The SED is dominated by two large peaks, one at high energies in the γ-ray band and one at lower energies. The low-energy peak is found between IR and soft X-rays, and the location follows the blazar sequence outlined in Sec. 2.1. For HBLs the low-energy peak lies in the UV/soft X-rays, whereas for LBLs and FSRQ the peak is found in the IR/optical part of the spectrum. The shape of the peak is consistent with synchrotron emission from relativistic electrons in the jet, and reflects the particle acceleration potential in the jets. As the electrons interact with the jet magnetic field, non-thermal radiation is emitted as synchrotron emission. The peak therefore indicates the maximum energy attainable in the jet. The correlation between the synchrotron luminosity and total jet power is studied in e.g. Cavagnolo et al. (2010).

The origin of the high-energy peak is still under debate. Fitting the observed peak with a leptonic model of inverse Compton scattering of the electrons with ambient photon fields will fit some blazars – although far from all.

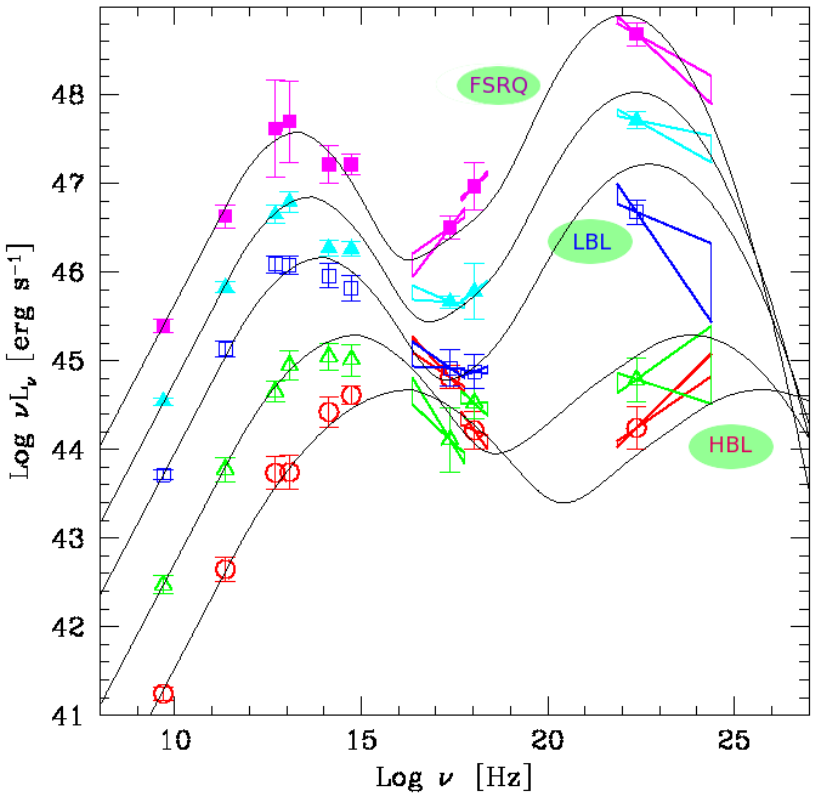

Fig. 2.4: SED of blazars shows the trend along the sequence: with decreasing synchrotron peak, the bolometric luminosity increases, as does the dominance of the γ-ray peak over the synchrotron peak (see text). Figure taken from Donato et al. (2001), see also Fossati et al. (1998). The blazar sequence classes are shown for clarity.

Thus, hadronic models are proposed, where relativistic protons in the jet will interact with the same photon fields producing observable γ-rays. As the γ-ray luminosity traces the bolometric jet luminosity, the peak at these energies therefore reflects the jet power.

Related decays in the hadronic interactions also lead to a comparable flux of neutrinos. With the discovery of astrophysical neutrinos in *IceCube*, a further study into the link between neutrino production and AGN is therefore warranted. Another output from these interactions will be cosmic ray protons, which are also extensively studied.

A more detailed discussion on the leptonic and hadronic emission models is found in Ch. 5.

2.3 Space Density and Evolution: X-ray Detected AGN

In this section we discuss the evolution of X-ray detected radio-loud AGN/quasar population over cosmic time. We make a first distinction between radio-loud and -quiet AGN based on a fractional estimate of these two populations by Urry and Padovani (1995), such that radio-loud AGN account for about 10% of all AGN. This is the fraction given for radio-selected AGN and we use this as a conservative measure of the radio-loud population. We follow the distinctions of various AGN populations as outlined in Sec. 2.1.

We focus on observational studies of AGN in the X-ray band, as X-ray emission from a compact source is a clear indicator of an AGN observation. This is because it points to the accretion onto a powerful SMBH at the AGN centre, thus an X-ray survey of the AGN population provides a near complete data set without need for complementary observations in other wavebands. All X-ray luminous objects with an observed luminosity above $\log(L_{\rm X}[\text{erg s}^{-1}]) = 42$ measured in the hard X-ray band are safely considered AGN (Mushotzky 2004) and so this will act as a guiding lower luminosity limit. The upper luminosity limit is taken as $\log(L_{\rm X}[\text{erg s}^{-1}]) = 47$ – the Eddington luminosity of an AGN with a $9M_{\odot}$ SMBH (see Table 5.1).

Furthermore, as the cosmic X-ray background (CXRB) is largely due to AGN emission (e.g. Fabian and Barcons 1992; Barger 2005) it traces the history of accretion onto SMBHs, and surveys working in different X-ray bands will select observationally different AGN populations. The soft X-ray band ($\lesssim$ 1 keV) selects unobscured Type-I AGN. In hard X-rays ($\lesssim$ 10 keV) obscured Type-II AGN are preferentially detected. The very high X-ray band ($\gtrsim$ 15 keV) will select beamed AGN sources with emission from FSRQs accounting for the entire CXRB above 500 keV (Ueda et al. 2003; Hasinger et al. 2005; Ajello et al. 2009).

We also consider γ-ray surveys that detect blazar sources. Combined with lower-energy surveys, the space density variations along the blazar sequence are identified.

Due to these selection effects, we ensure a wide spread of different AGN types by concentrating on three published surveys: the soft X-ray band (0.5 –

2 keV) study by Hasinger et al. (2005), the hard X-ray band ($2-8$ keV) study of Silverman et al. (2008), and the very hard ($15-55$ keV) study by Ajello et al. (2009), thus obtaining a population of unobscured in the soft, both obscured and unobscured AGN in the hard band, and blazars in the very high X-ray band. The source data of blazars is additionally explored by the γ-ray surveys giving a population of FSRQs (Ajello et al. 2012) and BL Lacs and its sub-classes in Ajello et al. (2014).

2.3.1 The X-ray Luminosity Function

A common representation of the number density of a population is the luminosity function (LF). The differential X-ray LF (XLF) is a measure of the number of objects in a given population, N, per unit co-moving volume, $V_{\rm c}$, and unit X-ray log-luminosity $\log L_{\rm X}$, as a function of $L_{\rm X}$, in units of erg s^{-1}, and redshift z (Ueda et al. 2003),

$$\frac{d\Psi(L_{\rm X},z)}{d\log L_{\rm X}} = \frac{d^2N(L_{\rm X},z)}{dV_{\rm c}\,d\log L_{\rm X}}\ . \tag{2.1}$$

It is common to express this definition in terms of luminosities as a base-10 logarithm (we use *log* to refer to base-10 logarithm, and *ln* to refer to the natural logarithm), due to the many orders of magnitude covered (e.g. Ueda et al. 2003; Hasinger et al. 2005; Silverman et al. 2008). However, not all XLF prescriptions do this (e.g. Ajello et al. 2009), so it is useful to note the conversion between the two forms,

$$\frac{d\Psi(L_{\rm X},z=0)}{d\log L_{\rm X}} = \ln(10)L_{\rm X}\frac{d\Psi(L_{\rm X},z=0)}{dL_{\rm X}}\ . \tag{2.2}$$

The local XLF (i.e. evaluated at $z=0$) can be expressed as a simple power law (Ajello et al. 2009),

$$\frac{d\Psi(L_{\rm X},z=0)}{d\log L_{\rm X}} = {\rm A}_0\ \ln(10)\left(\frac{L_{\rm X}}{L_*}\right)^{1-\tilde{\Upsilon}_2}\ ; \tag{2.3}$$

however, observationally there is a break, and with a high enough source count, this break can be seen and a double power law (e.g. Ueda et al. 2003) can be fitted to the observational data. The faint and bright end slopes are dictated by the indices Υ_1 and Υ_2, respectively, for luminosities below and above the

break luminosity L_* (Ueda et al. 2003), such that

$$\frac{d\Psi(L_{\rm X}, z=0)}{d\log L_{\rm X}} = {\rm A}_0 \left[\left(\frac{L_{\rm X}}{L_*} \right)^{\Upsilon_1} + \left(\frac{L_{\rm X}}{L_*} \right)^{\Upsilon_2} \right]^{-1} . \tag{2.4}$$

The normalisation $\rm A_0$ is determined using maximum likelihood routines, and the other parameters are model dependent (Ueda et al. 2003; Hasinger et al. 2005; Silverman et al. 2008; Ajello et al. 2009).

The evolution of the XLF depends on the chosen model which best fits the observations. The most basic expressions are the pure luminosity evolution (PLE) and pure density evolution (PDE) models, and do not to represent observational data well in their simplest form.

As the name suggests, the PLE model evolves the observed luminosities with a redshift-dependent evolution function $e_{\rm L}(z)$. Similarly, the PDE model evolves the present day XLF (that is, the local number density of the population) by a redshift-dependent evolution function $e_{\rm D}(z)$. The evolving luminosity function is then

$$\frac{d\Psi(L_{\rm X}, z)}{d\log L_{\rm X}} = \begin{cases} \dfrac{d\Psi[L_{\rm X}/e_{\rm L}(z), z=0]}{d\log L_{\rm X}} & \text{(PLE)} \\ \dfrac{d\Psi(L_{\rm X}, z=0)}{d\log L_{\rm X}} e_{\rm D}(z) & \text{(PDE)} \end{cases} \tag{2.5}$$

The form of the evolution of the PLE model can be chosen as given in Ajello et al. (2009),

$$e_{\rm L}(z) = (1+z)^{\upsilon_1 + \upsilon_2 z} , \tag{2.6}$$

for which the indices υ_1 and υ_2 determine the behaviour of the evolution with respect to redshift. For a simple PLE, $\upsilon_2 = 0$, and the evolution factor is reduced to a standard power law. To fit observations, however, the modified PLE (MPLE) model requires an extra dependency on redshift.

The PDE model is commonly evolved by a general form, which is also in some cases applied to the PLE model (e.g. Ueda et al. 2003; Hasinger et al. 2005). Here the indices υ_1 and υ_2 determine the evolution before and after a

redshift break z_*, and

$$e_{\rm D}(L_{\rm X}) = \begin{cases} (1+z)^{\upsilon_1} & [z \leqslant z_*] \\ [1+z_*(L_{\rm X})]\left[\dfrac{1+z}{1+z_*(L_X)}\right]^{\upsilon_2} & [z > z_*] \end{cases} . \tag{2.7}$$

There are however difficulties when adopting these simple models to describe the evolving luminosity function. The PLE model is found to underestimate the data of low luminosities ($\log L_{\rm X} < 45$) and redshifts $z = 0.8 - 1.6$ (Ueda et al. 2003; Hasinger et al. 2005), whereas the PDE model tends to underestimate the data at high luminosities ($\log L_{\rm X} \geqslant 44.5$) and redshifts $z = 1.6 - 3.0$ (Ueda et al. 2003). In order to find an acceptable description for the evolving luminosity function over the whole redshift-luminosity region, modified versions of these models have been suggested (see e.g. Aird et al. 2010). In the luminosity dependent density evolution (LDDE) model (Ueda et al. 2003) the evolution factor is a function of both the X-ray luminosity and redshift, giving the evolving XLF as

$$\frac{d\Psi(L_{\rm X}, z)}{d\log L_{\rm X}} = \frac{d\Psi(L_{\rm X}, z=0)}{d\log L_{\rm X}} e_{\rm LD}(L_{\rm X}, z) \quad \text{(LDDE)} . \tag{2.8}$$

The evolution factor is given by

$$e_{\rm LD}(L_{\rm X}, z) = \begin{cases} (1+z)^{\upsilon_1} & [z \leqslant z_*(L_{\rm X})] \\ [1+z_*(L_{\rm X})]\left[\dfrac{1+z}{1+z_*(L_{\rm X})}\right]^{\upsilon_2} & [z > z_*(L_{\rm X})] \end{cases} , \tag{2.9}$$

where the break redshift is determined by a luminosity dependent characteristic redshift cut-off, $z_{\rm c}$,

$$z_*(L_{\rm X}) = \begin{cases} z_c \left(\dfrac{L_{\rm X}}{L_{\rm c}}\right)^{\alpha} & [L_{\rm X} \leqslant L_{\rm c}] \\ z_{\rm c} & [L_{\rm X} > L_{\rm c}] \end{cases} . \tag{2.10}$$

These are all model dependent parameters.

An added dependency on luminosity can be introduced on the evolution indices υ_1 and υ_2 for a better fit with observation (e.g. Hasinger et al. 2005):

$$\begin{aligned} \upsilon_1(L_{\rm X}) &= \upsilon_{1,\rm c} + \beta_1(\log L_{\rm X} - \log L_{\rm c}) \\ \upsilon_2(L_{\rm X}) &= \upsilon_{2,\rm c} + \beta_2(\log L_{\rm X} - \log L_{\rm c}) \end{aligned} . \tag{2.11}$$

2.3.2 AGN X-ray Surveys

We consider surveys that cover different X-ray bands, selecting AGN populations with slightly different observed properties. The observed properties are associated with the different AGN populations through the unification model based on viewing angles; in the soft X-ray band we see unobscured Type-I AGN (Hasinger et al. 2005); and the hard X-ray band selects a mix of both obscured Type-II and unobscured Type-I AGN (Silverman et al. 2008). At the very hardest X-rays beamed AGN/quasar populations (Ajello et al. 2009) are observed.

Modelling the evolution of the variety of sampled AGN allows us to study the differences in their evolutionary history, and will therefore also provide a means to discriminate between populations in regards to HE emissions based on the AGN properties and evolution, and specifically the HE neutrino production of AGN as a class of objects, and within each AGN population. The three surveys provide the relevant XLF model prescriptions needed to calculate the AGN population densities, with model parameters determined using maximum likelihood routines.

Completeness of the survey is ensured through a well-defined description of how the flux limit varies across the area of the sky (sky coverage), and an optical and redshift identification of the sources in the survey. Complete samples are reported in two of the surveys (Hasinger et al. 2005; Ajello et al. 2009), whereas the incompleteness of the third is corrected for as a function of both optical magnitude and X-ray flux (Silverman et al. 2008). This is due to the two former surveys selecting unobscured AGN/quasar sources and the latter containing a large contribution from obscured AGN, which (particularly at high redshifts) is difficult to resolve.

Two methods are commonly used to test the evolution of the AGN populations. The $\log N - \log \Phi$ analysis evaluates the number of detected sources as a function of the source flux Φ, given by $N(> \Phi) = \mathrm{A}\Phi^{-\varsigma}$. For a non-evolving population the Euclidean distribution is described by $\varsigma = 3/2$. This is from a simple argument that the flux $\Phi \propto d^{-2}$, the number of sources is proportional to the volume enclosed by the distance to the source, i.e. $N \propto d^3$, and

$dN/d\Phi \propto \Phi^{-5/2}$. Non-evolving sources above a flux limit Φ is $N(>\Phi) \propto \Phi^{-3/2}$, and a deviation from this slope is interpreted as a non-uniform distribution of sources. A positively evolving population will have an index $\varsigma > 3/2$. This method is sensitive to the survey completeness, and as it assumes a uniform source population, it may not be as useful for surveys covering large redshifts.

The second test of evolutionary trends is the $V/V_{\rm max}$ test (Schmidt 1968) which takes into account the evolution of the LF over cosmic time. This method tests the ratio between the co-moving volume enclosed by a detected object of a given flux Φ and the maximum volume $V_{\rm max}$ for which the detection could happen given the detector sensitivities. The $V/V_{\rm max}$ distribution is expected to be uniform, and for a non-evolving population the $V/V_{\rm max}$ ratio will be 0.5. A positively evolving population will have a ratio $0.5 < V/V_{\rm max} < 1$, whereas a negative evolution will show an excess in values between 0 and 0.5. This implies that at higher redshifts, the negatively evolving population was less dense or numerous. A generalised version of this method was developed by Avni and Bahcall (1980).

The three surveys we consider use a cosmological prescription of $\Omega_\Lambda = 0.7$ with a Hubble constant of $H_0 = 70$ km s^{-1} Mpc^{-1}. Each survey is briefly described below.

The (0.5-2 keV) X-ray Survey by Hasinger et al. (2005) have selected 994 unobscured Type-I AGN in the soft X-ray band (0.5-2 keV), using eight independent samples from the *ROSAT*, *XMM-Newton* and *Chandra* surveys. Out of a total 2566 soft X-ray sources, only 86 were unidentified, which gives a completeness of 97%. The Type-I AGN population dominates in soft X-ray surveys, and the selection of the sample was based on optical and X-ray classification methods. They derive a global evolving soft XLF using the $V_{\rm max}$ method.

Hasinger et al. (2005) find that the space density of Type-I AGN with luminosities $\log L_{\rm X} > 45$ decline significantly towards high redshift, with a cutoff redshift of $z \approx 2$. Low-luminosity AGN ($43 < \log L_{\rm X} < 44$) are found to peak at $z \sim 1$, and for the lowest luminosity sampled AGN ($42 < \log L_{\rm X} < 43$) the peak is found between redshifts $0.5 < z < 0.7$. The clear change of

shape of the XLF as a function of redshift thus shows a luminosity dependent density evolution for Type-I AGN/quasars.

The survey data is fit to PLE and LDDE models (Sec. 2.3.1). The former fails to trace the behaviour of low-luminosity ($\log L_{\rm X} < 44$) sources, and in the intermediate redshift ($0.5 < z < 1.8$) regime. The latter deviates from data at lower luminosity bins ($42 < \log L_{\rm X} < 43$) at redshifts $0.015 < z < 0.2$.

The (2-8 keV) X-ray Survey by Silverman et al. (2008) have measured the hard XLF of AGN from a sample of 682 AGN using the *Chandra* multi-wavelength project (ChaMP) to select luminous AGN ($\log L_{\rm X} > 44$), and the *Chandra* Deep Fields to provide low-luminosity data. They make no distinction of the various AGN sources sampled, that is, if they are Type-I or Type-II AGN. They report adequate completeness ($> 50\%$) and in their analysis compensate for this with a correction factor.

They measure the XLF up to a redshift of ~ 5 and find that 31 of the AGN sources are of redshifts $z > 3$. Above this redshift they observe a significant decline in numbers, similar to the evolution of the luminous QSOs. Whereas the lowest luminosity objects ($\log L_{\rm X} < 43.5$) are too scarcely sampled to determine the evolution, they do find the most luminous AGN ($\log L_{\rm X} > 44.5$) peak around redshifts of $z \sim 2$. Lower luminosity AGN ($43.5 < \log L_{\rm X} < 44.5$) are abundant at around a redshift of $z \sim 1$. This agrees well with previous studies, where more luminous AGN were more prevalent at earlier epochs and the peak activity of less luminous AGN is found at later times. They fit the data with both PLE, MPLE and LDDE models (see Sec. 2.3.1) and find that the PLE model represents data at low redshifts well, but it may overestimate low-luminosity AGN at higher redshifts. The best-fit LDDE model fits the data overall, and also agrees with previous work.

The (15-55 keV) X-ray Survey by Ajello et al. (2009) includes a sample of X-ray selected blazars above 15 keV using the *Swift*/BAT survey, with 38 blazars in total in a redshift range of $0.03 < z < 4.0$. Of these 38, 26 are classified as FSRQs and 12 as BL Lacs. Furthermore, of the BL Lacs, 9 are of HBL type, and the rest are classified as LBL types. With less than 5% unidentified sources in the total sample, they consider incompleteness negligible in their

blazar catalogue.

The brightest blazars ($\log L_{\rm X} > 47.3$) evolve strongly up to a redshift peak at $z \approx 4.3$ which is driven by the FSRQ population, being the only sources detected at high redshifts by *Swift*/BAT. Their results thus support the idea that luminous blazars formed very early in the Universe, followed by a rapid decrease in number density. Lower luminosity blazars are too scarce for their evolution to be determined. BL Lacs are found to have negligible evolution, however with a scarce sample over a small range of redshifts $0.01 < z < 1.0$ only a simple PLE model can be fitted to this sample. The evolution of the larger FSRQ and total blazar samples are best fit with an MPLE model (see Sec. 2.3.1).

2.4 Space Density and Evolution: γ-ray Detected AGN

We also consider the evolution of the blazar population using γ-ray surveys. These surveys detect beamed γ-ray emission from blazars, and combined with surveys covering other wavebands the broadband SEDs can be constructed. Through these studies the concept of the blazar sequence has emerged, which allows for a variation across the blazar population to be quantified. This is described in Sec. 2.1, and summarised in Table 2.2.

The γ-ray surveys have probed the extragalactic γ-ray background (EGB), and thus attempt to resolve the diffuse emission which is thought to be populated by AGN and blazars because the isotropic γ-ray signal would imply an extragalactic origin. Estimates of the contribution from blazar/quasar sources vary from $20\% - 100\%$ (Abdo et al. 2010b). The γ-ray emission from blazar and quasar sources is often modelled through the Inverse Compton emission processes in the jets, or alternatively through neutral pions decaying as $\pi^0 \rightarrow \gamma\gamma$. Hence, these surveys are useful in determining the leptonic or hadronic content of AGN jets.

2.4.1 The γ-ray Luminosity Function

The γ-ray luminosity function (γLF) represents the number density distribution as a function of γ-ray luminosity L_γ and comoving volume $V_{\rm c}$. The latter is measured through determining the source redshifts. The functional

form follows the XLF outlined in Sec. 2.3.1, and the γLF can be scaled using the XLF LDDE model (Eqns. 2.8-2.11). This approach has been used to explore the blazar contribution to the EGB, taking into account the blazar sequence (Inoue and Totani 2009; Inoue et al. 2010; Abazajian et al. 2011; Harding and Abazajian 2012; Murase et al. 2014). The γLF is found by scaling the XLF by a parameter representing the fraction of X-ray detected AGN observed as blazars (Inoue and Totani 2009).

Another approach is the modelling of the blazar density evolution with an added dependency on the intrinsic photon index, ρ (Ajello et al. 2012, 2014). The differential representation of the blazar space density is a function of the luminosity L_γ, redshift z, and photon index ρ,

$$\frac{d\Psi(L_\gamma, z, \rho)}{d\log L_\gamma} = \frac{d^3N(L_\gamma, z, \rho)}{dL_\gamma\ dV_c\ d\rho}\ . \tag{2.12}$$

The photon index distribution is modelled as a Gaussian, so that

$$\frac{d\Psi(L_\gamma, z=0, \rho)}{d\log L_\gamma} \propto e^{-(\rho-\mu)^2/2\sigma^2}\ , \tag{2.13}$$

where σ and μ are the Gaussian dispersion and mean, respectively. An added dependency on luminosity can be introduced for the mean index (Ajello et al. 2014), with the characteristic index μ_c and luminosity L_c,

$$\mu(L_\gamma) = \mu_c + \beta_\mu(\log L_\gamma - \log L_c)\ . \tag{2.14}$$

The local γLF is modelled with a double power-law form (cf. the XLF form in Eqn. 2.4) multiplied by the luminosity-dependent photon index distribution,

$$\frac{d\Psi(L_\gamma, z=0, \rho)}{dL_\gamma} = \frac{A_0}{\ln(10)L_\gamma}\left[\left(\frac{L_\gamma}{L_*}\right)^{\Upsilon_1} + \left(\frac{L_\gamma}{L_*}\right)^{\Upsilon_2}\right]^{-1} \times \frac{dN(\rho, L_\gamma)}{d\rho}\ . \tag{2.15}$$

If the photon index distribution is independent of luminosity, that factor falls out of the above equation. The form of the evolution factor depends on the luminosity function model used, i.e. a pure luminosity evolution (PLE) and pure density evolution (PDE) takes the form

$$e(z) = (1+z)^{\upsilon 1(L_\gamma)} e^{z/\upsilon 2} \tag{2.16}$$

And the luminosity dependent density evolution (LDDE) is given by

$$e_{\rm LD}(L_\gamma, z) = \left[\left(\frac{(1+z)}{1+z_*(L_\gamma)} \right)^{\upsilon 1(L_\gamma)} + \left(\frac{(1+z)}{1+z_*(L_\gamma)} \right)^{\upsilon 2} \right]^{-1} , \tag{2.17}$$

with

$$\upsilon 1(L_\gamma) = \upsilon_{1,\rm c} + \beta_\upsilon (\log L_\gamma - \log L_{\rm c}) \tag{2.18}$$

and

$$z_*(L_\gamma) = z_{\rm c} \left(\frac{L_\gamma}{L_{\rm c}} \right)^{\alpha} . \tag{2.19}$$

Whereas the PLE/PDE evolution factor is one at redshift $z = 0$, this is not the case for the LDDE model. The γLF parameterisation for each model is then

$$\frac{d\Psi(L_\gamma, z, \rho)}{dL_\gamma} = \begin{cases} \dfrac{d\Psi(L_\gamma / e(z), \rho)}{dL_\gamma} & \text{PLE} \\ \dfrac{d\Psi(L_\gamma, z=0, \rho)}{dL_\gamma} e(z) & \text{PDE} \\ \dfrac{d\Psi(L_\gamma, z=0, \rho)}{dL_\gamma} e_{\rm LD}(L_\gamma, z) & \text{LDDE} . \end{cases} \tag{2.20}$$

2.4.2 AGN γ-ray Surveys

The *Fermi γ-ray Space Telescope* has, since 2011, carried out an all-sky survey with its imaging instrument, the Large Area Telescope (LAT). It has collected the largest data set of γ-ray selected blazars to date, and we focus on two surveys using this data to sample FSRQs (Ajello et al. 2012) and BL Lacs (Ajello et al. 2014). Both surveys use the concordance cosmology with $H_0 = 71$ km s^{-1} Mpc^{-1} and $\Omega_\Lambda = 0.73$.

The *Fermi* FSRQ survey subset contains 186 sources, from a full sample of 433 sources of various classifications, including pulsars and starburst galaxies in addition to other radio galaxies (Ajello et al. 2012). Incompleteness is limited by imposing a lower flux limit of approximately 10^{-8} photons cm^{-2} s^{-1}, corresponding to the faintest FSRQ, thus obtaining a sample of only 7% unassociated sources. FSRQs evolve positively, with the brightest quasars peaking in number density at a redshift of $z \sim 2$. In agreement with trends of the evolution of X-ray selected AGN found in e.g. Ueda et al. (2003), the

faint sources peak later, which for γ-ray selected blazars is located at $z \sim 0.6$. Similarly, the low-luminosity sources are more numerous at later times. Combined with data from *Swift*/BAT, a luminosity-independent LF is derived, best fitted to an LDDE model (see Sec. 2.4.1), and the contribution to the γ-ray background is predicted at $\approx 9.3\%$.

The *Fermi* BL Lac survey subset contains 211 sources, from a full sample of 486 sources of various classifications, including pulsars and starburst galaxies in addition to other radio galaxies (Ajello et al. 2014). Though they report an incompleteness of 9% in the BL Lac sample, they find it does not affect the analysis. The majority of the BL Lac population evolves positively, peaking at a redshift $z \approx 1.2$. With estimates along the blazar sequence, they find that the high-synchrotron peaked (HSP, analogous of the HBL BL Lacs) class diverge from this trend with a negative evolution, increasing for redshifts $z \lesssim 0.5$. Though the LDDE model of the γLF is found to fit the data best, the PLE model also fit adequately (see Sec. 2.4.1).

2.5 Beaming effects on the blazar population

Emission from relativistic jets emitted from the cores of radio-loud AGN is heavily affected by Doppler beaming and strong relativistic aberration. This will affect the observed luminosity function of these populations. Specifically, the observed luminosity will be considerably brighter for sources displaying a jet in our line of sight, as is the case with blazars. The observed luminosity L for a relativistic jet relates to the emitted luminosity $\mathcal{L}$ by

$$L = \delta^{\varrho} \mathcal{L} \ , \tag{2.21}$$

where $\delta = [\Gamma(1 - \beta \cos(\theta_{\rm v}))]^{-1}$ is the jet Doppler factor, βc is the bulk velocity of the jet. The bulk Lorentz factor is $\Gamma = [1 - \beta^2]^{-1/2}$, and the viewing angle is $\theta_{\rm v} = 1/\Gamma$. The exponent ϱ gives the enhancement of the luminosity. For a blazar type, for which only one jet is seen, the spectral index is given by $\varrho = 3 + \alpha$, where α is the spectral index. This exponent is due to aberration, whereby the emission is beamed forward due to the relativistic motions of the jet; contraction of the time interval, meaning more photons per unit time

Beaming of X-ray detected blazars

AGN population		Blazar (total)	FSRQ	BL Lac
$\rho_{\rm X}$		2.0	1.6	2.5
$\alpha_{\rm X}$		1.0	0.6	1.5
δ^{ϱ}		1.006×10^4	4.005×10^3	3.186×10^4
Lower Bound:	$\log \mathcal{L}_{\rm X}$	40.0	40.0	40.0
	$\log L_{\rm X}$	44.0	43.6	44.5
Upper Bound:	$\log \mathcal{L}_{\rm X}$	44.5	44.9	44.0
	$\log L_{\rm X}$	48.5	48.5	48.5

Table 2.3: Values used for the conversion between beamed ($L_{\rm X}$) and intrinsic ($\mathcal{L}_{\rm X}$) luminosities, for the total blazar sample, as well as the sub-types FSRQs and BL Lacs. X-ray luminosities are given in erg s^{-1}. The spectral index, α for each population is taken from Ajello et al. (2009), and the conversion factor δ^{ϱ} is calculated using a bulk jet Lorentz factor $\Gamma = 10.0$, and the power $\varrho = 3 + \alpha_{\rm X}$.

are observed; and the blueshifting of photons, as there are a factor δ^{α} more photons at the observed frequency than at the emitted frequency.

The observed and intrinsic luminosity functions (LF) of AGN have similar slopes at high luminosities. However, the observed LF flattens towards lower luminosities because it is sensitive to the lower cutoff and steepness of the Lorentz factor distribution. This effect is most apparent when using PLE models (see Sec. 2.3.1 and 3.7).

In Ch. 3 we derive the numbers based on the intrinsic luminosity, as this additional check allows us to exclude beamed objects that are intrinsically below an assumed threshold for AGN brightness. We here make a simplified assumption that all blazar objects derived from the XLF are beamed (though in reality this may not be the case). A common assumption is that anything brighter than $L_{\rm X} = 10^{42}$ erg s^{-1} can safely be assumed to be AGN. However, as blazar sources are highly beamed, we have set that lower boundary of the intrinsic luminosity to $L_{\rm X} = 10^{40}$ erg s^{-1} for these sources. This would exclude distant beamed objects with intrinsically lower luminosity, but that may be beamed to AGN-like luminosities, e.g. X-ray binaries.

We assume the same lower luminosity for γ-ray bright blazars if the beaming power $\varrho \approx 3$ fo BL Lacs or ≈ 4 for FSRQs, but a lower limit of $\mathcal{L}_\gamma = 10^{39}$ erg s^{-1} if the beaming power $\varrho \approx 4$ for BL Lacs, and ≈ 5 for FSRQs following Ajello et al. (2012) and Ajello et al. (2014).

For X-ray detected blazars, we assume the spectral index ($\alpha_{\rm X}$) from photon index ($\rho_{\rm X}$) data given in Ajello et al. (2009) (see their Fig. 2) and derive the bounds on the observed beamed luminosity, summarised in Table 2.3. The jet Doppler factor, $\delta \simeq 10.0167$ is calculated with an assumed Lorentz factor $\Gamma = 10.0$ and viewing angle $\theta_{\rm v} = 0.1$ radians.

For γ-ray detected blazars, we assume the spectral indices (α_γ) from the photon index (ρ_γ) data in Ajello et al. (2012) and Ajello et al. (2014), and use the beaming relation in Eqn. 2.21. The lower γ-ray luminosity limits are summarised in Table 2.4. The Doppler factor is determined with the bulk Lorentz factor $\Gamma = 10.0$ and viewing angle $\theta_{\rm v} = 0.1$ radians. We note that BL Lacs may have lower Lorentz factors (Ajello et al. 2014), although for simplicity we assume one value for all sources.

Beaming of γ-ray detected blazars

blazar population	FSRQ		BL Lac		HSP		HSP/ISP		ISP/LSP		LSP	
ρ^a_γ	2.44		2.10		1.97		2.26		2.32		2.0	
	[min]	[max]	[min]	[max]	[min]	[max]	[min]	[max]	[min]	[max]	[min]	[max]
$\log L_\gamma$	44.5	49.5	44.0	49.0	44.0	49.0	44.0	49.0	44.5	49.0	44.5	49.0
$\rho_\gamma(L_\gamma)$	–		1.97	2.29	1.88	2.10	1.94	2.22	2.30	2.18	2.37	2.22
α_γ	1.44		0.97	1.29	0.88	1.10	0.94	1.22	1.30	1.18	1.37	1.22
ϱ	4.44		3.97	4.29	3.88	4.10	3.94	4.22	4.30	4.18	4.37	4.22
$\log \mathcal{L}_\gamma$	40.6	45.1	40.0	44.7	40.0	44.9	40.1	44.8	40.2	44.8	40.1	44.8

Table 2.4: Values used for the conversion between beamed (L_γ) and intrinsic ($\mathcal{L}_\gamma$) luminosities, for the FSRQ sample and the total BL Lac population, as well as the SED-classes HSP, combined HSP and ISP, combined ISP and LSP, and the LSP class. γ-ray luminosities are given in erg s^{-1}. The spectral index, α for each population is taken from Ajello et al. (2012) and Ajello et al. (2014) a) For BL Lacs and the SED blazar classes, the photon index quoted here is the characteristic photon index, ρ_* in Eqn. 2.14. b) the beaming factor δ^ϱ, in units of 10^4 is calculated using a bulk jet Lorentz factor $\Gamma = 10.0$, and the power $\varrho = 3 + \alpha_\gamma$.

Chapter 3

AGN Luminosity Function and Population Calculations

The evolution of the massive black holes is tightly linked to the large-scale structure evolution in the Universe. AGN, with their super-massive black holes at their centre, can influence galactic dynamics and evolution through feedback of material triggering star formation, or conversely quenching of star formation as the AGN outflows drive off the interstellar medium of their host galaxies (see e.g. Silk and Rees 1998; Page et al. 2012). Determining the details of the AGN properties driving these processes will provide constrains on the evolution of the constituents in the Universe. Observable neutrino emission will furthermore give clear indications of the relative peak activity of sources emitting thermal and non-thermal radiation.

In the following we derive the AGN population evolution for a variety of classes using X-ray (Sec. 3.1) and γ-ray (Sec. 3.4) surveys that were described in Ch. 2.

3.1 AGN Populations Derived from X-ray Surveys

The general trend of the evolving X-ray detected AGN population is, that the activity of the brightest AGN peaked at a very early cosmological epoch of the history of the Universe, followed by a rapid decline for luminous blazars. The lower luminosity AGN peak at a more local epoch. The surveys (described in Ch. 2) find that the AGN source evolution depends on both luminosity and redshift. The X-ray luminosity function (XLF) models commonly used are

therefore modified versions of the simple pure luminosity evolution model, or the more complex luminosity dependent density evolution (LDDE) model. The surveys are limited by redshift due to observational constraints and sensitive to luminosity. In the following we derive the evolution of AGN populations over several cosmological epochs, and therefore extrapolate the XLF behaviour at low redshifts to higher redshifts. We thus assume the local behaviour is indicative of that at the very early epochs.

We obtain the evolutionary tracks and population sizes of X-ray detected AGN in the Universe through two methods. First, we extract the data from the postscript source code of the soft X-ray (Hasinger et al. 2005), hard X-ray (Silverman et al. 2008), and very hard X-ray (Ajello et al. 2009) surveys. We interpolate the data, which provides us with a preliminary representation of the AGN evolution throughout the history of the Universe. We then use the best-fit XLF prescription of the observational data given in the surveys to calculate the evolutionary trends ourselves. We also calculate the X-ray luminosity distributions of AGN at various cosmological epochs.

3.1.1 AGN Population Derivations: Interpolation.

From Hasinger et al. (2005) we obtain a sample of luminous Type I AGN selected in the soft $(0.5-2$ keV) X-ray band. Silverman et al. (2008) provide data for luminous hard X-ray AGN $(2-8$ keV) (i.e. both Type I and type-II). In the very hard X-ray band $(15-55$ keV) the survey of Ajello et al. (2009) provides data on number densities of blazars.

By accessing the postscript files of the relevant plots from those publications, the coordinate points of redshift and number density, $[z, n(z)]$ of the objects in these surveys are extracted. The number density plots are reproduced in the original luminosity bins to ensure accuracy. The data are grouped into redshift intervals of size $\Delta z = 0.2$ and interpolated to fit all intervals using a spline method. To cover the full redshift range $(0 < z < 9)$, following the redshift range plotted in Ajello et al. (2009), endpoints have been linearly extrapolated. The number densities of the AGN populations are then found within each redshift bin.

In Figs. 3.1, 3.2 and 3.3 we show the reproduced number density plots for

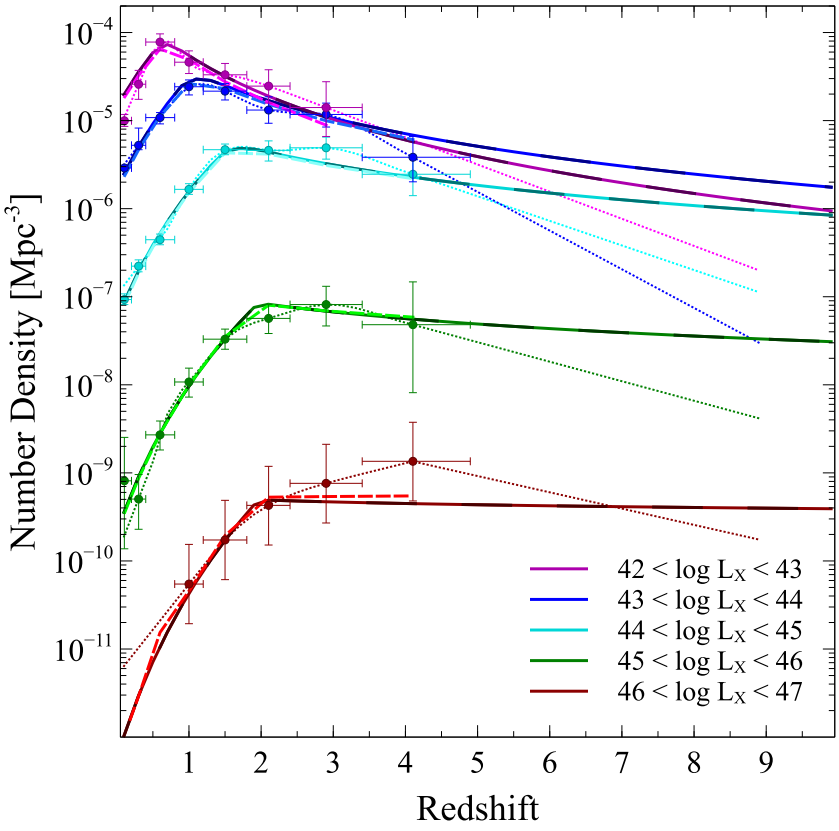

Fig. 3.1: Number density evolution of Type-I AGN, compare Fig (5a) in Hasinger et al. (2005). The plot shows the extracted soft X-ray AGN evolution data points and errors, with our calculated evolution by interpolation (dotted lines) using the extracted data points. Each curve and associated data points represent the number density for sources of varying X-ray luminosities. The short dashed lines are the extracted LDDE model tracks. The solid lines show the calculated number densities from the best-fit XLF, calculated in terms of $\log L_{\rm X}$, discussed in Sec. 3.1.2. The long dashed lines are the counterpart calculations in the $L_{\rm X}$ formulation of the XLF to show agreement.

the three AGN surveys, where the data points and errors are extracted from the relevant publications. The dotted lines are the extrapolated evolutionary tracks, calculated from the extracted data points.

Fig. 3.1 shows the extracted data points from the original plot in Hasinger et al. (2005), including the error bars. These points cover a redshift range of $0 < z < 4.8$. The dotted lines show the interpolated number density evolutions for AGN in five different luminosity bins. The density evolution of the brightest sources is modified from the linear extrapolation at the

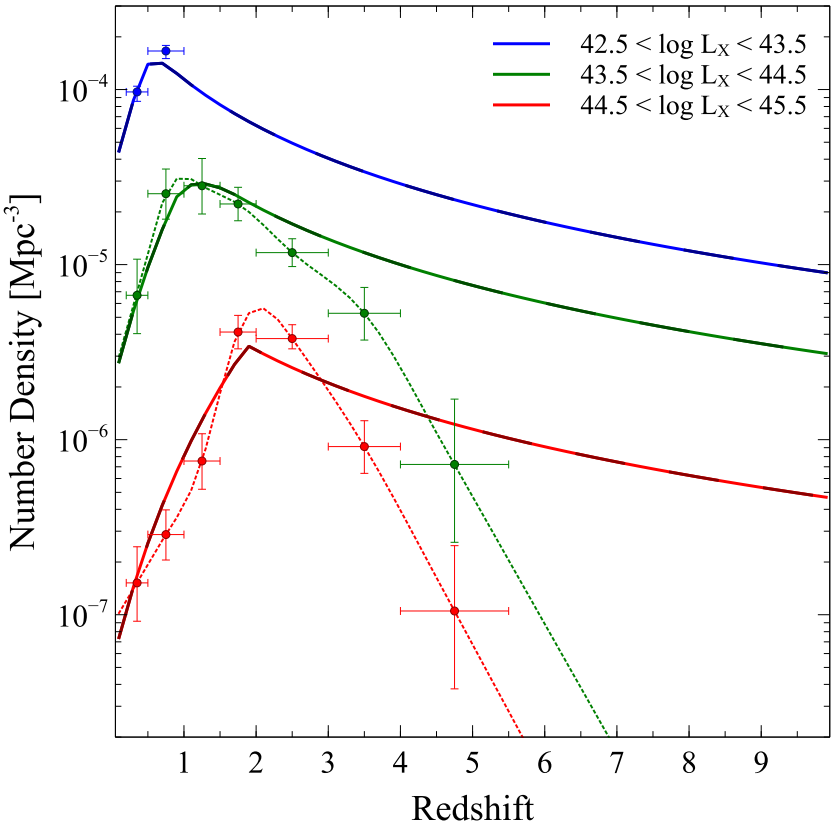

Fig. 3.2: Number density evolution of Type-I and Type-II AGN, compare Fig (13) in Silverman et al. (2008). The plot shows the extracted hard X-ray AGN evolution data points and errors, overplotted with our calculated tracks by extrapolation using the extracted data points (dotted lines). The solid lines show the calculated XLF in $\log L_{\mathrm{X}}$, and the dashed lines are the counterpart calculations in L_{X} formulation of the XLF to show the agreement (see Sec. 3.1.2).

last datapoint, to follow the downward trend of the evolutionary tracks for luminosity class $45 < \log L_{\mathrm{X}} < 46$. This is because a linear extrapolation would give an unphysical increasing evolution towards higher redshifts.

Fig. 3.2 shows the data points and error bars extracted from the original plot in Silverman et al. (2008). The data covers a redshift range of $0 < z < 5$. The data gives the density evolution in three luminosity bins, however only the two brightest bins cover the full redshift range. The evolution of the faintest AGN is only given by two data points, and an evolution can therefore not be determined by interpolation. However, we have calculated the evolution by interpolation for the two bright luminosity bins, and extrapolated out to a

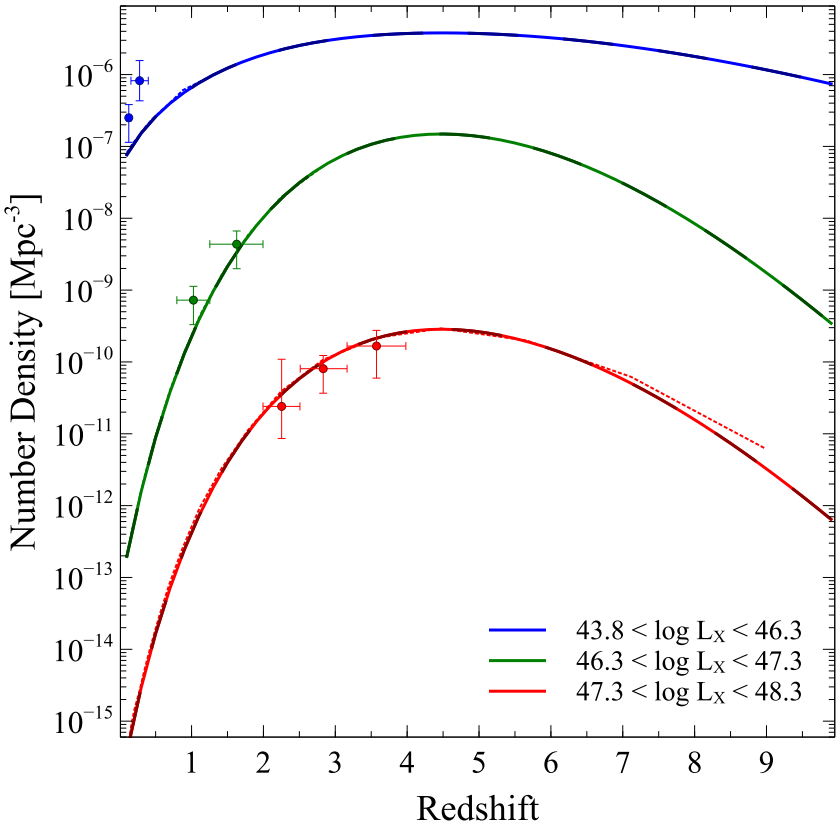

Fig. 3.3: Number density evolution of blazars, compare Fig (10a) in (Ajello et al. 2009). The plot shows the extracted very hard X-ray AGN evolution data points and errors, overlaid with the curves we have calculated from the best-fit XLF model parameters provided (their MPLE model 7), and our calculated tracks by extrapolation using the extracted data points (dotted lines). The solid lines show the calculated XLF in $\log L_X$ space, and the long dashed lines are the counterpart calculations in L_X formulation of the XLF to show the agreement (see Sec. 3.1.2).

redshift of $z = 9$.

The data for the evolution of blazars is found in Ajello et al. (2009), which is plotted in Fig. 3.3. As seen the data is scarce, in particular for the faintest of the three luminosity bins given. The original plot gives the data points with error bars up to a redshift of $z < 4$, as well as the best-fit XLF calculations up to a redshift of $z < 9$. As we cannot determine an evolution from interpolating the data points, we extract the points along their XLF-determined evolution as well, and interpolate between these points, which is given as dotted lines in the plot. Overplotted are our calculations of the XLF, in solid lines, which

follow the interpolated lines.

The interpolated evolution tracks give a good fit with the extracted data points. However, as the surveys do not cover the full redshift range we want to study, the linear extrapolation is unreliable. Most evident is that displayed in Fig. 3.1, where the evolution does not show the expected peak towards higher luminosities. Furthermore, the lack of data at lower luminosities will not allow any sensible track to be drawn to represent evolution over several cosmological epochs, as seen in Figs. 3.2. The data for blazars is particularly scarce at all luminosities (see 3.3), thus we rely on the XLF entirely for these sources.

A second method for deriving the number density evolution is therefore applied. Using the prescription of the XLF for each survey outlined in the above section, we derive the evolutionary tracks, shown in the Figs. 3.1, 3.2 and 3.3 as solid lines. As seen in Fig. 3.2, the extrapolated evolution tracks differ from our XLF calculations, using the best-fit model parameters provided in Silverman et al. (2008). A slight discrepancy is shown in Fig. 3.3 between the extracted and calculated XLF evolutions at the highest redshifts for the brightest luminosity bin.

3.1.2 AGN Population Derivations: XLF Calculations.

The form of the XLF has already been outlined in Sec. 2.3.1, and the published surveys we use in this work apply these prescriptions to their analysis. For each population we calculate the differential XLF, as well as the number densities as a function of redshift and luminosity, obtaining the total number of AGN classes over several cosmological epochs. For comparison we have calculated the XLF both in terms of luminosity and log-luminosity. Whereas Silverman et al. (2008) follow the formulation given, there are slight deviations found in the case of the soft XLF parameters of (Hasinger et al. 2005) and those of the very hard X-ray survey of (Ajello et al. 2009), briefly mentioned in Sec. 2.3.1.

In the XLF prescription of Hasinger et al. (2005), the model parameters are normalised to $\log L_{\rm X} = 44$ at characteristic redshift $z_{\rm c}$. To fit the global model to the observations we thus recalculate to find the best-fit parameters

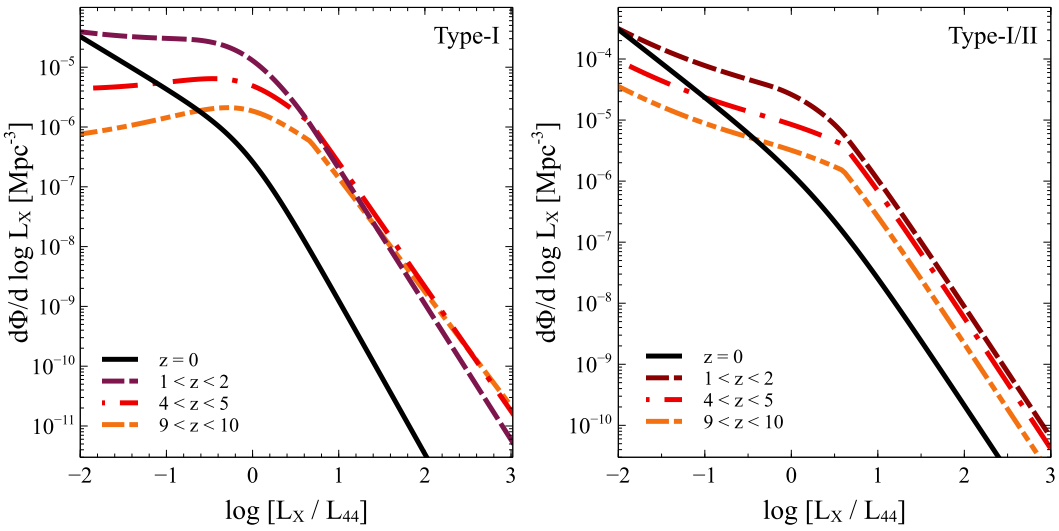

Fig. 3.4: XLF of Type-I and Type-II AGN populations: the local XLF (solid line) is compared to higher redshift bins of $1 < z < 2$ (dashed), $4 < z < 5$ (dash-dot) and $9 < z < 10$ (dash-dot-dot). Left panel: Type-I AGN population derived from the best-fit model in Hasinger et al. (2005). Right panel: AGN population of both types, derived from the best-fit model in Silverman et al. (2008).

of the local XLF, i.e. at $z = 0$. The parameters are summarised in Table 3.1. To find the characteristic redshift z_c from the normalised cut-off redshift $z_{*,44}$ we use Eqn. 2.10, with the given characteristic luminosity L_c. The evolution indices were also given in terms of indices normalised to $\log L_X = 44$, thus for consistency we express these in terms of L_c (Eqn. 2.11). The XLF normalisation is recalculated given that

$$A_{44} = \frac{d\Psi(\log L_X = 44, z = z_{*,44})}{d \log L_X} = 2.62 \times 10^{-7} \text{ Mpc}^{-3} , \tag{3.1}$$

and the local XLF, i.e. at $z = 0$, is

$$A_{44,0} = \frac{d\Psi(\log L_X = 44, z = 0)}{d \log L_X} , \tag{3.2}$$

we obtain our new normalisation $A_0 = A_{44}/A_{44,0}$.

We calculate therefore the XLF of the Type-I AGN from the soft X-ray survey; Type-I and -II AGN from the hard X-ray survey; and blazars, including the subgroups FSRQs and BL Lacs from the very hard X-ray survey. The best-fit parameters for each population were found by the authors of the relevant papers through maximum likelihood routines, and are summarised in Table

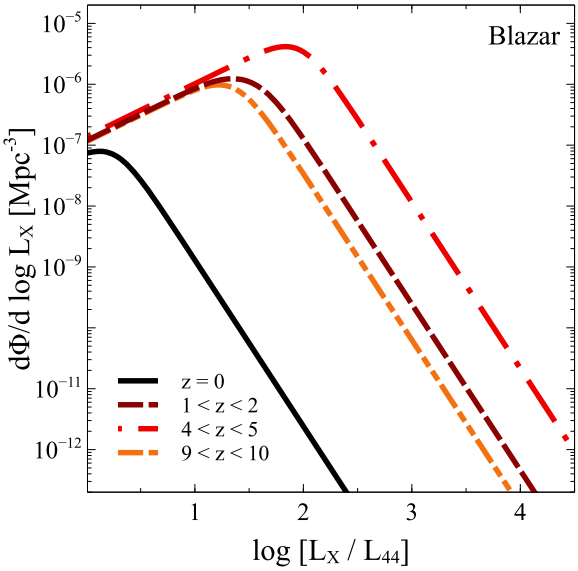

Fig. 3.5: XLF of blazars derived from the best-fit models in Ajello et al. (2009): the local XLF (solid line) is compared to higher redshift bins of $1 < z < 2$ (dashed), $4 < z < 5$ (dash-dot) and $9 < z < 10$ (dash-dot-dot).

3.1. The best-fit XLF follow a LDDE model for the former two surveys, and (modified) PLE models for the blazar survey.

We first calculate the XLF in the luminosity bins as given in the publications, as shown in Figs. 3.1, 3.2 and 3.3. We then define our own luminosity bins, such that we find the evolution of radio-galaxies in equal log-L_X bins in the range $42 < \log L_X < 47$, as discussed in Sec. 2.3. For blazars, we follow the luminosity range given in Table 2.4. Furthermore, we determine the evolution in the redshift range $0 < z < 10$.

The blazar population and FSRQ population are well described by the MPLE prescription with a common double power law present day XLF (Eqn. 2.4), where the evolution has a non-zero υ_2 index. The BL Lac population is fit by a simple PLE model, with the present day XLF described as a single power law (Eqn. 2.3), and where $\tilde{\upsilon}_2 = 0$.

We look at how the luminosity function behaves with luminosity and redshift for the different populations, and assume the XLF at lower redshifts can be extrapolated to higher redshifts. As such we span the AGN evolution from redshifts $0 < z < 10$, using the redshift ≈ 10 as an upper limit (as seen in

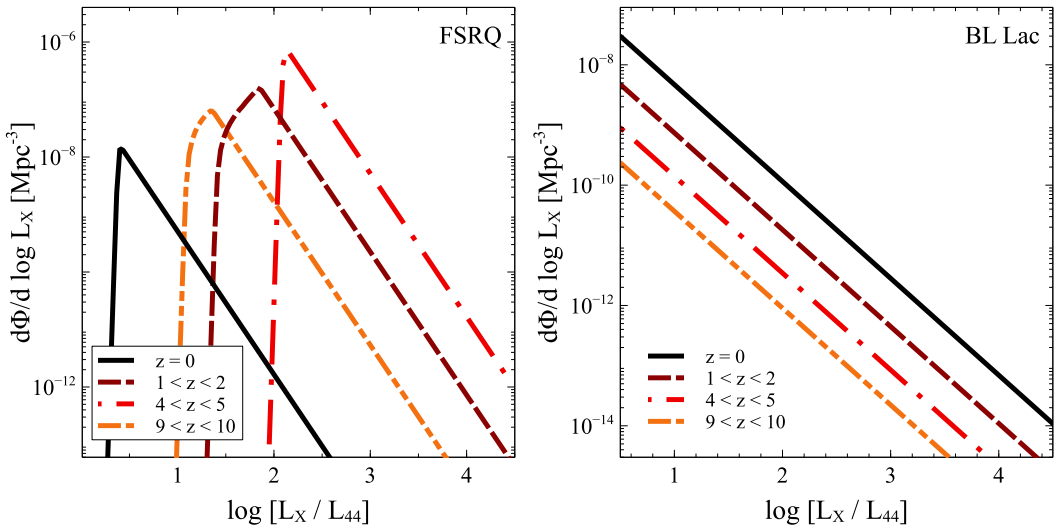

Fig. 3.6: XLF of the blazar sub-populations derived from the best-fit models in Ajello et al. (2009): the local XLF (solid line) is compared to higher redshift bins of $1 < z < 2$ (dashed), $4 < z < 5$ (dash-dot) and $9 < z < 10$ (dash-dot-dot). Left panel: FRSQ population. Right panel: BL Lac population.

Figs. 3.4-3.6). We note, however, that the oldest quasar is seen at redshift $z = 5.5$ (Romani 2006), and the oldest QSO is found at a redshift ≈ 7 thus far (Mortlock et al. 2011).

Comparing the XLF calculated in several redshift bins to the local XLF, we find that the brightest AGN are preferentially found at higher redshifts. Locally, however, low-luminosity AGN dominate, seen in Figs. 3.4 and 3.5). Type-I and the combined Type-I and -II XLFs show similar trends. However the latter is about an order of magnitude larger in population size (Fig. 3.4). Furthermore, it has a larger domination of lower-luminosity AGN at higher redshifts, where the Type-I XLF declines. At high luminosities, the Type-I XLF is dominated by sources at higher redshifts, where the Type-I and -II population maintains the domination of sources in the later epoch $1 < z < 2$. The overall peak activity for these two sets of AGN populations occurs in the redshift bin of $1 < z < 2$, with the exclusion of the brightest Type-I AGN.

The blazar population is more abundant in the past than at local redshifts with a peak in the redshift bin $4 < z < 5$. The population declines on all redshifts towards lower luminosities, shown in Fig. 3.5. Blazars are dominated by FSRQs (Fig. 3.6) at high luminosities ($\log L_X > 46$), with the

FITTED XLF MODEL PARAMETERS

MODEL	POWER-LAW PARAMETERS				EVOLUTION PARAMETERS						
	A_0	$\log L_*$	Υ_1	$\Upsilon_2, \tilde{\Upsilon}_2$	$\upsilon_{1,c}, \tilde{\upsilon}_1$	$\upsilon_{2,c}, \tilde{\upsilon}_2$	z_c	$\log L_c$	α	β_1	β_2
HLDDE	6.691×10^{-7} [c]	43.94	0.87	2.57	5.169[c]	-1.098[c]	1.9633[c]	44.67	0.21	0.7	0.6
SLDDE	-6.077[a]	44.33	2.15	1.10	4.00	-1.5	1.9	44.6	0.317	–	–
AMPLE (blazar)	1.379×10^{-7}	1.81[b]	-0.87	2.73	3.45[f]	-0.25[f]	–	–	–	–	–
AMPLE (FSRQ)	0.175×10^{-7}	2.42[b]	-50.0[d]	2.49	3.67[f]	-0.30[f]	–	–	–	–	–
APLE (BL Lac)	0.830×10^{-7}	1.0[b]	–	2.61[e]	-0.79[f]	–	–	–	–	–	–

Table 3.1: Summary of the fitted parameters for each XLF model, as given in the relevant papers: models with first letter H are given in Hasinger et al. (2005); first letter S refers to models from Silverman et al. (2008); first letter A are given in Ajello et al. (2009). PLE: pure luminosity evolution; MPLE: modified versions of PLE; LDDE: luminosity dependent density evolution. a) the value represents the logged normalisation constant, log A, as is given in Silverman et al. (2008). b) the value represents the unlogged value of the break luminosity, L_*, where the luminosities are all normalised by 10^{44} erg s^{-1}. c) recalculated values from the given parameters that were normalised to $\log L_X = 44$. d) in these calculations we used $\gamma_1 = -50.0$ (see Ajello et al. 2009). e) The BL Lac XLF model uses the single power law expression (Equation 2.3), with index $\tilde{\Upsilon}_2$. f) The blazar, FSRQ and BL Lac XLFs assume an evolution defined by the indices $\tilde{\upsilon}_1$ and $\tilde{\upsilon}_2$.

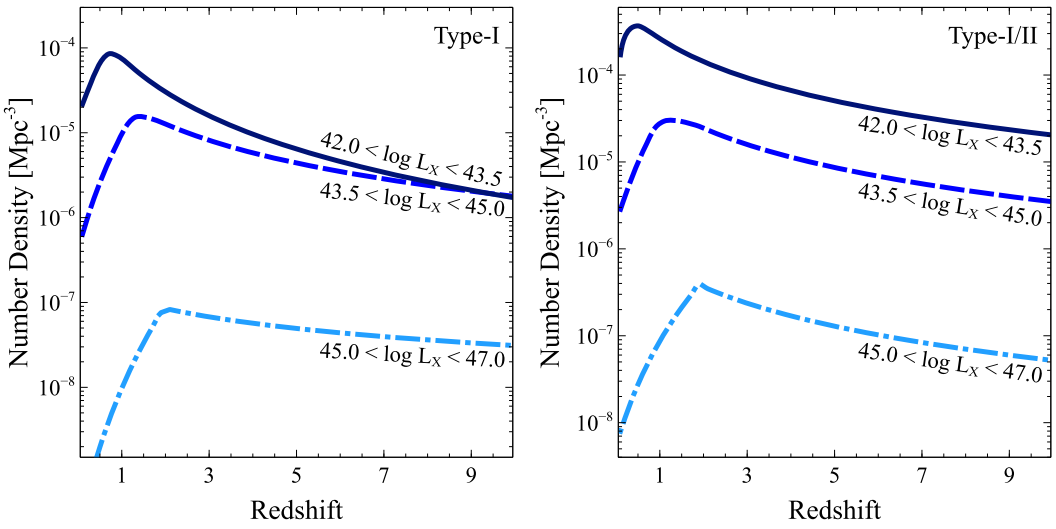

Fig. 3.7: Number density evolution of Type-I and Type-II AGN populations, in bins of X-ray luminosity of $42.0 < \log L_{\rm X} < 43.5$ (solid line), $43.5 < \log L_{\rm X} < 45.0$ (dashed), and $45.0 < \log L_{\rm X} < 47.5$ (dash-dot). Left panel: Type-I AGN population density derived from the best-fit model in Hasinger et al. (2005). Right panel: density of the AGN population of both types, derived from the best-fit model in Silverman et al. (2008).

brightest objects most numerous between redshifts 4 and 5. BL Lacs (Fig. 3.6) however, are found to be predominantly of lower luminosity, and located at lower redshifts. Their numbers decline towards higher luminosities, and the population is dominant among blazars in the local Universe.

We carry out our calculations assuming the distribution of luminosities obtained from these XLFs represent the AGN populations well - though we note the possibility of missing low-luminosity AGN, or a Compton-thick AGN contribution in the surveys, especially at high redshifts (see e.g. Fabian 2004, and references therein). The *Swift*/BAT is not sensitive to low-luminosity low-redshift sources, and the faint end of the BL Lac XLF in particular might be under-representative of the real population, reflected in the results of Ajello et al. (2009) and earlier radio-selected surveys of blazars.

We use the XLFs to calculate the number densities, and subsequently obtain the total number of radio-loud AGN within each population, over a range of luminosities and redshifts. The form of the XLF is given in terms of log-luminosities for Silverman et al. (2008) and in terms of luminosities for Ajello et al. (2009). We therefore calculate the XLFs in both forms according

to the conversion in Equation 2.2 to make sure we obtain the same results when deriving the population sizes. The number density of the populations is found by introducing the co-moving volume (Peacock (2007), see Appendix A), within each redshift bin. It is measured as

$$\frac{dV_{\rm c}}{dz} = 16\pi \left(\frac{c}{H_0}\right)^3 \frac{(\Omega z + (\Omega - 2)[\sqrt{1+\Omega z} - 1])^2}{\Omega^4 (1+z)^3 \sqrt{1+\Omega z}} \,, \tag{3.3}$$

and we use the cosmological prescriptions given in the relevant papers to maintain consistency of each population ($\rm H_0 = 70$ km s^{-1} Mpc^{-1}, $\Omega_\Lambda = 0.7, \Omega_{\rm M} = 0.3$). The X-ray luminosities are normalised by $L_{44} = 10^{44}$ erg s^{-1} in our calculations. The number density evolution is calculated in bins of X-ray luminosity, and comparing the various population densities reveals the trend that Type-I, and Type-I and -II AGN had their peak activity at redshifts $0.5 < z < 2$, whereas the blazars peaked at a much earlier time, $4 < z < 5$, seen in Figs. 3.7, 3.8 and 3.9.

It is clear that the evolution of the Type-I population closely resembles that of the combined Type-I and -II populations (Fig. 3.7). The higher luminosity bins show a steeper decline towards higher redshifts, when compared to their lower-luminosity counterparts, hence reflecting a rapid peak activity period, followed by a decline towards local epochs.

The blazar population consistently peak around redshift $z \approx 4.5$ for the various luminosity bins (Fig. 3.8). The lowest luminosity bin appears flatter than the others, which may be due to the beaming effects, as the luminosities we observe would be strongly enhanced by this phenomenon (see Sec. 2.5). This is also seen in the lowest luminosity bin of the FSRQ population (Fig. 3.9), which again accounts for the majority of the full blazar sample, and follows a similar evolutionary track. As the XLF collapses for lower luminosities, as seen in Fig. 3.5, the density evolution is calculated for sources brighter than $\log L_{\rm X} = 46.0$. The evolutionary tracks of the BL Lac population (Fig. 3.9) follow the single power-law of the XLF, and the BL Lac population is thus dominant at local redshifts and declining towards early times regardless of luminosity.

The XLF is computed without taking into account the radio-loudness

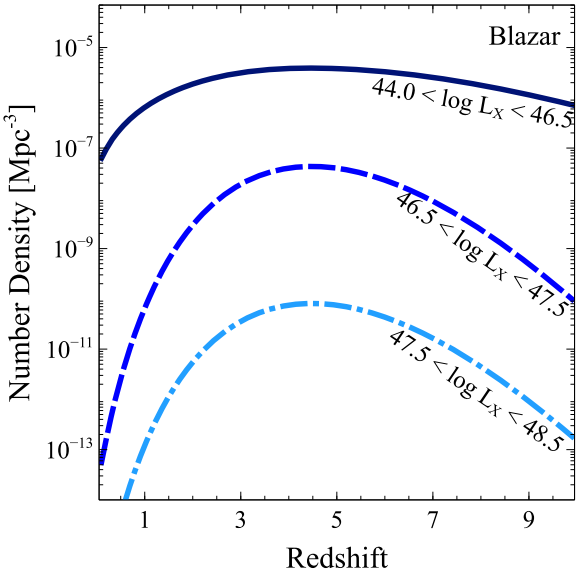

Fig. 3.8: Number density evolution of blazars derived from the best-fit model in Ajello et al. (2009) in bins of X-ray luminosity of $44.0 < \log L_{\rm X} < 46.5$ (solid line), $46.5 < \log L_{\rm X} < 47.5$ (dashed), and $47.5 < \log L_{\rm X} < 48.5$ (dash-dot).

and missing ("unseen" or faint) sources in the total population. The Type-I and the combined Type-I and -II populations consist of both radio-quiet and radio-loud sources. We are concerned with the radio-loud fraction in this work, thus require only 10% of these populations. However, to account for the radio-loud sources that are missing in the survey, we follow Zinn et al. (2011), and assume that a fraction of 10% of the population is observed. Thus, in the case of the XLF of Type-I population and the combined Type-I and -II populations, the two correction factors cancel, and the calculations will reflect the full radiogalaxy/quasar populations with the correction factor $\Theta_{\rm CF} = 1$.

In the case of the blazars however, their nature implies radio-loudness, hence this is already accounted for. To account for all blazars we use a correction factor based on the opening angle of the jet to include the misaligned fraction of blazars. Assuming a modest bulk Lorentz factor $\Gamma = 10$, and that it relates to the half opening angle by $\omega_{\rm j} = \Gamma^{-1} = 0.1$ radians, we obtain the correction factor as a ratio between the solid angle of a full sphere to the solid angle the jet projects to on this sphere. The viewing angle is $\theta_{\rm v} = \omega_{\rm j}$, so that a jet with an opening angle of $2\omega_{\rm j}$, will be not be in our line of sight if the

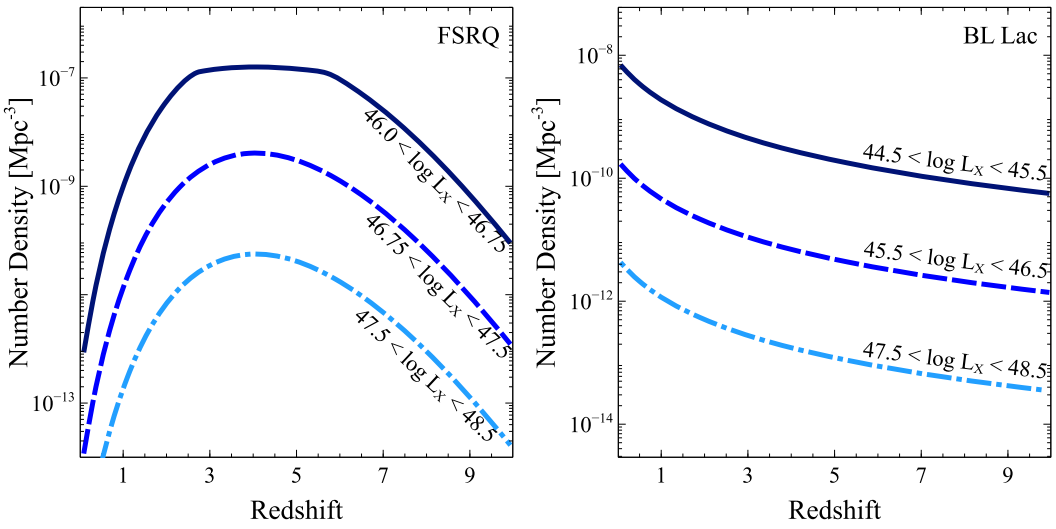

Fig. 3.9: Number density evolution of FSRQ and BL Lac populations derived from the best-fit models in Ajello et al. (2009). Left panel: FSRQ population, in bins of $46.0 < \log L_{\rm X} < 46.75$ (solid line), $46.75 < \log L_{\rm X} < 47.5$ (dashed), and $47.5 < \log L_{\rm X} < 48.5$ (dash-dot). Right panel: BL Lac population, in bins of $44.5 < \log L_{\rm X} < 45.5$ (solid line), $45.5 < \log L_{\rm X} < 46.5$ (dashed), and $47.5 < \log L_{\rm X} < 48.5$ (dash-dot).

viewing angle is larger than the half opening angle. These misaligned sources will therefore be accounted for through

$$\Theta_{\rm CF} = \frac{4\pi}{\Omega} = \frac{4\pi}{2\pi(1-\cos(\omega_{\rm j}))} = \frac{4\pi}{2\pi(\frac{\omega_{\rm j}^2}{2})} = 4\Gamma^2 \ . \tag{3.4}$$

This gives a correction factor of 400, which agrees with estimates of a few hundred, or $2\Gamma^2$ (Ajello et al. 2009; Ghisellini et al. 2010; Volonteri et al. 2011), and we apply this correction to the blazar sample, as well as the sub-classes to obtain the full blazar/quasar population throughout the history of the Universe.

We then compute the redshift and luminosity distributions of all complete populations, and calculate the number of sources in bins of both redshift and luminosity. We obtain the number distribution of the AGN populations over redshift, $N(z)$, by integrating into bins of luminosity as a function of redshift in the range $0 < z < 10$,

$$\frac{dN(z)}{dz} = \Theta_{\rm CF} \int_{\log L_{\rm X,1}}^{\log L_{\rm X,2}} \frac{d\Psi(L_{\rm X}, z)}{d\log L_{\rm X}} \frac{dV_{\rm c}}{dz} d\log L_{\rm X} \ . \tag{3.5}$$

The number distribution of the AGN populations over X-ray luminosity,

$N(L_{\rm X})$ is found by integrating the XLF over redshift as a function of X-ray luminosity, such that

$$\frac{dN(L_{\rm X})}{d\log L_{\rm X}} = \int_{z_1}^{z_2} \frac{d\Psi(L_{\rm X}, z)}{d\log L_{\rm X}} \frac{dV_{\rm c}}{dz} dz \ . \tag{3.6}$$

By multiplying the population distribution by the size of the redshift or luminosity bin, Δz or $\Delta \log L_{\rm X}$, we obtain the total population over redshift or luminosity, respectively. We choose the appropriate luminosity range, with each bin spanning an equal size for a consistent comparison. Evaluating the maximum luminosity of an AGN, according to the Eddington luminosity dictated by the SMBH at the AGN centre, we find the maximum log-luminosity $\sim \log L_{\rm X} = 47.0$. Thus, for the Type-I and Type-I and -II AGN populations our range follows that of Silverman et al. (2008), spanning five orders of magnitude, from an estimated lowest AGN X-ray log-luminosity of 42 to a maximum of 47.

In the case of blazars, we need to account for the beaming of these objects, hence, take into account the minimum intrinsic X-ray luminosity, for which we set to $\log \mathcal{L}_{\rm X} = 40.0$. As such we only take those above this intrinsic luminosity to be actual blazar objects, and thus avoid confusion with objects that fall below this luminosity, such as X-ray binaries and other luminous objects that could be observed at these redshifts. Assuming a representative value for the spectral index across the objects of each of the blazar populations we use, for the subsamples BL Lacs, $\alpha_{\rm X} = 1.5$; for FSRQs, $\alpha_{\rm X} = 0.6$; and the total blazar sample we use $\alpha_{\rm X} = 1.0$ (see Figure 2, Ajello et al. (2009)). This means that the lowest observed luminosity for FSRQs is set at $\log L_{\rm X} = 43.6$; for blazars is $\log L_{\rm X} = 44.0$, and for BL Lacs it is set to $\log L_{\rm X} = 44.5$ (see Sec. 2.5 for details). However as already mentioned, the XLF of FSRQs limits us to lower luminosity of $\log L_{\rm X} = 46.0$ for this particular population.

3.2 Number derivation of X-ray detected populations

We have checked that the XLF in terms of log-luminosities and luminosities produce the same results, according to the conversion given in Equation (2.2). The numbers we derive for each population, either in bins of redshift or luminosity, therefore come in two representations which are consistent with each

other. These numbers then form the source-data for our neutrino spectra, thus it is of great importance that these derivations are sound. In this section we show the final derivations of the population sizes which are used to calculate the expected neutrino spectra from these populations.

For the Type-I data derived from the XLF prescription given in Hasinger et al. (2005), and Type-I and -II AGN, derived from the XLF given in Silverman et al. (2008), we first calculate the given log-form of the XLF, and then doing the conversion, we repeat calculations. The slight differences between the two are due to the binning in the calculations. For the blazar types, we reverse the order, as the XLFs given in Ajello et al. (2009) are given in terms of un-logged luminosities. In addition to the full blazar sample, we have also derived the size of the FSRQ and BL Lac sub-groups, using their best fit models from Ajello et al. (2009).

The derived population numbers are tabulated in Tables 3.2 (Type-I AGN), 3.3 (Type-I and Type-II AGN), 3.4 (blazars), 3.5 (FSRQs), and 3.6 (BL Lacs). We calculate the ratio between the two methods of calculation and find they are in agreement.

3.3 Results from Calculations of X-ray Detected AGN

We calculate for all five populations the distributions in redshift and X-ray luminosity. We correct for missing, or misaligned sources in each population. As expected, we find that Type-I and Type-II AGN activity peak later than blazars, which can be readily seen in Figs. 3.10 and 3.11. The former evolutions peak between redshifts of 0.5 and 2, whereas blazars (including FSRQ, but not BL Lac sources) peak at redshifts between 4 and 5. The less powerful BL Lacs peak at redshifts closer to $z = 1$, similar to the Type-I and -II AGN.

The peak activity of Type-I and -II AGN decreases in redshift with decreasing X-ray luminosity, seen on the left panels in the Fig. 3.10, whereas for the blazars, the peak does not shift significantly. The location of the peak in the redshift distribution suggests that the most luminous blazars and bright quasars formed at an early time in the history of the Universe, and rapidly decreased in density towards later times. Though this implies that black holes

Derived Type I population size

z bin	$\left.\frac{dN(\log L_{\rm X})}{d\log L_{\rm X}}\right\|_z \times \Delta \log L_{\rm X}$	$\left.\frac{dN(L_{\rm X})}{dL_{\rm X}}\right\|_z \times \Delta L_{\rm X}$	$\left\|\frac{N(\log L_{\rm X})-N(L_{\rm X})}{N(\log L_{\rm X})}\right\|$
0-1	5.106×10^6	5.107×10^6	2.45×10^{-4}
1-2	8.223×10^6	8.225×10^6	2.45×10^{-4}
2-3	4.227×10^6	4.228×10^6	2.45×10^{-4}
3-4	2.251×10^6	2.252×10^6	2.45×10^{-4}
4-5	1.319×10^6	1.319×10^6	2.45×10^{-4}
5-6	8.333×10^5	8.335×10^5	2.45×10^{-4}
6-7	5.581×10^5	5.582×10^5	2.45×10^{-4}
7-8	3.914×10^5	3.915×10^5	2.45×10^{-4}
8-9	2.848×10^5	2.848×10^5	2.45×10^{-4}
9-10	2.136×10^5	2.136×10^5	2.45×10^{-4}
0-10	2.341×10^7	2.341×10^7	2.45×10^{-4}
Log-L bin	$\left.\frac{dN(z)}{dz}\right\|_{\log L_{\rm X}} \times \Delta z$	$\left.\frac{dN(z)}{dz}\right\|_{L_{\rm X}} \times \Delta z$	$\left\|\frac{N(\log L_{\rm X})-N(L_{\rm X})}{N(\log L_{\rm X})}\right\|$
42.0 - 42.5	6.797×10^6	6.797×10^6	7.98×10^{-7}
42.5 - 43.0	5.684×10^6	5.684×10^6	2.43×10^{-6}
43.0 - 43.5	5.032×10^6	5.032×10^6	2.83×10^{-6}
43.5 - 44.0	3.815×10^6	3.815×10^6	1.59×10^{-6}
44.0 - 44.5	1.650×10^6	1.650×10^6	7.31×10^{-6}
44.5 - 45.0	3.776×10^5	3.777×10^5	8.53×10^{-5}
45.0 - 45.5	3.813×10^4	3.813×10^4	2.16×10^{-7}
45.5 - 46.0	3.404×10^3	3.404×10^3	2.23×10^{-7}
46.0 - 46.5	3.068×10^2	3.068×10^2	2.18×10^{-7}
46.5 - 47.0	2.807×10^1	2.807×10^1	2.16×10^{-7}
42.0 - 47.0	1.004×10^8	1.004×10^8	2.19×10^{-5}

Table 3.2: Estimated numbers of the Type I population, calculated using the XLF prescription given in Hasinger et al. (2005), in log-luminosity (left column) and luminosity (centre column). The right-most column gives the ratio between the two sets of numbers.

Derived Type I/II population size

z bin	$\left.\frac{dN(\log L_{\rm X})}{d\log L_{\rm X}}\right\|_z \times \Delta \log L_{\rm X}$	$\left.\frac{dN(L_{\rm X})}{dL_{\rm X}}\right\|_z \times \Delta L_{\rm X}$	$\left\|\frac{N(\log L_{\rm X})-N(L_{\rm X})}{N(\log L_{\rm X})}\right\|$
0-1	2.217×10^7	2.218×10^7	2.45×10^{-4}
1-2	2.925×10^7	2.926×10^7	2.45×10^{-4}
2-3	1.767×10^7	1.767×10^7	2.45×10^{-4}
3-4	1.070×10^7	1.070×10^7	2.45×10^{-4}
4-5	6.883×10^6	6.884×10^6	2.45×10^{-4}
5-6	4.672×10^6	4.673×10^6	2.45×10^{-4}
6-7	3.314×10^6	3.314×10^6	2.45×10^{-4}
7-8	2.435×10^6	2.436×10^6	2.45×10^{-4}
8-9	1.843×10^6	1.843×10^6	2.45×10^{-4}
9-10	1.429×10^6	1.429×10^6	2.45×10^{-4}
0-10	1.004×10^8	1.004×10^8	2.45×10^{-4}
Log-L bin	$\left.\frac{dN(z)}{dz}\right\|_{\log L_{\rm X}} \times \Delta z$	$\left.\frac{dN(z)}{dz}\right\|_{L_{\rm X}} \times \Delta z$	$\left\|\frac{N(\log L_{\rm X})-N(L_{\rm X})}{N(\log L_{\rm X})}\right\|$
42.0 - 42.5	5.067×10^7	5.067×10^7	9.00×10^{-7}
42.5 - 43.0	2.451×10^7	2.451×10^7	1.05×10^{-6}
43.0 - 43.5	1.310×10^7	1.310×10^7	1.40×10^{-5}
43.5 - 44.0	7.247×10^6	7.247×10^6	1.82×10^{-6}
44.0 - 44.5	3.601×10^6	3.601×10^6	7.82×10^{-5}
44.5 - 45.0	1.130×10^6	1.130×10^6	1.73×10^{-7}
45.0 - 45.5	1.273×10^5	1.273×10^5	1.73×10^{-7}
45.5 - 46.0	1.172×10^4	1.172×10^4	2.24×10^{-7}
46.0 - 46.5	1.015×10^3	1.015×10^3	2.41×10^{-7}
46.5 - 47.0	8.612×10^1	8.612×10^1	2.51×10^{-7}
42.0 - 47.0	1.004×10^8	1.004×10^8	5.07×10^{-6}

Table 3.3: Estimated numbers of the Type-I and type-II population, calculated using the XLF prescription given in Silverman et al. (2008), in log-luminosity (left column) and luminosity (centre column). The right-most column gives the ratio between the two sets of numbers.

Derived blazar population size

z bin	$\left.\frac{dN(\log L_{\rm X})}{d\log L_{\rm X}}\right\|_z \times \Delta \log L_{\rm X}$	$\left.\frac{dN(L_{\rm X})}{dL_{\rm X}}\right\|_z \times \Delta L_{\rm X}$	$\left\|\frac{N(\log L_{\rm X})-N(L_{\rm X})}{N(\log L_{\rm X})}\right\|$
0-1	9.937×10^6	9.939×10^6	1.99×10^{-4}
1-2	6.585×10^7	6.586×10^7	1.99×10^{-4}
2-3	1.319×10^8	1.319×10^8	1.99×10^{-4}
3-4	1.643×10^8	1.643×10^8	1.99×10^{-4}
4-5	1.576×10^8	1.576×10^8	1.99×10^{-4}
5-6	1.276×10^8	1.276×10^8	1.99×10^{-4}
6-7	9.138×10^7	9.140×10^7	1.99×10^{-4}
7-8	5.951×10^7	5.952×10^7	1.99×10^{-4}
8-9	3.583×10^7	3.582×10^7	1.99×10^{-4}
9-10	2.013×10^7	2.014×10^7	1.99×10^{-4}
0-10	8.640×10^8	8.642×10^8	1.99×10^{-4}
Log-L bin	$\left.\frac{dN(z)}{dz}\right\|_{\log L_{\rm X}} \times \Delta z$	$\left.\frac{dN(z)}{dz}\right\|_{L_{\rm X}} \times \Delta z$	$\left\|\frac{N(\log L_{\rm X})-N(L_{\rm X})}{N(\log L_{\rm X})}\right\|$
44.0 - 44.5	3.921×10^7	3.921×10^7	9.38×10^{-9}
44.5 - 45.0	1.049×10^8	1.049×10^8	8.04×10^{-9}
45.0 - 45.5	2.533×10^8	2.533×10^8	2.47×10^{-9}
45.5 - 46.0	3.630×10^8	3.630×10^8	4.41×10^{-7}
46.0 - 46.5	9.811×10^7	9.811×10^7	1.83×10^{-6}
46.5 - 47.0	5.226×10^6	5.226×10^6	4.90×10^{-7}
47.0 - 47.5	2.265×10^5	2.265×10^5	5.69×10^{-7}
47.5 - 48.0	9.773×10^3	9.773×10^3	5.78×10^{-7}
48.0 - 48.5	4.217×10^2	4.217×10^2	5.83×10^{-7}
44.0 - 48.5	8.640×10^8	8.640×10^8	5.29×10^{-7}

Table 3.4: Estimated numbers of the total blazar population, calculated using the XLF prescription given in Ajello et al. (2009), in log-luminosity (left column) and luminosity (centre column). The right-most column gives the ratio between the two sets of numbers.

Derived FSRQ population size

z bin	$\left.\frac{dN(\log L_{\rm X})}{d\log L_{\rm X}}\right\|_z \times \Delta \log L_{\rm X}$	$\left.\frac{dN(L_{\rm X})}{dL_{\rm X}}\right\|_z \times \Delta L_{\rm X}$	$\left\|\frac{N(\log L_{\rm X})-N(L_{\rm X})}{N(\log L_{\rm X})}\right\|$
0-1	7.404×10^{3}	7.404×10^{3}	6.14×10^{-5}
1-2	6.559×10^{5}	6.560×10^{5}	6.14×10^{-5}
2-3	5.014×10^{6}	5.014×10^{6}	6.14×10^{-5}
3-4	7.220×10^{6}	7.220×10^{6}	6.14×10^{-5}
4-5	6.420×10^{6}	6.421×10^{6}	6.14×10^{-5}
5-6	4.613×10^{6}	4.614×10^{6}	6.14×10^{-5}
6-7	1.715×10^{6}	1.715×10^{6}	6.14×10^{-5}
7-8	3.596×10^{5}	3.597×10^{5}	6.14×10^{-5}
8-9	5.527×10^{4}	5.527×10^{4}	6.14×10^{-5}
9-10	6.548×10^{3}	6.548×10^{3}	6.14×10^{-5}
0-10	2.607×10^{7}	2.607×10^{7}	6.14×10^{-5}
Log-L bin	$\left.\frac{dN(z)}{dz}\right\|_{\log L_{\rm X}} \times \Delta z$	$\left.\frac{dN(z)}{dz}\right\|_{L_{\rm X}} \times \Delta z$	$\left\|\frac{N(\log L_{\rm X})-N(L_{\rm X})}{N(\log L_{\rm X})}\right\|$
43.6 - 44.0	2.411×10^{-25}	2.411×10^{-25}	3.32×10^{-7}
44.0 - 44.5	2.393×10^{0}	2.393×10^{0}	0.00
44.5 - 45.0	2.193×10^{4}	2.193×10^{4}	2.01×10^{-6}
45.0 - 45.5	9.429×10^{5}	9.429×10^{5}	7.93×10^{-5}
45.5 - 46.0	7.444×10^{6}	7.441×10^{6}	3.50×10^{-4}
46.0 - 46.5	2.394×10^{7}	2.394×10^{7}	2.03×10^{-5}
46.5 - 47.0	2.000×10^{6}	2.000×10^{6}	4.17×10^{-7}
47.0 - 47.5	1.138×10^{5}	1.138×10^{5}	4.12×10^{-7}
47.5 - 48.0	6.473×10^{3}	6.473×10^{3}	4.13×10^{-7}
48.0 - 48.5	3.682×10^{2}	3.682×10^{2}	4.04×10^{-7}
43.6 - 48.5	3.447×10^{7}	3.447×10^{7}	2.94×10^{-4}
46.0 - 48.5	2.606×10^{7}	2.606×10^{7}	1.87×10^{-5}

Table 3.5: Estimated numbers of the FSRQ population, calculated using the XLF prescription given in Ajello et al. (2009), in log-luminosity (left column) and luminosity (centre column). The column on the right gives the ratio between the two sets of numbers. As the XLF collapses below $\log L_{\rm X} = 46.0$, this is the effective lower bound used in the work presented in Ch. 2.

Derived BL Lac population size

z bin	$\left.\frac{dN(\log L_{\rm X})}{d\log L_{\rm X}}\right\|_z \times \Delta \log L_{\rm X}$	$\left.\frac{dN(L_{\rm X})}{dL_{\rm X}}\right\|_z \times \Delta L_{\rm X}$	$\left\|\frac{N(\log L_{\rm X})-N(L_{\rm X})}{N(\log L_{\rm X})}\right\|$
0-1	7.971×10^4	7.972×10^4	1.57×10^{-4}
1-2	6.717×10^4	6.718×10^4	1.57×10^{-4}
2-3	3.271×10^4	3.271×10^4	1.57×10^{-4}
3-4	1.714×10^4	1.714×10^4	1.57×10^{-4}
4-5	9.832×10^3	9.834×10^3	1.57×10^{-4}
5-6	6.069×10^3	6.070×10^3	1.57×10^{-4}
6-7	3.969×10^3	3.969×10^3	1.57×10^{-4}
7-8	2.717×10^3	2.717×10^3	1.57×10^{-4}
8-9	1.931×10^3	1.931×10^3	1.57×10^{-4}
9-10	1.416×10^3	1.415×10^3	1.57×10^{-4}
1-10	2.227×10^5	2.227×10^5	1.57×10^{-4}
Log-L bin	$\left.\frac{dN(z)}{dz}\right\|_{\log L_{\rm X}} \times \Delta z$	$\left.\frac{dN(z)}{dz}\right\|_{L_{\rm X}} \times \Delta z$	$\left\|\frac{N(\log L_{\rm X})-N(L_{\rm X})}{N(\log L_{\rm X})}\right\|$
44.5 - 45.0	1.880×10^5	1.880×10^5	8.55×10^{-8}
45.0 - 45.5	2.945×10^4	2.945×10^4	9.19×10^{-8}
45.5 - 46.0	4.615×10^3	4.615×10^3	9.40×10^{-8}
46.0 - 46.5	7.230×10^2	7.230×10^2	9.54×10^{-8}
46.5 - 47.0	1.133×10^2	1.133×10^2	9.75×10^{-8}
47.0 - 47.5	1.775×10^1	1.775×10^1	8.80×10^{-8}
47.5 - 48.0	2.781×10^0	2.781×10^0	9.54×10^{-8}
48.0 - 48.5	4.357×10^{-1}	4.357×10^{-1}	1.00×10^{-7}
44.5 - 48.5	2.229×10^5	2.229×10^5	4.18×10^{-6}

Table 3.6: Estimated numbers of the BL Lac population, calculated using the XLF prescription given in Ajello et al. (2009), in log-luminosity (left column) and luminosity (centre column). The right-most column gives the ratio between the two sets of numbers. The luminosity binned numbers imply that there is a high luminosity cut-off ($\log L_{\rm X} < 48.0$) which is consistent with the BL Lac being a low-luminosity population.

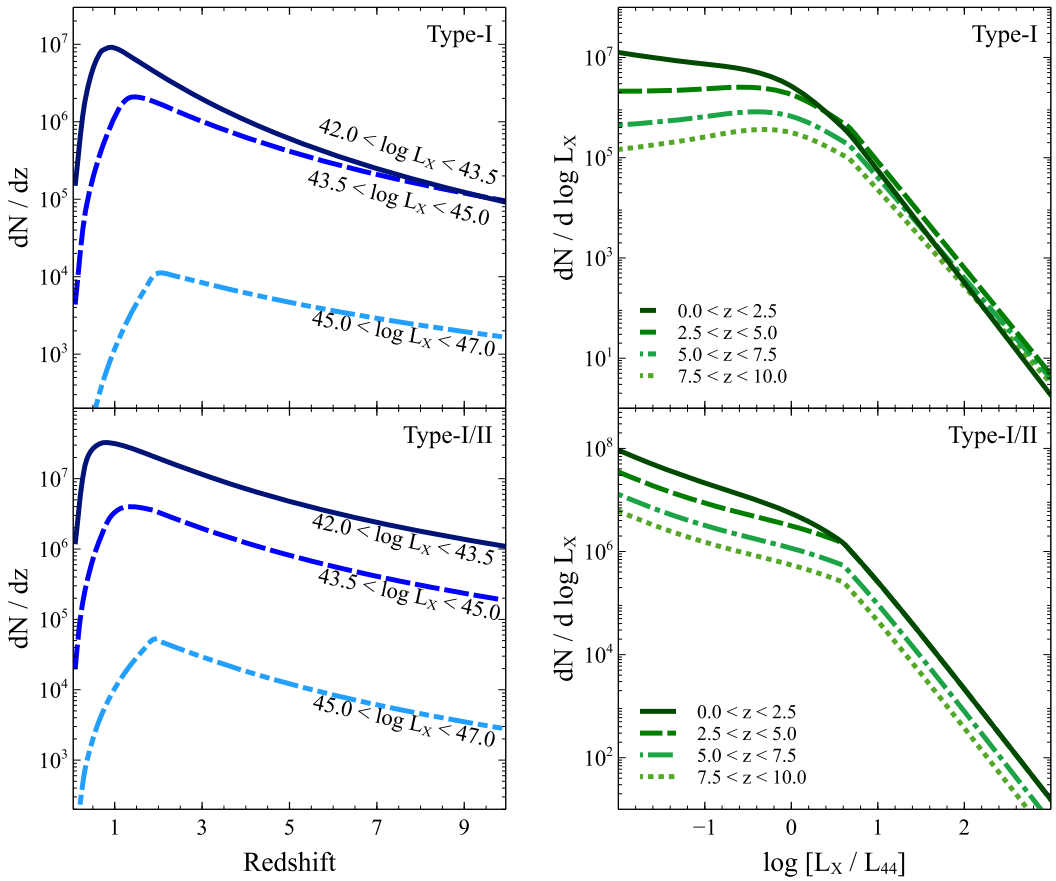

Fig. 3.10: Redshift and luminosity distributions of Type-I and Type-I and -II AGN populations. Panels on the left show the redshift distributions in three luminosity bins, and panels on the right show the luminosity distributions in four bins of redshift, for the Type-I population in the top panels, and the Type-I and -II population in the bottom panels.

formed early on in the Universe, and that the conditions of the early Universe were favourable to the formation of very luminous AGN, the observational limitations at higher redshifts is restricting a study of low-luminosity AGN at the same distances (Ajello et al. 2009).

In Figs. 3.10 and 3.11 both the redshift distribution and luminosity distribution lead to a similar conclusion in that luminous blazars/quasars formed, and peaked in activity, early on before rapidly declining, whereas the less powerful AGN have their peak at a later time. The distribution over redshift tells us that for a given population, the peak is found at a given redshift (e.g. ~ 4 for blazars/quasars, $\sim 1-2$ for a typical luminous AGN), implying that the heyday of the population was at this given point in the history of the Universe,

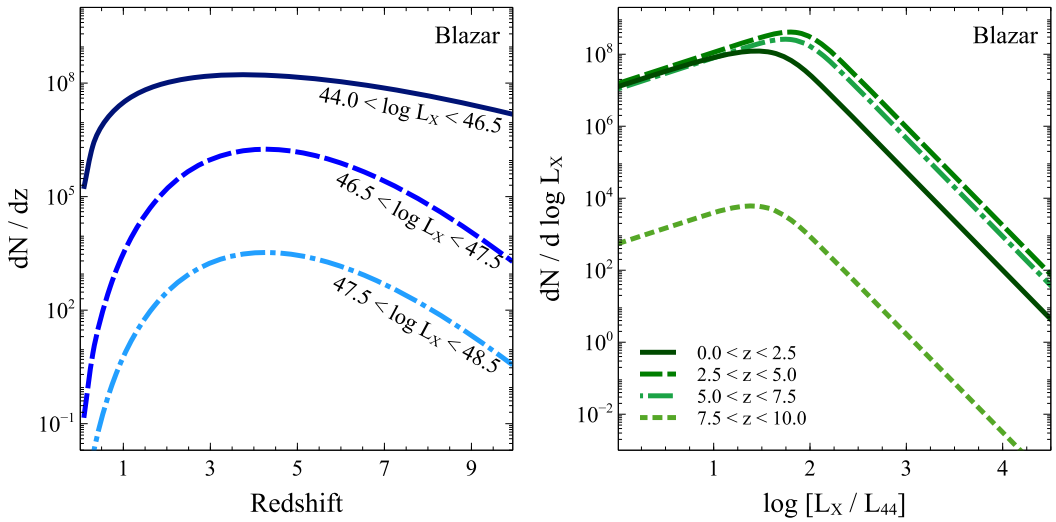

Fig. 3.11: Redshift and luminosity distributions of blazars. The panel on the left shows the redshift distributions in luminosity bins: $44.0 < \log L_{\rm X} < 46.5$ (solid line), $46.5 < \log L_{\rm X} < 47.5$ (dashed), and $47.5 < \log L_{\rm X} < 48.5$ (dash-dot). The panel on the right show the luminosity distributions bins of redshift.

and has since declined.

We can conceptually explain the luminosity distribution in a slightly different way. The distribution over luminosities suggests that the luminosity of the objects is linked to the temporal evolution of the population, such that we find brighter AGN dominating at earlier times in the history of the Universe, and the closer to more local redshifts we move, the populations are dominated by the more faint objects. This can be seen for Type-I AGN in the top right panel of Fig. 3.10, where there is a significant shift from the dominance of the local redshift bin for lower luminosity AGN, to the bin of peak activity for more luminous AGN. This is not so obvious for the Type-I and -II population, as the gap between the local redshift bin and the earlier bins decreases as one moves to higher luminosities. The luminous blazar populations (Fig. 3.11) show a dominance in the redshifts enclosing its peak activity, and maintains this dominance, as the sources show a rapid decline at lower luminosities. The low-luminosity BL Lac sources (Fig. 3.12) reflect their simple model evolution, with a linear increase towards lower luminosities, throughout dominated by local sources.

It is therefore no surprise perhaps that we find the most luminous AGN

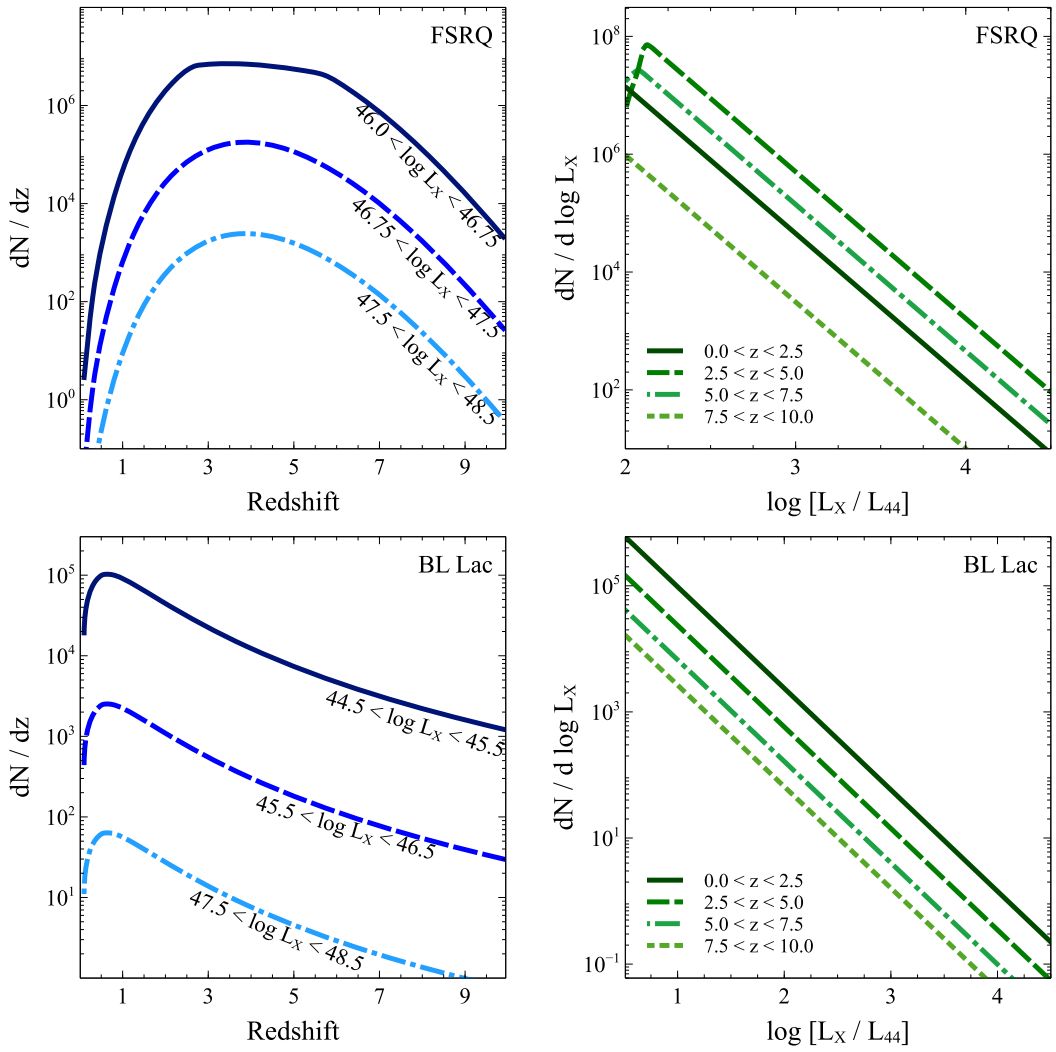

Fig. 3.12: Redshift and luminosity distributions of FSRQ sources (top panels), and BL Lac sources (bottom panels). Panels on the left show the redshift distributions in luminosity bins: FSRQs $46.0 < \log L_{\rm X} < 46.75$ (solid line), $46.75 < \log L_{\rm X} < 47.5$ (dashed), and $47.5 < \log L_{\rm X} < 48.5$ (dash-dot); BL Lacs of $44.5 < \log L_{\rm X} < 45.5$ (solid line), $45.5 < \log L_{\rm X} < 46.5$ (dashed), and $47.5 < \log L_{\rm X} < 48.5$ (dash-dot). Panels on the right show the luminosity distributions bins of redshift.

(the blazar/quasar populations) peaking considerably earlier than the fainter and more common AGN, which have been surveyed by e.g. Silverman et al. (2008). In a young and smaller Universe it would be a higher frequency of merging black holes providing the favourable conditions for the quasar activity we see in the past – however as the universe expanded, the number of quasars declined rapidly. In line with this, for Type-I, and Type-I and -II AGN,

Derived AGN Space Densities

AGN population:	Space density [Mpc^{-3}] :
Type-I AGN	6.65×10^{-6}
Type-I and Type-II AGN	2.85×10^{-5}
Blazars	2.46×10^{-4}
FSRQs	7.41×10^{-6}
BL Lacs	6.33×10^{-8}

Table 3.7: Derived AGN space densities for the various populations, in the redshift range $0 < z < 10$. Type-I and the combined Type-I and -II populations are derived in the luminosity range $42 < \log\ L_{\mathrm{X}} < 47$, blazars in range $44 < \log\ L_{\mathrm{X}} < 48.5$, FSRQs in range $46 < \log\ L_{\mathrm{X}} < 48.5$, and BL Lacs $44.5 < \log\ L_{\mathrm{X}} < 48.5$. See text for details.

brighter AGN are found at higher redshifts, whereas lower luminosity sources are dominant more locally, however in both cases, the dominant redshifts are $1 < z < 2$ (fainter sources) to $2 < z < 3$ (brighter sources). In the case of blazars, and the more numerous sub-class of FSRQs, a similar trend occurs. However these sources are at the lowest luminosities dominant in the very local universe ($0 < z < 1$), and the brightest sources are dominating the high redshift universe, peaking at $4 < z < 5$.

We use these calculation to derive the size of each population, and determine the space density of these populations in the total volume we have investigated. We multiply our distributions in each bin by the size of the redshift or luminosity interval, and sum each contribution, for which the details can be found in Sec. 3.2. Our chosen redshift range of $0 < z < 10$, encloses a volume of 3.519×10^{12} Mpc^3 (Wright 2006) for the cosmology given in Hasinger et al. (2005); Silverman et al. (2008); Ajello et al. (2009), and we derive the space densities of each population, summarised in Table 3.7. The order of magnitude of the calculated space densities agrees well with published space density estimations of various AGN populations (e.g. Takami et al. (2012), for local space densities of UHECR sources, and also Yoshiguchi et al. (2003) and references therein), such as Seyferts (i.e. radio-quiet AGN) estimated at $\sim 10^{-3}$ Mpc^{-3}, which should be an order of magnitude or so higher than our radio-loud pop-

ulation. It also agrees well with that of radio-loud AGN, if these are UHECR sources, measured to $\sim 10^{-4}$ Mpc^{-3}; that of BL Lacs as $\sim 10^{-7}$ Mpc^{-3}, and in terms of unification, FRIs are measured to $\sim 10^{-5}$ Mpc^{-3}, for which the discrepancy might be for our case the lack of low-luminosity BL Lac detected. The (local) majority of this population might therefore be missed in our estimate. The FRII space density has been measured to $\sim 10^{-8}$ Mpc^{-3}, however, because these are local measurements, and the FSRQs are observed at high redshifts, this might explain the discrepancy if the unification is applicable, as the space density of the FSRQ is expected to have declined rapidly since its peak activity at around $z = 4.5$.

3.4 FSRQs Derived from γ-ray Surveys

We follow the same procedure as we did in Sec. 3.1.2 to derive the space density of FSRQs. Similar to the X-ray derived space densities, we find that the activity of luminous FSRQs peak at an earlier time than the lower-luminosity sources, and is followed by a rapid decline towards the local epoch. We furthermore assume that the evolution found in the survey can be extrapolated to higher redshifts, assuming the local behaviour of the γLF is also applicable at the early epochs of AGN formation.

3.4.1 FSRQ Population Derivations: γLF Calculations.

The analytical form of the γLF is described in Sec. 2.4.1, and the survey we use to derive the number evolution of FSRQs is given in Ajello et al. (2012). The best-fit model takes an LDDE form, and corresponding model parameters are found through maximum likelihood methods by Ajello et al. (2012). These are summarised in Table 3.8. We also follow the limits on the γ-ray luminosity and photon index given in the survey publication.

We calculate the differential γLF and the number density as a function of redshift and luminosity. We then obtain the redshift and luminosity distribution of the population, and derive the total number density of AGN over several cosmological epochs. The upper redshift limit is given as $z = 6$ in Ajello et al. (2012), however the analysis is independent of the redshift (Ajello et al. 2014). We therefore extrapolate the lower redshift evolution to an upper limit of

FSRQ γLF MODEL PARAMETERS

POWER-LAW		EVOLUTION		SPECTRAL INDEX	
A_0^a:	3.06	$\upsilon_{1,c}$	7.35^c	μ_c	2.44^c
L_*^b	0.84	υ_2	-6.51	σ	0.18
Υ_1	0.21	z_c	1.47	ρ_{min}	1.80
Υ_2	1.58	α	0.21	ρ_{max}	3.0

Table 3.8: Summary of the fitted parameters for the FSRQ γLF model, as given in Ajello et al. (2012). The model follows an LDDE form, which refers to a luminosity dependent density evolution. a) Normalisation constant in units of 10^{-9} Mpc^{-3} erg^{-1} s. b) The break luminosity is normalised by 10^{48} erg s^{-1}. c) The parameterisation for the FSRQ population has luminosity independent values for the low-redshift index υ_1 and mean of the photon index μ.

$z = 10$. We do however use the range of photon indices given, which are summarised in Table 3.8.

Blazar luminosities are strongly beamed in our direction. The observed γ-ray luminosities will therefore differ from the intrinsic luminosity, as discussed for the X-ray detected blazars in Sec. 3.1.2. We use the beaming relation between intrinsic and beamed luminosity, $\mathcal{L}_\gamma$ and L_γ respectively,

$$L_\gamma = \delta^\varrho \mathcal{L}_\gamma \tag{3.7}$$

to determine the lower limit to the observed γ-ray luminosity. We use $\varrho = 3 + \psi_\gamma$, and ψ_γ is the spectral index, $\psi_\gamma = -(1 - \rho)$ (see Sec. 2.5), and find $\log L_{\gamma,\mathrm{min}} = 44.5$ for the FSRQ population. A correction factor is introduced to account for misaligned blazars to obtain an estimate of the full blazar population. In the radio-loud unification model (Urry and Padovani 1995) these sources would account for the FR-I and FR-II radio galaxy populations, considering either BL Lacs or FSRQs, respectively. As we did for the X-ray detected AGN, we use the correction factor $\Theta_{\mathrm{CF}} = 4\Gamma^2$, and assume the bulk Lorentz factor is $\Gamma = 10$, with a viewing angle of 0.1 radians. A Lorentz factor of 10 agrees well with estimates in e.g. Ajello et al. (2012) (and references therein) for FSRQs.

We calculate the luminosity and redshift distribution of the FSRQs, and

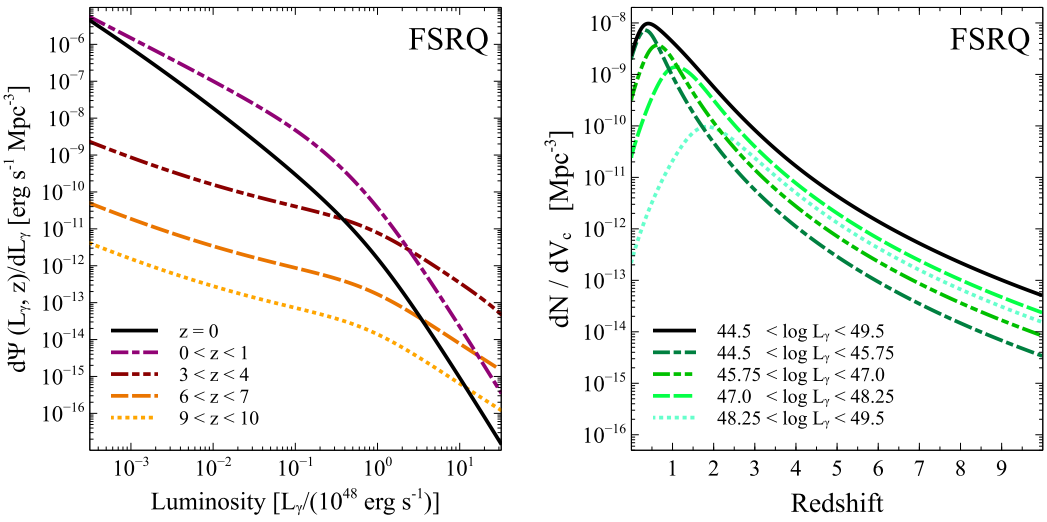

Fig. 3.13: *Left:* Differential γLF for the FSRQ population. It is given at different redshifts, and show that the evolution flattens towards the faint end, and steeply falls towards higher luminosities. This latter gradient flattens at higher redshifts. *Right:* Number density evolution of the FSRQ population, in bins of luminosity. The activity of the brightest of the FSRQ sources peak at $z \approx 2$. The peak decreases in redshift with decreasing source luminosity, and the lowest-luminosity FSRQs peak at a redshift of $z < 0.5$.

obtain the estimated population densities in the redshift range $0 < z < 10$, and the luminosity ranges of $44.5 < \log L_\gamma < 49.5$. The upper luminosity limit is adopted from Ajello et al. (2012). The FSRQ population has a steep decline towards higher luminosities at low redshift, with the luminosity function flattening towards higher redshifts, as seen in Fig. 3.13.

We integrate the luminosity function in bins of luminosity, and obtain the number density of the populations over several cosmological epochs (Fig. 3.13. The activity of the brightest blazars peak at significantly earlier times, with the peak shifts to lower redshift with decreasing luminosity. For the FSRQ population the density evolution of the brightest sources peaks at $z \approx 2$, decreasing down to a peak of $z < 0.5$ for the lowest luminosity FSRQs at redshifts above $z \approx 2.5$, implying that the brightest sources dominate over the lower-luminosity sources.

Derived FSRQ population

z bin	$\left.\frac{dN(L_\gamma)}{dL_\gamma}\right\|_z \Delta L_\gamma \Theta_{\rm CF}$	L_γ bin	$\left.\frac{dN(z)}{dz}\right\|_{L_\gamma} \Delta z \Theta_{\rm CF}$
0-1	8.114×10^4	44.5 - 45.0	1.832×10^4
1-2	4.235×10^4	44.5 - 45.0	1.861×10^4
2-3	5.660×10^3	45.5 - 46.0	1.904×10^4
3-4	8.201×10^2	46.0 - 46.5	1.938×10^4
4-5	1.584×10^2	46.5 - 47.0	1.919×10^4
5-6	3.950×10^1	47.0 - 47.5	1.733×10^4
6-7	1.194×10^1	47.5 - 48.0	1.193×10^4
7-8	4.174×10^0	48.0 - 48.5	4.903×10^3
8-9	1.635×10^0	48.5 - 49.0	1.234×10^3
9-10	7.018×10^{-1}	49.0 - 49.5	2.445×10^2
0-10	1.302×10^5	44.5 - 49.5	1.302×10^5

Table 3.9: Estimated numbers of the FSRQ population, calculated using the γLF prescription given in Ajello et al. (2012). The column on the left gives FSRQ binned in redshift over the full luminosity range ($44.5 < \log L_\gamma < 49.5$). The column on the right gives the size of the FSRQ population binned in luminosity, and considered over the full redshift range ($0 < z < 10$).

3.5 Number derivation of γ-ray detected FSRQs

The numbers we derive for the γ-ray detected FSRQ population are either in bins of redshift or luminosity, depending on the distribution they are obtained form. In this section we show the final derivations of the population size. Table 3.9 gives the derived numbers in each redshift or luminosity bin.

3.6 Results from Calculations of γ-ray Detected FSRQs

Convolving the γLF with the co-moving volume of the Universe gives the redshift or luminosity distributions of the FSRQ population. The differential co-moving volume is

$$\frac{dV_{\rm c}}{dz} = 16\pi \left(\frac{c}{H_0}\right)^3 \frac{(\Omega z + (\Omega - 2)[\sqrt{1+\Omega z} - 1])^2}{\Omega^4 (1+z)^3 \sqrt{1+\Omega z}} \,, \tag{3.8}$$

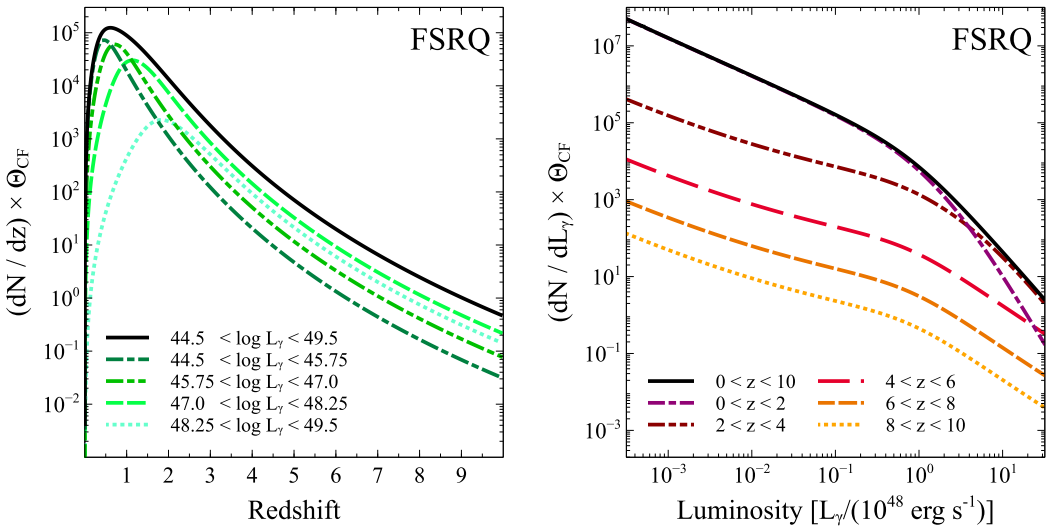

Fig. 3.14: Redshift and luminosity distributions of the FSRQ population, corrected for misaligned sources. *Left:* the redshift distributions show that the peak activity of FSRQs increases in redshift with increasing luminosity. *Right:* the luminosity distributions show that the brightest FSRQ sources dominate the population at redshifts above $z > 2$.

and we use the cosmological prescriptions given in the relevant paper to maintain consistency ($H_0 = 71$ km s^{-1} Mpc^{-1}). By integrating over luminosity, we obtain the redshift distributions, that allow us to differentiate between the low- and high-luminosity blazar evolutions.

The redshift and luminosity distributions of FSRQ sources are shown in Fig. 3.14. The redshift distributions show that lower-luminosity FSRQs are dominating at redshifts $z < 1$, and the most abundant sources at $z < 0.5$ are the lowest-luminosity sources ($\log[L_\gamma$ erg s$^{-1}] < 45.75$). The bright sources ($\log[L_\gamma$ erg s$^{-1}] > 47.0$) dominate at higher redshifts, $z > 2$. This agrees with the evolution of the X-ray detected blazars (Sec. 3.3). The FSRQ luminosity distributions show that the brightest sources dominate in the $2 < z < 4$ redshift range.

The space density of FSRQs, $\rho_{\rm FSRQ}$ for a comoving volume out to redshift $z = 10$ ($V_{\rm c} = 3.6 \times 10^{12}$ Mpc^3 (Wright 2006)) is

$$\rho_{\rm FSRQ} = \frac{N(z, L_\gamma) \times \Theta_{\rm CF}}{V_{\rm c}} \ . \tag{3.9}$$

The density we find for the FSRQ population is $\approx 4 \times 10^{-8}$ Mpc^{-3} for both the redshift and luminosity distributions, which agrees with local estimates for the

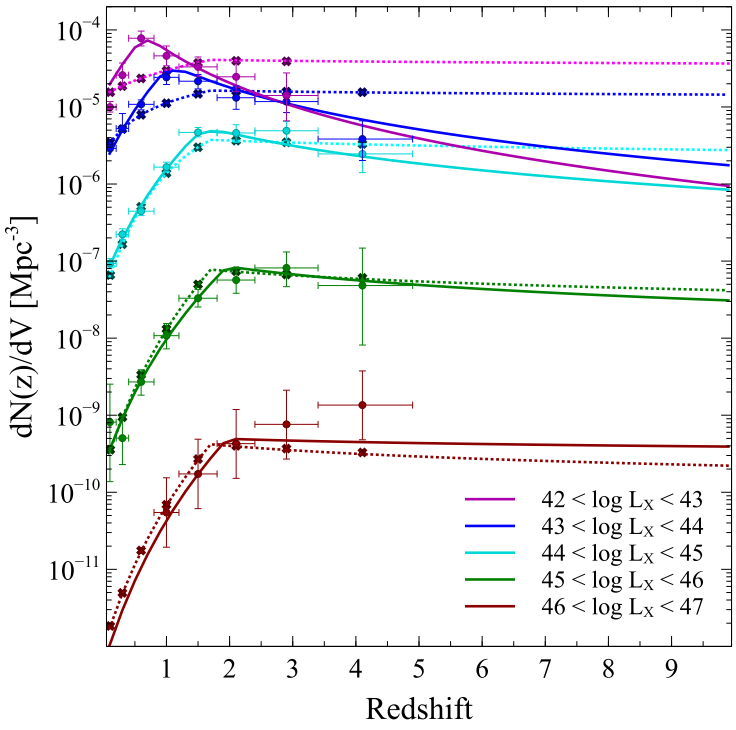

Fig. 3.15: Comparison of Type-I XLF models: The best fit LDDE model of Hasinger et al. (2005) (solid lines) is used in our work (see Ch. 2). The model fits well with the data points, and whereas the decline towards higher redshifts is steep at low luminosities, it becomes flatter towards the brightest sources. The PLE (dotted lines) follow the evolutionary tracks of the LDDE model, however diverges at low luminosities.

population, using cosmic ray data (e.g. Takami et al. (2012), for local space densities of UHECR sources, and also Yoshiguchi et al. (2003) and references therein), given at $\sim 10^{-8}$ Mpc^{-3}.

3.7 Additional XLF model calculations

Here we present the additional calculations of the XLF of the various populations, and various XLF models. The additional calculations are made to further study the ones used in the main project. Thus we calculate a selection of the various models for which best-fit parameters are available in the survey publications, and here we present the results of these, as well as any additional plots for which we find useful to complement the main aim of this work.

The unobscured AGN were studied in Hasinger et al. (2005), and they provided two global XLF model prescriptions. The best-fit LDDE model was used

in our work, and is summarised in Table 3.1 as well as in Table 3.10. It shows excellent fit with the data points, particularly at lower luminosities, as seen in Fig. 3.15. Towards the brightest sources, however, the high-redshift data points have large errors. The PLE model follows the evolution of the LDDE model and the data points at higher redshifts, however, the high-redshift end becomes flatter towards lower luminosity sources. Furthermore, it does poorly at representing the lowest luminosity sources at local redshifts.

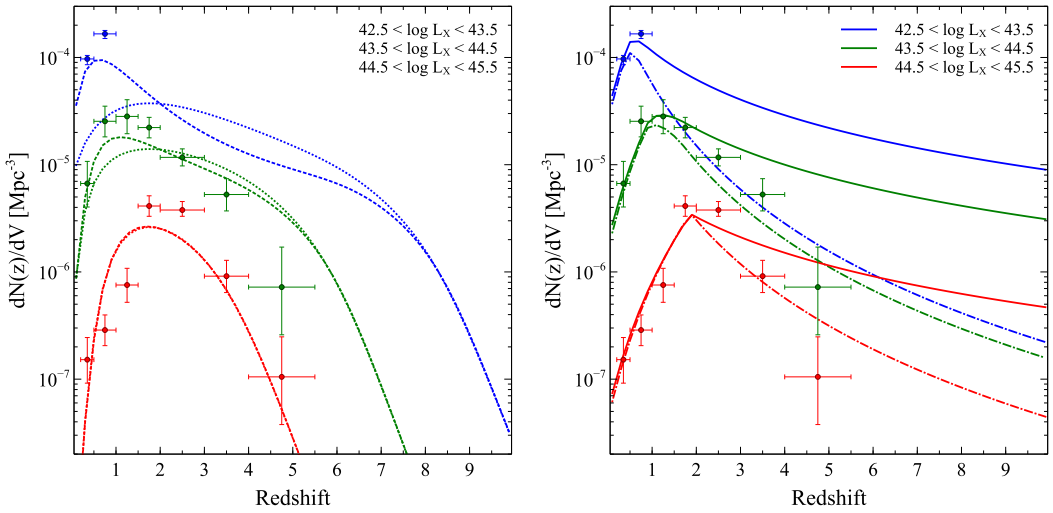

(a) Comparison of PLE and MPLE models

(b) Comparison of LDDE models

Fig. 3.16: Comparison of Type-I and type-II XLF models: the figure on the left (Fig. a) shows the comparison of the PLE (dotted lines) and MPLE (dashed lines) models, for three luminosity bins. Figure (b) on the right shows the comparison of the two best-fit LDDE models. The best-fit model used in our work (solid lines) was chosen over the LDDE model (dash-dotted lines), due to the excessively steep decline towards higher redshifts in the latter.

For the Type I and Type-II population we chose to use the best-fit model prescription of Silverman et al. (2008), summarised in Table 3.1. Moreover, they gave prescriptions for additional models; and we here show the PLE, MPLE and an additional LDDE model to compare with the LDDE model we use for our calculations in Ch. 2. The PLE derived models, seen in Fig. 3.16a show a strong cut-off at higher redshifts, and particularly at the lowest luminosities they fail to fit the data points for the evolutionary tracks. The MPLE model is slightly more successful at later times. The comparison of

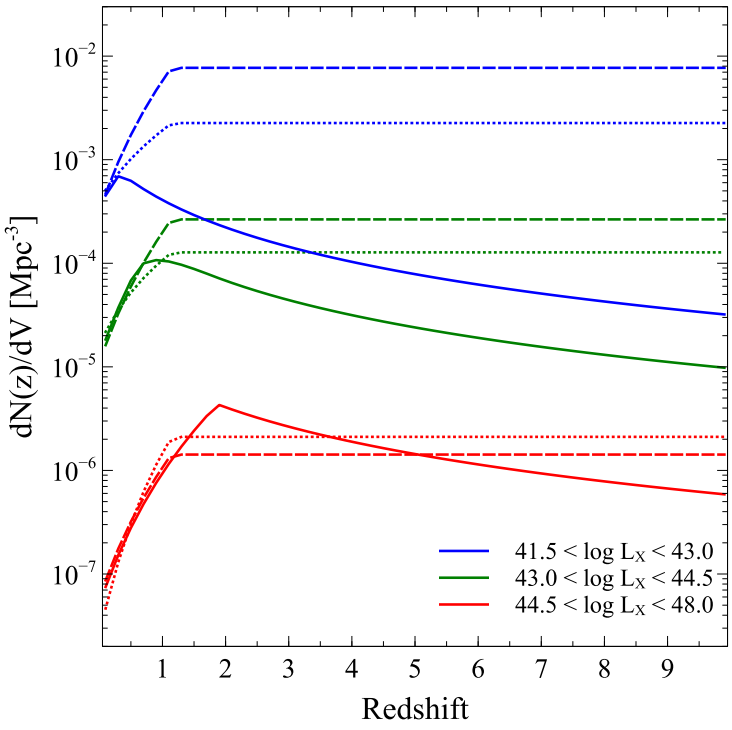

Fig. 3.17: Comparison of Type-I and -II XLF models: Their best fit LDDE model (solid lines) show a similar form to the LDDE model used in our work (see Fig. 3.16b). The PLE (dotted lines) and PDE (dashed lines) are similar in evolution, however the PDE model gives consistently higher densities for lower luminosities, but falls below the PLE model at higher luminosities.

the two LDDE models, seen in Fig. 3.16b, show that the model we chose to use has a much flatter decline towards higher redshifts than the other LDDE model. The latter was measured to higher redshifts ($0.2 < z < 5.5$), and does thus attempt to fit with the high-redshift data points. However, we chose the former LDDE model, measured to a redshift of ($0.2 < z < 3$), that was able to better fit the low luminosity track data points, as well not declining too steeply towards high redshifts. Given the large errors on the high-redshift data-points, this model provides us with the best estimate of both the obscured and unobscured radio-loud AGN population.

To compare with the Type-I and Type-II XLF prescribed by Silverman et al. (2008), we also look at the hard XLF prescriptions of Ueda et al. (2003) of the same population, measured up to a redshift of $z = 3$. The evolutionary tracks produced from the PLE, PDE and LDDE model parameters are shown

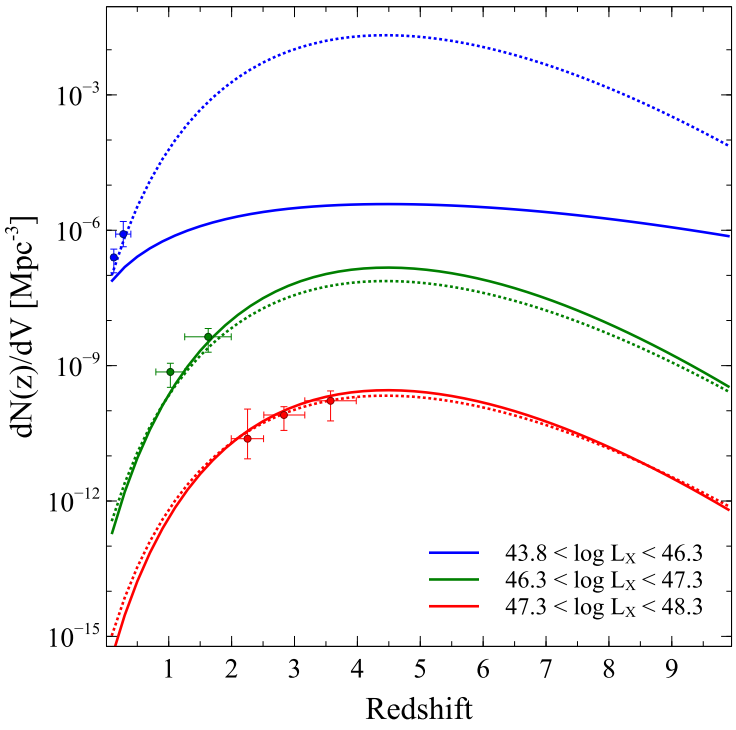

Fig. 3.18: Comparison of the blazar XLF models: the PLE (dotted lines) and PDE (solid lines) for three luminosity bins. Particularly at the lowest luminosities is the flattening in the PLE model obvious, compared to the PDE model. Data points extracted from the original plots are given to show the fit of the two models.

in Fig. 3.17, and the LDDE model prescribed in this paper is similar to the shape of the evolutionary tracks produced by the LDDE model prescribed by Silverman et al. (2008). Note however, the luminosity bins differ for the two representations.

The additional models presented in Ajello et al. (2009) are the PLE (also quoted in Table 3.1) and PDE models. We show in Fig. 3.18 the comparison of these models, and illustrate the flattening in the PLE model. Whereas at high luminosities, the models agree well, the flattening is beginning to appear in the intermediate luminosity bin, and very obvious in the faint luminosity bin. This is due to the beaming of the blazar luminosities, so that in the PLE model, where the luminosities are evolved over redshift, the effects on the observed radiation show clearly. In the PDE models, the number density is evolved, hence, the modelled evolution does not show such a trend.

FITTED XLF MODEL PARAMETERS

MODEL	$z=0$ PARAMETERS				EVOLUTION PARAMETERS							
	A_0	$\log L_*$	Υ_1	Υ_2	$\upsilon_{1,c}$	$\upsilon_{2,c}$	z_c	$\log L_c$	α	β_1	β_2	
HPLE	1.85×10^{-7}	43.33	0.39	2.29	2.67	-0.2	1.70	–	–	–	–	
HLDDE	2.62×10^{-7}	43.94	0.87	2.57	4.7	-1.5	1.42	44.67	0.21	0.7	0.6	
SPLE	-5.332^a	44.92	2.80	0.77	1.69	-0.87	1.9	–	–	–	–	
SMPLE	-5.238^a	44.88	2.76	0.42	-0.60	-8.18	2.0	–	-1.04	–	–	
SLDDE	-6.077^a	44.33	2.15	1.10	4.00	-1.5	1.9	44.6	0.317	–	– -	
UPLE	1.41×10^{-7}	43.66	0.82	2.37	2.70	0.0	1.15	–	–	–	–	
UPDE	2.64×10^{-6}	44.11	0.93	2.23	4.20	0.0	1.14	–	–	–	–	
ULDDE	5.04×10^{-6}	43.94	0.86	2.23	4.23	-1.5	1.9	44.6	0.335	–	–	
AMPLE	1.379×10^{-7}	1.81^b	-0.87	2.73	3.45	-0.25	–	–	–	–	–	–
AMPDE	0.948×10^{-7}	1.95^b	-0.83	2.54	11.62	-0.85	–	–	–	–	–	–

Table 3.10: Summary of the fitted parameters for each XLF model, as given in the relevant papers: models with first letter H are given in Hasinger et al. (2005); first letter S refers to models from Silverman et al. (2008); models with first letter U are found in Ueda et al. (2003); first letter A are given in Ajello et al. (2009). PLE: pure luminosity evolution; PDE: pure density evolution; MPLE/MPDE: modified versions of PLE/PDE; LDDE: luminosity dependent density evolution. a) the value represents the logged normalisation constant, $\log A$, as is given in Silverman et al. (2008). b) the value represents the unlogged value of the break luminosity, L_*, where the luminosities are all normalised by 10^{44} erg/s.

Chapter 4

The Cosmological Evolution of Neutrinos from AGN Jets

The existence of astrophysical UHE neutrinos has been theorised for decades, but only recently confirmed. The dedicated neutrino observatory *IceCube* has detected a few tens of high-energy neutrino events, with energies reaching $\sim 10^6$ GeV (Aartsen et al. 2013; IceCube Collaboration 2013; Aartsen et al. 2015b). However, the statistics are yet too low to derive any significant information on the origin of these events, leading to a number of speculations (e.g. Halzen 2014, and references therein). The detections are consistent with an extragalactic origin from energy considerations, however a confirmation requires further event detections by *IceCube* and future neutrino observatories, as well as further studies into neutrino generation.

The production of such energetic particles requires a source population with strong magnetic fields and strong radiative emission – i.e. cosmic accelerators.

The AGN/quasar population has emerged as a prime candidate for neutrino production. Identified regions of high-energy emission include the core, knotty regions along the AGN jet, and the terminal shock region in AGN jet lobes as they interact with the intergalactic medium.

Convolving the observed evolutionary tracks of these source populations, derived from photonic AGN surveys, with a model of the evolving neutrino spectral energy distribution at cosmological epochs can reveal the conditions

of the source environments as far back as the formation of these populations. The diffuse neutrino background over cosmic time will hint at the relative power of the source populations at higher redshifts compared with the power emitted today. Hence, the cosmological evolution of neutrinos is of interest, in particular as a probe of the bright phase of galactic formation (i.e. at redshifts $10 - 30$, see Berezinskii and Ozernoi 1981) from which only neutrinos would have survived virtually unattenuated.

It is an abundant source population, and in support of the GZK criterion mentioned in Sec. 1, there exist AGN in our cosmic neighbourhood. The closest is Centaurus A, an FR-I radiogalaxy, at a distance of only 3.4 Mpc (Evans et al. 2004), corresponding to a redshift of $z \approx 0.0008$ and can therefore be considered a local ($z \approx 0$) source. The local space density of AGN is estimated from cosmic ray observations at about 10^{-4} Mpc^{-3} (see e.g. Takami et al. 2012; Yoshiguchi et al. 2003, and references therein; see also Tab. 3.7). Their evolutionary history spans several cosmological epochs, as they are thought to be among the first sources formed during the bright phase. These sources could therefore serve as a population for which neutrino production may be traced back to a time when the Universe was only a fraction of its size today.

AGN furthermore display large variations in characteristics (see Ch. 2), ranging from observed emission along the electromagnetic spectrum (from radio to X-ray and γ-rays), to observed morphology of the jets (Sec. 2.1; the FR-I and FR-II dichotomy). Suitable locations for neutrino production determined from observations of high-energy emission are the AGN cores, the jets, and hotspots in the jet lobes of FR-II radio galaxies (see Figs. 1.12 and 2.1). In addition, the evolutionary tracks vary across the AGN classes, thus the contribution from each class to the cosmic neutrino flux will vary correspondingly.

In this chapter, we focus on the radio-loud AGN population as this offers a well-studied classification scheme and accompanying thorough (∼complete) space density surveys – in particular in X-rays and γ-rays (Ch. 2). We estimate the diffuse neutrino background from various radio-loud AGN populations at

several cosmological epochs. As point source detection of neutrinos is yet premature in current detectors (e.g. *IceCube*), we calculate the total diffuse neutrino background that can be detected today.

We compare the neutrino production efficiencies from a number of AGN types with the flux limits, and in this way aim to verify if all AGN types are indeed neutrino producers. In light of the X-ray surveys we use, we also verify if two models of neutrino production in AGN jets, following a commonly accepted production scenario, are applicable.

Sec. 4.1 outlines some key models on HE production of neutrinos in AGN and general considerations that are important in determining neutrino emission from primary interactions of protons on ambient media. Here we also describe the two models we use to calculate the diffuse neutrino energy evolution in the Universe. Our resulting energy spectra at different cosmological epochs from several AGN populations are presented in Sec. 4.2. The expected diffuse neutrino spectra are presented, and we compare our results with the current limits on detection from *IceCube* and PAO. We do not distinguish between neutrinos and anti-neutrinos in the analysis. The results presented in this chapter are also found in Jacobsen et al. (2015).

4.1 Neutrino Production Models

Neutrino production in AGN jets has been extensively studied, as described below. AGN are attractive neutrino producers because they are known to be emitters of non-thermal radiation, harbouring an enormous source of energy in the central accreting SMBH. The emission of relativistic jets offers further evidence of the high-energy production in these sources. It is still unknown whether these are purely leptonic, or have a hadronic component – an issue neutrino astrophysics will be able to shed light on.

The radio-loud component in AGN spectra indicates synchrotron emission by a population of relativistic electrons in the jets.The radiation fields are therefore readily available for efficient pγ interactions in a lepto-hadronic jet. As the relativistic electrons travel in the jet magnetic fields, they emit synchrotron emission which is observed in the the radio-loud AGN energy spectra

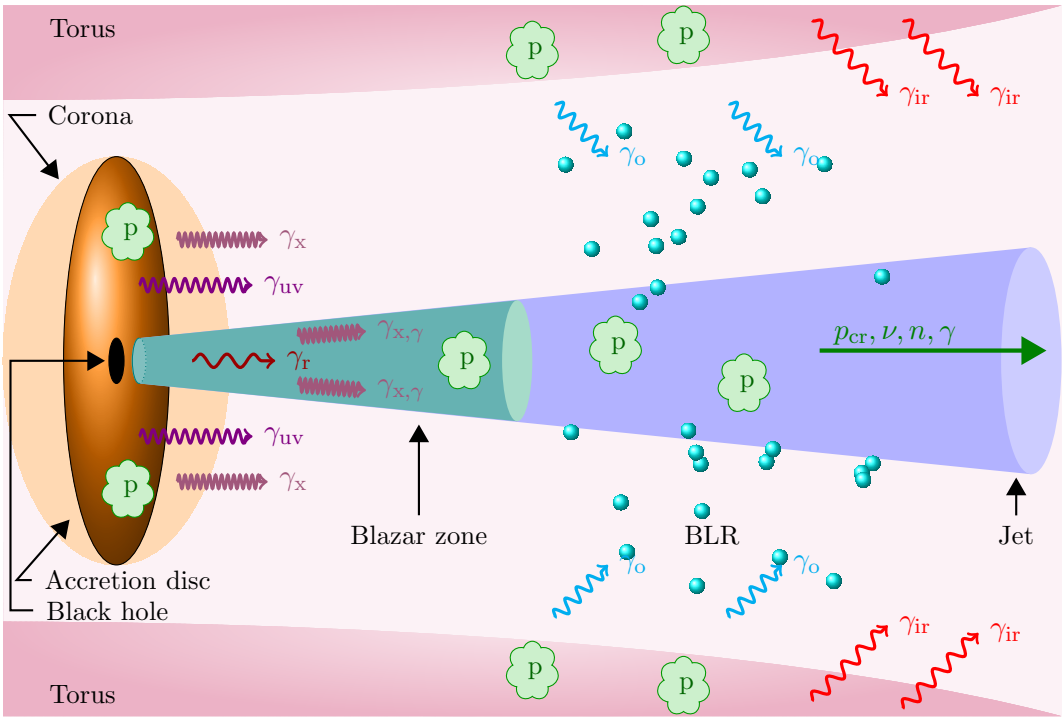

Fig. 4.1: Schematic illustration of the inner regions of AGN jets. In the AGN core the accretion disc emits UV-radiation, and the corona upscatters the UV-photons to X-ray energies. Similarly, core radiation is rescattered in the dusty torus as infra-red emission. In the jet, the majority of the emission processes take place in the blazar zone; relativistic electrons produce radio synchrotron emission, γ_r and through inverse Compton scattering X-ray and γ-ray photons are produced. The BLR produces optical photons γ_o. Proton targets are found in the accretion disc, the jet, and the torus. The relativistic protons interact with the target fields, producing an outflow of neutrinos, γ-rays, neutrons and CR-protons.

as strong relative to radio-quiet AGN. In blazar SEDs, the synchrotron emission can explain the low-energy peak. The peak at γ-ray energies in SEDs of blazars can be explained by both leptonic inverse Compton processes as well as the hadronic decay of neutral pions (see Ch. 5). The latter would therefore be accompanied by an associated neutrino signal. A direct neutrino detection would confirm the latter, and the study of associated photon emission (i.e. through pion decay) can provide clues about this.

4.1.1 Target radiation and matter fields

Assuming a lepto-hadronic jet content, protons and electrons will be accelerated to ultra-high energies. The acceleration mechanism is uncertain; however, shocks are commonly invoked in jet models (see Sec. 5.2.1). The production

of neutrinos in these sources require the UHE protons to interact with matter or radiation fields within the AGN system.

The availability of various target fields, illustrated in Fig. 4.1, depends on the location of the neutrino production in the AGN system. The neutrino spectra are calculated with a number of dependencies, one of which is the choice of interaction channel (pp or pγ). The production rates are heavily dictated by the densities of the target fields and the energy of the photon radiation will determine the cross section of the pγ interaction.

The core has been modelled as a possible location (and would therefore also include production in radio-quiet AGN, e.g. Stecker et al. 1991; Nellen et al. 1993; Stecker 2005, 2013). Radiation fields include UV-photons and a proton population in the accretion disc and the upscattered X-ray photons in the corona (Nellen 1994; Stecker and Salamon 1996; Kachelrieß et al. 2009). The protons are in this case accelerated in the accretion disc, or just above, and will diffuse back to the disc, and interact with the accretion disc matter or radiation fields.

Neutrino production in the jets has the benefit of the internal synchrotron radiation field. Often the main emission processes are assumed to occur close to the base of the jet within a region sometimes referred to as the *blazar zone* (Fig. 4.1, see e.g. Sikora et al. 2005; Murase et al. 2014). Close to the core regions, the accretion disc and coronal radiation and matter fields are also available for pγ-interactions (Atoyan and Dermer 2001; Neronov and Semikoz 2002; Anchordoqui et al. 2004; Kachelrieß et al. 2009; Cuoco and Hannestad 2008; Koers and Tinyakov 2008; Becker and Biermann 2009). Knots observed along the jet, thought to be shock regions, are also possible production sites. Synchrotron radiation, its existence a consequence of the interaction between the relativistic electrons and the magnetic field, is extensively used as a target field along the jet such as in the *proton blazar* model of Mannheim (1993) and the *synchrotron proton blazar* model of Mücke and Protheroe (2001). As a natural radiation field emerging in jets, it is however commonly assumed in a number of proposed models, (e.g. Biermann and Strittmatter 1987; Halzen and Zas 1997; Mücke and Protheroe 2001; Atoyan and Dermer 2001;

Dermer et al. 2007; Cuoco and Hannestad 2008; Becker and Biermann 2009; Becker et al. 2011; Reynoso et al. 2012; Dermer et al. 2014)

An extension to this model scenario is the *synchrotron mirror model* of Reimer et al. (2005), for which radiation produced through SSC within the jet is reflected off external clouds, and thus back into the jet. In addition, the cold matter content in the jet provides a target for pp-interactions (Reynoso et al. 2011; Becker Tjus et al. 2014). The hotspots in the outer lobes of the AGN jets are possible production sites because the interaction between the jet plasma and interstellar and intergalactic media produces shock conditions, and has been considered for both pp and pγ-interactions (Biermann and Strittmatter 1987; Cuoco and Hannestad 2008; Becker Tjus et al. 2014).

External radiation includes that of the BLR, which is considered an important factor in high-energy production in e.g. FSRQs (Atoyan and Dermer 2001, 2003; Dermer et al. 2012; Murase et al. 2014; Dermer et al. 2014). Cold protons and infra-red radiation from the torus have also been considered (Becker and Biermann 2009; Dermer et al. 2012; Murase et al. 2014).

4.1.2 Normalisation of the neutrino spectra

The search for possible neutrino point sources began as an extension to the search of UHECR sources. The first step was to identify sources of strong radio, X-ray or γ-ray emission, as well as the observed UHECR flux, as these are signs of high-energy processes within the source. These observations impose constraints on the neutrino flux, and are used to normalise the neutrino spectrum.

The neutrino emission spectrum is usually constructed by considering the spectrum of the relativistic protons accelerated through e.g. shocks. In this case, the primary spectrum follows a power law,

$$\frac{dN}{dE_\mathrm{p}} \propto E_\mathrm{p}^{-\alpha_\mathrm{p}} \ , \tag{4.1}$$

with $\alpha_\mathrm{p} \approx 2-2.2$. First order Fermi acceleration is often the preferred mechanism as its resultant energy distribution is consistent with the observed slope of the cosmic ray spectrum (Bell 1978).

The spectra of the escaping emission deriving from the proton population

closely follows a power law described by the index $\alpha_{\rm p}$, with the exception of regions where the energy losses include proton interactions. A useful scaling of the neutrino spectrum is therefore to assume the fraction of energy distributed among the secondary particles or emitted as cosmic ray flux which may then be compared to the observed γ-ray or UHECR spectrum.

Radio emission implies that relativistic electrons interact with magnetic fields in the jet. If the jet content is lepto-hadronic, then a population of relativistic protons may be found in these sources as well (e.g. Mannheim 1993). Among AGN/quasars the radio galaxies Cen A, M87, and the quasar 3C 273 (the first identified quasar Schmidt 1963) were among the first AGN sources to be considered as neutrino producers (Silberberg and Shapiro 1977; Margolis et al. 1978). Due to the strong radio emission from these sources, a ratio between the radio emission in our Galaxy to that of the radio source was used to scale the possible correlated neutrino emission from radio sources (Silberberg and Shapiro 1977; Margolis et al. 1978) with target fields being either ambient cold gas and dust surrounding the nucleus in an accretion disc or ambient clouds, or even the X-ray radiation from accretion processes (Silberberg and Shapiro 1979; Eichler 1979). This approach was later extended with a more physical explanation, linking the total power of the jet to the maximum achievable energy of the accelerated protons (Becker et al. 2005).

This approach can be extended using the *jet-disc symbiosis model* (Falcke and Biermann 1995), where the total power of the jet (radio power) is related to the disc luminosity of the AGN. In this way, the X-ray luminosity can be used to normalise the spectrum of neutrinos. For models in which neutrino production occur in the AGN core (Mannheim 1995), or assuming the X-ray emission is produced through the cascading emission from high-energy production in radio-quiet AGN (Stecker and Salamon 1996), the X-ray luminosity provides a reasonable scaling.

Blazars are known emitters of strong γ-radiation and, assuming the emission originates in hadronic interactions, it offers a useful normalisation spectrum (Mannheim 1995; Protheroe 1996; Halzen and Zas 1997;

Halzen and O'Murchadha 2008; Cuoco and Hannestad 2008; Arteaga-Velázquez 2012; Tchernin et al. 2013; Murase et al. 2014; Tavecchio et al. 2014). The TeV emission in blazars is also used to model hadronic flaring models, and to compare the spectra with that of quiescent periods to explore the physical conditions leading to these enhanced emission episodes (Rachen and Mészáros 1998; Atoyan and Dermer 2001, 2003; Reimer et al. 2005; Dermer et al. 2007; Becker et al. 2011; Dermer et al. 2014). However, the fraction of the diffuse γ-ray background originating in blazar emission is highly uncertain, and the γ-ray normalisation is used predominantly in point-source studies.

The observed UHECR spectrum has been used to normalise the neutrino spectrum since the neutrino emission derives from the same energetic parent distribution in the source (Waxman and Bahcall 1999; Mannheim 1999; Tavecchio et al. 2014). Pierre Auger Collaboration et al. (2007, 2008) reported a correlation between UHECRs and nearby AGN which subsequently inspired a number of papers to study the expected neutrino emission with the most nearby AGN, namely Cen A and M87, as well as the diffuse neutrino flux (Halzen and O'Murchadha 2008; Cuoco and Hannestad 2008; Koers and Tinyakov 2008; Becker and Biermann 2009; Kachelrieß et al. 2009).

4.1.3 Koers and Tinyakov (KT) Neutrino Production Model

The neutrino production model of Koers and Tinyakov (2008) is built on the tradition of scaling the observed neutrino flux with the observed cosmic ray flux. As briefly mentioned above, the study was motivated by the UHECR observations by Pierre Auger Collaboration et al. (2007, 2008) (PAO), which correlated the cosmic ray event to nearby AGN. Their model follows that of Cuoco and Hannestad (2008), adopting a candidate point source, Cen A, suspected of being the origin of observed cosmic ray events, as described in Sec. 4.1.

Cuoco and Hannestad (2008) calculates the neutrino flux from Cen A, given that PAO reported two UHECR events correlated within 3 degrees of it. Cen A is considered a typical neutrino- and UHECR-producing AGN. In the model adopted by Koers and Tinyakov (2008) the protons are shock-accelerated to ultra-high energies, and are magnetically confined to a region

close to the core (Fig. 4.2) where they interact with the ambient radiation fields. Interactions with matter fields are disfavoured because efficient shock acceleration requires a low matter density (Cuoco and Hannestad 2008).

The protons produce neutrons and neutrinos through the photohadronic interaction

$$\mathrm{p} + \gamma \rightarrow \mathrm{n} + \pi^{+} \ , \tag{4.2}$$

and the neutrinos will escape, thus tracing the secondary neutron spectrum. These secondary neutrons will, however, interact with the ambient photon fields in photo-induced decays, thus losing energy before escaping confinement, following

$$\mathrm{n} + \gamma \rightarrow \mathrm{p} + \pi^{-} \ . \tag{4.3}$$

The softer neutrons decay to produce the observed UHECR spectrum through

$$\mathrm{n} \rightarrow \mathrm{p} + \mathrm{e}^{-} + \bar{\nu}_{\mathrm{e}} \ . \tag{4.4}$$

A consequence of this process is that at the highest energies, the neutrino flux is harder than that of the UHECRs.

The number density of the photon field in the core follows a power law $n(\varepsilon) \propto \varepsilon^{-2}$ (Koers and Tinyakov 2008). The production spectra resulting from the photohadronic interactions with the photon field follow those given in Mannheim et al. (2001). The UHECR spectrum will, in the production scenario described, have two breaks. The first break occurs at the energy when the optical depth for pγ losses is unity, i.e. $\tau_{\mathrm{p}\gamma}(E_{\beta}) = 1$. For a proton injection function of $Q_{\mathrm{p}}(E_{\mathrm{p}}) \propto E_{\mathrm{p}}$, the proton spectrum is given by

$$N_{\mathrm{p}}(E_{\mathrm{p}}) \sim Q_{\mathrm{p}}(E_{\mathrm{p}}) t_{\mathrm{p}}(E_{\mathrm{p}}) \ , \tag{4.5}$$

where the time scale $t_{\mathrm{p}}(E_{\mathrm{p}})$ is the sum of the energy loss timescales affecting protons, i.e. pγ interactions and adiabatic cooling. If the parameter β_1 is assigned to whichever is largest of the velocity of the adiabatic expansion or the shock velocity, the proton spectrum is described by

$$N_{\mathrm{p}}(E_{\mathrm{p}}) \propto \begin{cases} \beta_1^{-1} E_{\mathrm{p}}^{-2} & (E_{\mathrm{p}} < \beta_1 E_{\beta}) \\ E_{\beta} E_{\mathrm{p}}^{-3} & (E_{\mathrm{p}} > \beta_1 E_{\beta}) \ . \end{cases} \tag{4.6}$$

The exponential cutoff of the spectrum, determined by the maximum proton energy, is omitted here, as the cut-off occurs beyond the region of interest in the model. The photon field density in the core follows a power law, $n(\varepsilon) \propto \varepsilon^{-2}$ (Koers and Tinyakov 2008). The fractional proton energy loss per interaction is $\kappa_{\rm p} \approx 0.2$. The fraction of proton energy distributed to its secondary particles ($\kappa_{{\rm p}\to i}$, where $i = (\nu, \gamma, {\rm n})$ for neutrinos, gamma-rays, and neutrons, respectively) per interaction in AGN jets can then be given by

$$\begin{aligned} \kappa_{{\rm p}\to\nu} &\approx 0.1 \\ \kappa_{{\rm p}\to\gamma} &\approx 0.1 \\ \kappa_{{\rm p}\to n} &\approx 0.5 \ . \end{aligned} \tag{4.7}$$

The energy per particle is for neutrinos $\langle E_\nu \rangle \approx 0.033 E_{\rm p}$, and for neutrons $\langle E_{\rm n} \rangle \approx 0.83 E_{\rm p}$. The average relative neutrino to neutron energy is then $\bar{\epsilon} = \langle E_\nu \rangle / \langle E_{\rm n} \rangle = 0.04$ (Mannheim et al. 2001). The neutron injection function is related to the proton spectrum (Eqn. 4.6) through the timescale of neutron production by photohadronic interactions, and gives

$$Q_{\rm n}(E_{\rm n}) \propto \begin{cases} \beta_1^{-1} E_{\rm n}^{-1} & (E_{\rm n} < \beta_1 E_\beta) \\ E_\beta E_{\rm n}^{-2} & (E_{\rm n} > \beta_1 E_\beta) \ . \end{cases} \tag{4.8}$$

The neutron injection function is related to the muon neutrino injection function by

$$Q_{\nu_\mu}(E) = \frac{2}{3\bar{\epsilon}^2} \frac{\kappa_{{\rm p}\to\nu}}{\kappa_{{\rm p}\to n}} \, Q_{\rm n}(E/\bar{\epsilon}) \ . \tag{4.9}$$

The neutrons will then subsequently either escape to produce cosmic ray protons, or suffer energy losses in nγ interactions. The latter occurs at energies above $\beta_2 E_\beta$, when the optical depth for the interaction, $\tau_{{\rm n}\gamma} = 1$. The cosmic ray spectrum will therefore differ from the neutron spectrum above this energy, and the cosmic ray injection function is

$$Q_{cr}(E_{\rm p}) \propto \begin{cases} \beta_1^{-1} E_{\rm p}^{-1} E_\beta^{-1} & (E_{\rm p} < \beta_1 E_\beta) \\ E_{\rm p}^{-2} & (\beta_1 E_\beta < E_{\rm p} < \beta_2 E_\beta) \\ \beta_2 E_\beta E_{\rm p}^{-3} & (\beta_2 E_\beta < E_{\rm p}) \ . \end{cases} \tag{4.10}$$

The breaks are close in energy, hence a single break energy, $E_{\rm br,cr}$, can be adopted. This can be determined from the observed γ-ray spectrum, because the γ-rays interact through pair production with the same photon field. There is therefore a break in the spectrum at an energy $E_{\rm br,\gamma}$ when the optical depth for the interaction is $\tau_{\gamma\gamma} = 1$. Cuoco and Hannestad (2008) gives $E_{\rm br,\gamma} \simeq 200$ MeV, and the break in the UHECR spectrum is given by $E_{\rm cr,br} \simeq 3 \times 10^8 E_{\rm br,\gamma} \simeq 10^8$ GeV, consistent with an X-ray populated photon field. The break in the neutrino spectrum is then at an energy of $E_{\nu,\rm br} = \bar{\epsilon} E_{\rm cr,br} = 4 \times 10^6$ GeV (Koers and Tinyakov 2008).

The model assumes an optically thin source, so the synchrotron emission of mesons can be neglected, and the energy of the pions is therefore distributed to its decay products. The model considers muon neutrinos, produced in flavour ratio $(\nu_{\rm e} : \nu_\mu : \nu_\tau)_{\rm production} = (1 : 2 : 0)$ and through propagation, the observed ratio will be $(\nu_{\rm e} : \nu_\mu : \nu_\tau)_{\rm observed} = (1 : 1 : 1)$ after oscillations. The expected muon neutrino flux is given (in units of GeV^{-1} cm^{-2} s^{-1}) as

$$\begin{aligned} \phi_\nu^{\rm KT,CenA}(E_\nu) &= \left(\frac{dN_\nu}{dE_\nu}\right)^{\rm KT,CenA} \\ &= A_\nu^{\rm KT,CenA} \left(\frac{E_\nu}{1\ {\rm GeV}}\right)^{-\rho_\nu} \times \min\left(1, \frac{E_\nu}{E_{\rm br,\nu}}\right) , \end{aligned} \tag{4.11}$$

with the index $\rho_\nu = 1.7$. The neutrino and UHECR spectra are therefore harder than the primary proton spectrum by one power before the break. After the break the UHECR spectrum is softer by one power than the primary proton spectrum, but the neutrino spectrum will follow the neutron spectrum (Eqns. 4.6, 4.8, 4.10). The normalisation of the spectrum is given by considering the UHECR flux associated with Cen A derived from PAO observations, and is evaluated at the threshold energy in the PAO analysis ($E_{\rm th} = 57$ EeV) $\phi_{\rm cr}^{\rm CenA} = 5 \times 10^{-21}$ cm^{-2} s^{-1}. The normalisation is then

$$\begin{aligned} A_\nu^{\rm KT,CenA} &= \frac{\phi^{\rm CenA}(E_{\rm th})}{3} \frac{\kappa_{\rm p\to\nu}}{\kappa_{\rm p\to n}} \frac{\bar{\epsilon}^{(\rho_\nu - 1)}(\rho_\nu - 1)}{E_{\rm th}^{1-\rho_\nu} E_{\nu,\rm br}} \\ &\approx 3 \times 10^{-11}\ {\rm GeV}^{-1}\ {\rm cm}^{-2}\ {\rm s}^{-1} . \end{aligned} \tag{4.12}$$

Koers and Tinyakov (2008) then calculate the associated diffuse flux, assuming that Cen A is representative of AGN producing UHECRs, and hence

neutrinos. They take into account all sources by constructing a neutrino boost factor, $H(E_{\rm th})$ that relates the diffuse neutrino flux to the Cen A neutrino flux through

$$\frac{\phi_\nu^{\rm diff}}{\phi_\nu^{\rm CenA}} = \frac{\phi_{\rm cr}^{\rm diff}(E_{\rm th})}{\phi_{\rm p}^{\rm CenA}(E_{\rm th})} H(E_{\rm th}) \tag{4.13}$$

$$= 1.9 H(E_{\rm th})\ {\rm sr}^{-1}\ . \tag{4.14}$$

This boost factor assumes that the UHECR flux from Cen A has travelled with negligible energy loss. In estimating the diffuse neutrino flux from distant sources, the boost factor takes into account the difference in the mean free path of the neutrinos and cosmic rays as they propagate through space. The cosmic rays are highly attenuated at larger distances. Therefore, the neutrino flux received from distant (unresolved) AGN will be stronger than the UHECR flux from the same sources. Their boost factor is constructed independently of a source model, and they expect the diffuse neutrino flux is 200 to 5000 times that expected to originate in Cen A. This result is source model dependent, for which the former estimate is based on a non-evolving source model, and the latter with strong evolution.

4.1.4 Becker and Biermann (BB) Neutrino Production Model

The production model of Becker and Biermann (2009) is similarly motivated by the UHECR events detected by PAO. As a few events were reported to correlate with Cen A, they consider the production of neutrinos in FR-I AGN. The jets of this class of AGN show a distribution of knots along the jet with strong non-thermal radio emission, where shocks are responsible for the acceleration of electrons. In the model protons are similarly accelerated in these regions. The magnetic field is anchored in the accretion disc, and is assumed to initially scale with the distance along the jet as $B \sim d_{\rm j}^{-2}$. Further out in the jet it drops as $B \sim d_{\rm j}^{-1}$, as the shock waves along the jet reheat its content, enabling it to maintain a magnetic field capable of confining particles at larger distances from its base (Becker and Biermann 2009).

The jet structure is modelled with moving shock regions from the base of the jet ($\sim 30 R_{\rm g}$) to $\sim 3000 R_{\rm g}$, where the first knot (and therefore the first stationary shock) is located. $R_{\rm g} = G M_{\rm BH} c^{-2}$ is the gravitational radius of the

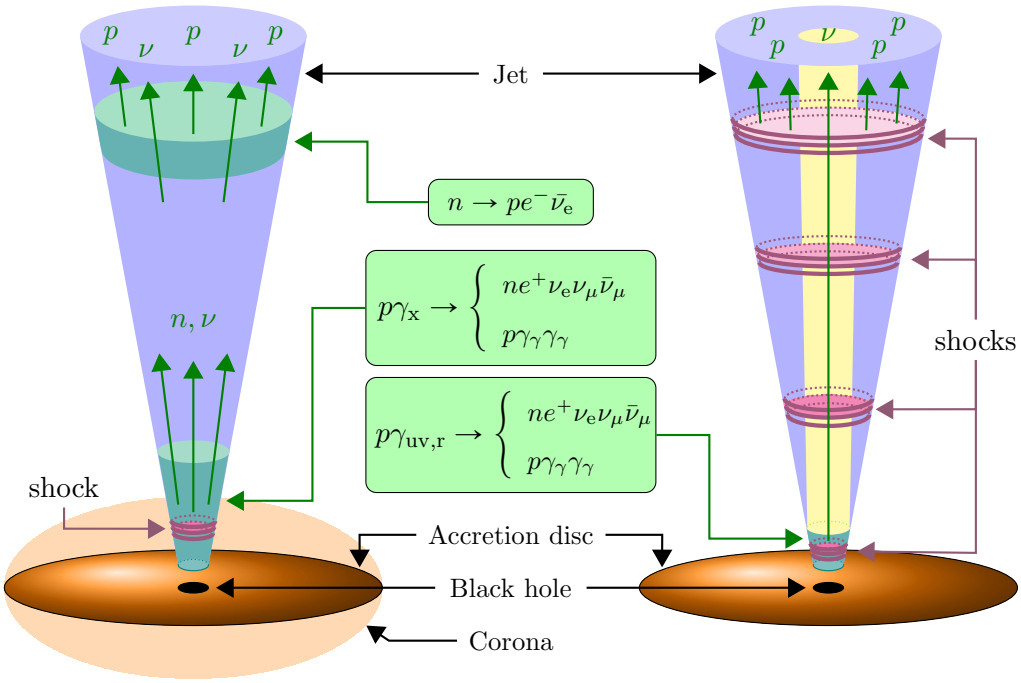

Fig. 4.2: *Left:* Schematic illustration of the neutrino production in the jet based on the prescription described in Koers and Tinyakov (2008) (not to scale). Neutrinos are produced through energetic protons interacting with X-ray photons from the disc corona. Neutrinos and neutrons escape the confinement. Whereas the neutrinos leave the jet, the neutrons will decay to produce observed UHECR protons and neutrinos. *Right:* Schematic illustration of the neutrino production in the jet based on the prescription described in Becker and Biermann (2009) (not to scale). Neutrinos are produced at the base of the jet by energetic protons interacting with UV and radio photon fields from the accretion disc and jet, respectively. The neutrino emission is beamed in a collimated jet. The UHECR protons are produced in the last strong shock region of the jet.

central black hole of mass $M_{\rm BH}$. Repeating stationary shocks then occur along the jet (Fig. 4.2).

Becker and Biermann (2009) consider three sources of target fields to interact with the energetic protons, namely disc photons, jet synchrotron photons, and cold protons in the torus. The number density of the disc photons is given by

$$n(\varepsilon_{\gamma_{\rm disc}}) = \frac{L_{\rm disc}}{4\pi\ d_{\rm j}^2\ c\ \varepsilon_{\rm disc}} \approx 0.083\ L_{\rm disc}\ d_{\rm j}^{-2}\ , \tag{4.15}$$

where the disc photon energy is assumed $\varepsilon_{\rm disc} = 20$ eV $= 3.204 \times 10^{-11}$ erg,

consistent with the observed UV-energies of the disc radiation. The mean free path of the protons in the photon field is $\ell_{\mathrm{p}\gamma_{\mathrm{disc}}} = [n(\varepsilon_{\gamma_{\mathrm{disc}}})\sigma_{\mathrm{p}\gamma}]^{-1}$, where the total cross section of the pγ interaction is $\sigma_{\mathrm{p}\gamma} = 9 \times 10^{-28}$ cm^2. The optical depth of the interaction is

$$\tau_{\mathrm{p}\gamma_{\mathrm{disc}}} = \frac{d_{\mathrm{j}}\ \omega_{\mathrm{j}}}{\ell_{\mathrm{p}\gamma_{\mathrm{disc}}}}. \tag{4.16}$$

For a typical FR-I AGN, the half opening angle of the jet is $\omega_{\mathrm{j}} = 0.1$, the black hole mass given by $M_{\mathrm{BH}} = 10^7 M_{\odot}$, and the disc luminosity is

$$L_{\mathrm{disc}} \approx \epsilon_{\mathrm{edd}} \times 10^{44}\ \mathrm{erg\ s^{-1}}\ , \tag{4.17}$$

with the Eddington accretion rate $\epsilon_{\mathrm{edd}} \sim 0.1$ (Becker and Biermann 2009). The optical depth can then be estimated as $\tau_{\mathrm{p}\gamma_{\mathrm{disc}}} \sim 0.02$ at a distance of $d_{\mathrm{j}} \sim 3000 R_{\mathrm{g}}$, and decreasing outward along the jet.

The proton field of the torus has an optical depth of

$$\begin{aligned} \tau_{\mathrm{p}p_{\mathrm{torus}}} &= \chi \sigma_{\mathrm{p}p} \\ &\approx 2 \times 10^3\ , \end{aligned} \tag{4.18}$$

where Becker and Biermann (2009) estimate the column depth of the torus $\chi \sim 4 \times 10^{23}$ cm^{-2}, and the cross section of the proton-proton interaction $\sigma_{\mathrm{p}p} \approx 5 \times 10^{-27}$ cm^2.

In the jet, the synchrotron radiation density in the jet frame is

$$\begin{aligned} n(\varepsilon_{\gamma_{\mathrm{synch}}}) &\approx \frac{L_{\mathrm{knot}}}{\Gamma_{\mathrm{j}}\ 4\pi\ d_{\mathrm{j}}^2\ c\ \varepsilon_{\mathrm{synch}}} \\ &\approx 4.053 \times 10^5\ L_{\mathrm{knot}}\ d_{\mathrm{j}}^{-2}\ , \end{aligned} \tag{4.19}$$

with a photon energy of $\varepsilon_{\mathrm{synch}} = 6.550 \times 10^{-18}$ erg, or frequency of $\nu_{\mathrm{synch}} = 1$ GHz, thus emitting in the radio. The luminosity of the knot is estimated as a fraction ϵ_{knot} of the total jet radio luminosity so that

$$L_{\mathrm{knot}} \approx \epsilon_{\mathrm{knot}} \times 10^{40}\ \mathrm{erg\ s^{-1}}\ . \tag{4.20}$$

Assuming a bulk Lorentz factor of the jet, $\Gamma_{\mathrm{j}} = 10$, the fraction $\epsilon_{\mathrm{knot}} = 0.1$, a half opening angle and black hole mass as above, and at a distance of $d_{\mathrm{j}} \sim 3000 R_{\mathrm{g}}$, the optical depth in the synchrotron radiation field is $\tau_{p\gamma_{\mathrm{disc}}} \sim 0.9$.

The synchrotron radiation field will therefore dominate over the other targets. The optical depth of the disc depends on the accretion rate and for a less efficient rate, as is observed in some FR-I, the optical depth would approach zero. The proton target in the torus is negligible.

The density of the synchrotron field decreases with distance, with the adiabatic expansion of the knots, and so does the optical depth. Therefore, it is expected that the dominant pγ interactions occur at the first strong shock where the jet is still collimated and the optical depth for interactions with the synchrotron field is of the order unity. In their calculations they therefore assume $\tau_{p\gamma_{\rm synch}} = 1$ (Becker and Biermann 2009).

The energetic protons therefore interact with the synchrotron field predominantly at the base of the jet, at the first strong shock. Protons escaping this region travel along the jet and are accelerated in the subsequent stationary shocks. When the optical depth is too low for hadronic interactions, the protons will escape as UHECRs. The neutrino and UHECR fluxes will therefore follow the primary proton energy spectrum. Therefore

$$\left(\frac{dN_{\rm cr}}{dE_{\rm cr}}\right) \propto \left(\frac{dN_{\nu}}{dE_{\nu}}\right) \ , \tag{4.21}$$

when evaluated within the supergalactic plane, where the events implying the PAO correlations are assumed to originate (Becker and Biermann 2009). Therefore, the spectral indices of the two spectra are assumed to be equal, i.e. $\rho_{\nu} \approx \rho_{\rm p}$. The UHECR spectrum has an observed index $\rho_{\rm cr} = 2.7$, but Becker and Biermann (2009) remark that stochastic shock acceleration produces a spectrum of 2.3 or flatter; hence, the steep spectrum of UHECR emission may not reflect the intrinsic spectrum. As such, in their model they use an index of 2 and 2.3.

The proton population follows the bulk motion of the relativistic jet, described in terms of the Lorentz factor $\Gamma_{\rm j}$. The opening angle of the jet cone is determined from the Lorentz factor of the jet bulk motion, as $\omega_{\rm j} \propto \Gamma_{\rm j}^{-1}$, hence the solid angle of the emission goes as $\Omega_{\rm j} \propto \Gamma_{\rm j}^{-2}$. The cone of emission differs as the neutrino flux is predominantly produced at the base of the jet. As the primary protons move with the relativistic jet content upon interacting with

the photon field, the neutrinos are emitted in a beamed cone with a much smaller opening angle than the UHECR emission which escapes further along the jet (Fig. 4.2). The Lorentz factor of the emission therefore differs as the neutrinos are emitted in much stronger shocks occurring closer to the core. Becker and Biermann (2009) assume a ratio of the Lorentz factors as

$$\frac{\Gamma_\nu}{\Gamma_{\rm cr}} \approx 3 \ . \tag{4.22}$$

In the Becker and Biermann (2009) model, any neutrino detection needs to originate in blazar-type AGN due to the beamed emission, whereas a cosmic ray point source may have a jet misaligned with our line of sight. They therefore need to consider the difference in redshift dependence for the two emissions, which depends on the source distribution. To account for that of the neutrino emission, they use a radio luminosity function of flat spectrum radio sources in Dunlop and Peacock (1990), for which they interpret the abundance of low-luminosity sources as the FR-I type blazars. For the cosmic rays they use the FR-I radio luminosity function in Willott et al. (2001). The dependence is expressed as

$$\varphi = \int_{z_{\rm min}}^{z_{\rm max}} \int_{L_{\rm min}}^{L_{\rm max}} dz dL \frac{1}{4\pi D_{\rm L}^2} \frac{d\Psi_{\rm r}}{dL} \frac{dV_{\rm c}}{dz} \ , \tag{4.23}$$

with the radio luminosity function $d\Psi_{\rm r}/dL$ and the comoving volume element $dV_{\rm c}/dz$ (see Sec. 2.3.1). The factor $1/4\pi D_{\rm L}^2$ takes into account the decrease of flux suffered for emission from sources at luminosity distance $D_{\rm L}$ (see Sec. A.3). Becker and Biermann (2009) take the minimum redshift to be $z = 0.0008$ for cosmic rays, where the closest FR-I contributing to the emission is located – namely Cen A. The lower limit for the neutrino emission is given by the location of the Perseus A as the closest contributing flat spectrum source, with $z = 0.018$. The upper limit of the redshift integration is conservatively taken as the size of the supergalactic plane, i.e. $z = 0.03$, thus assuming that the sources contributing to the cosmic ray flux are spread across this plane. The larger number of sources decreases the redshift dependence of the cosmic ray emission, relative to assuming a smaller volume containing the contributing sources. The ratio describing the redshift dependence for the two emissions is

then found to be

$$\frac{\varphi_\nu}{\varphi_{\rm cr}} \approx 0.1 \ . \tag{4.24}$$

The energy estimates of the photohadronic interaction is dictated by the energy distributed amongst the secondaries. Assuming the delta resonance channel, the branching ratio for the charged pion path is 1/3. In the decay of the pion, half its energy will be converted to ν_μ energy. Assuming standard oscillation effects on propagation, the ratios are the same assumed in Sec. 4.1.3, i.e. $(\nu_e : \nu_\mu : \nu_\tau) = (1 : 2 : 0)_{\rm production} \rightarrow (1 : 1 : 1)_{\rm observed}$. Becker and Biermann (2009) therefore relates the emission of the neutrino and UHECR from their respective cones by a factor of $\tau_{\rm p\gamma}/12$ to account for the fraction of energy which goes to the neutrino population. The (muon) neutrino spectrum for a single source,will therefore follow

$$\begin{aligned} \phi_\nu^{\rm BB,ss}(E_\nu) &= \left(\frac{dN_\nu}{dE_\nu}\right)^{\rm BB,ss} \\ &= A_\nu^{\rm BB} E_\nu^{-\rho_\nu} \ , \end{aligned} \tag{4.25}$$

again omitting the exponential decay of the spectrum. Contrary to the KT model, the spectrum does not contain a break. This is because the break predicted in the model occurs at much lower energies, as the break resulting from the photohadronic interaction depends on the energy of the target photon fields. Whereas the KT model used a target with X-ray energies, i.e. a break at high energies, the BB model uses the synchrotron target, hence the break is found at low energies. The normalisation (Becker and Biermann 2009; Argüelles et al. 2010) is given by

$$\begin{aligned} A_\nu^{\rm BB} &= \frac{\varphi_\nu}{\varphi_{\rm cr}} \left(\frac{\Gamma_\nu}{\Gamma_{\rm cr}}\right)^{\rho_{\rm p}+1} \frac{\tau_{\rm p\gamma}}{12} \left(\frac{m_\pi}{4}\right)^{\rho_{\rm p}-2} (\rho_{\rm p}-1) A_{\rm CR}^{\rm SGP} \\ &= 1.4 \times 10^{-10} \ {\rm GeV \ cm^{-2} \ s^{-1} \ sr^{-1}} \ , \end{aligned} \tag{4.26}$$

with the normalisation for the cosmic ray spectrum in the supergalactic plane as

$$\begin{aligned} A_{\rm CR}^{\rm SGP} &= N(> E_{\rm PAO}^{\rm min})(E_{\rm PAO}^{\rm min})^{\rho_p - 1} \\ &= 4 \times 10^{10} \ {\rm GeV \ cm^{-2} \ s^{-1} \ sr^{-1}} \ . \end{aligned} \tag{4.27}$$

The threshold energy of PAO is $E^{\rm min}_{\rm PAO} = 5.7 \times 10^{10}$ GeV. The integral flux of the UHECR emission is measured from the number of events weighted by the exposure of PAO at threshold energy, to $N(> E^{\rm min}_{\rm PAO}) = 7{\times}10^{-21}$ cm^{-2} s^{-1} sr^{-1}.

4.2 High-Energy Neutrino Spectra from AGN Jets

Assuming UHE neutrinos originate in AGN jets following the scenario outlined above we calculate the expected neutrino flux to be detected in observatories on Earth. We use the prescription of Koers and Tinyakov (2008) (Sec. 4.1.3) to model the production in the source. We compare the resulting neutrino spectra to those calculated using the model of Becker and Biermann (2009) (Sec. 4.1.4).

We assume single source neutrino energy spectra based on the two production models and convolve these with the space densities of various AGN classes that were calculated in Sec. 2.3. As the spectrum obtained corresponds to the received flux, the emitted flux at source is related through a shift corresponding to the redshift of the source. Then, the neutrino energy upon production at source $\mathcal{E}$ is related to the observed energy E_0 by

$$\mathcal{E} = (1 + z)E_0 \ . \tag{4.28}$$

We calculate the neutrino spectrum in the source frame by integrating the spectrum over redshift and luminosity. We want to investigate the contribution to the total diffuse neutrino flux at various cosmological epochs, hence our integration limits are increments (z_a, z_b) in the range $0 < z < 10$. The upper limit is assumed to account for possible sources well into the epoch of reionisation. As seen in Ch. 2 however, the photon flux contributions from sources beyond $z \sim 3 - 5$ are dominated by the flux from nearby sources. We also want to examine the contributions made in bins of source luminosity (L_a, L_b), and therefore integrate in increments within the luminosity range determined from the various source populations over the full redshift range. The population-dependent luminosity ranges are summarised in Table 4.1.

Assuming a range of black hole masses $10^6 M_\odot < M_{\rm BH} < 10^{10} M_\odot$ and an Eddington accretion rate of $\xi_{\rm acc} \sim 0.1$, we expect no AGN to be intrinsically brighter than $\mathcal{L}^{\rm max}_{\rm X} \approx 10^{47}$ erg s^{-1}. We set a lower bound on the intrinsic

AGN X-ray Luminosity Bounds

	Radio galaxies	Blazars	FSRQs	BL Lacs
$(\log\ L_{\rm X})_{\rm min}$	42.0	44.0	46.0[a]	44.5
$(\log\ L_{\rm X})_{\rm max}$	47.0	48.5	48.5	48.0[b]

Table 4.1: AGN X-ray luminosity bounds for radio galaxies, blazars, and the subclasses of blazars, FSRQ and BL Lac. The radio galaxy luminosity bounds are adopted from those of the X-ray surveys of Hasinger et al. (2005); Silverman et al. (2008). For the blazar types, the limits were set considering the intrinsic luminosity, and applying the beaming relation to obtain the observed luminosity (see Sec. 2.5). *a*) Though beaming calculations gave $(\log\ L_{\rm X})_{\rm min} = 43.6$, this limit is constrained due to calculations of the FSRQ XLF. *b*) Beaming calculations gave $(\log\ L_{\rm X})_{\rm max} = 48.6$, but through the BL Lac XLF calculations, this limit is lowered.

luminosity to $\mathcal{L}_{\rm X}^{\rm min} \approx 10^{40}$ erg s^{-1} to avoid contamination of the high redshift AGN densities by other distant bright objects, e.g. X-ray binaries. X-ray binaries, though commonly with luminosities around 10^{38} erg s^{-1}, may show beamed luminosities comparable to the fainter blazars. The neutrino flux in the source frame is then

$$\phi_\nu^{\rm model,s} = \int_{L_{\rm a}}^{L_{\rm b}} \int_{z_{\rm a}}^{z_{\rm b}} \phi_\nu^{\rm model}(\mathcal{E})\ \frac{d\Psi(L,z)}{dL\ dV_{\rm c}} \frac{dV_{\rm c}}{dz}\ dL\ dz\ . \tag{4.29}$$

The contribution from the source density at a given redshift is given in the luminosity function $d\Psi/dL\,dV_{\rm c}$ evaluated in the comoving volume element $dV_{\rm c}/dz$. Taking into account cosmological effects, the propagation will affect the observed intensity, $\mathbb{I}_\nu^{\rm model,0} = E_\nu^2 \phi_\nu^{\rm model,0}$, as

$$\mathbb{I}_\nu^{\rm model,0} = (1+z)^{-4} \mathbb{I}_\nu^{\rm model,s}\ . \tag{4.30}$$

The power of four comes from the redshift distortions on the energy (Eqn. 4.28) and the Lorentz boost on the intensity of the emission due to the Lorentz invariant quantity $\mathbb{I}/f^3 = \text{const}$. This causes the depletion of intensity received at increasing redshift, as well as a shift of the break in the spectrum towards lower energies. The break is due to the optical depth of the processes responsible for neutrino production and is unity at the given energy in the source, hence above this energy the spectrum will be flatter.

A number of theoretical limits and constraints are set on the neutrino flux from e.g. considering the UHECR energy spectrum. A commonly referenced limit is that estimated by Waxman and Bahcall (1999); Waxman (2011) – the so-called *WB bound*. However, experimental limits have been set by a number of observatories as discussed in Sec. 1.3, which includes limits determined from events observed by *IceCube*. We therefore compare our expected diffuse neutrino spectra obtained through our calculations with the most constraining limits set at a given energy (see Fig. 1.16); namely the IC-3yr sensitivity (Aartsen et al. 2014b) for $E_\nu < 10^7$ GeV, and the PAO-9yr limit (Aab et al. 2015) that covers energies up to about 10^{10} GeV. We will also show the derived power-law neutrino spectrum (Aartsen et al. 2015b).

4.2.1 KT Neutrino Model Calculations

This model is outlined in Sec. 4.1.3, for which the FR-I AGN Cen A is assumed to be a representative UHECR and neutrino producing AGN. The processes which lead to neutrino emission occur in the core of the AGN, with the X-ray photon field taken to originate in the corona surrounding the AGN nucleus.

We first calculate the observed Cen A neutrino spectrum predicted by the model. Its redshift is estimated at a physical distance of $D_\mathrm{p} = 3.4$ Mpc, with an X-ray disc luminosity of $L_\mathrm{X}^\mathrm{CenA} = 4.8 \times 10^{41}$ erg s^{-1}, measured in the 2-10 keV band (Evans et al. 2004). Its distance, corresponding to a redshift of $z \approx 0.0008$ (Wright 2006), can therefore be considered a local source (i.e. $z \approx 0$). As the model described in Koers and Tinyakov (2008) has omitted the exponential cutoff of the spectrum due to the maximum proton energy achievable in the source, we assume an arbitrary cut-off of $E_\mathrm{max} = 5{\times}10^{10}$ GeV, at which the highest energy UHECR event is observed. The Cen A neutrino flux (Eqn. 4.11) is then calculated as

$$\begin{aligned}\phi_\nu^\mathrm{KT,CenA}(E_\nu) &= \left(\frac{dN_\nu}{dE_\nu}\right)^\mathrm{KT,CenA} \\ &= A_\nu^\mathrm{KT,CenA}\left(\frac{E_\nu}{1\ \mathrm{GeV}}\right)^{-\rho_\nu} \times \min\left(1, \frac{E_\nu}{E_{\mathrm{br},\nu}}\right) \exp\left(-\frac{E_\nu}{E_\mathrm{max}}\right) ,\end{aligned} \tag{4.31}$$

with the normalisation given in Eqn. 4.12. The neutrino spectral index is

$\rho_\nu = 1.7$. Fig. 4.3 shows the neutrino spectrum of Cen A calculated at $z = 0$, as well as calculated at various cosmological epochs within the assumed redshift range ($0 < z < 10$). From the figure, it is evident that the observed spectrum decreases in intensity with increasing redshift, and the break of the spectrum shifts to lower energies. These features are due to the cosmological effects suffered by the emission.

We adopt a luminosity scaling model to account for the variations in AGN brightness. As the disc luminosity is a measure of the accretion rate, the brightness is a measure of the power of the AGN. Therefore, the model is based on the assumption that, with increasing brightness of the AGN, the rate of neutrino production increases. Hence, we have a relation of X-ray (disc) intensity to the neutrino intensity in Cen A as

$$\zeta^{\mathrm{CenA}} = \left(\frac{\mathbb{I}_\nu}{\mathbb{I}_\mathrm{X}}\right)^{\mathrm{CenA}} . \tag{4.32}$$

The luminosity distance D_L of a local source equals its physical distance D_p, hence $D_\mathrm{L} = 3.4$ Mpc $= 1.049 \times 10^{25}$ cm. The X-ray photon intensity of Cen A is then $\mathbb{I}_\mathrm{X}^{\mathrm{CenA}} = L_\mathrm{X}^{\mathrm{CenA}}(4\pi D_\mathrm{L}^2)^{-1} = 3.47 \times 10^{-10}$ erg cm^{-2} s^{-1}. For a given X-ray luminosity we scale the neutrino emission of an AGN by that of Cen A by

$$\zeta^{\mathrm{AGN}} = \eta\zeta^{\mathrm{CenA}} , \tag{4.33}$$

with the scaling parameter η, and

$$\zeta^{\mathrm{AGN}} = \left(\frac{\mathbb{I}_\nu}{\mathbb{I}_\mathrm{X}}\right)^{\mathrm{AGN}} . \tag{4.34}$$

We therefore obtain the luminosity scaling for the AGN neutrino flux,

$$\phi_\nu^{\mathrm{AGN}} = \phi_\nu^{\mathrm{CenA}}\tilde{\phi}^{\mathrm{KT,LS}} \tag{4.35}$$

with

$$\tilde{\phi}^{\mathrm{KT,LS}} = \eta\frac{L_X^{\mathrm{AGN}}}{L_X^{\mathrm{CenA}}} . \tag{4.36}$$

We assume the simplest case is a linear relation, and $\eta = 1$. The linear assumption then reflects our expectations of brighter AGN producing a higher rate of neutrinos than their low-luminosity counterparts. If a source with X-ray luminosity fixed at the KT reference luminosity (i.e. that of Cen A), is

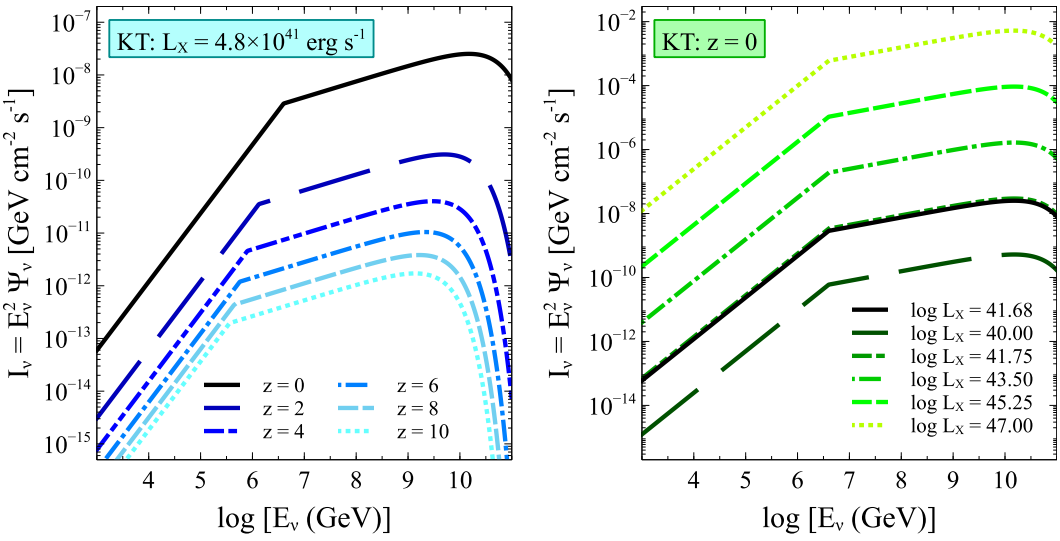

Fig. 4.3: Single source neutrino spectra expected from calculations based on the KT production model. *Left:* The KT model reference source X-ray luminosity is that of Cen A. As a local source, the expected neutrino flux from Cen A is given by the curve denoted $z = 0$ (black line). With increasing source location, the observed intensity is expected to decrease due to cosmological effects. *Right:* The luminosity scaling of the KT single source neutrino spectra is calculated at a fixed redshift ($z = 0$). The black line corresponds to the Cen A neutrino spectrum. The coloured lines represent sources with X-ray luminosities in the range $40.0 < \log L_{\rm X} < 47.0$. Brighter AGN thus produce significantly higher intensities of neutrinos than a lower-luminosity source using this luminosity scaling model.

located at increasing distances, the observed neutrino intensity of the source will decrease according to Eqn. 4.30, and the break of the spectrum similarly shifts to lower energies. Applying the X-ray luminosity scaling (Eqn. 4.35) on the single source spectrum, fixed at $z = 0$, shows how the scaling affects the observed neutrino spectrum for sources of varying X-ray luminosities. Then, the sources fainter than the KT reference X-ray luminosity will produce lower neutrino emission than a source with brighter X-ray luminosity, illustrated in the right panel of Fig. 4.3.

In Ch. 2 we calculated the space densities of various AGN populations, derived from X-ray surveys (Hasinger et al. 2005; Silverman et al. 2008; Ajello et al. 2009). We estimated both the redshift and luminosity distributions, and we use these results to calculate the observed diffuse neutrino flux. The contributions from various cosmological epochs are calculated by con-

volving the neutrino production model with the AGN luminosity distributions that were calculated in bins of redshift. We sum the contribution along the luminosity distribution in bins of redshift, thus

$$\phi_\nu^{\mathrm{KTdiff},z} = \phi_\nu^{\mathrm{AGN}} \times \frac{N_{\mathrm{AGN}}(\log L_{\mathrm{X}})}{d\log L_{\mathrm{X}}}\bigg|_{z_{\mathrm{a}}}^{z_{\mathrm{b}}} \Delta(\log L_{\mathrm{X}}) \ , \tag{4.37}$$

integrated over the luminosity range of the respective AGN populations. The integration of luminosity was done over the respective range for each population (Table 4.1) in log-luminosity. We then have a neutrino energy spectrum in bins of redshift for each population. The sum of redshift contributions gives the total diffuse neutrino flux expected to be observed by a detector on Earth.

We also calculate the flux contributions from each luminosity bin, following

$$\phi_\nu^{\mathrm{KTdiff},L} = \phi_\nu^{\mathrm{AGN}} \times \frac{N_{\mathrm{AGN}}(z)}{dz}\bigg|_{\log L_{\mathrm{a}}}^{\log L_{\mathrm{b}}} \Delta z \ , \tag{4.38}$$

integrated over the full redshift range. The resultant luminosity bin contributions for each AGN population are summed to obtain the expected total diffuse neutrino spectrum. To ensure our calculations are done appropriately, the total diffuse spectra calculated from redshift and luminosity bins for a given source population should coincide. In Figs. 4.4-4.8 the resulting spectra are plotted for each population, which illustrates that in all cases the total diffuse spectra obtained from the redshift and luminosity data do indeed agree. The spectra are then compared with the *IceCube* experimental flux limit which, in each case, is added to the plot.

We study the neutrino emission derived for Type-I and Type-II radio galaxy populations. First we consider only Type-I RGs, that are unobscured AGN. Second, we consider a mix of both Type-I and -II RGs, hence a mix of observational characteristics, as these are both unobscured and obscured AGN. In Ch. 2 we derived the space densities, and took into account the radio-loud fraction – and of these, the "unseen" proportion – to obtain an estimate of the total population extending redshifts 0 through 10. The X-ray luminosity range considered for these populations is $42.0 < \log L_{\mathrm{X}} < 47.0$. The relative trends of the neutrino emission from the redshift and luminosity contributions are similar for the two populations, with the observed neutrino

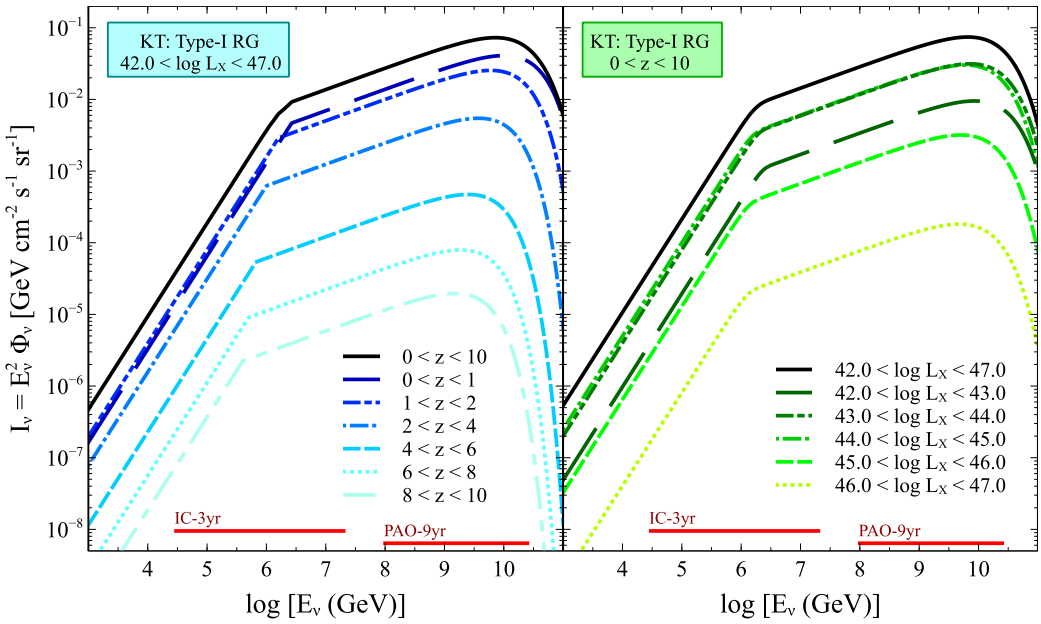

Fig. 4.4: Contribution to the diffuse neutrino energy flux from Type-I radio galaxies, expected from the KT neutrino model. Total diffuse contributions from the populations are represented by the black lines. The spectra are compared with experimental limits set by *IceCube* and PAO. *Left:* Diffuse flux contributions from Type-I RGs at cosmological epochs. Each spectral contribution is evaluated over the full range of luminosities, and the sum gives the total diffuse flux. *Right:* Diffuse flux contributions from Type-I RGs in bins of the X-ray luminosity of the source, evaluated over all cosmological epochs ($0 < z < 10$).

flux from Type-I RGs (Fig. 4.4) about an order of magnitude lower than for the mixed Type-I and -II RG population (Fig. 4.5). This is expected as the former population can be assumed a subset of the latter population.

The dominant epoch contributing to the diffuse neutrino emission is the most local ($0 < z < 1$), with decreasing intensity towards lower redshifts. With each subsequent epoch, the break in the spectrum is also shifted to lower energies, thus the low-energy part of the neutrino spectrum contains a comparable contribution from the epoch enclosed by $1 < z < 2$. This is most apparent in the spectra of Type-I RGs (Fig. 4.4). There is a greater contribution from Type-I sources in the epoch enclosed by $2 < z < 4$ than from the mixed population, relative to other epochs. This becomes clear when comparing to the redshift distributions of the AGN populations (Fig. 3.10), where the former peaks slightly earlier than the mixed population.

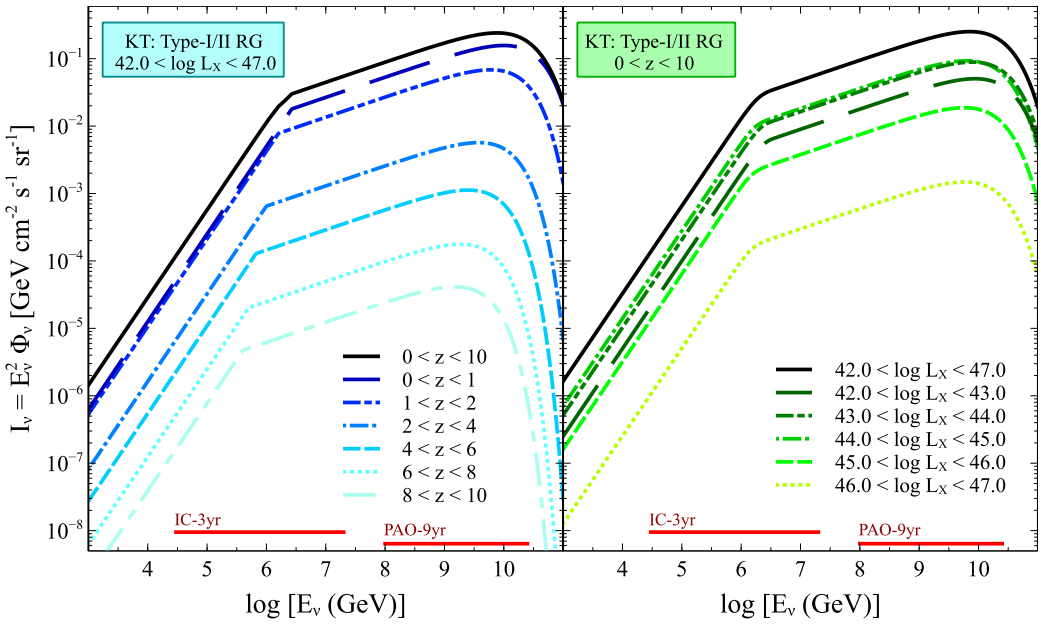

Fig. 4.5: Contribution to the diffuse neutrino energy flux from Type-I and -II radio galaxies, expected from the KT neutrino model. Total diffuse contributions from the populations are represented by the black lines. The spectra are compared with experimental limits set by *IceCube* and PAO. *Left:* Diffuse flux contributions from Type-I and -II RGs at cosmological epochs. Each spectral contribution is evaluated over the full range of luminosities, and the sum gives the total diffuse flux. *Right:* Diffuse flux contributions from Type-I and -II RGs in bins of the X-ray luminosity of the source, evaluated over all cosmological epochs ($0 < z < 10$).

The dominant neutrino emitting RGs are those with X-ray luminosities between $43.0 < \log L_{\rm X} < 45.0$, where sources on the bright end of that range dominate the low-energy neutrino spectrum, i.e. before the break in Figs. 4.4 and 4.5. The neutrino spectra from the brightest RGs are almost two orders of magnitude lower than spectra from sources located at epochs of peak activities. The low neutrino emission of the brightest RGs therefore reflect their low numbers and that peak activity occurs at higher redshifts, given the luminosity scaling model we use (Eqn. 4.36). The dominant redshift from each luminosity bin can also be deduced from the location of the break and cut-off in the spectrum, as these shift to lower energies with increasing redshift. The low neutrino emission from the faint sources (i.e. $\log L_{\rm X} < 43.0$) is due to their intrinsically low luminosity. We know from studying the space

densities of these sources that they are numerous, particularly at low redshifts.

The dominant contribution to the diffuse neutrino flux is therefore from low-to-intermediate luminosity RGs, predominantly located in the local Universe, as predicted by the KT model. Nevertheless, the model predicts that both populations are expected to produce a diffuse neutrino energy spectrum which lies 5 to 6 orders of magnitude above the *IceCube* experimental limit.

The diffuse neutrino flux from the blazar population and the FSRQ and BL Lac subclasses are presented in Figs. 4.6, 4.7, and 4.8. These were calculated similarly to the radio galaxy neutrino spectra with one addition. Due to the highly beamed emission from blazars, their observed luminosity is boosted following the relation

$$L_{\rm X} = \delta^{\varrho} \mathcal{L} \ , \tag{4.39}$$

where $\varrho = 3 + \alpha_{\rm X}$ (see Sec. 2.5). The spectral index $\alpha_{\rm X}$ for each blazar class is given in Ajello et al. (2009), and we scale the neutrino spectrum by the intrinsic luminosity in Eqn. 4.36.

The neutrino spectrum of the blazar population is dominated by sources in the epoch $2 < z < 4$ (Fig. 4.6). At the very highest energies, the local epoch dominates the spectrum. The higher redshift contributions are shown with decreasing intensity. Whereas the brightest blazars produce the least intense neutrino emission, the dominant emission comes from $45.5 < L_{\rm X} < 46.0$. The spectral break shows that the brightest blazars are found at higher redshifts than the fainter blazars. Though this population produces a lower-intensity spectrum than those of the radio galaxy populations, it is about five orders of magnitude above the *IceCube* limit.

The number density calculations of the FSRQ population greatly constrain the luminosity range, reflecting that it is a high-luminosity population. It makes up a large part of the total blazar population and traces the trends shown in the neutrino spectrum for the blazars closely. It is known to be a high-luminosity population of low space density, and predominantly found at higher redshifts. This is reflected in the neutrino spectrum (Fig. 4.7), where the dominant contribution is from the epoch within $2 < z < 4$. Whereas emission from the local Universe is prominent as well, the epochs surrounding

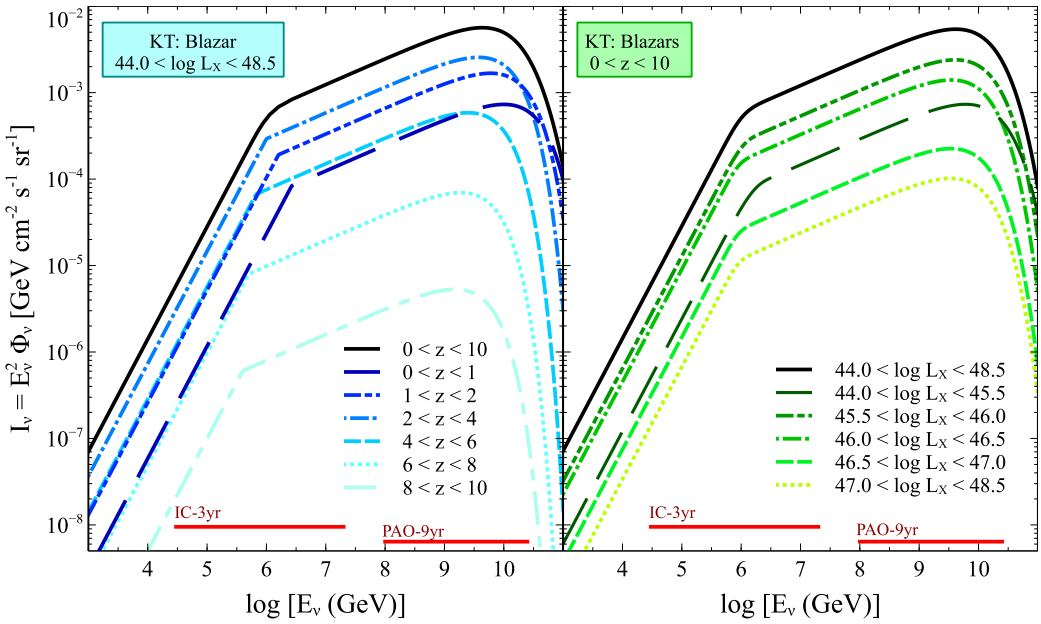

Fig. 4.6: Contribution to the diffuse neutrino energy flux from blazars, expected from the KT neutrino model. Total diffuse contributions from the populations are represented by the black lines. The spectra are compared with experimental limits set by *IceCube* and PAO. *Left:* Diffuse flux contributions from blazars at cosmological epochs. Each spectral contribution is evaluated over the full range of luminosities, and the sum gives the total diffuse flux. *Right:* Diffuse flux contributions from blazars in bins of the X-ray luminosity of the source, evaluated over all cosmological epochs ($0 < z < 10$).

peak activity of $z \approx 4$ produce the majority of the neutrino emission from this population. The FSRQ neutrino spectrum is dominated by the contribution from the $46.0 < L_{\rm X} < 46.5$ and, with each subsequent luminosity bin, the intensity is decreasing. The FSRQ diffuse neutrino spectrum is about four orders of magnitudes greater than the *IceCube* limit, which implies that this high-luminosity population is also rejected in the KT model.

The BL Lacs are the low-luminosity counterparts of the FSRQs and are detected mostly at lower redshifts, demonstrated by the number density calculations in Ch. 2. By comparing the spectral break in the BL Lac neutrino spectra binned in luminosity to the break in the FSRQ neutrino spectra, it can be shown that the former is residing more locally than the latter population.The diffuse neutrino spectrum from the population is greatly dominated by local sources, with the neutrino intensity dropping rapidly with increasing

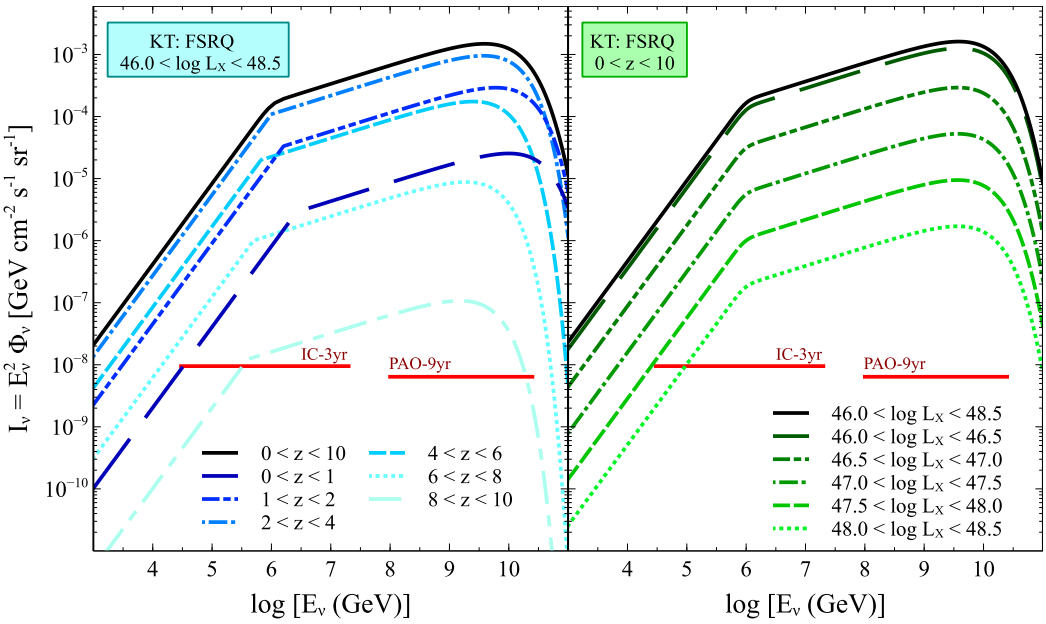

Fig. 4.7: Contribution to the diffuse neutrino energy flux from FSRQs, expected from the KT neutrino model. Total diffuse contributions from the populations are represented by the black lines. The spectra are compared with experimental limits set by *IceCube* and PAO. *Left:* Diffuse flux contributions from FSRQs at cosmological epochs. Each spectral contribution is evaluated over the full range of luminosities, and the sum gives the total diffuse flux. *Right:* Diffuse flux contributions from FSRQs in bins of the X-ray luminosity of the source, evaluated over all cosmological epochs ($0 < z < 10$).

redshift. The neutrino spectra from the BL Lac population is dominated by the lower luminosity bins, and decreases in intensity with increasing luminosity. Given its low space density at higher redshifts and the low-luminosity nature of the population it may not be surprising to see sources above $z > 2$ falling below the *IceCube* limit. Given that the majority of the known BL Lac population is local the model suggests that we may reject this population as a possible neutrino producer as well.

4.2.2 BB Neutrino Model Calculations

This model is outlined in Sec. 4.1.4, and we follow the same method of calculation to obtain the diffuse neutrino flux spectra as in Sec. 4.2.1. We assume a generic neutrino single source spectrum based on this model, in which Becker and Biermann (2009) consider FR-I AGN with the dominant photon field being the synchrotron radiation at the base of the jet. As FR-I AGN are

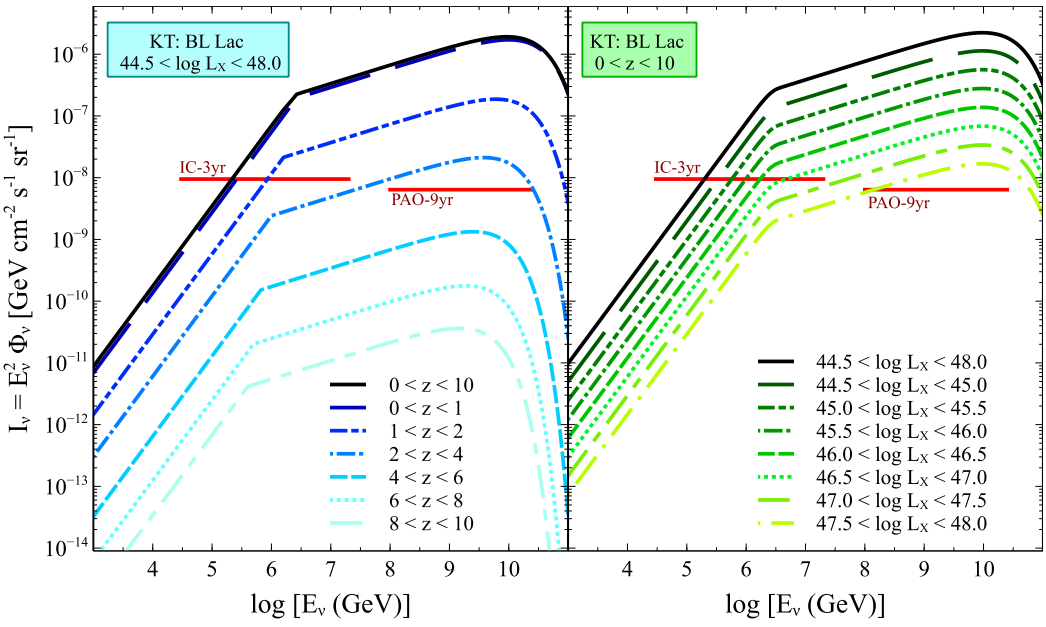

Fig. 4.8: Contribution to the diffuse neutrino energy flux from BL Lacs, expected from the KT neutrino model. Total diffuse contributions from the populations is represented by the black line. The spectra are compared with experimental limits set by *IceCube* and PAO. *Left:* Diffuse flux contributions from BL Lacs at cosmological epochs. Each spectral contribution is evaluated over the full range of luminosities, and the sum gives the total diffuse flux. *Right:* Diffuse flux contributions from BL Lacs in bins of the X-ray luminosity of the source, evaluated over all cosmological epochs ($0 < z < 10$).

brightest at the base of the jet, these sources would then be suitable for the model. They also consider the blazars which are aligned FR-I AGN in the viewing angle unification scheme.

The single source neutrino flux (Eqn. 4.25) is calculated as

$$\begin{aligned}\phi_\nu^{\mathrm{BB,ss}}(E_\nu) &= \left(\frac{dN_\nu}{dE_\nu}\right)^{\mathrm{BB,ss}} \\ &= A_\nu^{\mathrm{BB}} E_\nu^{-\rho_\nu} \exp\left(-\frac{E_\nu}{E_{\mathrm{max}}}\right) \ , \end{aligned} \tag{4.40}$$

where we have assumed a spectral cut-off at the energy corresponding to the most energetic UHECR observed, $E_{\mathrm{max}} = 5 \times 10^{10}$ GeV, and the normalisation of the spectrum is given by

$$A_\nu^{\mathrm{BB,ss}} = 1.4 \times 10^{-10} \ \mathrm{GeV\ cm^{-2}\ s^{-1}\ sr^{-2}} \ . \tag{4.41}$$

The normalisation of the spectrum, A_ν^{BB} (Eqn. 4.26), incorporates a scaling

relation of the X-ray disc luminosity to the neutrino flux. This is achieved by using the jet-disc symbiosis model by Falcke and Biermann (1995). This model relates the total jet power $L_{\rm jet}$ to the disc luminosity $L_{\rm disc}$ through simple energy conservation considerations in the accretion process. Then

$$\kappa_{\rm d-j} = \frac{L_{\rm jet}}{L_{\rm disc}} \ , \tag{4.42}$$

where the parameter $\kappa_{\rm d-j}$ is between zero (if there is no jet), and infinity (if there is no accretion disc), however Falcke and Biermann (1995) consider $\kappa_{\rm d-j} \lesssim 1$ to be reasonable. We adopt the value $\kappa_{\rm d-j} = 0.15$ from Becker et al. (2005).

The relation between the jet power and the synchrotron luminosity of the jet is estimated in Cavagnolo et al. (2010) from studies using *Chandra* (X-ray) and Very Large Telescope (VLT) (radio) data. They find that

$$L_{\rm jet} \approx 5.8 \times 10^{43} \left(\frac{L_{\rm synch}}{10^{40}} \right)^{0.7} \ {\rm erg \ s^{-1}} \ . \tag{4.43}$$

For a synchrotron luminosity of $L_{\rm synch} = 10^{40}$ erg s^{-1} the corresponding disc luminosity is

$$L_{\rm disc} = \frac{L_{\rm jet}}{\kappa_{\rm d-j}} \approx 3.87 \times 10^{44} \ {\rm erg \ s^{-1}} \ , \tag{4.44}$$

using Eqns. 4.42 and 4.43. We can then construct a luminosity scaling relation between the disc luminosity (i.e. $L_{\rm X}$) and the synchrotron luminosity, by rearranging Eqn. 4.43 to give

$$L_{\rm synch} \approx 2 \times 10^{-24} (L_{\rm disc})^{10/7} \ . \tag{4.45}$$

We substitute this relation into the equation for the optical depth of the pγ interactions in the jet synchrotron field, so that

$$\tau_{{\rm p}\gamma_{\rm synch}} = d_{\rm j} \omega_{\rm j} \sigma_{{\rm p}\gamma} n(\varepsilon_{\gamma_{\rm synch}}) \tag{4.46}$$

$$= \frac{\omega_{\rm j} \sigma_{{\rm p}\gamma} \epsilon_{\rm knot}}{4\pi \ c \ \Gamma_{\rm j} \ d_{\rm j} \ \varepsilon_{\rm synch}} 2 \times 10^{-24} (L_{\rm disc})^{10/7} \ . \tag{4.47}$$

We assume the fixed values given in Becker and Biermann (2009), discussed in Sec. 4.1.4, and that $\tau_{{\rm p}\gamma_{\rm synch}} = 1$. Hence, we can write

$$\tau_{{\rm p}\gamma_{\rm synch}} \approx 2 \times 10^{-64} (L_{\rm X})^{10/7} \ , \tag{4.48}$$

where the X-ray luminosity $L_{\rm X}$ represents the disc luminosity, and when it is given by Eqn. 4.44 we ensure that $\tau_{{\rm p}\gamma_{\rm synch}} = 1$. We substitute these relations into the BB flux model, and obtain the single source neutrino spectrum given by Eqn. 4.40, for an FR-I with reference X-ray luminosity, $L_{\rm X}^{\rm BB1,ss}$ given by Eqn. 4.44. The luminosity scaling for the AGN neutrino flux is then

$$\tilde{\phi}^{\rm BB,LS1} = \left(\frac{L_{\rm X}^{\rm AGN}}{L_{\rm X}^{\rm BB1,ss}} \right)^{10/7} , \tag{4.49}$$

and we calculate the AGN neutrino spectrum as

$$\phi_{\nu}^{\rm AGN} = \phi_{\nu}^{\rm BB,ss} \tilde{\phi}^{\rm BB,LS1} . \tag{4.50}$$

We assume a second scaling model, which was used in Becker et al. (2005) to scale the radio luminosity in the knots of core dominated flat spectrum sources to their disc luminosities. The scaling relation uses the disc-jet symbiosis model of Falcke and Biermann (1995); Falcke et al. (1995). The jet luminosity at radio frequencies is given in Falcke et al. (1995) (in units of erg s^{-1}) as

$$\begin{aligned} L_{\rm s} &= 6.7 \times 10^{42} \delta^{2.17} \sin^{0.17}[\theta_{\rm v}] (x_{\rm e,100})^{0.83} \\ &\quad \times (\kappa_{\rm d-j})^{1.42} \left(\frac{6}{\Gamma_{\rm j}} \right)^{1.8} \left(\frac{L_{\rm disc}}{10^{46}} \right)^{1.42-\zeta} \qquad (4.51) \\ &\approx 3.27 \times 10^{-15} (L_{\rm disc})^{1.27} , \qquad (4.52) \end{aligned}$$

where the Doppler factor of the jet is $\delta = [\Gamma_{\rm j}(1 - \beta_{\rm j} \cos[\theta_{\rm v}])]^{-1}$, and the factor $x_{\rm e,100} = 1$ accounts for the ratio of relativistic electrons to relativistic protons in the jet. The index $\zeta = 0.15$ is an additional velocity scaling to the disc luminosity due to the argument of accretion dependence of the bulk velocity of the jet (Falcke et al. 1995). Then, for a source with radio luminosity of 10^{40} erg s^{-1} the corresponding disc luminosity is $L_{\rm disc} \approx 1.04 \times 10^{43}$ erg s^{-1}. The optical depth can then be expressed as

$$\tau_{{\rm p}\gamma_{\rm synch}} \approx 2 \times 10^{-55} (L_{\rm X})^{1.27} , \tag{4.53}$$

and our second scaling model goes as

$$\tilde{\phi}^{\rm BB,LS2} = \left(\frac{L_{\rm X}^{\rm AGN}}{L_{\rm X}^{\rm BB,ss}} \right)^{1.27} . \tag{4.54}$$

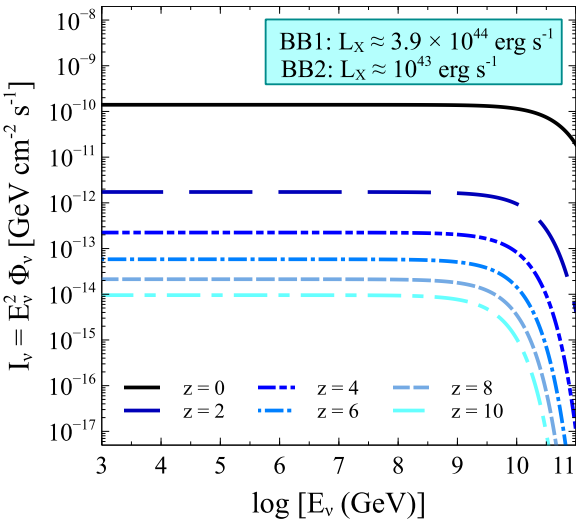

Fig. 4.9: Single source spectra calculated based on the BB neutrino production model, for sources located at redshifts $0 < z < 10$, for sources with $L_X^{AGN} = L_X^{BB,ss}$. The black line represents the BB reference flux. This flux corresponds to a single source reference source luminosity of $L_X = 3.9 \times 10^{44}$ erg s^{-1} and $L_X = 10^{43}$ erg s^{-1}, for the two scaling models considered, BB1 and BB2 respectively (see text). With increasing redshift, there is a corresponding decrease in intensity.

We follow the same method of calculation as we did for the KT model calculations in Sec. 4.2.1. Fig. 4.9 shows the reference single source spectrum derived for the BB model, for a reference source located at different cosmological epochs. The two scaling models used are denoted by BB1 and BB2, with a reference luminosity of $L_X = 3.9 \times 10^{44}$ erg s^{-1} and $L_X = 10^{43}$ erg s^{-1}, respectively. Compared to the single source spectrum of the KT model (Fig. 4.3) we find that the BB model single source neutrino spectrum is about one order of magnitude less intense than that of the KT model, for which Cen A is the reference source. Because the emission suffers the same cosmological effects, the models predict the same scale of decreasing intensity, and shift of the spectral cut-off to lower energies with increasing redshift.

The luminosity scaling is illustrated in Fig. 4.10. Due to the differences in the luminosity scaling between the KT and BB model, the latter predicts the neutrino spectrum for a given source luminosity over three orders of magnitude lower than the spectrum expected in the KT model (Fig. 4.3). In addition, the two scaling models applied to the BB model show that the BB1 calculations

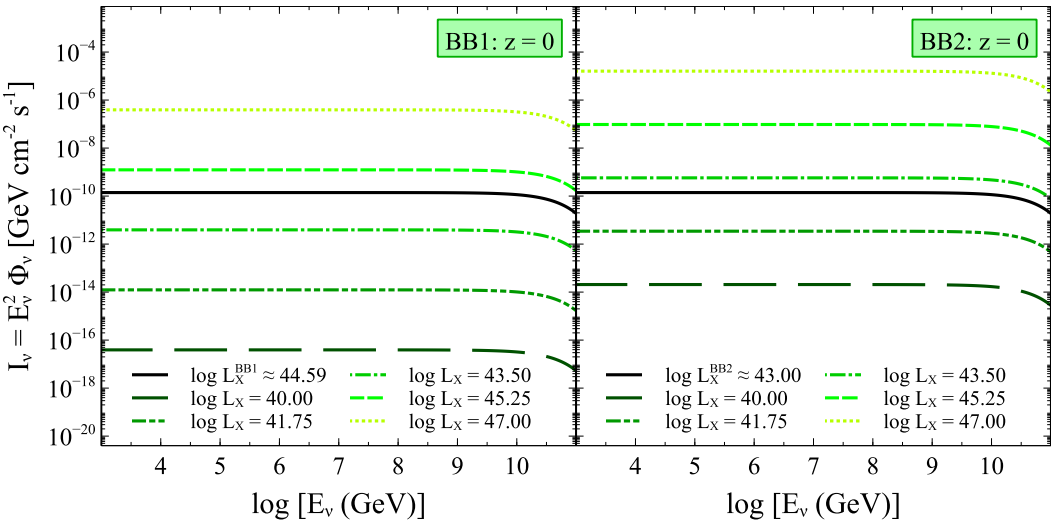

Fig. 4.10: Single source spectra calculated based on the BB neutrino production model, for sources of different luminosities, evaluated at $z = 0$. The plot on the left uses scaling model 1 (Eqn. 4.49). The black line corresponds to the reference luminosity, $L_X^{BB1,ss} \approx 3.9 \times 10^{44}$ erg s^{-1}. The plot on the right uses the second scaling model (Eqn. 4.54), with a reference luminosity of $L_X^{BB2,ss} \approx 10^{43}$ erg s^{-1} (black line). Both plots show neutrino intensity increasing with increasing source luminosity however, due to differences in the scaling models, the BB2 model produces significantly brighter neutrino luminosity than the BB1 model for a given source luminosity.

produce a more prominent drop in intensity for a given source luminosity than the BB2 calculations do (Fig. 4.10). Due to the power law on the luminosity scaling model used for the BB1 model calculations (Eqn. 4.49), the change in intensity is steeper in the BB1 model calculations than the BB2 and KT model spectra. This indicates the importance of choosing an accurate luminosity scaling model.

We follow the general diffuse neutrino flux calculations in bins of redshifts and luminosity, given in Eqns. 4.37 and 4.38 respectively, to obtain the neutrino emission predicted by the BB model. The two luminosity scaling models are applied, hence we show two sets of spectra for each AGN population. The resultant spectra are plotted in Figs. 4.11-4.15, and show that the total flux derived from contributions in redshift and luminosity bins agree.

The diffuse flux calculations for Type-I RGs are summarised in Fig. 4.11. For both luminosity scaling models the intensity varies significantly more when

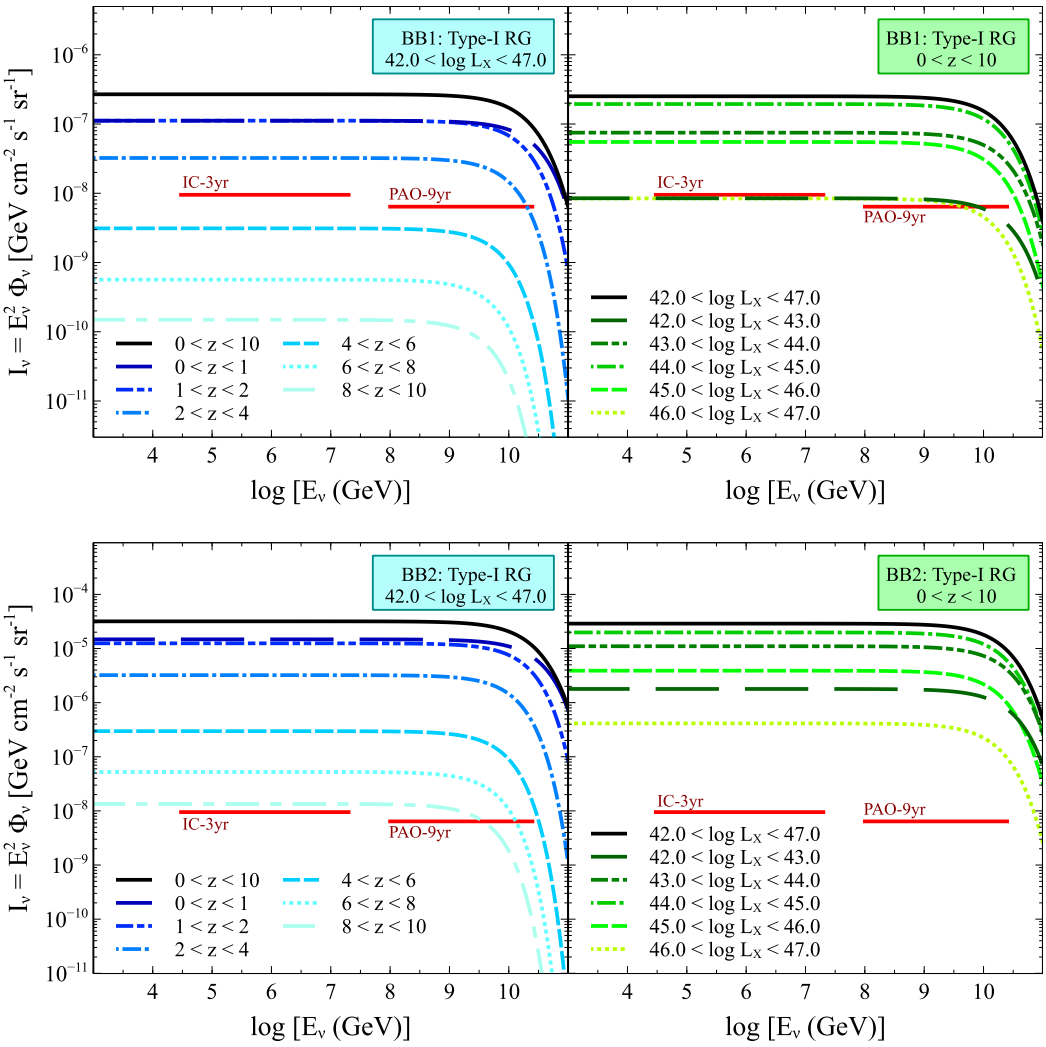

Fig. 4.11: Contribution to the diffuse neutrino energy spectrum from Type-I radio galaxies, expected from the BB model calculations. The total diffuse flux from the population is represented by the black line. The spectra are compared with experimental limits set by *IceCube* and PAO. The upper panels give the results using the BB1 scaling model (Eqn. 4.49), whereas the lower panels correspond to the BB2 (Eqn. 4.54) calculations. *Left:* Diffuse flux contributions from Type-I RGs at cosmological epochs. Each spectral contribution is evaluated over the full range of luminosities. *Right:* Diffuse flux contributions from Type-I RGs, in bins of X-ray source luminosity, evaluated over the full redshift range.

we look at contributions from redshift bins rather than luminosity bins. For both models the local epoch ($0 < z < 2$) dominates the total flux, and the most distant epoch ($8 < z < 10$) contributes least, with three orders of magnitude difference. Similarly, sources with X-ray luminosities enclosed by $44.0 < L_{\rm X} < 45.0$ dominate the total flux when evaluated over the full redshift range for

both luminosity scaling models.

In the panels summarising the contributions based on source luminosity (right hand side of Fig. 4.11) we see that the luminosity scaling model is an essential factor in the determination of neutrino spectra. Due to the reference X-ray luminosity of the BB1 scaling model being much greater than that of the BB2 model, the first model more efficiently suppresses the contribution from the abundant low-luminosity sources relative to the bright ones. Because the scaling index of the BB1 model is greater than that of the BB2 model (1.43 and 1.27, respectively), the model also enhances the bright contribution in addition to a steeper suppression of faint sources.

The resulting diffuse spectrum from Type-I RGs exceed the *IceCube* flux limit by 1.5 to 3.5 magnitudes in the case of the BB1 and BB2 calculations, respectively. Whereas the BB1 model produces spectra for which sources beyond $z = 4$, $43.0 < \log L_{\mathrm{X}}$ and $\log L_{\mathrm{X}} > 46.0$ fall below the *IceCube* limit, essentially all contributions resulting from the use of the BB2 scaling exceed it. Similarly to the result of the KT model on this population, the BB model suggests that this population can be rejected as neutrino producers.

Similarly to the resulting neutrino spectra for the KT model, the mixed Type-I and -II population produce a diffuse neutrino spectrum which is comparable to that of the unobscured Type-I population, but scaled up by just under one order of magnitude. The results are plotted in Fig. 4.12, and show that the contributions from each cosmological epoch is decreasing in intensity with increasing redshift, with the dominant epoch enclosed by $0 < z < 1$, i.e. the most local sources. Only sources beyond $z = 4$ fall below the *IceCube* limit for Type-I and -II RGs with the BB1 scaling; however, source contributions from all epochs exceed the limit for the BB2 model. The cut-off in the spectrum is also seen to shift to lower energies with higher redshift, as is expected due to cosmological effects on the emission.

The source luminosity bin dominating the neutrino spectrum is $44.0 < \log L_{\mathrm{X}} < 45.0$, with the scaling models producing slight variations in the dominance of the faint sources. The BB1 scaling, as we saw with the Type-I neutrino spectra, suppresses the contribution from faint sources, therefore the

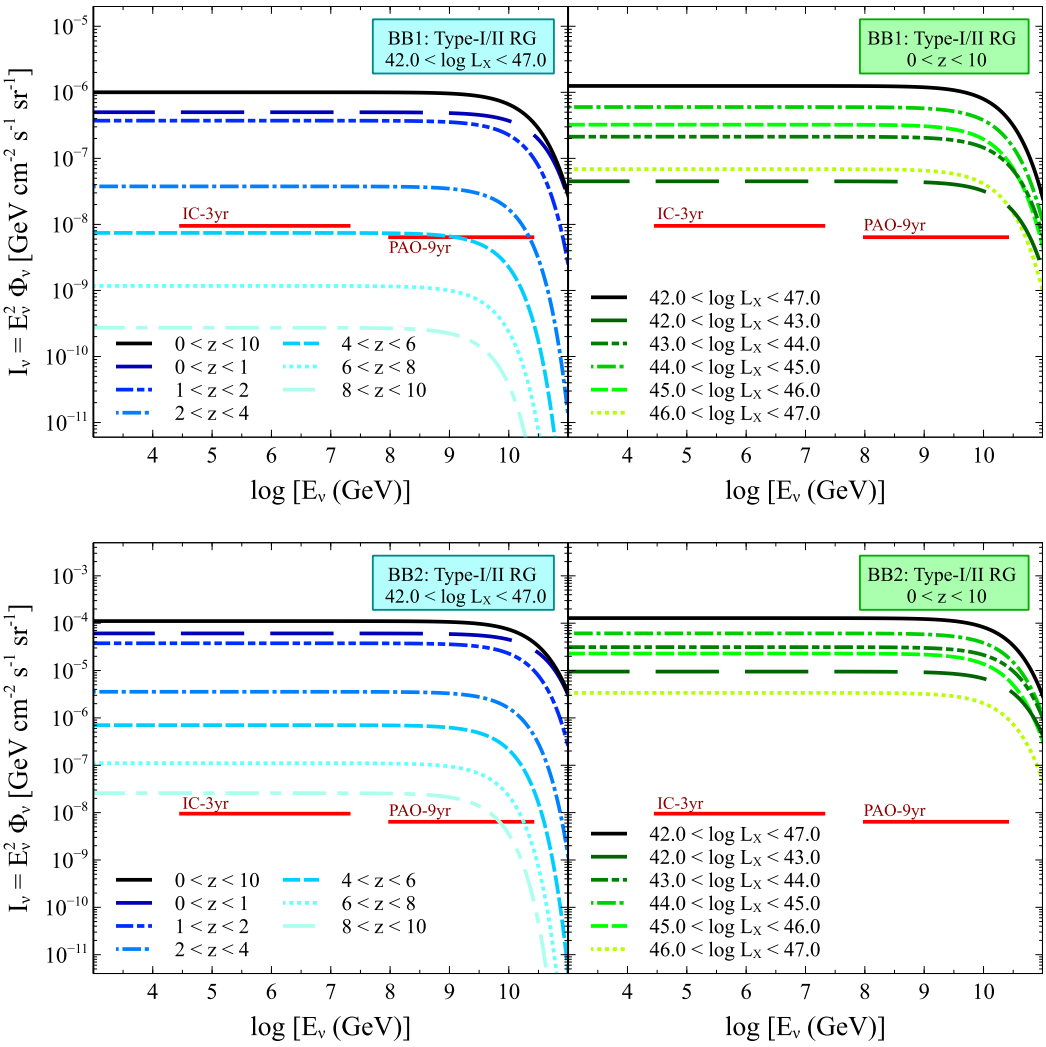

Fig. 4.12: Contribution to the diffuse neutrino energy spectrum from Type-I and -II radio galaxies, expected from the BB model calculations. The total diffuse flux from the population is represented by the black line. The spectra are compared with experimental limits set by *IceCube* and PAO. The upper panels give the results using the BB1 scaling model (Eqn. 4.49), whereas the lower panels correspond to the BB2 (Eqn. 4.54) calculations. *Left:* Diffuse flux contributions from Type-I and -II RGs at cosmological epochs. Each spectral contribution is evaluated over the full range of luminosities. *Right:* Diffuse flux contributions from Type-I and -II RGs in bins of X-ray source luminosity, evaluated over the full redshift range.

dominant emission comes from mid- to high-luminosity sources. The BB2 model, in addition to producing overall enhanced spectra, produce a much stronger contribution from faint sources. Since the total diffuse emission lies well above for all resulting calculations (up to two orders of magnitude for the

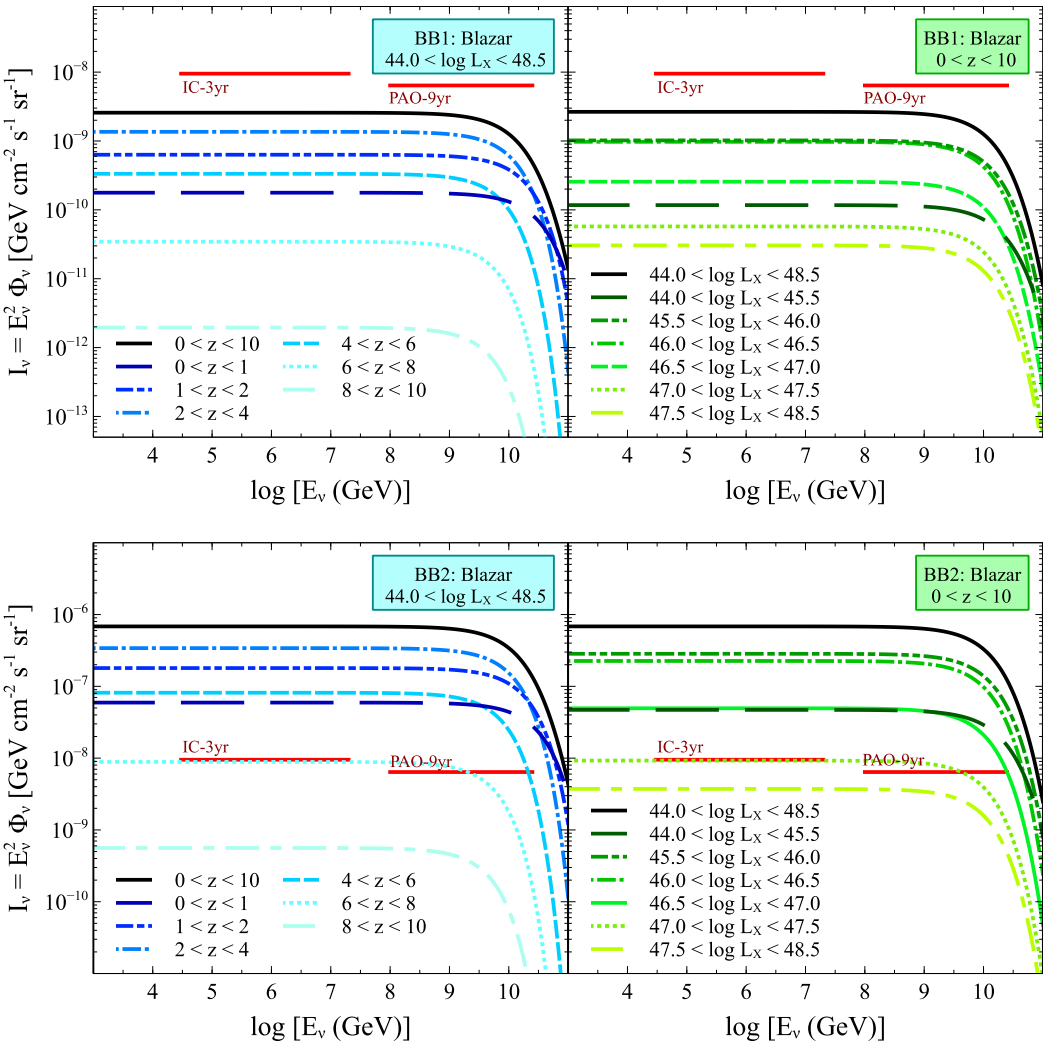

Fig. 4.13: Contribution to the diffuse neutrino energy spectrum from blazars, expected from the BB model calculations. The total diffuse flux from the population is represented by the black line. The spectra are compared with experimental limits set by *IceCube* and PAO. The upper panels give the results using the BB1 scaling model (Eqn. 4.49), whereas the lower panels correspond to the BB2 (Eqn. 4.54) calculations. *Left:* Diffuse flux contributions from blazars at cosmological epochs. Each spectral contribution is evaluated over the full range of luminosities. *Right:* Diffuse flux contributions from blazars in bins of X-ray source luminosity, evaluated over the full redshift range.

Type-I and -II RG population) and since these sources are known to exist in the local Universe, the comparison with the *IceCube* limit implies that these populations are not sources of high-energy neutrinos. The shift of the spectral cut-off again reflects that the brightest sources are found at higher redshifts and that the low-luminosity RGs are predominantly local.

The diffuse neutrino flux from the blazar population (Fig. 4.13) are calculated using the intrinsic X-ray source luminosities when scaling the spectra. Again we applied the two luminosity scaling models, presented as BB1 and BB2, referring to the model in Eqn. 4.49 and Eqn. 4.54 respectively. We find that the dominant cosmological epoch reflects the peak activity of the population in the $2 < z < 4$ range. Whereas the RG population contributions decreased with increasing epoch, the blazar population in the epochs of $1 < z < 2$ and $4 < z < 6$ contributes more than the most local epoch. This is not surprising as the local space density of blazars is low. Dominant sources have X-ray luminosities of $45.5 < \log L_{\rm X} < 46.5$, with the faintest and brightest bins carrying the lowest contribution of neutrino intensity.

Again, the blazar neutrino spectra highlight the importance of a well-defined luminosity scaling model. Whereas the BB1 scaling results in a total neutrino flux falling below the *IceCube* limit, the BB2 model shows the total blazar neutrino intensity of nearly two orders of magnitude in excess of the limit. Following the BB1 scaling model, the population can be considered as possible neutrino producers, but the BB2 model would indicate we can reject the population.

The diffuse neutrino flux contribution from FSRQs (Fig. 4.14) follows closely that of the full blazar population. The dominant contribution to the neutrino flux is similarly in the $2 < z < 4$ epoch, with the $1 < z < 2$ and $4 < z < 6$ epochs following in decreasing intensity. The luminosity bin responsible for the majority of the neutrino emission is the $46.0 < \log L_{\rm X} < 46.5$ bin, with decreasing intensity towards brighter sources. Given the FSRQ population is a high-luminosity population, this reflects the trends seen for the bright blazar sources in Fig. 4.13.

BL Lacs are low-luminosity blazars, and are often found to evolve negatively, if at all, in AGN surveys (Ch. 2, see e.g. Ajello et al. 2009). We find, using our derived space densities of this population, the diffuse neutrino flux is fully dominated by the local epoch ($0 < z < 1$) and rapidly decreases with increasing redshift (Fig. 4.15). This reflects the local dominance of BL Lac sources over FSRQs when considering the total blazar population.

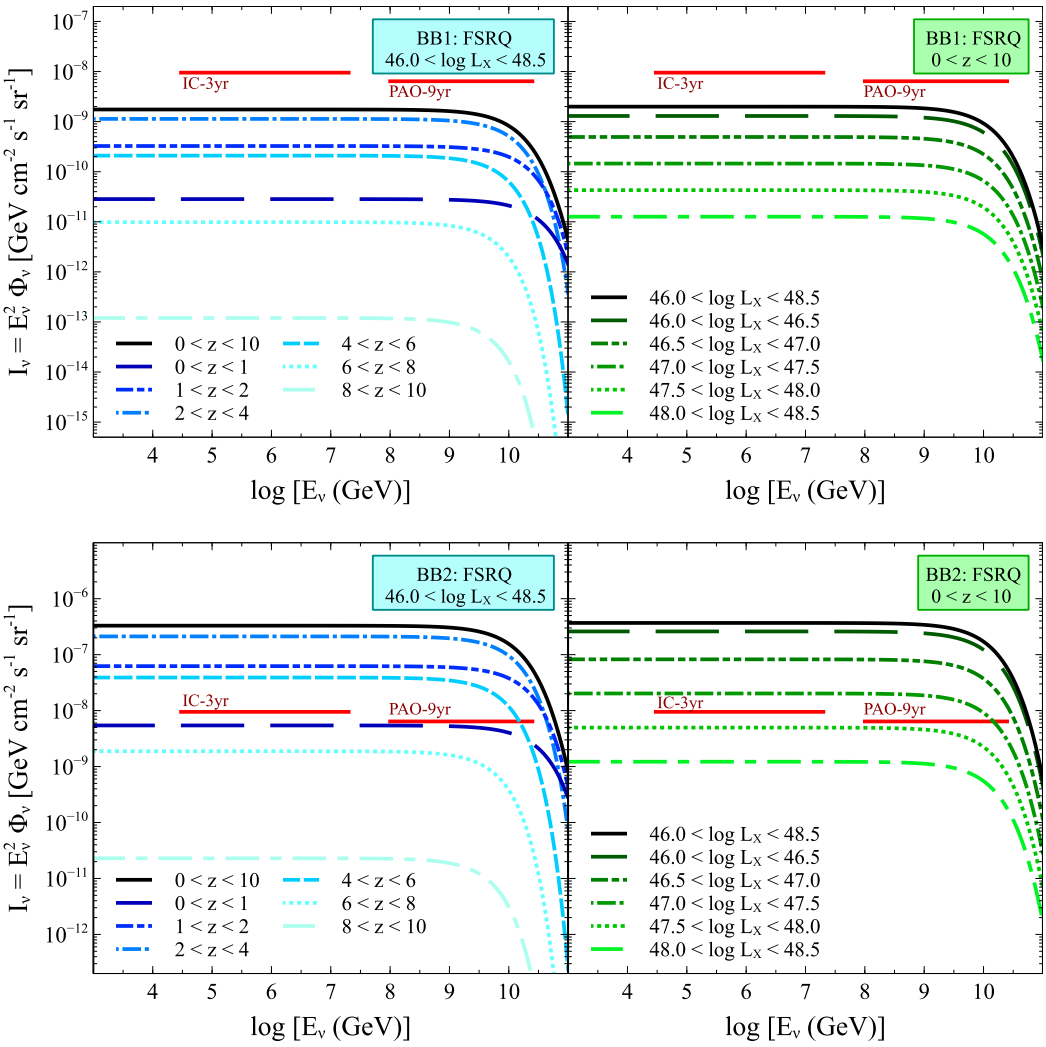

Fig. 4.14: Contribution to the diffuse neutrino energy spectrum from FSRQs, expected from the BB model calculations. The total diffuse flux from the population is represented by the black line. The spectra are compared with experimental limits set by *IceCube* and PAO. The upper panels give the results using the BB1 scaling model (Eqn. 4.49), whereas the lower panels correspond to the BB2 (Eqn. 4.54) calculations. *Left:* Diffuse flux contributions from FSRQs at cosmological epochs. Each spectral contribution is evaluated over the full range of luminosities. *Right:* Diffuse flux contributions from FSRQs in bins of X-ray source luminosity, evaluated over the full redshift range.

Due to the low-luminosity nature of the population, it is dominated by the faintest of the luminosity bins, with decreasing intensity towards higher luminosity. The spread is small in terms of the contribution from the luminosity bins, and more so when applying the BB1 scaling model rather than the BB2 model. In both models the BL Lac population produce a neutrino

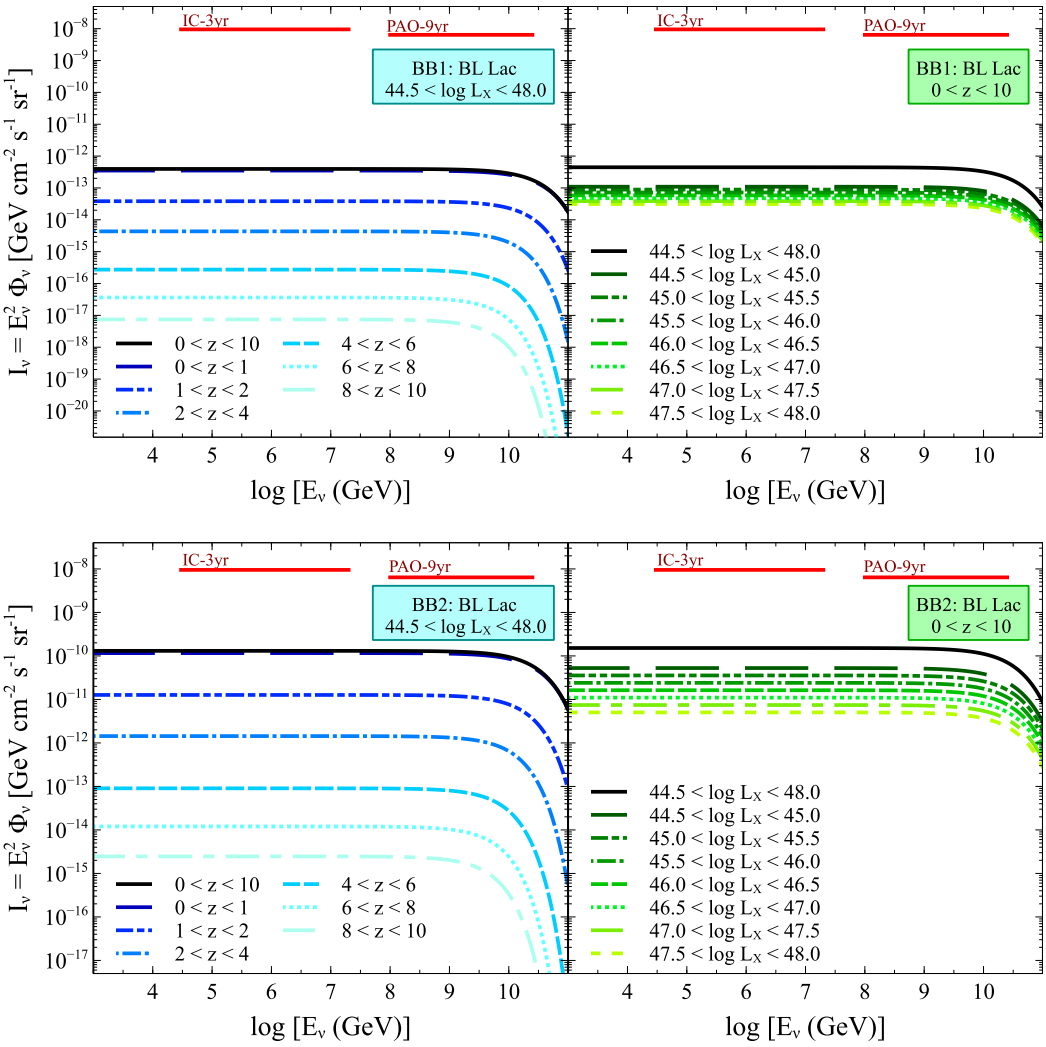

Fig. 4.15: Contribution to the diffuse neutrino energy spectrum from BL Lacs, expected from the BB model calculations. The total diffuse flux from the population is represented by the black line. The spectra are compared with experimental limits set by *IceCube* and PAO. The upper panels give the results using the BB1 scaling model (Eqn. 4.49), whereas the lower panels correspond to the BB2 (Eqn. 4.54) calculations. *Left:* Diffuse flux contributions from BL Lacs at cosmological epochs. Each spectral contribution is evaluated over the full range of luminosities. *Right:* Diffuse flux contributions from BL Lacs in bins of X-ray source luminosity, evaluated over the full redshift range.

flux below the *IceCube* flux limit, hence it is the only population that can be considered a possible neutrino machine from the BB model analysis, regardless of scaling model applied. Though the BL Lacs are the most abundant of the blazar population, the BB model predictions show that the FSRQ population contributes far more to the diffuse neutrino flux background. This reflects the

scaling model where we assume that brighter AGN produce neutrinos at a higher rate.

4.3 Cosmological Diffuse Neutrino Flux Results

The resultant energy spectra obtained from the KT model analysis is shown in Fig. 4.16, and the results from the BB model calculations are summarised in Fig. 4.17. For each AGN population the total diffuse neutrino spectrum derived from the redshift analysis agrees with that from the luminosity analysis, as is illustrated in the figures. For each population we see that the energy spectra derived from the luminosity analysis trace the redshift derived spectra, hence we know that the two methods of calculation agree. The total flux for each AGN population is compared with the *IceCube* and PAO flux limits, as was done in the individual plots.

We find that the KT model suggests all AGN populations are rejected as possible neutrino producers. Our calculations show that the model overestimates the resultant flux levels compared to the flux limits. From the individual bins, we found that nearly no single contribution fell below the flux limits, except some of the less populated BL Lac bins (i.e. the very distant and very bright). The dominant contribution is from the most local redshifts, and intermediate to low-luminosities. The model may therefore be overestimating the neutrino flux from Cen A, carrying on the estimate to the diffuse flux prediction.

The BB model predicts significantly lower neutrino flux from the various AGN populations – up to five orders of magnitude, depending on the scaling model used. The BB1 scaling model calculations show that all blazar sources produce neutrino flux below the flux limits, although the BB2 scaling results in slightly elevated neutrino spectra which leads to excluding all AGN populations as neutrino producers, except for the BL Lac population. In both model analyses the radio galaxy populations may be excluded as a possible origin of high-energy neutrinos.

The difference between the three resulting spectrum calculations show that the scaling relation between the X-ray source luminosity and the neutrino

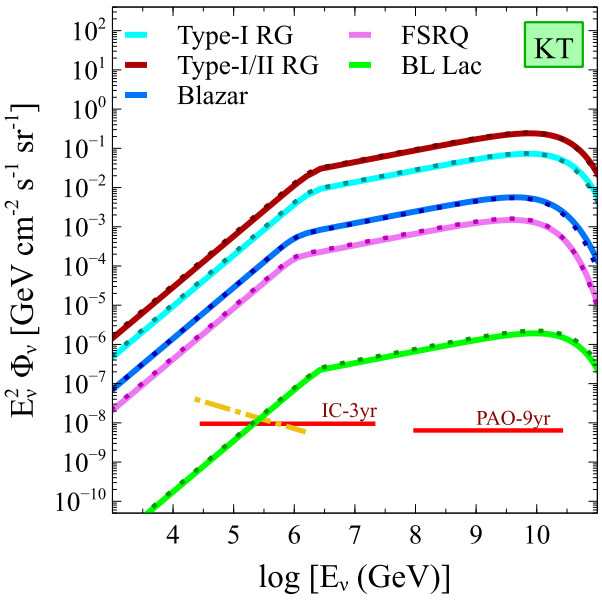

Fig. 4.16: The total diffuse neutrino flux from all AGN populations considered. The solid lines represent the total flux calculated from the redshift analysis, whereas the overplotted dotted lines represent the calculated flux from the luminosity analysis. The spectra are compared with experimental limits set by *IceCube* and PAO. The KT model overestimates the flux from all populations. The dash-dotted line corresponds to the *IceCube* best-fit diffuse neutrino spectrum (Aartsen et al. 2015b), given in Eqn. 1.58.

luminosity is crucial. The three scalings in the KT, BB1 and BB2 models gave three widely different reference source luminosities; the Cen A luminosity $L_{\rm X}^{\rm KT} = 4.8 \times 10^{41}$ erg s^{-1}, $L_{\rm X}^{\rm BB1} = 3.9 \times 10^{44}$ erg s^{-1}, and $L_{\rm X}^{\rm BB2} = 10^{43}$ erg s^{-1} respectively. Furthermore, the KT scaling model used a linear relation whereas the BB scaling models used power laws of indices 1.43 (BB1) and 1.27 (BB2). This scaling affects the neutrino production efficiency of AGN brighter and fainter than the respective single-source X-ray luminosity, evaluated at a given redshift, as shown in Fig. 4.18.

Overall the BB model prescription produces a lower neutrino flux than that of the KT model. The scaling models show that that of the BB1 calculations favours the bright over the low-luminosity sources. This trend is weaker in the BB2 model, and the KT scaling favours the fainter sources.

In the case of the KT model, which assumes Cen A as a representative of a population of AGN producing high-energy neutrinos, the luminosity scaling

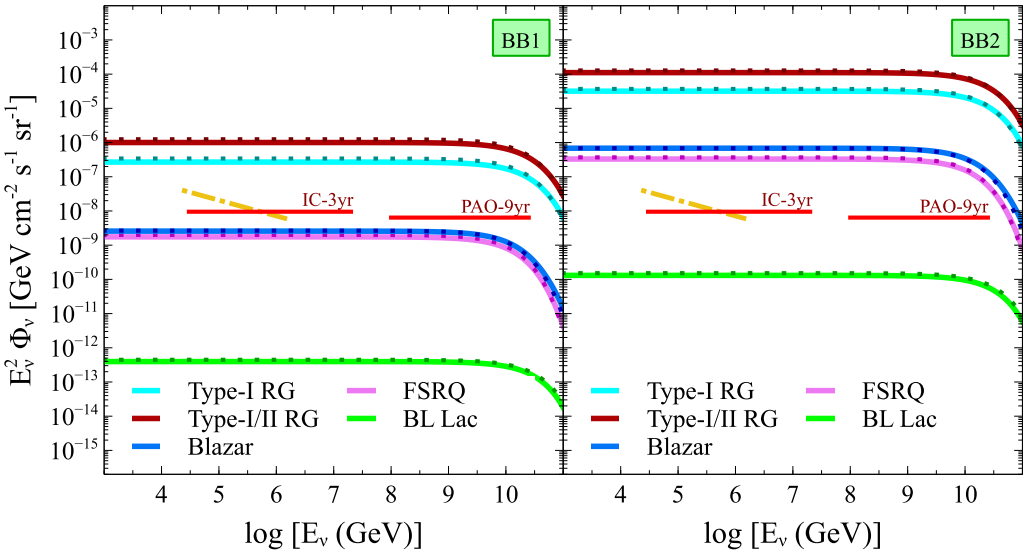

Fig. 4.17: The total diffuse neutrino flux from all AGN populations considered. The solid lines represent the total flux calculated from the redshift analysis, whereas the overplotted dotted lines represent the calculated flux from the luminosity analysis. The spectra are compared with experimental limits set by *IceCube* and PAO. We find that the left hand BB1 model produces neutrino energy spectra significantly more consistent with the *IceCube* limit, with the entire blazar population as possible neutrino producers. The BB2 model predicts that BL Lacs are considered efficient neutrino machines consistent with the flux limit. The dash-dotted line corresponds to the *IceCube* best-fit diffuse neutrino spectrum (Aartsen et al. 2015b), given in Eqn. 1.58.

may apply only to Cen A and not the general AGN population. If this main assumption of the model is incorrect, and Cen A is not a typical AGN producing high-energy neutrinos, the calculations show that Cen A may be an extraordinarily efficient neutrino producing AGN, as is noted by Koers and Tinyakov (2008). Scaling the diffuse neutrino flux with the emission from Cen A will then naturally lead to an overestimate.

However, the model is based on the UHECR correlations to the vicinity of Cen A, and this link between UHECRs and neutrinos in the model may offer another incorrect assumption. The UHECR correlation with Cen A indicated the PAO observed events may have been accidental, as discussed by Lemoine and Waxman (2009). They suggest that FR-Is, and BL Lacs by extension in the AGN unification model, are incapable of accelerating protons or

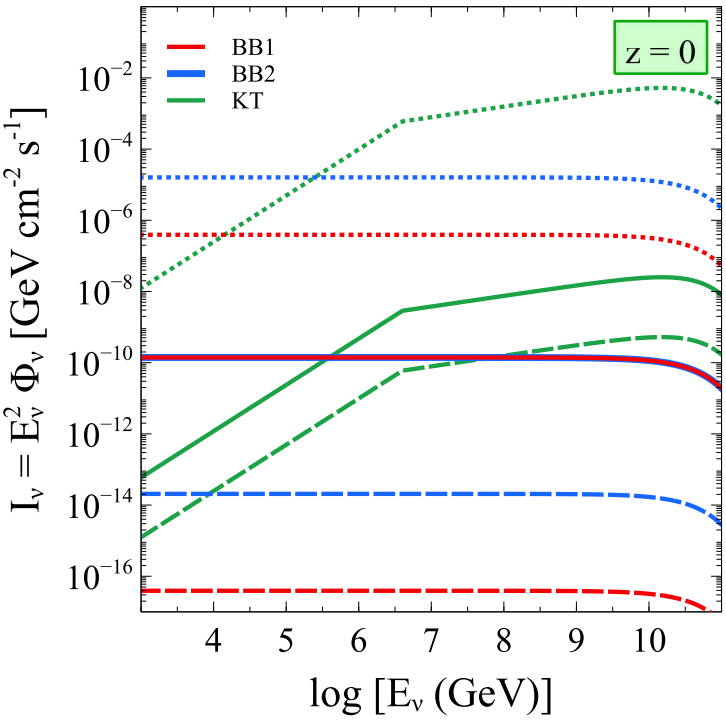

Fig. 4.18: Neutrino efficiency of KT and BB single source spectra evaluated at $z = 0$. Solid lines give the neutrino flux spectrum from the the reference source for each model. The X-ray luminosity of the BB1 source is $\log L_X = 44.59$; that of the BB2 source is $\log L_X = 43.00$; and that of KT is Cen A-*like*, with $\log L_X = 41.68$. To illustrate the scaling model, we plot the neutrino output from sources with $\log L_X = 40.00$ (dashed lines) and $\log L_X = 47.00$. The scaling of the KT model favours the faint sources. The BB1 model favours the brighter sources, as does the BB2 model, but the trend is weaker than for the BB1 model.

nuclei to necessary energies because their magnetic luminosities are too low. The model of Reynoso et al. (2011) would to some extent support the lower energy of the primary protons, and estimate the maximum proton energy in Cen A is $E_{\rm p,max}^{\rm CenA} \sim 10^7$ GeV. A source which may provide a better reference is the local M87 source, which is explored in Jacobsen and Saxton (in prep.).

We assume the XLF prescriptions derived from the X-ray surveys are correct, and the results presented in this section are calculated using the best-fit parameters derived from statistical methods in Hasinger et al. (2005); Silverman et al. (2008); Ajello et al. (2009). As seen in Fig. 3.2, we obtained evolutionary tracks from interpolating between the data points which we extracted from the relevant plots in Silverman et al. (2008). Though the lumi-

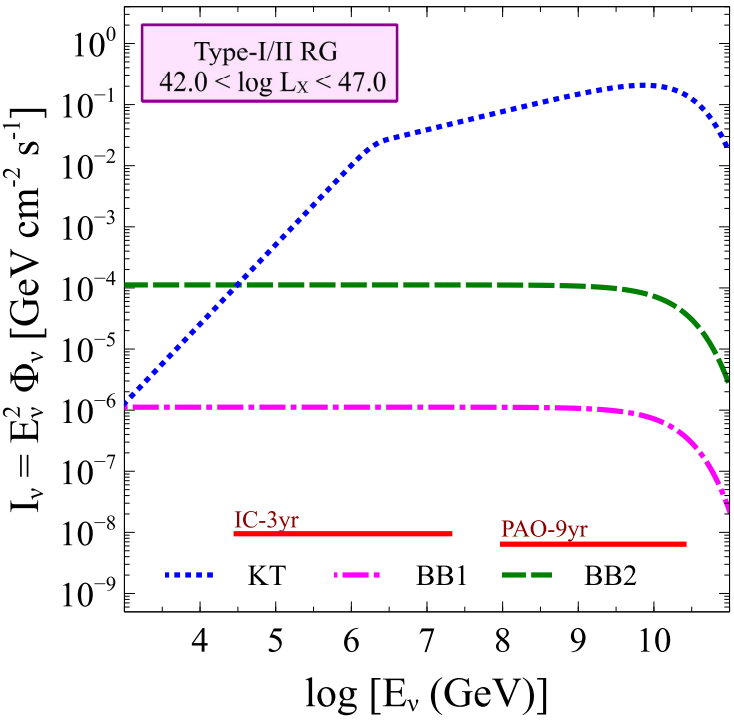

Fig. 4.19: Diffuse fluxes from Type-I and -II using the MPLE model to calculate the number densities. This model gives significantly different evolutionary tracks from the LDDE model, and are similar to the tracks from interpolating extrapolated points (see Fig. 3.16a). The total diffuse neutrino fluxes do however not differ from those derived from the number density of Type-I and -II AGN as expected; the dominant emission comes from local sources, and the local evolution of AGN is approximately the same for both XLF calculations.

nosity bin of the faintest sources cannot be derived, we see that the brighter bins give much steeper evolutionary tracks towards higher redshifts. These tracks closely follow the MPLE model tracks that we show in Fig. 3.16a. Hence, we have calculated the neutrino output with this model to see if the large discrepancy between the flux limits and neutrino flux from Type-I/II AGN is lowered. As seen in Fig. 4.19, this still does not solve the issue, as the majority of the neutrino producing sources are local, and the difference between the MPLE and LDDE prescriptions is the cutoff at higher redshifts.

If FSRQs are producing the neutrinos, this poses another issue. Kotera et al. (2010) have ruled out FR-IIs as UHECR sources, in which case cosmic ray normalisation of the neutrino spectra will not be possible.

There may however be neutrino emission from these sources if the UHECR emission is absorbed before propagating out of the source or local environment. Other avenues of normalisation must be made, e.g. the X-ray luminosities as we have done in this chapter, or a relation with γ-ray luminosity of blazars (Dermer et al. 2014).

We introduce a scale factor attributed to the fraction of the AGN population capable of producing neutrinos, so that the number of AGN which are neutrino machines is given by $\eta N_{\rm AGN}$. The scale factor may also represent a difference in the duty cycle between the neutrino and X-ray generation. This is also a plausible explanation to the overestimated spectra, as the spectra are scaled with the X-ray luminosity. In this case, the scale factor represents the fraction of the X-ray lifetime that the AGN produces neutrinos.

Whereas the scale factor introduced to the KT model spectra is, for the radio galaxy emission around seven orders of magnitude, the one for the BB model spectra is only one or two orders of magnitude. This would imply that some of the assumptions made in the calculations of the KT model are incorrect, given that the same AGN source sample was used for both sets of calculations.

In calculating the AGN populations, we took into account the fraction of "unseen", too faint or misaligned sources. Therefore, the population sizes should reflect the full population, regardless of observational biases. In the AGN unification model, the parent populations of the blazars are considered to be FR-I and FR-II radio galaxies. Hence, our estimated 10% of the AGN samples surveyed in Hasinger et al. (2005) and Silverman et al. (2008) to be considered as radio galaxies may have been too generous as the AGN were X-ray selected – i.e. tracing the disc luminosity, and was therefore blind to radio-loudness of the sources.

4.4 Conclusion

The diffuse neutrino fluxes we have calculated using the model prescription of Koers and Tinyakov (2008) and Becker and Biermann (2009) and the data from current state-of-the-art X-ray surveys of AGN exceed the observational

flux limits set by *IceCube* and PAO. This implies the following (Jacobsen et al. 2015):

- Cen A may not be a typical neutrino producing AGN, as is commonly assumed. If Cen A is exceptionally efficient in producing high-energy neutrinos the scaling of the neutrino fluxes leads to an overestimated diffuse flux, shown in our calculations (Fig. 4.16). As the models are motivated by the correlation between UHECRs and local AGN, an accidental correlation between Cen A and UHECR events would lower the estimate in the KT model.

- A universal scaling model between neutrino luminosity and the accretion power (i.e. X-ray luminosity) does not apply across all AGN classes. This requires a more complex scaling model, with a dependence on AGN types. We have used a linear (KT) and power law (BB1 and BB2) scaling model prescription, whereby the steepest scaling given by the BB1 model suppresses the contribution from the locally abundant low-luminosity sources. This model therefore enhances the neutrino contribution from the epoch coinciding with the peak activity of bright AGN ($2 < z < 4$).

- Some AGN are not neutrino sources, or their production efficiency is negligible. There may be a power threshold, above which the acceleration of charged particles is efficient, and neutrino production is allowed to occur. Low-luminosity FR-Is may not be sufficiently powerful to generate a population of particles with energies of 10^{20} eV (Lemoine and Waxman 2009). The unification of FR-Is with BL Lacs would then rule out this blazar subclass as well. Energy loss calculations of the jet of Cen A find that the maximum proton energy does not exceed 10^7 GeV (Reynoso et al. 2011), which is supported by indications of lower Lorentz factors in FR-Is than in FR-IIs (Dermer et al. 2014). FR-IIs are unfavoured as UHECR producers (Kotera et al. 2010), and if FR-IIs are the parent population of FSRQs, then a correlation between neutrino and CR emission may be weak or negligible. A highly efficient jet environment could lead to the decay of the UHECR population be-

fore escaping the confinement, implying that only neutrinos would be observable.

- Neutrino production and X-ray emission have different duty cycles. There may exist an alternating duty cycle of the baryonic and leptonic flows in the jets, or neutrino production could occur during a fraction of the X-ray lifetime of the AGN.

- It is a combination of some of the above.

The need for a more detailed neutrino model to estimate the neutrino evolution is clearly needed, for which the processes within the source may be more closely monitored. Additionally, the analysis of the BB model provided a comparison of luminosity scaling models which highlights the importance of an accurate scaling of the neutrino emission. In our case we use the link to the accretion power of the AGN nucleus through the disc (X-ray) luminosity, and find that the linear case with Cen A as a reference gives spectral emission at a much higher level than the scaling models based on the jet-disc symbiosis model.

We see from the two model (KT and BB) calculations that the spectral features of the neutrino flux can provide valuable insight to the sources they come from. With increasing detections in a more detailed observed neutrino flux spectrum may be constructed. An analysis following the above will then be able to look at the possible luminosities and cosmological epochs of the sources.

Chapter 5

Blazar Neutrino Luminosity Function

Blazars are possible neutrino machines (Ch. 4), estimated from two neutrino production models convolved with the radio-loud fraction of X-ray detected AGN, where we consider both radio galaxies and blazars. We extend the work towards the construction of a neutrino luminosity function for blazar sources (BνLF). Blazars are suitable laboratories for the study of the jet processes through their highly beamed luminosity and well-defined SEDs, allowing a further investigation of the distribution of high-energy neutrinos over several cosmological epochs and luminosity bins.

The two production models considered (Koers and Tinyakov 2008; Becker and Biermann 2009) were motivated by the correlation of nearby AGN with UHECR events detected by PAO. The observed UHECR flux was used to normalise the neutrino spectrum, assuming the inherent link between cosmic ray and neutrino emission. The neutrino spectrum follows the observed cosmic ray spectrum. The power-law cosmic ray spectrum indicates an acceleration mechanism within the jet, such as shocks; hence, the spectrum of neutrinos is derived from the relativistic proton population, and scaled by branching ratios of their interactions with radiation fields.

The construction of a BνLF requires further development of the correlation between neutrino production and jet physics, such as the γ-ray luminosity and evolution of the jet structure. In the following we discuss some general properties of the blazar population (Sec. 5.1) and establish the necessary jet physics, such as the relation between the jet power and the accretion

power of the central engine, and the energy distributions in the jet (Sec. 5.2). Using the prescription of the lepto-hadronic production model presented in Reynoso et al. (2011), we investigate variations which may appear in the jet across the blazar sequence. In this way we may determine more accurately how neutrino production is dependent on details of the jet physics. In Secs. 5.3 we discuss the relevant radiative processes in blazar jets. The energy loss processes in jets are central to the determination of the eventual neutrino flux emitted in these sources.

A number of models of hadronic emission are briefly summarised in Sec. 5.4. We use the prescription of the lepto-hadronic model (Reynoso et al. 2011) to calculate energy losses for typical sources along the blazar sequence (Sec. 5.5). This establishes a first approach to the study of neutrino production efficiencies across the blazar sequence (Jacobsen et al. in prep.).

A second approach is investigated in Sec. 5.6, where we build on the simple luminosity scaling models used in Ch. 4. Using the resultant single-source neutrino spectra calculated for Cen A in Reynoso et al. (2011), we invoke scaling models with a parameter $\eta \neq 1$, including dependencies on redshift. We present the results of this study in Sec. 5.7.

5.1 General properties of the blazar population

Variations in neutrino production efficiencies across the blazar sources can be investigated considering trends in the properties of the blazar sub-classes. The blazar sequence is an observed trend in the emission of blazar sources, giving rise to a SED classification scheme (see Sec. 2.1). The shape of the SED gives clues into the processes within the jet, and is characterised by two prominent peaks (see Fig. 2.4). At lower energies it peaks in the radio, due to synchrotron emission of relativistic electrons travelling in the jet magnetic field. The high-energy peak is prominent in γ-rays, and is either of leptonic origin (through inverse Compton scattering on relativistic electrons), or hadronic in origin (through the decay of neutral pions).

As described in Sec. 2.1, both the synchrotron peak and the γ-ray peak shift to lower energies along the sequence (HBL towards FSRQ). The high-

energy peak in the γ-ray band is found to increasingly dominate over the low-energy peak in the SED with increasing source luminosity, as the γ-ray luminosity is a tracer of the bolometric luminosity.

Each of the blazar populations along the sequence are furthermore seen to vary in both luminosity and cosmological evolution. These evolutions are highlighted in estimates of the space density for sources along the sequence (Ajello et al. 2012, 2014, see also Sec. 3.5).

Setting constraints on neutrino production in AGN jets using the properties described across the blazar sequence will therefore indicate the evolution of the high-energy neutrinos, and therefore also shed light on the blazar population, and by extension the radio-loud AGN population. The jet composition is unknown, and neutrinos are therefore prime candidates for its determination, as neutrino emission implies a hadronic origin.

5.2 Jet Power

The AGN emission is driven by accretion onto its central supermassive black hole. If the accreting matter has non-zero angular momentum, an accretion disc may form. The conversion of rest-mass energy converted to radiation is determined by the mass accretion rate, $\dot{M}$,

$$L_{\rm rad} = \xi_{\rm rad} \dot{M}_{\rm accr} c^2 \ , \tag{5.1}$$

where the efficiency factor $\xi_{\rm rad}$ gives the fraction of converted energy, and is assumed of the order $\xi_{\rm rad} \sim 0.1$. Luminosity is therefore directly determined by the mass of the central SMBH. The Eddington luminosity is the upper limit to the radiative output by an accreting black hole, determined by the gravitational and radiative forces in hydrostatic equilibrium. Assuming hydrogen plasma, it is then given by

$$L_{\rm Edd} = \frac{4\pi \ G \ M_\bullet \ m_{\rm p} c}{\sigma_{\rm T}} \tag{5.2}$$

$$= 1.26 \times 10^{38} \left(\frac{M_\bullet}{M_\odot} \right) \ {\rm erg \ s^{-1}} \ . \tag{5.3}$$

Mass accretion - luminosity relation

$\log(M_\bullet\ [\times M_\odot])$	$\log(L_{\rm Edd}\ [{\rm erg\ s^{-1}}])$	$\dot{M}_{\rm accr}[M_\odot\ {\rm yr}^{-1}]$
6.0	44	$\sim 10^{-3}$
7.0	45	$\sim 10^{-2}$
8.0	46	$\sim 10^{-1}$
9.0	47	~ 1

Table 5.1: Mass accretion - luminosity relation. The mass of the black hole is directly linked to the luminosity of the source. The link between the mass accretion power of the central black hole is therefore correlating to the emission. See text for details.

The corresponding mass accretion rate is

$$\dot{M}_{\rm Edd} = \frac{L_{\rm Edd}}{c^2} \tag{5.4}$$

$$= 2.22 \times 10^{-9} \left(\frac{M_\bullet}{M_\odot}\right) M_\odot\ {\rm yr}^{-1}\ . \tag{5.5}$$

The relation between black hole mass and luminosity is summarised in Table 5.1. The total power generated in a radio-loud AGN will broadly be distributed to the accretion disc, the jets, and some fraction will be advected into the black hole, so that:

$$L_{\rm disc} = \xi_{\rm disc}\dot{M}_{\rm accr}c^2 \tag{5.6}$$

$$L_{\rm jet} = \xi_{\rm jet}\dot{M}_{\rm accr}c^2 \tag{5.7}$$

$$L_{\rm adv} = \xi_{\rm adv}\dot{M}_{\rm accr}c^2\ . \tag{5.8}$$

For simplicity we assume the advected component is negligible or independent of the mass accretion rate. We then have

$$L_{\rm jet} \propto L_{\rm Edd} \propto L_{\rm disc}\ , \tag{5.9}$$

and

$$L_{\rm jet} = \frac{\xi_{\rm jet}}{\xi_{\rm disc}} L_{\rm disc}\ . \tag{5.10}$$

Studies on the correlation of the jet luminosity and that of the disc have formed the foundation of the jet-disc symbiosis model (Falcke and Biermann 1995; Falcke et al. 1995). Also later studies have found correlations to

the mass accretion rate, with differences seen in blazar classes implying some variation of the accretion efficiency (e.g. Sbarrato et al. 2014, see also Ghisellini and Tavecchio (2008) and references therein).

The fraction of the kinetic power in the jet which originates in these relativistic particles is given as $L_{\rm rel} = \xi_{\rm rel} L_{\rm kin}$. Assuming a neutral jet plasma, there is one proton for each electron; however, the power carried by the two populations may be expressed by

$$\xi_{\rm e,p} = \frac{L_{\rm p}}{L_{\rm e}} \ , \tag{5.11}$$

and for a hadronic jet $\xi_{\rm e,p} > 1$ (Vila and Romero 2010).

Jet formation is commonly accredited to magnetically driven acceleration (e.g. Blandford and Payne 1982; Sauty et al. 2002; Marscher 2009; Spruit 2010). The magnetic field lines threading the accretion disc is wound up in a helix, either due to the differential rotation of the ergosphere around the black hole (e.g. Blandford and Znajek 1977) or the inner accretion disc (or both). The magnetic pressure is lowered as the field expands travelling away from the black hole, which causes magnetic stresses to accelerate the flow along the jet axis. For the jet to become relativistic, the magnetic energy density must be much larger than the rest mass energy density, and the jet is initially Poynting flux dominated (Sikora et al. 2005; Marscher 2009). Internal instabilities are driven by the current flow in the jet, heating the plasma, resulting in the conversion of Poynting flux to kinetic energy density (e.g. Hardee 2006, and references therein). The details of this transition in AGN jets are not fully understood.

The acceleration process is halted when there is equipartition between the energy densities of the kinetic and magnetic jet components. The energy density of the magnetic field is

$$U_{\rm B} = \frac{B^2}{8\pi} \ . \tag{5.12}$$

The kinetic component includes the electron and proton populations, with energy densities

$$U_i = \gamma_i m_i c^2 \ n_i \ , \tag{5.13}$$

where n_i is the number density of the particle population, and the particle energy given by $E_i = \gamma_i m_i c^2$. The power of the jet can be expressed in terms of the energy densities U_i of the kinetic and magnetic components (Ghisellini 2013) by

$$P_{\rm j} = \pi R_{\rm j}^2 \ \Gamma_{\rm j}^2 \ \beta_{\rm j} c \ (U'_{\rm B} + U'_{\rm kin}) \ , \tag{5.14}$$

in comoving jet frame, from here on assigned to primed variables. The bulk Lorentz factor and jet speed are given by $\Gamma_{\rm j}$ and $\beta_{\rm j} c$, respectively. The size of the jet is given by the radius $R_{\rm j}$.

The jet energy content therefore has both a kinetic and magnetic component, i.e.

$$L_{\rm jet} = L_{\rm kin} + L_{\rm B} \ , \tag{5.15}$$

The kinetic luminosity is given in terms of the mass loading rate in the jet, $\dot{M}_{\rm j}$,

$$L_{\rm kin} = (\Gamma_{\rm j} - 1)\dot{M}_{\rm j} c^2 \ , \tag{5.16}$$

When equipartition occurs $L_{\rm kin} = L_{\rm B}$, hence

$$L_{\rm kin} = \frac{L_{\rm jet}}{2} = \frac{\xi_{\rm jet}}{2} L_{\rm Edd} \ . \tag{5.17}$$

The launch of the jet is thought to occur at sub-pc scales, anchored in the inner accretion disc, close to the central black hole. The gravitational radius gives a length scale

$$R_{\rm g} = \frac{G M_\bullet}{c^2} \ , \tag{5.18}$$

The jet is formed no more than a hundred gravitational radii from the central SMBH (Komissarov 2011). Assuming the launch is in the region of the black hole ergosphere, Reynoso et al. (2011) takes the jet launch to occur at 50 $R_{\rm g}$. The structure of the magnetic field is initially helical; however, the current-driven instabilities in the jet will lead to a more chaotic arrangement, as the jet content transitions from being magnetically dominated to kinetically dominated.

The magnetic field strength decays with the expansion of the jet, as a ratio of the jet radius at a distance $d_{\rm j}$ to the base of the jet flow, $d_{\rm j,0}$; $R_{\rm j}/R_{\rm j,0}$. The

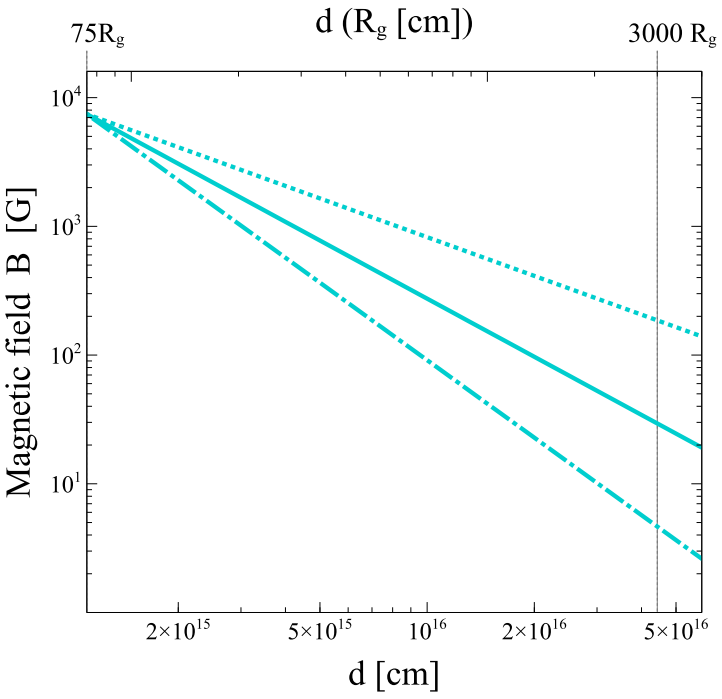

Fig. 5.1: The structure of the magnetic field is sensitive to the distance along the jet, represented by the index ϑ (Eqn. 5.19). As $1 < \vartheta < 2$, we plot the structure of the field with a low dependence on distance along the jet ($\vartheta = 1.0$, dotted) and high dependence ($\vartheta = 2.0$, dash-dotted). The solid line represents the magnetic field with a dependence following $\vartheta = 1.5$.

radius can be expressed, in terms of the radial distance d_j and the half-opening angle ω_j, as $R_\mathrm{j} = d_\mathrm{j} \tan(\omega_\mathrm{j})$. Then

$$B = B_0 \left(\frac{d_\mathrm{j}}{d_\mathrm{j,0}} \right)^{-\vartheta} . \tag{5.19}$$

In an axisymmetric structure, the toroidal component of the magnetic field decays slowly, as $B_\perp \propto d_\mathrm{j}^{-1}$, whereas the poloidal component decreases as $B_\parallel \propto d_\mathrm{j}^{-2}$ (e.g. Spruit et al. 1997; Heinz and Begelman 2000; Spruit 2010; Komissarov 2011). The structure of the magnetic field along the jet can therefore be modelled with an index $\vartheta \in (1, 2)$ (see Reynoso et al. 2011, see also Fig. 5.1).

Given equipartition the initial magnetic field strength $B_\mathrm{j,0}$ can be derived, as $U_\mathrm{B} = U_\mathrm{kin}$ in this region. The kinetic energy density can be expressed (see

Eqn. 5.13) as

$$U_{\rm kin} = \frac{L_{\rm kin}}{\pi d_{\rm j}^2 \ \beta_{\rm j} c} \ , \tag{5.20}$$

and the magnetic energy density is given in Eqn. 5.12, so that

$$B_0 = \sqrt{\frac{8 L_{\rm kin}}{d_{\rm j,0}^2 \ \beta_{\rm j} c}} \ , \tag{5.21}$$

(see also Reynoso et al. 2011). The velocity of the jet is $v_{\rm j} = \beta_{\rm j} c$.

As the jet reaches high bulk speeds (i.e. a large $\Gamma_{\rm j}$), the magnetically driven acceleration and the conversion to a kinetically dominated jet slows down. A jet can therefore have either a high energy conversion rate, or large jet speed (Spruit 2010).

Assuming an initial Lorentz factor at the point of jet launch, $\Gamma_{\rm j,0} = \Gamma_{\rm j}(d_{\rm j,0})$, the evolution of the Lorentz factor can be determined from the equipartition of the magnetic and kinetic energy density at this point. Conservation of energy gives a relation between the energy densities. At the launching point $U_{\rm kin} + U_{\rm B} = 2U_{\rm B}$. Therefore,

$$\Delta d \ \pi R_{\rm j}^2 (U_{\rm kin} + U_{\rm B}) = \Delta d \ \pi R_{\rm j,0}^2 \ 2U_{\rm B} \ . \tag{5.22}$$

Using the expressions for the magnetic jet structure (Eqn. 5.19) and the energy density of the magnetic field (Eqn. 5.12), the kinetic component is given by

$$U_{\rm kin} = \frac{B_{\rm j,0}^2}{8\pi} \left(\frac{d_{\rm j,0}}{d_{\rm j}} \right)^2 \left[2 - \left(\frac{d_{\rm j,0}}{d_{\rm j}} \right)^{2\vartheta - 2} \right] \ . \tag{5.23}$$

As the kinetic component can be described as in Eqns. 5.16 and 5.20, where

$$\frac{\Gamma_{\rm j}(\Gamma_{\rm j} - 1)}{\Gamma_{\rm j} + 1} = \frac{(B_0 R_{\rm j,0})^2}{8 \dot{M}_{\rm j} c} \left[2 - \left(\frac{d_{\rm j,0}}{d_{\rm j}} \right)^{2\vartheta - 2} \right] \tag{5.24}$$

$$\equiv \sqrt{Y_\Gamma} \ , \tag{5.25}$$

and the solution

$$\Gamma_{\rm j} = \frac{1}{3} \left(1 + \left[1 + 18 Y_\Gamma + 3\sqrt{3} \sqrt{Y_\Gamma + 11 Y_\Gamma^2 - Y_\Gamma^3} \right]^{1/3} + \frac{3 Y_\Gamma + 1}{\left[1 + 18 Y_\Gamma + 3\sqrt{3} \sqrt{Y_\Gamma + 11 Y_\Gamma^2 - Y_\Gamma^3} \right]^{1/3}} \right) \tag{5.26}$$

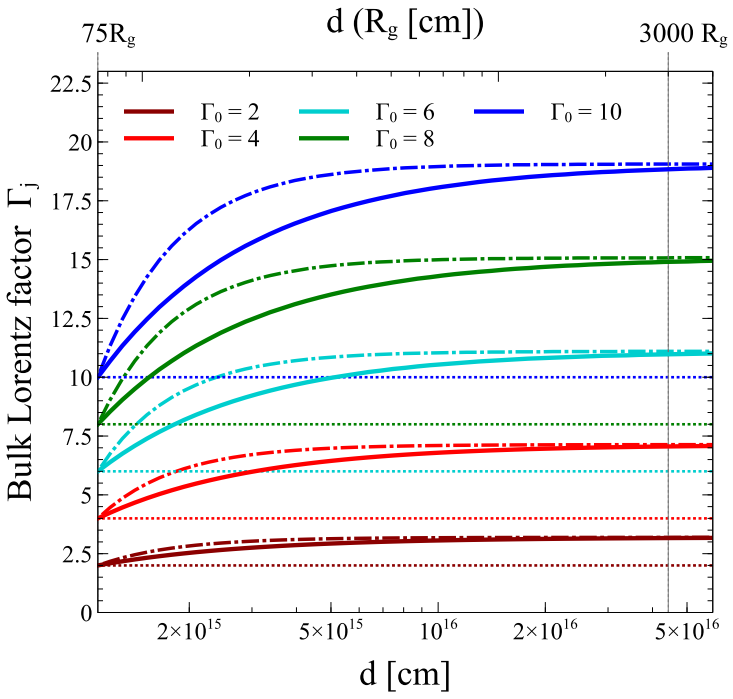

Fig. 5.2: Evolution of the bulk Lorentz factor along the jet. Assuming a typical value for the central black hole mass ($M_\bullet = 10^8\ M_\odot$), the opening angle ($\omega_\mathrm{j} = 0.05$ radians) and the location of the jet launch from the core ($d_0 = 75 R_\mathrm{g}$), we vary the initial Lorentz factor Γ_0. The evolution is much stronger for a high initial value. We also vary the dependence on jet distance of the magnetic field ($\vartheta = 1.0$, dotted; $\vartheta = 1.5$, solid; $\vartheta = 2.0$, dash-dotted). A higher index ϑ gives a much steeper increase close to the jet launch.

(Reynoso et al. 2011). The evolution of the Lorentz factor is sensitive to the initial value, Γ_0 and the magnetic field strength dependence on the distance along the jet, ϑ (Fig. 5.2). For a high initial Lorentz factor, the evolution is significantly stronger than for a low value. This may be particularly important for the behaviours of AGN jets, as the lower luminosity BL Lac sources have a smaller Lorentz factor than the bright FSRQs (e.g. Dermer et al. 2014). Varying the index for magnetic dependence shows a steep increase at smaller scales, with a flattening to produce the same Lorentz factor at larger scales, for a larger value of ϑ. However, no evolution is seen for the Lorentz factor for the minimum value of $\vartheta = 1.0$.

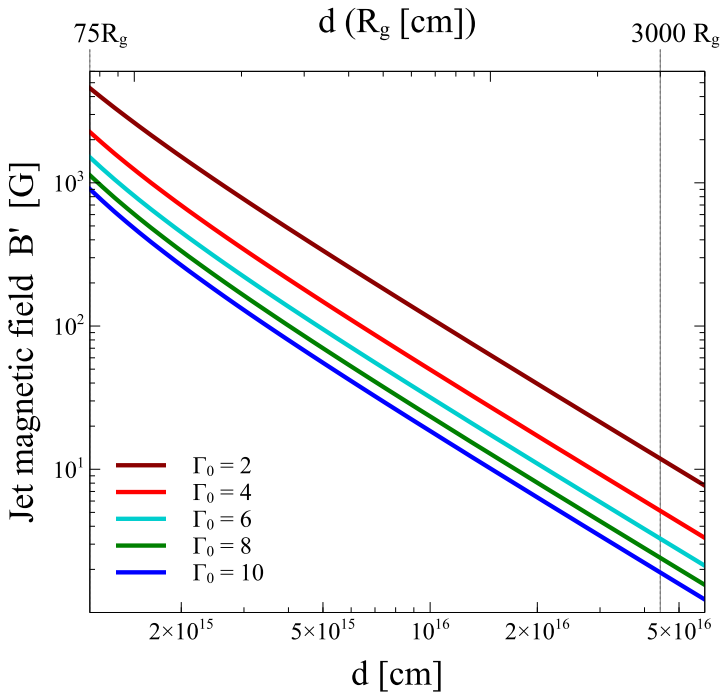

Fig. 5.3: We show the dependence on the magnetic field structure in the jet frame with the initial bulk Lorentz factor, Γ_0. A low value corresponds to a significantly stronger magnetic field than a high Lorentz factor.

The structure of the magnetic field in comoving (jet) frame is given by

$$B' = \sqrt{\frac{3}{2\Gamma_{\rm j} + 1}}\, B \tag{5.27}$$

(Heinz and Begelman 2000), where the comoving magnetic field is the root mean square of the magnetic field components, $B' = \langle B'_{\rm x'} \rangle + \langle B'_{\rm y'} \rangle + \langle B'_{\rm z'} \rangle$. The magnetic field structure is sensitive to the initial Lorentz factor, Γ_0, seen in Fig. 5.3, so that a higher Lorentz factor suppresses the strength of the field. The steepness of the magnetic field dissipation along the jet is determined by the index ϑ, seen in Fig. 5.1. As the magnetic field determines the radio power of the jet, this has consequences for the emission produced in the jet.

5.2.1 The confinement and acceleration of particles in jets

When the jet is kinetically dominated, instabilities in the jet can lead to turbulence and shock formation. Formation of standing, or moving, shocks which are observed as bright blobs (knots) due to the heated plasma interactions in

the region, allow for the creation of high-energy populations of electrons and protons.

As the turbulent jet structures and irregularities arise in a kinetically dominated environment, the location along the jet where this occurs can therefore be determined in terms of a fraction $\xi_{\rm B}$ representing the magnetic energy density in this acceleration region, to its value in the launch region (Reynoso et al. 2011). Then,

$$\xi_{\rm B} = \frac{(\Delta d\ \pi R_{\rm j,acc}^2) U_{\rm B}}{(\Delta d\ \pi R_{\rm j,0}^2) U_{\rm B,0}}\ , \tag{5.28}$$

giving

$$\xi_{\rm B} = \left(\frac{d_{\rm j,acc}}{d_{\rm j,0}}\right)^{(2-2\vartheta)}\ , \tag{5.29}$$

and the injection point to the acceleration region as

$$d_{\rm j,acc} = d_{\rm j,0}\ (\xi_{\rm B})^{1/(2-2\vartheta)} \tag{5.30}$$

The power law synchrotron spectrum implies a non-thermal distribution of electrons of $\propto E_{\rm e}^{-\rho}$, which can be explained through shock acceleration.

5.2.2 Fermi acceleration

Particle acceleration due to Fermi processes can explain the arising power-law emission from AGN jets. Energetic particles gain energy through the elastic scattering off magnetic irregularities in the jet (e.g. Bell 1978; Rieger et al. 2007). Each scattering results in a small energy gain; however, over many scatterings the average gain gives rise to a power-law energy distribution, given by

$$N(\gamma_i) \propto \gamma_i^{-\rho}\ , \tag{5.31}$$

where γ_i is the Lorentz factor for a particle i when evaluated in the jet frame. The Fermi processes lead to a power-law distribution of the accelerated particles, and the details of the acceleration process determine the acceleration timescale.

Diffusive, or first order Fermi, acceleration, involves a non-relativistic shock wave moving through the jet plasma. The shock speed is then $v_{\rm s} \ll c$, and the energy gain is dependent on the shock compression factor $\mathbb{V}$. The

particle is confined by scattering off self-generated Alfvén waves, thus crossing the shock front upstream and downstream, and for each crossing, gaining energy (Bell 1978). The energy gain of a particle crossing the shock back and forth many times is

$$\Delta E \propto E_0 \beta \ , \tag{5.32}$$

where $\beta = v/c$, and the velocity $v = v_1 - v_2$, the velocities before and after the the shock front, and $\mathbb{V} = v_1/v_2$.

This acceleration mechanism explains the observed knot features in AGN jets, which are identified as regions where shock fronts exist. In strong shocks the resulting particle distribution obtains a power-law spectrum with $\rho \sim 2$, which is consistent with the high-energy synchrotron emission, as well as the observed cosmic ray spectrum. It cannot, however, explain the extended non-thermal emission seen in AGN (Rieger et al. 2007).

Second order Fermi acceleration is a stochastic process, where particles scatters off irregularities in magnetic clouds. The clouds move with speeds $\beta \ll c$, and the acceleration is given by the energy gain from repeated scattering,

$$\Delta E \propto E_0 \beta^2 \ . \tag{5.33}$$

The acceleration is therefore slower, as $\beta \ll 1$, but continuous, and gives a power-law distribution which is flatter than that arising from first order Fermi processes, i.e. $\rho < 2$ (Rieger et al. 2007).

5.3 Radiative processes in blazar jets

In Sec. 1.1.4 we discussed hadronic processes, which lead to the production of neutrinos. In the following we outline radiative processes particularly important in astrophysical jets responsible for high-energy emission. In Fig. 4.1 the various sources of the observed (and assumed) emission are illustrated. From the accretion disc thermal UV photons are produced. In the torus, these will be re-scattered by dust and gas to infra-red frequencies. Accretion disc photons upscattered in the hot corona by electrons produce X-ray emission. From the broad line region (BLR) a population of optical photons are emitted. In the jet, relativistic electrons will accelerate in the magnetic

field producing radio-emission, which dominates the lower energy peak in the blazar SED. Either through synchrotron self-Compton (SSC) or inverse Compton (IC) mechanisms, the photons are upscattered to X-ray and γ-ray, and are observed as the leptonic high-energy signal dominating the γ-ray peak in the blazar SED.

In hadronic models, the interactions of relativistic protons will produce a comparable, if not greater signal at these highest energies through proton-photon (pγ) interactions, with either the internal photon populations in the jet, or the external populations, such as direct accretion disc photons, the coronal photons, or from the torus or BLR. In addition there are proton-proton (pp) interactions, whereby the energetic protons interact with ambient cold matter fields in the jet or in the surrounding environment. In both cases, the emission of cosmic ray (CR) protons, pions and neutrons is expected, whereby the pions and neutrons will lead to the emission of γ-ray photons and neutrinos, and CR-protons.

As discussed in Sec. 1.2.3, the maximum attainable energy in the jet is dependent on the balance of heating and cooling processes. In order to determine the eventual emission of high-energy particles, all energy loss rates must therefore be accounted for.

5.3.1 Synchrotron radiation

Synchrotron emission is produced when relativistic charged particles are accelerated in magnetic fields, as they gyrate around the field lines. This is illustrated in Fig. 5.4. An electron or positron, with energy $E_{\rm e} = \gamma_{\rm e} m_{\rm e} c^2$, travels with uniform circular motion, with a pitch angle $\alpha_{\rm p}$. As the magnitude of acceleration is constant, and its direction is perpendicular to the velocity vector, the particle thus follows a helical path along the magnetic field line. The emission is beamed in the direction of motion in a cone with half angle $\omega_{\rm j} \approx \gamma_{\rm e}^{-1}$. The gyrating frequency is then given by

$$f_{\rm B} = \frac{q_{\rm e} B}{\gamma_{\rm e} m_{\rm e} c} \ . \tag{5.34}$$

The power emitted by a single particle is given per unit frequency as

$$P_{\rm synch}(f) = \frac{\sqrt{3} q_{\rm e}^3 B}{m_{\rm e} c^2} F(\eta) \ , \tag{5.35}$$

where $\eta = f/f_{\rm c}$, and the critical frequency

$$f_{\rm c} = \frac{3q_{\rm e}B}{4\pi m_{\rm e}c}\gamma_{\rm e} \ . \tag{5.36}$$

The synchrotron spectrum is approximated by a power law with spectral index α, so that $P(f) \propto f^{-\alpha}$. The function $F(\eta)$ is the integration of the modified Bessel function of the second kind, $K_{5/3}(\zeta)$,

$$F(\eta) = \eta \int_{\eta}^{\infty} d\zeta K_{5/3}(\zeta) \ . \tag{5.37}$$

This function can be approximated for small and large η, following

$$F(\eta) \approx \frac{4\pi}{\sqrt{3}\Gamma(\frac{1}{3})}\left(\frac{\eta}{2}\right)^{1/3} \quad \eta \ll 1 \tag{5.38}$$

$$F(\eta) \approx \left(\frac{\pi}{2}\right)^{1/2} e^{-\eta}\, \eta^{1/2} \quad \eta \gg 1 \ . \tag{5.39}$$

The synchrotron spectrum then peaks at $\eta \approx 0.29$ (Blumenthal and Gould 1970; Rybicki and Lightman 1979).

For a power law energy distribution of relativistic particles given by

$$N(E) = N_0 E^{-\rho} \ , \tag{5.40}$$

with the particle energy distribution index ρ, the total power radiated per unit frequency and unit volume is then the integral of the particle distribution (Eqn. 5.40) times the power emitted by a single particle (Eqn. 5.35). The total power radiated is then

$$P_{\rm synch}(f) \propto f^{-(\rho-1)/2} \ , \tag{5.41}$$

and thus the particle energy distribution index is related to the spectral index of the synchrotron emission spectrum by $\alpha = (\rho - 1)/2$.

The energy loss rate due to synchrotron emission for a given relativistic particle i (i.e. $\beta \approx 1$) is given by

$$t_{\rm synch}^{-1} = \frac{4}{3}\frac{\sigma_{\rm T}c}{m_{\rm e}c^2}\left(\frac{m_{\rm e}}{m_i}\right)^3 U_{\rm B}\gamma_i \ , \tag{5.42}$$

where

$$t_{\rm synch}^{-1} = \left|-\frac{dE}{dt}\right|\frac{1}{E} \ . \tag{5.43}$$

Thus, for electrons, synchrotron radiation is an efficient loss mechanism. However for a population of charged particles such as protons, the cooling rate is slower by a factor dictated by $(m_e/m_i)^3$ (Begelman et al. 1990).

The associated absorption process to synchrotron emission is called synchrotron self-absorption (SSA). In this process the synchrotron photons that are emitted in the magnetic field are absorbed by the same primary population (e.g. electrons). The SSA absorption coefficient is given by

$$\kappa_{\rm SSA} = -\frac{(\rho+2)c^2}{8\pi f^2}\int_{\rm E_i}^{\infty} P_{\rm synch}(f,E_i)\frac{N(E_i)}{E_i} \tag{5.44}$$

for a particle population with a power law distribution, given in Eqn. 5.40. This gives

$$\kappa_{\rm SSA} \propto f^{-(\rho+4)/2} \ . \tag{5.45}$$

The emission spectrum is then worked out by considering the radiative transfer equation,

$$\frac{d\mathbb{I}_f}{\kappa_{\rm SSA} d\ell} = \mathbb{I}_f + S_f \ , \tag{5.46}$$

giving the emission in terms of the source function S_f and optical depth $\tau_{\rm SSA}$,

$$\mathbb{I}_f = S_f(1-e^{-\tau_{\rm SSA}}) \ , \tag{5.47}$$

if we neglect the background. The optical depth for the SSA process is given by

$$\tau_{\rm SSA} = \int_{\ell} d\ell \ \kappa_{\rm SSA} \ . \tag{5.48}$$

Then, optical thickness will define the form of the synchrotron spectrum:

$$\mathbb{I}_f = \begin{cases} S_f \propto f^{5/2} & \tau_{SSA} > 1 \\ \tau_{\rm SSA} S_f \propto f^{-(\rho-1)/2} & \tau_{SSA} \ll 1 \ , \end{cases} \tag{5.49}$$

which is suppressed in the low-energy region, due to the SSA process.

5.3.2 Inverse Compton scattering

The scattering of photons off charged particles can change the energy of the participating particles. Compton scattering is the scattering of a photon off a charged particle, for which the incident photon has greater energy. The scattered photon thus loses energy to the scattering particle. In the low energy

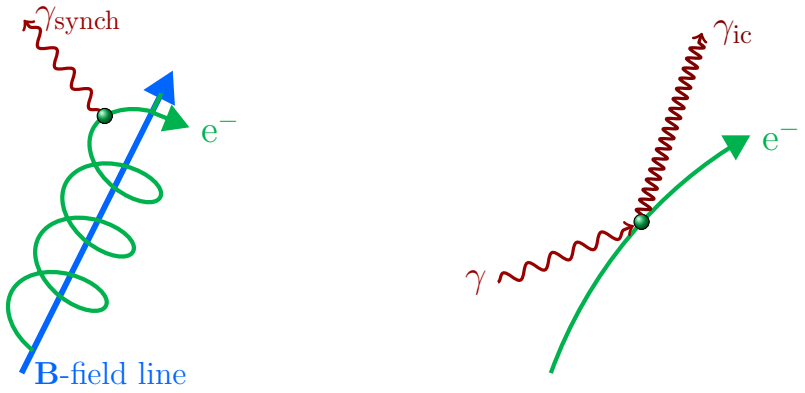

Fig. 5.4: Schematic illustration of synchrotron radiation and inverse Compton scattering. *Left:* Synchrotron emission emitted as the electron is travelling in the magnetic field. *Right:* A high-energy photon emitted in the inverse Compton scattering of a lower energy photon on the electron.

limit, this scattering process reduces to the classical Thomson scattering. If the charged particle, e.g. an electron, has sufficiently greater energy than the incident photon, the scattered photon gains energy from the electron through the inverse Compton scattering process, illustrated in Fig. 5.4. The differential cross section of the scattering is given by the Klein-Nishina formula,

$$\frac{d\sigma_{\rm KN}}{d\Omega} = \frac{R_{\rm e}^2}{2}\left(\frac{E_\gamma}{\varepsilon}\right)^2\left[\frac{\varepsilon}{E_\gamma}+\frac{E_\gamma}{\varepsilon}-\sin^2(\theta)\right] , \tag{5.50}$$

where the energy of the incident photon is ε, the energy of the scattered photon is given by E_γ, and the angle between the momenta of the two photons in the scattering is given by θ. The total cross section is then

$$\sigma_{\rm KN} = 2\pi R_{\rm e}^2\left[\frac{1+\varkappa_0}{\varkappa_0^3}\left(\frac{2\varkappa_0(1+\varkappa_0)}{1+2\varkappa_0}-\ln(1+2\varkappa_0)\right)\right. \tag{5.51}$$

$$\left. +\frac{1}{2\varkappa_0}\ln(1+2\varkappa_0)-\frac{1+3\varkappa_0}{(1+2\varkappa_0)^2}\right] , \tag{5.52}$$

with $\varkappa_0 = \varepsilon/m_{\rm e}c^2$ (Blumenthal and Gould 1970; Tucker 1975). In the non-relativistic limit, the cross section reduces to the Thomson cross section, with $\varkappa_0 \ll 1$:

$$\sigma_{\rm KN} \approx \sigma_{\rm T}(1-2\varkappa_0+\frac{26}{5}\varkappa_0^2+\dots) , \tag{5.53}$$

where the the Thomson cross section is $\sigma_{\rm T} = 8\pi R_{\rm e}^2/3$, and $E_\gamma \sim \varepsilon$. In the ultra-relativistic limit, with $\varkappa_0 \gg 1$, the cross section is given by

$$\sigma_{\rm KN} \approx \frac{3}{8}\frac{\sigma_{\rm T}}{\varkappa_0}\left[\ln(2\varkappa_0)+\frac{1}{2}\right] . \tag{5.54}$$

For an isotropic photon field with differential number density

$$dn_\gamma = \frac{dN_\gamma}{dV} = n(\varepsilon)d\varepsilon \ , \tag{5.55}$$

the energy density is given by

$$U_{rad} \equiv \int \varepsilon n(\varepsilon)\ d\varepsilon \ . \tag{5.56}$$

If scattered on a relativistic population of electrons, $\varepsilon \ll m_\mathrm{e}c^2$ in the electron frame of reference, the effects of the relativistic limit can be neglected, and the cross section is given by Eqn. 5.53.

The inverse Compton spectrum per electron is given by

$$\frac{dN_\gamma}{dtdE_\gamma} = \frac{3\sigma_\mathrm{T}c}{4\gamma_\mathrm{e}}\frac{n(\varepsilon)d\varepsilon}{\varepsilon}\mathbb{F}(q) \ , \tag{5.57}$$

with the function

$$\mathbb{F}(q) = 2q\ln(q) + (1+2q)(1-q) + \frac{1}{2}\frac{(\varkappa q)^2}{1+\varkappa q}(1-q) \ , \tag{5.58}$$

where

$$q = \frac{E_\gamma}{m_\mathrm{e}c^2\varkappa(1-\frac{E_\gamma}{m_\mathrm{e}c^2})} \ , \tag{5.59}$$

and

$$\varkappa = \frac{4\varepsilon\gamma_\mathrm{e}}{m_\mathrm{e}c^2} \ . \tag{5.60}$$

which determines the scattering regime. For $\varkappa \ll 1$, the domain is in the Thomson regime, whereas for $\varkappa \gg 1$ the Klein-Nishina limit applies. These equations are valid for all regimes as long as $\gamma_\mathrm{e} \gg 1$ (Blumenthal and Gould 1970).

The energy loss rate is

$$-\frac{dE_\mathrm{e}}{dt} = \int (E_\gamma - \varepsilon)\frac{dN_\gamma}{dtdE_\gamma}dE_\gamma \ , \tag{5.61}$$

hence, the inverse Compton cooling rate is

$$t_\mathrm{IC}^{-1} = \frac{3c\sigma_\mathrm{T}(m_\mathrm{e}c^2)^2}{4E_\mathrm{e}^3}\int_{\varepsilon_\mathrm{min}}^{E_\mathrm{e}} d\varepsilon\frac{n(\varepsilon)}{\varepsilon}\int_\varepsilon^{\frac{\varkappa E_\mathrm{e}}{\varkappa+1}} dE_\gamma\mathbb{F}(q)(E_\gamma-\varepsilon) \ . \tag{5.62}$$

The limits of the scattered photon is determined from considering the kinematics of the process,

$$\varepsilon \geqslant E_\gamma \geqslant \frac{\varkappa}{1+\varkappa}\ \gamma_\mathrm{e}m_\mathrm{e}c^2 \ , \tag{5.63}$$

If the target photon field is synchrotron radiation produced by the same electron population interacting in the surrounding magnetic field, this particular case of inverse Compton scattering is called synchrotron self-Compton (SSC).

5.3.3 Free-free (bremsstrahlung) radiation

Free-free (bremsstrahlung) emission is radiation due to the deceleration of a charged particle when interacting with the Coulomb field of another charged particle or ion. It is often called free-free radiation if the incoming particle is free and is not being captured upon interaction. The kinetic energy lost in the deceleration is emitted as a photon, and electrons are particularly efficient radiators as the acceleration is inversely proportional to the mass of the particle. The bremsstrahlung energy spectrum is found by convolving the emission from a single electron with the velocity distribution of the electron population. In addition a quantum mechanical correction factor must be included. In non-relativistic cases, this factor is ~ 1; however, it will be significant when treating relativistic populations, as the photons emitted will be of similar energies to the incident particle.

For an electron population with a Maxwell-Boltzman distribution of velocities, the emission is thermal. The total power per unit volume and frequency is then

$$\begin{aligned}\frac{dP}{dV\,df} &= \left(\frac{2\pi}{3kTm_{\rm e}}\right)^{1/2}\frac{2^5\pi q_{\rm e}^6}{3m_{\rm e}c^3}Z^2 n_{\rm e} n_i e^{hf/kT}\overline{G}_{\rm bs}(T,f) \\ &= 6.842\times10^{-38}T^{-1/2}Z^2 n_{\rm e} n_i \overline{G}_{\rm bs}(T,f)\ . \end{aligned} \tag{5.64}$$

where the number densities for the electron population and the ionised plasma is given by $n_{\rm e}$ and n_i, respectively, and since a fully ionised plasma is assumed, the atomic proton number $Z = 1$. The Gaunt factor $\overline{G}_{\rm bs}(T,f)$ is averaged over all velocities. Integrating over frequency then gives the power per unit volume,

$$\begin{aligned}\left.\frac{dP}{dV}\right|_{\rm therm} &= \left(\frac{2\pi kT}{3m_{\rm e}}\right)^{1/2}\frac{2^5\pi q_{\rm e}^6}{3hm_{\rm e}c^3}n_{\rm e} n_i \overline{\overline{G}}_{\rm bs}(T) \\ &= 1.442\times10^{-27}T^{1/2} n_{\rm e} n_i \overline{\overline{G}}_{\rm bs}(T)\ . \end{aligned} \tag{5.65}$$

The Gaunt factor is now frequency and velocity averaged, and lies between 1 and 5, and a value of 1.2 gives reasonably accurate results

(Rybicki and Lightman 1979).

Relativistic bremsstrahlung radiation can be calculated through the Weizsäker-Williams method of virtual quanta. This method considers the emission process in the electron rest frame, so that a virtual photon of the Coulomb field is Compton scattered off the electron. In the observers frame, the resulting emission is seen as bremsstrahlung radiation,

$$\left.\frac{dP}{dV}\right|_{\rm rel} = 1.442 \times 10^{-27} T^{1/2} n_{\rm e} n_i (1 + 4.4 \times 10^{-10} T) \overline{\overline{G}}_{\rm bs}(T) \ , \tag{5.66}$$

for a thermal distribution of a population of electrons where $kT > m_{\rm e}c^2$. The emission is therefore modified to include a relativistic correction (Blumenthal and Gould 1970; Novikov and Thorne 1973; Rybicki and Lightman 1979).

For a power law distribution of ultra-relativistic electrons, i.e.

$$N(E) = N_0 E^{-\rho} \ , \tag{5.67}$$

the bremsstrahlung emission is non-thermal, and the emission spectrum follows the power law distribution of the electrons, integrating over energy

$$\left.\frac{dP}{dV}\right|_{\rm PL} \propto f^{-\rho+1} \ , \tag{5.68}$$

however softer by one power. The radiative loss rate due to bremsstrahlung is then given by

$$t_{\rm bs}^{-1} = 4 R_{\rm e}^2 \alpha_{\rm FS} c n_i \overline{\overline{G}}_{\rm bs} \ , \tag{5.69}$$

with the Gaunt factor in a fully ionised plasma (Longair 1994),

$$\overline{\overline{G}}_{\rm bs} = \ln(2\gamma_{\rm e}) - \frac{1}{3} \ . \tag{5.70}$$

5.3.4 Energy loss rates of hadronic interactions

The details of the pp- and pγ- interactions were discussed in Sec. 1.1.4. The energy loss rates of hadronic processes are found by considering the cross sections of the interactions. The total cross section of the interaction can be separated into an elastic and an inelastic part. However, only the inelastic scattering process involves the production of secondaries, due to a large enough energy transfer for the quarks and gluons to interact (Koers et al. 2006).

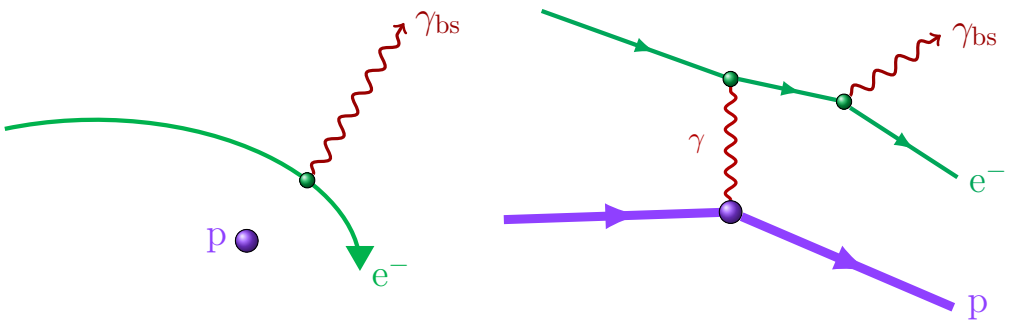

Fig. 5.5: Illustration of the bremsstrahlung mechanism. *Left:* The electron decelerates as it interacts with the Coulomb field of the proton (or ion), and emits bremsstrahlung radiation. *Right:* The method of virtual quanta, where a virtual photon of the proton field is Compton scattered off the electron in the electron rest frame. In the observer frame the emission is seen as bremsstrahlung radiation.

The inelastic cross section for the pp-interaction is approximated to

$$\sigma_{\rm pp}(E_{\rm p}) = (34.3 + 1.88\mathbb{L} + 0.25\mathbb{L}^2) \times \left[1 - \left(\frac{E_{\rm th}}{E_{\rm p}}\right)^4\right]^2 \times 10^{-25}\ {\rm cm}^2 \qquad (5.71)$$

(Kelner et al. 2006), with $\mathbb{L} = \ln(E_{\rm p}/{\rm TeV})$, for an incident proton with energy $E_{\rm p}$. The energy loss rate of the interaction is

$$t_{\rm pp}^{-1} = n_{\rm p} c \sigma_{\rm pp} K_{\rm pp}\ , \qquad (5.72)$$

with the density of the proton target field, n_p, and the fractional energy loss per interaction given in the inelasticity coefficient, $K_{\rm pp} = 0.5$ (Begelman et al. 1990).

The inelastic collision of an energetic proton with a photon field can be the source of neutrinos through photomeson production. The cross section of this interaction is approximated in Atoyan and Dermer (2001) to the sum of a simple step function to account for single- and multi-pion production channels, as a function of photon energy in the proton rest frame, i.e. The single-pion cross section component is then

$$\sigma_{{\rm p}\gamma,1}(\varepsilon^*) = \begin{cases} 3.4 \times 10^{-30}\ {\rm cm}^2 & 200\ {\rm MeV} \leqslant \varepsilon^* \leqslant 500\ {\rm MeV} \\ 0 & {\rm otherwise}\ , \end{cases} \qquad (5.73)$$

and the multi-pion part given by

$$\sigma_{\mathrm{p}\gamma,2}(\varepsilon^*) = 1.2 \times 10^{-30}\ \mathrm{cm}^2 \quad 500\ \mathrm{MeV} \leqslant \varepsilon^* \ . \tag{5.74}$$

The inelasticity coefficient for the interaction is then $K_{\mathrm{p}\gamma} = 0.2$ in the single-pion energy range, and $K_{\mathrm{p}\gamma} = 0.6$ for energies corresponding to the multi-pion production channel, shown in Eqns. 5.73 and 5.74, respectively (Atoyan and Dermer 2001).

For an isotropic photon distribution, the energy loss rate is given by

$$t_{\mathrm{p}\gamma}^{-1} = \frac{c}{2\gamma_{\mathrm{p}}^2} \int_{\varepsilon}^{\infty} d\varepsilon \frac{n(\varepsilon)}{\varepsilon^2} \int_{\varepsilon^*_{\mathrm{th},\pi}}^{\varepsilon^*} d\varepsilon^* \varepsilon^* \sigma_{\mathrm{p}\gamma}(\varepsilon^*) K_{\mathrm{p}\gamma}(\varepsilon^*) \ . \tag{5.75}$$

5.4 Hadronic Emission Models in Blazars

The unknown jet composition has led to models of hadronic, leptonic, and mixed compositions. They agree on the leptonic origin of the synchrotron emission in the jet; however, the γ-ray emission could originate in both leptonic and hadronic scenarios. The hadronic models assign at least some of the γ-rays to the decay of neutral pions produced in interactions between energetic protons and radiation or matter fields. In the event of pion production a charged pion population would decay into neutrinos. The blazar population is observed as highly beamed emission as the jet is directed in our line of sight. A neutrino signal from these sources will therefore be enhanced, and point source detection may be possible in the future as the neutrino observatories become increasingly more sensitive and accurate.

There is a possible differentiation at the highest γ-ray energies, where the predicted emission from hadronic and leptonic models diverges (Takami et al. 2013). A synchrotron peak at higher energies indicates an electron population suffering from energy losses, and lower jet power. Electrons are efficient radiators, which limits the continued upscattering of the synchrotron photons to even higher energies, hence providing a cut-off in the γ-ray spectrum of these sources. This is reflected in the HBL/HSP population (see Abdo et al. 2010a; Ajello et al. 2014; Mücke et al. 2003; Reynoso et al. 2011). If the γ-ray emission originate in the decay of pions, the production is linked to the relativistic proton population which has the potential to produce particles with

much higher energies due to its high rest mass. The energy threshold of pion production is much higher than pair production, hence at high energies pion production will dominate (Begelman et al. 1990).

The relativistic electron and proton content is assumed to travel with the jet flow at relativistic speeds. Emission due to their interactions along the jet requires both leptonic and hadronic processes to be considered. The electron losses are accounted for through synchrotron and inverse Compton processes. At lower energies protons suffer losses in Bethe-Heitler pair production, whereas at higher energies the losses due to interactions with radiation and matter fields, and subsequent pion production, are dominant (Begelman et al. 1990).

The internal jet synchrotron radiation field provides an excellent target for hadronic interactions. However, external fields are also possible. The interaction with direct accretion disc radiation, upscattered coronal radiation, or reprocessed accretion disc radiation in the BLR or torus provide targets which may vary significantly in energy and density. The availability of target fields may vary across the sequence, with FSRQs requiring denser radiation fields, whereas the SEDs of some lower-luminosity BL Lacs seem to agree with the synchrotron dominant radiation (see Dermer et al. 2014).

This has motivated a number of interaction scenarios, such as pure (synchrotron self-Compton) SSC models, where the jet synchrotron field is the dominant target for interactions, or including external fields like the BLR, torus, or reflected emission. Additionally, models take into account the structure of the jet, with one-zone models assuming the region of interest can be considered in one comoving frame. Two-zone models have been successful in explaining an enhancement of the inverse Compton or neutrino emission, with a fast, relativistic spine, and a slower outer layer (see e.g. Tavecchio et al. 2014, and references therein).

5.5 High-energy Neutrino Emission from Blazars

Studying the emission from blazars naturally hints at the processes within the jet features. The modelling of neutrino emission from AGN sources may

Cen A parameters		
Black hole mass:	$M_\bullet[M_\odot]$	10^8
Base of the jet:	$d_{\mathrm{j},0}$	50 $\mathrm{R_g}$
Kinetic to Eddington ratio:	ξ_{kin}	0.1
Magnetic dependence on jet distance:	ϑ	1.5
Magnetic to kinetic energy ratio	ξ_{B}	0.38

Table 5.2: Model parameters of Cen A used in Reynoso et al. (2011).

therefore be developed by combining information obtained from photonic observations (e.g. γ-ray surveys) and knowledge of hadronic interaction processes that may occur within the jet.

The SED of blazars of varying luminosities have uncovered an apparent sequence of increasing dominance of the high-energy peak over the low-energy peak and decreasing frequency of the peaks with increasing bolometric luminosity. This can then be quantified as a sequence from low-luminosity, high-frequency synchrotron peaked HBLs (HSPs); through intermediate-frequency peaked IBL (ISP) blazars; and high-luminosity, and low-frequency peaked LBLs (LSPs). These are commonly counted as BL Lac-type blazars, with the latter class sharing many features with the high-luminosity FSRQs (see e.g. Fossati et al. 1998; Ghisellini et al. 1998).

Identifying the key parameters of the sequence will therefore indicate differences in the physical properties of these classes, which in turn will enable us to derive variations in the expected neutrino output from each source population. Radio galaxies come in two types (FR-Is and FR-IIs) and the different morphology of their jets (edge-dimmed and edge-brightened, respectively) suggests that the ability to carry jet content to the lobes of bright FR-IIs is not found in FR-Is, whose main activity is closer to the base of the jet. If the radio-loud unification scheme is assumed, then these features should transfer to the division of the low-luminosity BL Lacs and FSRQs.

The evolution of the bulk Lorentz factor of the jet determines the extent of the jet structure, and variations in this parameter are expected along the blazar sequence. BL Lacs are expected to have a significantly lower bulk

Lorentz factor than FSRQs. The magnetic field structure in the jet indicates the strength of the synchrotron emission in the source. A stronger magnetic field would imply higher rates of synchrotron emission, hence a depletion of the high-energy particles to further cascade into high-energy emission, e.g. γ-rays, neutrinos, and cosmic rays. This interpretation fits the blazar sequence, for which the HBLs are strongly dominated by synchrotron processes. Seen in Fig. 5.3, a higher Lorentz factor gives a decreased magnetic field in the jet frame. The Lorentz factor is therefore one parameter which we vary along the sequence, summarised in Table 5.3.

The synchrotron radio emission is however only a fraction of the total power of the jet, and the bolometric luminosity is traced by the γ-ray emission, which is populated by emission due to (leptonic) inverse Compton scattering or (hadronic) neutral pion decays – or both. We use the lepto-hadronic model prescribed by Reynoso et al. (2011), following the jet structure as described above to follow the emission processes to the eventual emission of neutrinos. Using γ-ray surveys that have estimated the relative population density of the various blazar classes, we may therefore identify the efficient neutrino producers among the blazars, and provide constraints on the sources and the physical processes within the jets.

High-energy interactions and production occur close to the base of the jet. This is consistent with observations of energetic regions close to the core in FR-I AGN. In blazars the zone of high-energy emission is assumed to happen in the inner regions of the jet. We assume key parameters to define each blazar class, summarised in Table 5.3. Here the bulk Lorentz factor increases with increasing (γ-ray) luminosity, and the viewing angle ($\theta_{\rm v}$) is found to be slightly larger in BL Lacs than FSRQs (Ajello et al. 2014). As we consider blazars, we assume the half-opening angle ($\omega_{\rm j}$) is the maximum possible to qualify as a blazar, i.e. $\omega_{\rm j} = \theta_{\rm v}$.

Cen A is the closest FR-I. In determining key parameters for our blazar sequence candidates we adopt Cen A values to describe some common jet features. These are summarised in Table 5.2.

Blazar model parameters

	HBL	IBL	LBL	FSRQ
$\log(L_\gamma$ [erg s^{-1}])	$44.0 - 49.0$	$44.0 - 49.0$	$44.5 - 49.0$	$44.5 - 49.5$
$\Gamma_{\rm j,0}$	4	6	8	10
$\Gamma_{\rm j,max}$	7	11	15	19
$E_{\rm e,max}$ [GeV]	1.1×10^3	1.7×10^3	2.3×10^3	2.9×10^3
$E_{\rm p,max}$ [GeV]	6.8×10^7	8.9×10^7	10^8	1.2×10^8

Table 5.3: Blazar model parameters used in the construction of the BνLF. A set of parameters typical for each blazar class, which will determine the output of some of the physical processes within the jets. This will in turn affect the energies attainable in the sources, and the available particles to subsequently produce high-energy neutrinos. See text for details.

5.5.1 Energy loss rates

The maximum energy that can be attained by the particle population in the jet is determined by factors such as the strength of the jet magnetic field, as outlined above. These energy loss processes determine the energy carried away as radiation, and the maximum energy that particles in the jet can reach is determined by the balance of these processes to the rate of energy gain through (shock) acceleration, i.e. limited when $t_{\rm loss} \leqslant t_{\rm gain}$. The energy gain due to acceleration is given at a rate

$$t_{\rm accel}^{-1} = \xi_{\rm acc} \frac{c\ q_e\ B'}{E'_i} \tag{5.76}$$

(Begelman et al. 1990), where the efficiency of the acceleration $\xi_{\rm accel}$ depends on the mechanism, e.g. Fermi shock acceleration for particles i. The derived maximum particle energies for each source model are summarised in Table 5.3. In addition to radiative processes, the jet also suffers from adiabatic losses (van der Laan 1966; De Young 1972). This timescale, which is determined by the radial expansion of the jet, is given by

$$t_{\rm ad}^{-1} = \frac{2}{3} \frac{\beta_{\rm j} c}{z} \ . \tag{5.77}$$

The synchrotron and bremsstrahlung loss rates are calculated in the jet frame using Eqns. 5.42 and 5.69, respectively. The synchrotron loss rate is found to

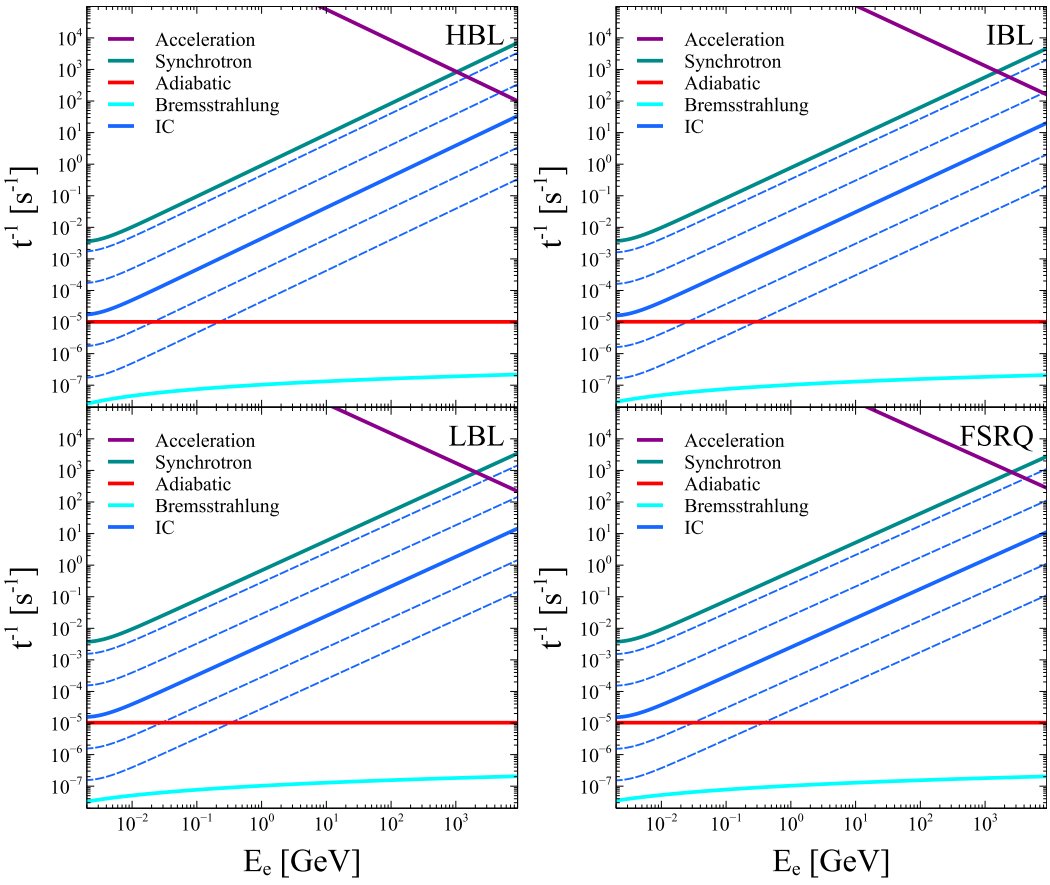

Fig. 5.6: Electron energy gain and loss rates in sources along the blazar sequence in the injection region. The cooling rate due to inverse Compton (IC) scattering is calculated using Eqn. 5.83, where the solid line correspond to $\lambda_{\mathrm{d-j}} = 1$, and the dashed lines, from top to bottom, have $\lambda_{\mathrm{d-j}} = 100, 10, 0.1, 0.01$. The synchrotron process is in all blazars the most efficient cooling mechanism for electrons, and therefore determines the maximum energy these particles can attain in the jet confinement.

increase along the sequence. In low luminosity sources, the electron energies suffer from strong synchrotron losses, whereas in the bright end of the sequence the synchrotron losses are lower, hence electrons may gain further in energy. This trend is seen in Fig. 5.6, which summarises the electron energy loss rates at the point of injection into the acceleration region, i.e. at $d_{\mathrm{j}} = d_{\mathrm{j,acc}}$. It reflects that the maximum energy of the particles is lower in these sources than the brighter end of the blazar sequence. This is the first hint at HBLs as less efficient neutrino producers.

The inverse Compton energy loss rate can be scaled with the synchrotron

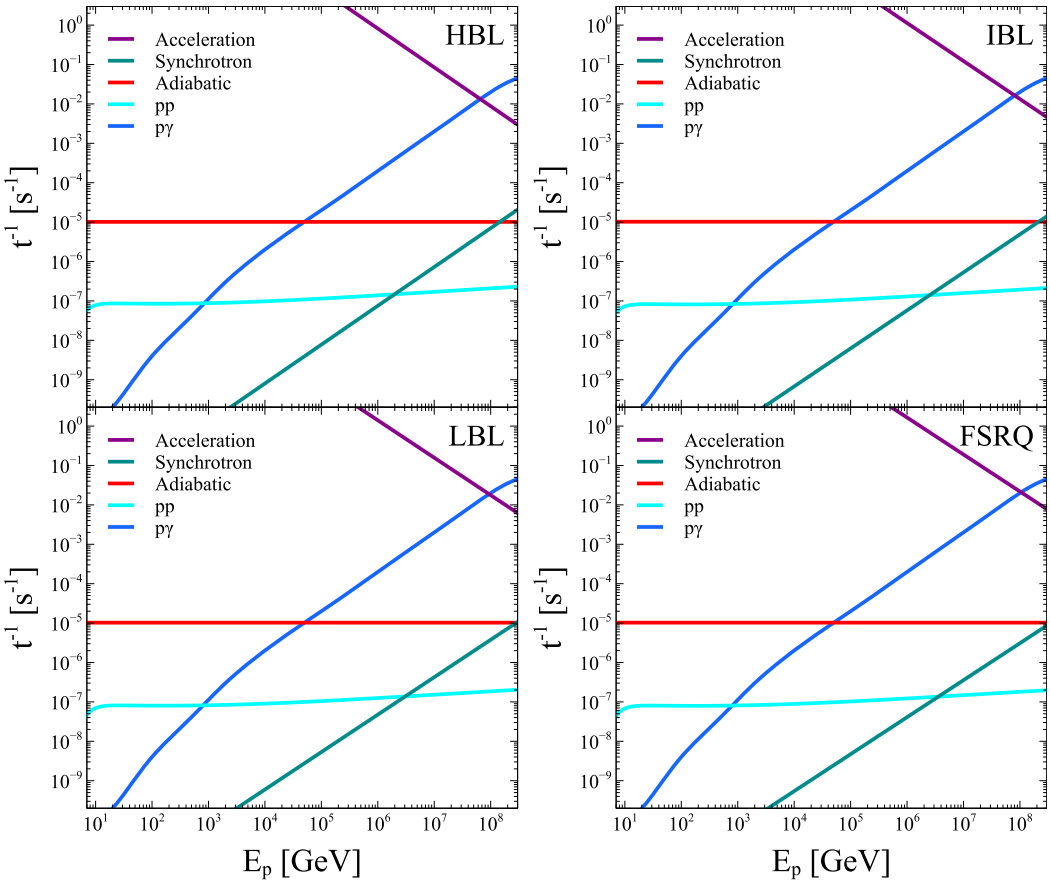

Fig. 5.7: Proton energy gain and loss rates in sources along the blazar sequence in the injection region. The cooling rates are calculated from equations given in Sec. 5.3, except the pγ loss rate which is adopted from the analysis of Cen A (Reynoso et al. 2011).

timescale as follows

$$\frac{t_{\rm IC}}{t_{\rm synch}} = \frac{U_{\rm B}}{U_\varepsilon} \tag{5.78}$$

(see Tucker 1975). The magnetic energy density (Eqn. 5.12) evolves along the jet following Eqn. 5.19. The radiative energy density can similarly be expressed as

$$U_\varepsilon = U_{\varepsilon,0} \left(\frac{d_{\rm j}}{d_{\rm j,0}} \right)^{-2} , \tag{5.79}$$

where

$$U_{\varepsilon,0} = \frac{L_\varepsilon}{4\pi d_{\rm j,0}^2 \, c} . \tag{5.80}$$

The inverse Compton loss rate can then be expressed in terms of the ratio of the radiative to magnetic energy density where the accretion disc and base

of the jet interact,

$$t_{\rm IC}^{-1} = \frac{U_{\varepsilon,0}}{U_{\rm B,0}} \left(\frac{d_{\rm j}}{d_{\rm j,0}} \right)^{2(\vartheta-1)} t_{\rm synch}^{-1} \ . \tag{5.81}$$

The radiative energy density can be expressed in terms of the known disc luminosity, hence relating the loss rate to the mass accretion rate through Eqn. 5.6. Assigning

$$\lambda_{\rm disc} = \left(\frac{U_{\varepsilon,0}}{U_{\rm B,0}} \right)_{\rm disc} \ , \tag{5.82}$$

the loss rate due to inverse Compton in the jet is scaled by $\lambda_{\rm d-j}$ to account for differences in the radiative energy densities in the disc and jet. This gives

$$t_{\rm IC}^{-1} = \lambda_{\rm disc} \lambda_{\rm d-j} \left(\frac{d_{\rm j}}{d_{\rm j,0}} \right)^{2(\vartheta-1)} t_{\rm synch}^{-1} \ . \tag{5.83}$$

The inverse Compton loss rate is found to be significantly lower than that of the synchrotron in all blazar classes, seen in Fig. 5.6. The maximum energy that the electron population in the source can attain is found by the balance of these processes, and vary along the sequence, such that the brighter end of the blazar sequence have a higher energy electron population than the low-luminosity end. These values are summarised in Table 5.3.

The energy loss rates of protons in the sources are shown in Fig. 5.7, evaluated in the injection region, $d_{\rm j,acc}$. The synchrotron cooling mechanism is less efficient for protons than electrons, with the most efficient cooling is due to pγ interactions. We adopt the pγ loss rate from Reynoso et al. (2011), using the FR-I radio galaxy Cen A as a reference, and scaling it with the appropriate bulk Lorentz factor of the source. Balancing the energy gain and losses affecting the protons we find the maximum proton energy attainable in the sources, summarised in Table 5.3.

5.6 Neutrino Luminosity Scaling

We construct a neutrino luminosity function (νLF) using Cen A to scale the neutrino output. In our calculations we adopt the single source neutrino spectrum for Cen A given in Reynoso et al. (2011) (hereafter the RMR model).

In this model the neutrinos originate from both pγ and pp interactions (see Fig. 5.8). Neutrino production from pγ-interactions occurs through energetic protons interacting with the (synchrotron) radiation fields in the jet, at around

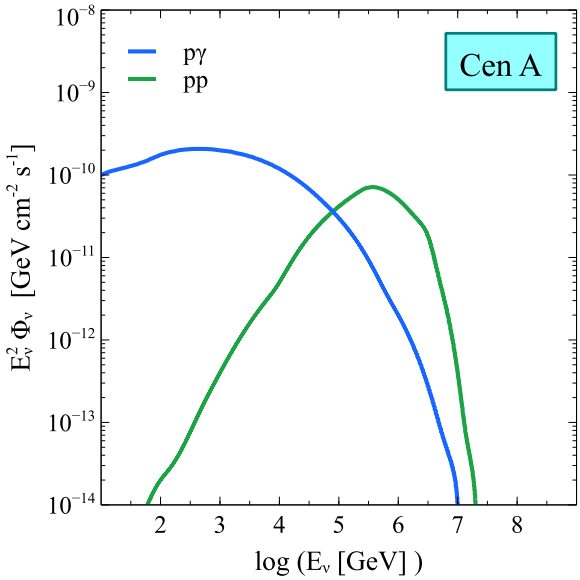

Fig. 5.8: Predicted neutrino intensity from Cen A by Reynoso et al. (2011), originating from both pγ and pp interactions.

50 gravitational radii from the AGN core. The pp-interactions involve cold proton fields that travel along the jet with the bulk motion. The pγ and pp interactions lead to the standard decay products described in Sec. 1.1.4, resulting in a population of high-energy neutrinos. Multiplicities of the pp-interaction is not taken into account, considering only the general inelastic cross section for the interaction (Eqn. 5.71).

Previously we have already found that the majority of spectral calculations overestimated the neutrino flux received from AGN populations. Thus, the neutrino production may not have been as efficient as described by the model for Cen A. We therefore consider a simple parametrisation by introducing a parameter η, which regulates the efficiency of the process. As discussed in Sec. 4.4, this parameter may represent a scenario whereby not all AGN are neutrino sources, or that the neutrino and X-ray duty cycles differ. The duty cycle of the lepton and baryon flows in the jets may be different, thus resulting in neutrino emission only occurring during a fraction of the X-ray lifetime.

Convolved with the blazar space densities derived in Ch. 3 we investigate the neutrino output at various cosmological epochs. We scale the spectra with the X-ray disc luminosity to that of Cen A, as we did in Sec. 4.2.1 – namely

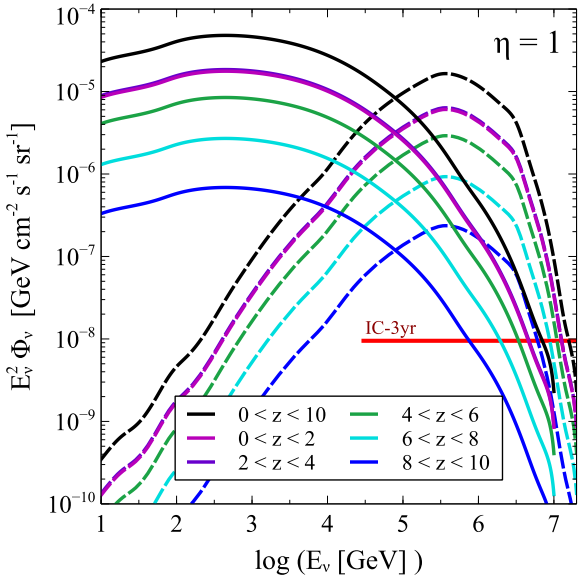

Fig. 5.9: Diffuse neutrino intensity from blazars using Cen A as a scaling reference with the RMR model prescription. The neutrinos originate from both pγ (solid curves) and pp (dashed curves) interactions. The spectra calculated from cosmological epochs extending $0 < z < 10$ are compared to the experimental flux limit (red horizontal line) set by the 3-year analysis of *IceCube*.

a scaling relation following

$$\tilde{\phi}^{\rm LS} = \eta \frac{L_X^{\rm AGN}}{L_X^{\rm CenA}} \ , \tag{5.84}$$

and we assume the luminosity scaling parameter $\eta = 1$. We also assume the same beaming corrections as we did in Ch. 3.

We apply the spectral scaling parameter to the Cen A spectra, such that for $\eta = 1$, Cen A is considered a good representation of the neutrino production rates in AGN. In this case, the blazar neutrino emission should follow that of Fig. 5.9. The pγ-neutrinos are predominantly found at lower energies, with the pp-neutrino contribution peaking at a neutrino energy nearly three orders of magnitudes higher than the pγ-neutrino emission. The contribution from the most local epoch considered ($0 < z < 2$) is comparable to that of the epoch within $2 < z < 4$, and neutrino emission from subsequent epochs decreases in intensity with increasing redshift.

We consider four cases motivated by the uncertainty of the neutrino production potential in Cen A, such that Cen A is either brighter or fainter than

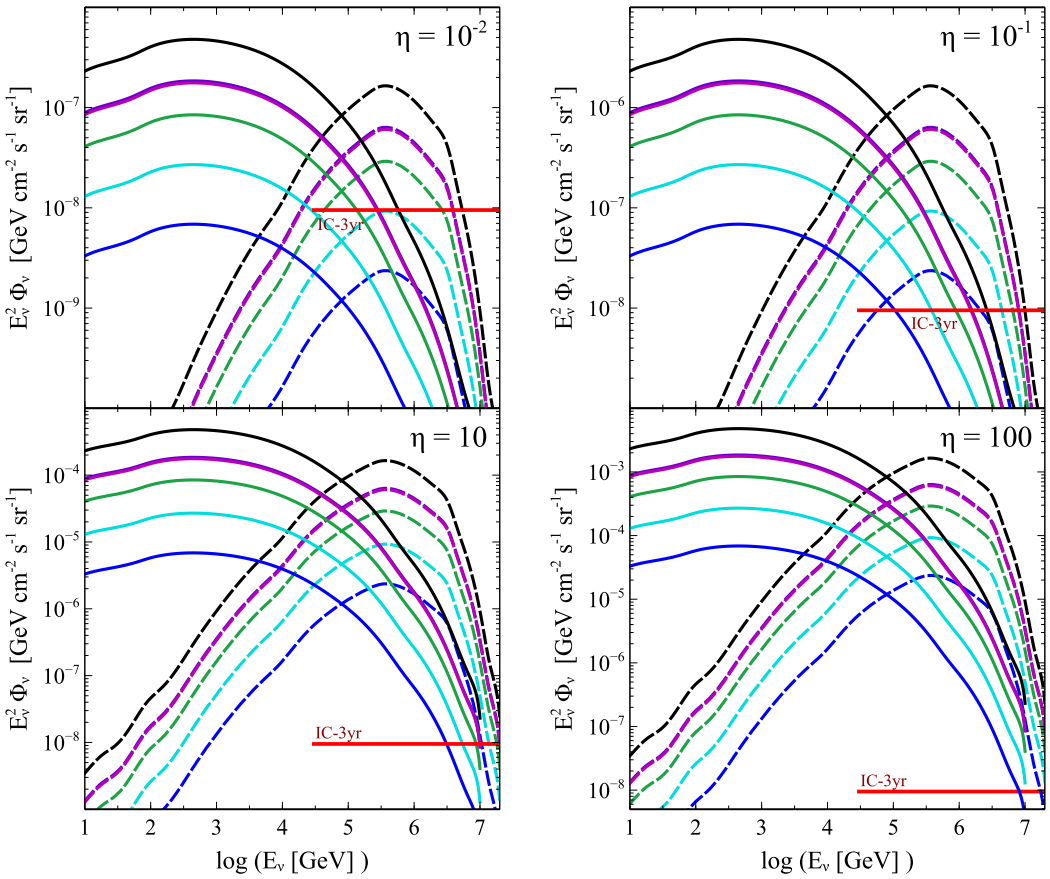

Fig. 5.10: Same as Fig. 5.9, but with $\eta = 10^{-2}$ (top left panel); $\eta = 10^{-1}$ (top right panel); $\eta = 10$ (bottom left panel); $\eta = 10^{2}$ (bottom right panel). The neutrino emission originates from both pγ (solid curves) and pp (dashed curves) interactions, and the diffuse spectra are compared to the *IceCube* flux limit (red horizontal line). Total diffuse emission (black lines) are found as the sum of contributions from various cosmological epochs: $0 < z < 2$ (magenta); $2 < z < 4$ (purple); $4 < z < 6$ (green); $6 < z < 8$ (cyan); $8 < z < 10$ (blue).

a typical neutrino producing AGN, measured by the scaling parameter η. This enables an investigation of the variations with redshift of the neutrino emission from AGN sources. The rate of emission is constant over cosmological epochs, with $\eta = (10^{-2}, 10^{-1}, 10, 100)$. The resulting neutrino spectra are shown in Fig. 5.10, with the extremes, i.e. $\eta = 10^{-2}$ and $\eta = 100$ represent scenarios where Cen A is either a hundred times brighter or fainter than a representative blazar source.

Seen from Fig. 5.10 the neutrino emission from blazars modelled on Cen A as a representative neutrino producer requires a spectral scaling parameter $\eta < 10^{-2}$ to be consistent with the current flux limit set by *IceCube*. This scal-

ing could then be interpreted as a fraction of blazar sources that are efficient neutrino producers, or that Cen A is an extremely efficient neutrino machine. It may also reflect the difference in duty cycles of the jet flows. Strong synchrotron emitting blazars (i.e. HBL types) are known to be abundant, and are also suggested poor neutrino producers, which could account for the bulk of blazars not contributing to the high-energy emission of neutrinos.

We know that blazars and AGN are strongly evolving over the history of the Universe. Introducing a redshift dependence on the spectral scaling, such that the neutrino efficiency in Cen A was higher in the past, i.e.

$$\eta(z) = 1 + z \ , \tag{5.85}$$

or if Cen A was fainter in the past, following

$$\eta(z) = \frac{1}{1+z} \ . \tag{5.86}$$

will reflect a variations in X-ray luminosity, i.e. accretion power of the AGN sources, over several cosmological epochs.

The resulting neutrino spectra from blazars with these scalings are shown in Fig. 5.11. The panel on the left hand side gives the diffuse emission from several cosmological epochs, where the Cen A emission is fainter in the past. In this case the intensity has overall decreased, and the most local epoch ($0 < z < 2$) is dominant. As the total diffuse spectra are still exceeding the *IceCube* limit by up to nearly three orders of magnitude, the local estimate of Cen A can be regarded excessively efficient, invoking the need of further suppression of the spectra.

The panel on the right shows the diffuse spectra for a scaling representing a higher efficiency in the past than today. The diffuse emission is exceeding the *IceCube* limit by over three orders of magnitude.

5.7 Results: Luminosity Scaling Models

The calculations using the νLF to investigate the blazar population, with Cen A as a typical neutrino producing source, show that a simple scaling is not consistent with the current flux limits set by *IceCube*. We have applied scaling models that do not evolve with redshift (see Fig. 5.10), which suggest

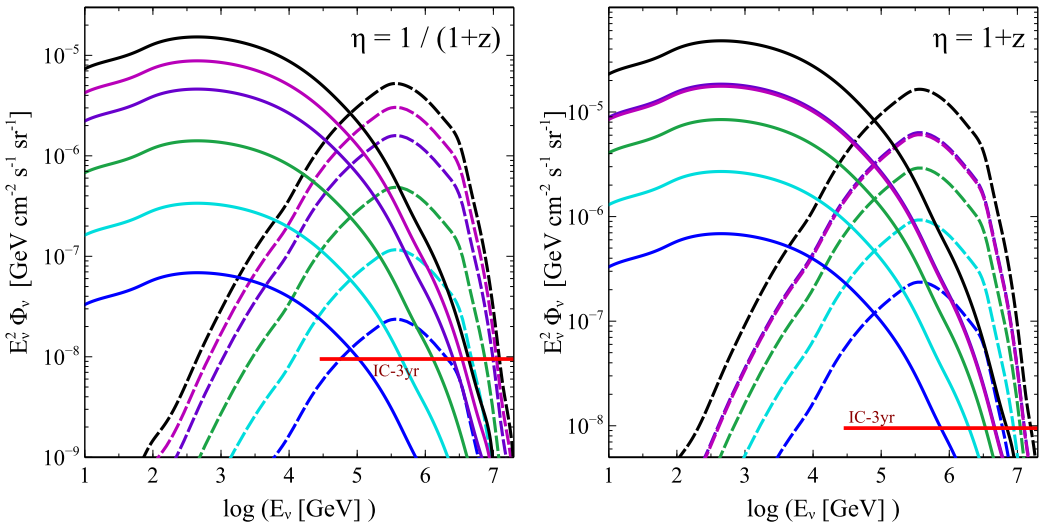

Fig. 5.11: Same as Fig. 5.9, but with a redshift dependent scaling, such that Cen A was fainter in the past (left panel) or was emitting stronger in the past (right panel). Neutrinos are produced through pγ interactions (solid lines) and pp interactions (dashed lines), and the total diffuse emission (black lines) are the sum of contributions from the cosmological epochs $0 < z < 2$ (magenta); $2 < z < 4$ (purple); $4 < z < 6$ (green); $6 < z < 8$ (cyan); $8 < z < 10$ (blue). The diffuse spectra are compared to the *IceCube* flux limit (red horizontal line)

that the neutrino efficiency of Cen A is too high to represent a typical rate in AGN/blazar sources. Applying a redshift dependent scaling improves the resulting spectra somewhat; however, they are still in excess of the *IceCube* flux limit, seen in Fig. 5.11.

The significance of the non-evolving scaling parameter is either that a persistent fraction over cosmic time does not contribute to the diffuse high-energy neutrino background, i.e. some AGN/blazars are not neutrino sources. This is consistent with high-peaked synchrotron blazars (i.e. HBLs/HSPs) being inefficient producers of the highest energy emission.

It furthermore shows that Cen A is not representative as a typical neutrino producing AGN source in this epoch or any other epochs throughout the history of the Universe. This is in agreement with our results in Ch. 4, for which Cen A is unrealistically efficient.

Another interpretation is that of the duty cycle of the emissions in the AGN system. As we scale these spectra with the disc luminosity, the scaling

implies a correlation between the high-energy particle production in the jet and the accretion power of the AGN. The fraction could then reflect that the X-ray duty cycle does not correlate with that of the neutrino emission, or that the central engine drives alternate flows of baryonic and leptonic flows in the jet. In this case a significantly more complex scaling model must be applied, taking into account the physics of the jet – which can be derived from a further study of γ-ray bright blazars. Or, perhaps, the hadronic flows are negligible in these systems all together.

The evolving scaling parameter probes the differences in the AGN environment over cosmic time. At an early epoch, e.g. at the formation of SMBHs, the conditions are expected to deviate significantly from today. AGN studies suggest that the activity of the brightest sources peaked much earlier than lower-luminosity systems, reflecting an increase in accretion power at earlier epochs. Hence a scaling similar to that of Eqn. 5.86 is reasonable.

However, as seen from the differences of peak activity from X-ray and γ-ray detected FSRQs in Ch. 3 the X-ray blazars peak much earlier ($z \sim 4$) than those detected in γ-rays ($z \approx 2$) This implies a difference in the evolution and duty cycle of the emissions. As the γ-ray luminosity traces the jet power, a scenario influenced by e.g. increased metallicity in the Universe with time, which in turn would affect the jet composition, can be invoked. In this case the accretion power of AGN peaks at earlier times, and the jet power peaks later when heavier elements are sufficiently abundant to mix in with a predominantly leptonic or Poynting flux dominated jet.

We compare the spectra with the best-fit diffuse neutrino spectrum derived from *IceCube* observations (Aartsen et al. 2015b), and find a spectral scaling parameter following

$$\eta(z) = \frac{\eta_0}{1+z} \ , \tag{5.87}$$

with $\eta_0 = 2 \times 10^{-3}$ (Fig. 5.12). In this particular case study we assume Cen A as a reference source, meaning that Fig. 5.12 indicates that Cen A is an excessively efficient neutrino producing source. The blazar population is therefore scaled by η_0, accounting for a lower neutrino production efficiency; or, a fraction of blazars that do not contribute to the neutrino background. It

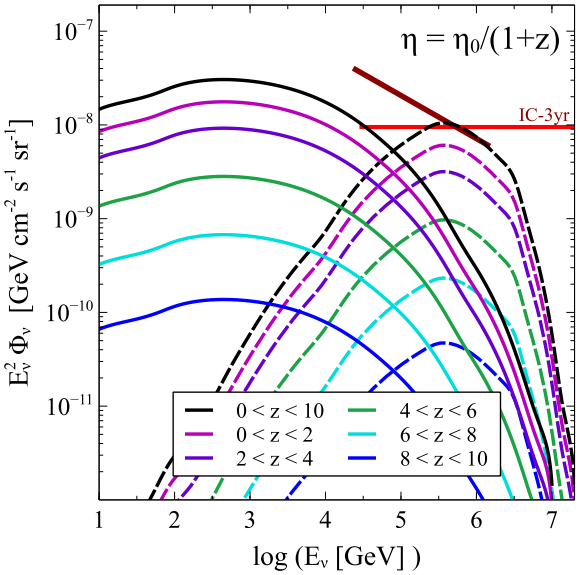

Fig. 5.12: Diffuse neutrino intensity from blazars, assuming Cen A as a reference neutrino producing source, and scaling the spectra with a redshift dependent parameter, such that Cen A was emitting stronger in the past, as well as being significantly brighter than a typical neutrino producing AGN. Neutrinos are produced through pγ interactions (solid lines) and pp interactions (dashed lines), and the total diffuse emission (black lines) are the sum of contributions from the cosmological epochs $0 < z < 2$ (magenta); $2 < z < 4$ (purple); $4 < z < 6$ (green); $6 < z < 8$ (cyan); $8 < z < 10$ (blue). The diffuse spectra are compared to the *IceCube* flux limit (red horizontal line), as well as the *IceCube* best-fit diffuse neutrino spectrum (Aartsen et al. 2015b), given in Eqn. 1.58.

may reflect the difference between the neutrino production duty cycle and that of the X-ray luminosity, which imply that the accreting source may fuel the jet with alternating jet flows; thus a baryonic emission may only be emitted during a fraction of the accreting lifetime of the AGN.

The redshift dependent factor implies that the efficiency was lower in the past, and with an increasingly more complex chemical composition of the environment allows for a higher jet power. However, with the expansion of the Universe, density drops, and we observe predominantly low-powered sources today.

In both cases, including information derived from γ-ray surveys of blazars will highlight some of these issues. The γ-ray brightness reflects the total jet power. Neutrino production in the jet is clearly closely tied to the emission

processes in the jet. A scaling model may therefore be constructed by including a more detailed correlation between the accretion power and the neutrino generation.

Chapter 6

Conclusions

6.1 Summary and Remarks

This thesis contains the research done on investigating the processes leading to neutrino production in AGN jets. Observations of cosmic rays and neutrinos at the highest energies point to an extragalactic source population. A number of candidates have been proposed, such as pulsars, SNRs, GRBs and AGN systems, all of which have the required power to accelerate hadrons to TeV-PeV energies.

AGN are a collection of X-ray bright objects, fuelled by accretion onto a supermassive black hole. Many of these show synchrotron radio emission, which implies that non-thermal radiative and particle acceleration processes are present within the sources. AGN jets are particularly attractive, as regions along the extended features are identified as sites of strong shocks, and the radio emission implies a population of relativistic electrons travelling in strong magnetic fields within the jet. These jet regions include the base of the jet, where the outflow interacts with the accreting inflow of material into the central black hole; knotty regions along the jet, where strong shocks are formed; and in the lobes of the jets, where hotspots are formed as the relativistic jet flow interacts with the intergalactic medium.

The morphology and emission vary across the diverse AGN population, and classification schemes based on observational features are commonly used to identify types of AGN. These types are families of sources determined from luminosity, inclination and viewing angles, and that can explain the physical

origin. As AGN emit over the full electromagnetic spectrum, photonic astronomy has studied AGN for decades. Large-scale surveys in radio, X-ray and γ-rays have mapped the space densities and the relative evolutionary trends of the various AGN classes. Point source observations, such as mapping the SEDs of blazar types, have revealed variations in the thermal disc emission and non-thermal jet emission.

Determining the neutrino output in these sources will therefore set constraints on the physical mechanisms and content of AGN jets. Considering neutrino production models the high-energy energy spectra of neutrinos from AGN jets are calculated. The resultant diffuse neutrino emission gives a prediction which may be compared with detections in current neutrino observatories, such as *IceCube*, and the planned *KM3NeT*.

With large AGN surveys, the contribution of neutrino emission from various cosmological epochs and sources of varying accretion power can be determined. Using AGN X-ray surveys, the disc luminosity, and therefore accretion potential of the sources, is traced. The source sample is then based on AGN accretion activity, and is insensitive to variations of non-thermal output. The radio-loud (i.e. jetted) fraction of these is assumed to be 10% of the total AGN population. Applying the neutrino emission from single AGN, the evolution of the high-energy neutrino emission can be determined originating in these sources.

The observational variations identified in the blazar sequence indicate differences in the physical properties within these sources. The space densities of blazars have been studied in γ-ray surveys using the *Fermi* telescope and combining these photon-based observations with current knowledge of neutrino production in the sources, a blazar neutrino luminosity function (νLF) can be constructed. This νLF can then help constrain the hadronic jet content, from which neutrinos are produced, and determine if these jets are predominantly baryonic, leptonic or electromagnetically dominated. The duty cycles of the various components can furthermore be explored using the neutrino emission, as the production path is invariably linked to the non-thermal particle populations present in the sources.

A firm detection of neutrinos, and a proper determination of the spectral properties will then, combined with the results of this thesis, enable these constraints to be made.

We have focussed our investigation using X-ray and γ-ray AGN surveys. This allows a study of the neutrino output in AGN, with the possibility to suppress the bias due to source geometry, e.g. jet inclination. The surveys of γ-ray bright blazars allow the study of interaction processes within individual sources, which have revealed quantifiable variations in the observed emission. In each case, the scaling of the neutrino energy spectrum is crucial.

At present, there are some uncertainties in how to relate the neutrino output to the photonic output. Thus, we need to consider various viable scenarios for the neutrino production channels in the AGN environment. The hadronic interactions lead to the observable emission of both cosmic rays and γ-rays through the decay of charged and neutral pions, respectively. The observed cosmic ray spectrum constrains the source population, requiring a population of protons within the jet that has been accelerated to observed energies, i.e. 10^{20} eV.

The observed correlation of UHECR detections and nearby AGN (Pierre Auger Collaboration et al. 2007, 2008) provides a scaling based on the UHECR flux observed from a given region, and thus scaling the neutrino spectrum with this emission, considering the production path taken, i.e. hadronic or photohadronic pion production. When extrapolating to the total diffuse emission, a correction factor is also included which deals with differences in the cosmic ray and neutrino propagation paths (e.g. Koers and Tinyakov 2008), or the difference in the source population evolutions (e.g. Becker and Biermann 2009).

One may, however, also use the observed γ-ray emission, which scales directly with the neutrino output if produced through neutral pion decays. The emission can however also originate in leptonic processes, such as inverse Compton scattering off either internal or external radiation fields. Assuming a fraction of the diffuse γ-ray background originating in the pion decay chain an estimate of the neutrino background can be estimated (e.g. Stecker et al. 1991;

Stecker 2005). Studying blazar SEDs has highlighted variations in the radio and γ-ray emission in the jets. These variations can furthermore constrain the available ingredients needed for high-energy production.

6.2 Future Work

Fully understanding the properties of AGN and their jets will be significantly helped by a strong detection of neutrinos originating in these sources. With the current leading high-energy neutrino observatory *IceCube* detecting neutrino events arriving on the Northern Hemisphere, the *KM3NeT* observatory is under construction in the Mediterranean sea, which will with an even larger volume detect neutrino events arriving on the Southern Hemisphere. *IceCube* has only been fully operational for a few years, and there is already a confirmation of these extragalactic high-energy neutrinos existence.

With increasing statistics in the dedicated observatories, the expected diffuse neutrino spectra derived in this research may be compared with an observed neutrino spectrum, similar to that of the UHECRs. In addition, point source detection may be a significant contribution. This will enable significantly tighter constraints to be set on hadronic interactions leading to the production of cosmic ray protons and neutrinos. This will in turn reveal processes that take place in the denser and brighter regions of AGN and their jets.

This work points to the importance of establishing a firm relation between the neutrino production and the photopion production processes. All are underpinned by the dynamical properties of the flows in the system, and in spite of the efforts, the physics of AGN jets is still poorly known. For instance, we do not know the details of particle acceleration processes in AGN near the central engine, nor do we know much about the chemical composition of jet plasmas. The jet may experience alternate duty cycles of e.g. hadronic and leptonic emission. This would affect the resultant neutrino spectra significantly. These conditions may be investigated through for example flaring episodes in AGN jets. Blazar SEDs change shape between quiescent and active states, and the relative shifts of the low-energy and high-energy peaks in the spectra require

physical processes within the source that reflect these changes. A study into the expected neutrino output correlated with the X-ray and γ-ray emission in the two states could pinpoint the exact processes.

In the meantime there are a number of tests that can be carried out, combining the prediction of neutrino emission with photonic observations. In this work we have focussed on the energetic proton interaction with the internal synchrotron fields. There are however a number of external radiation fields available, which also has been considered in other studies, as well as matter fields, which may also lead to the production of cosmic rays and neutrinos. In this way the νLF can be extended to involve more complex interaction scenarios which more closely resembles various AGN types.

In this thesis we have scaled the neutrino production efficiency of AGN with the accretion power through the observed X-ray luminosity. A further investigation to look at the correlation between neutrino production and radio emission of the jet will be useful to further probe the processes which lead to the observable emission. Similarly a continuation of the γ-ray detected blazar space densities will enable a further investigation of the correlation of high-energy particle production in these sources.

A further study into the relative distribution of neutrino emission originating from a range of cosmological epochs can then be used to study the evolution of powerful structures in the Universe. In that respect it will also be useful to determine similar νLFs for other candidate source populations, such as GRBs, pulsars and SNRs. To complete the cosmic neutrino puzzle it will be rewarding to investigate the processes leading to neutrinos on all energies (e.g. the CνB and stellar sources) to construct a full neutrino SED over cosmological time. This will enable us to view the structural formation of the contents in the Universe from the epoch of structure formation.

6.3 Conclusion

In the research presented in this thesis we investigate the origin of high-energy neutrinos, and their spectral distribution at various cosmological epochs. We consider AGN jets which are identified as prominent candidates for the pro-

duction of high-energy emission. We then explore the processes that lead to this emission to determine if AGN are efficient neutrino factories. We make use of published AGN surveys detecting X-ray and γ-ray bright sources to derive the redshift and luminosity distribution of these sources. The observational data allow us to derive the number evolution for several classes of AGN.

We first consider the KT and BB hadronic production models, that assume a scaling of the neutrino spectrum with the observed cosmic ray emission. Using the prescription for neutrino production described in these models we produce single source neutrino spectra, which we convolve with the derived distribution of X-ray detected AGN. We calculate the expected neutrino energy distribution at various cosmological epochs, as well as for sources of varying X-ray brightness. The sum of the components in each case gives us the expected diffuse neutrino emission on Earth.

Our calculations test a number of simplified assumptions in the production models, in particular the correlation between the accreting power of the AGN, hence the X-ray luminosity, and the resulting high-energy emission of neutrinos. We compare the energy spectra to current upper limits of the received neutrino flux set by *IceCube* and PAO. We find that the bulk of AGN sources would produce a neutrino flux far exceeding this limit, with some variations depending on the neutrino production model used. The radio galaxy population (Type-I (unobscured) and -II (obscured) RGs) are expected to produce a diffuse output of $\sim 10^{-2}$ GeV cm^{-2} s^{-1} sr^{-1} (KT model, Fig. 4.16); $\sim 10^{-4}$ GeV cm^{-2} s^{-1} sr^{-1} (BB2 model, Fig. 4.17); and $\sim 10^{-6}$ GeV cm^{-2} s^{-1} sr^{-1} (BB1 model, Fig. 4.17). The unobscured radio galaxies, that form a subset of the above population, produce a diffuse neutrino flux about half a magnitude lower than the full radio galaxy population for the given production model.

The neutrino spectra show that blazars, i.e. AGN with their jet pointing in our line of sight, are the only AGN class consistent with observations. Additionally, we demonstrate the importance of a reliable luminosity scaling model, and hence the need for an improved understanding of the emission processes in the jet. Variations in the scaling models are particularly appar-

ent for these source populations. The blazars and the FSRQ sub-population contribute to $\sim 10^{-5}$ GeV cm^{-2} s^{-1} sr^{-1} and $\sim 10^{-4}$ GeV cm^{-2} s^{-1} sr^{-1}, respectively, in the KT model. In the BB2 model we find the expected neutrino fluxes of $\sim 7 \times 10^{-7}$ GeV cm^{-2} s^{-1} sr^{-1} and $\sim 2 \times 10^{-7}$ GeV cm^{-2} s^{-1} sr^{-1} from these sources. The BB1 model however, shows that the blazar and FSRQs produce comparable fluxes around $\sim 2 \times 10^{-9}$ GeV cm^{-2} s^{-1} sr^{-1}. Hence in this model the emission is consistent with the *IceCube* limits. The low-luminosity, and locally abundant, BL Lac population cannot be rejected as a potential neutrino source in either model. In the KT model, the diffuse flux contribution of this source falls below the *IceCube* limit at lower neutrino energies ($\log[E_\nu(\mathrm{GeV}) \lesssim 5.5$). The spectral break occurs above this limit, with $\sim 2 \times 10^{-7}$ GeV cm^{-2} s^{-1} sr^{-1} at an energy of $\log[E_\nu(\mathrm{GeV}) \approx 6.5$. Both the BB model predictions place the BL Lac contribution below the *IceCube* limit, at $\sim 10^{-10}$ GeV cm^{-2} s^{-1} sr^{-1} and $\sim 3 \times 10^{-13}$ GeV cm^{-2} s^{-1} sr^{-1}, for the BB2 and BB1 models respectively.

We show explicitly, following the KT and RMR model prescriptions, that Cen A is unrealistically efficient as a neutrino producer, and is therefore not representative of a neutrino producing AGN.

To further investigate the exact processes that are relevant to neutrino production, we construct a neutrino luminosity function for blazar sources. These sources have a defined sequence in observable features in these γ-ray bright sources, and typical parameters, such as luminosity and Lorentz factor, can be assumed for each blazar class along the sequence. This will enable us to constrain possible AGN sources and the relative neutrino production efficiencies across the sequence. Using redshift and luminosity distributions of γ-ray bright blazar classes, we may infer further constraints on the conditions within the jet by comparing the diffuse neutrino spectra with current detection limits, such as the neutrino production duty cycle in AGN jets, and variations across the AGN population.

Appendix A

Structural Evolution of the Universe

At the core of any modern cosmological model we find the Cosmological Principle which tells us that, on large scales ($\gtrsim$ 100 Mpc), the universe is homogeneous and isotropic. An isotropic universe means that we find spatial uniformity in all directions, whereas a homogeneous universe means that all positions are identical in space. The Universe is in reality not entirely isotropic, but based on observational evidence such as the near-uniformity of the cosmic microwave background radiation, it is a reasonable assumption.

Isotropy does not imply the homogeneous property of the Universe, but is implied by introducing the Copernican principle, which says that an observer is at no position in space privileged. An observer will find that the Universe looks the same in all directions, and so it will be at whichever position chosen. The observed isotropy, together with the Copernican Principle thus implies the Cosmological Principle and is the cornerstone of the models we use to describe the Universe today.

Cosmology is the study of the origin and evolution of the Universe, and the following is a brief outline of the standard cosmological model, and the formulation of the important observables (see e.g. Coles and Lucchin 2002; Peacock 2007), some of which are essential to the execution of this work, and all of which set the cosmological background to any work done on cosmological scales. The currently accepted cosmological model is known as the concordance model, and it describes the overall evolution of the Universe, and its physical properties. At the foundation lie the Einstein field equations, a set

of equations that describe the gravitational interactions in terms of the curving of space-time by energy and matter. Furthermore, it takes into account cosmological effects such as the expansion of the Universe when defining travel time, distances, and volumes, and a formulation of comoving coordinates is therefore required.

A.1 Einstein's Field Equations

On large scales, the strongest force of nature is gravity. In Einstein's general theory of relativity the gravitational interaction is explained in terms of the curvature of the space-time, and is therefore a property of the very fabric of the Universe. Any model that aspires to describe the physical behaviour and properties of the Universe must therefore keep this at its foundation.

In relativity, the space-time metric $g_{\mu\nu}$ is defined to connect the coordinate value with the physical measure between two points in space-time. The space-time interval is given by

$$ds^2 = g_{\mu\nu} dx^\mu dx^\nu \ , \tag{A.1}$$

with the four-vector dx^μ, and where $dx^0 = dt$ is the timelike coordinate, and dx^i are the spacelike coordinates, with $i = 1, 2, 3$. Here we use the timelike signature $[+, -, -, -]$, so that a space-time interval corresponding to a free-falling particle is one of three possibilities; spacelike when $ds^2 < 0$, lightlike when $ds^2 = 0$, and timelike when $ds^2 > 0$. The lightlike path, known as the null path, is the path of a photon (or any massless particle), and connects points in space-time by a ray with the speed of light.

In general space-times, the motion of a free particle is described by the geodesic equation

$$\frac{d^2 x^\mu}{d\lambda^2} + \Gamma^\mu{}_{\alpha\beta} \frac{dx^\alpha}{d\lambda} \frac{dx^\beta}{d\lambda} = 0 \ , \tag{A.2}$$

with the affine parameter λ which increases along the particle path. Here, the Christoffel symbol corresponds to the gravitational force field, and is given by

$$\Gamma^\mu{}_{\alpha\beta} = \frac{1}{2} g^{\mu\nu} \left[\frac{\partial g_{\alpha\nu}}{\partial x^\beta} + \frac{\partial g_{\beta\nu}}{\partial x^\alpha} - \frac{\partial g_{\alpha\beta}}{\partial x^\nu} \right] \ , \tag{A.3}$$

with $g^{\alpha\mu} g_{\alpha\nu} = \delta^\mu{}_\nu$. In an expanding Universe, a working metric must link the physical distance to a comoving distance as the Universe evolves. It therefore

incorporates a scale factor, $a(t)$,

$$g_{\mu\nu} = \begin{bmatrix} 1 & 0 & 0 & 0 \\ 0 & -a(t)^2 & 0 & 0 \\ 0 & 0 & -a(t)^2 & 0 \\ 0 & 0 & 0 & -a(t)^2 \end{bmatrix} . \tag{A.4}$$

To describe the Universe, a system of particles need to be considered rather than a single path of a particle. It is thus useful to consider a fluid continuum, with defined properties such as density and pressure. For a perfect isotropic fluid, the equation of state is $\omega = P\rho^{-1}$, with the dimensionless equation of state parameter ω, pressure P, and the density ρ. The matter distribution can then be described in terms of the energy-momentum tensor,

$$T^{\mu\nu} = (P + \rho)u^\mu u^\nu - Pg^{\mu\nu} , \tag{A.5}$$

where the fluid four-velocity $u_\mu = g_{\mu\nu}u^\nu = g_{\mu\nu}(dx^\nu/ds)$ in covariant form, so that $x^\nu(s)$ describes the worldline of a fluid element. For the fluid element, the components of the tensor are then the rest frame energy density (T^{00}), the momentum density ($T^{0i} = T^{i0}$), and the momentum flux ($T^{ij} = T^{ji}$).

It is worth noting that the energy-momentum tensor describes the equivalence of mass and energy. For an expanding universe, its covariant derivative (denoted by the semicolon) is

$$T^{\mu\nu}{}_{;\mu} = T^{\mu\nu}{}_{,\mu} + \Gamma^\mu{}_{\mu\alpha}T^{\alpha\nu} + \Gamma^\nu{}_{\mu\alpha}T^{\mu\alpha} , \tag{A.6}$$

where the comma indicates a normal partial derivative. Conservation of mass and energy implies

$$T^{\mu\nu}{}_{;\mu} = 0 . \tag{A.7}$$

The curvature of the Universe is described by the Riemann-Christoffel tensor,

$$R^\alpha{}_{\beta\mu\nu} = \Gamma^\alpha{}_{\nu\beta,\mu} - \Gamma^\alpha{}_{\mu\beta,\nu} + \Gamma^\alpha{}_{\mu\gamma}\Gamma^\gamma{}_{\nu\beta} - \Gamma^\alpha{}_{\nu\gamma}\Gamma^\gamma{}_{\mu\beta} . \tag{A.8}$$

It vanishes everywhere if space-time is flat. Contracting the Riemann-Christoffel tensor gives the Ricci tensor

$$R_{\mu\nu} = g^{\alpha\beta}R_{\alpha\mu\beta\nu} , \tag{A.9}$$

where $R_{\alpha\mu\beta\nu} = g_{\alpha\gamma}R^{\gamma}{}_{\mu\beta\nu}$, and contracting the Ricci tensor gives the Ricci curvature scalar by

$$R = g^{\mu\nu}R_{\mu\nu} \ . \tag{A.10}$$

The Ricci tensor, the Ricci scalar, and the energy-momentum tensor, combines with the Einstein tensor, $G^{\mu\nu}$, to form the Einstein field equations:

$$\begin{aligned} G^{\mu\nu} &\equiv R^{\mu\nu} - \frac{1}{2}g^{\mu\nu}R \\ &= -8\pi G T^{\mu\nu} \ , \end{aligned} \tag{A.11}$$

in natural units, i.e. $c = 1$, and following the sign convension $[-,+,-]$ (Peacock 2007). The equation relates energy density and space-time geometry, and the constant $8\pi G$ comes from reducing the equation in the weak field limit for which Newtonian gravity applies, and considering the recovered Poisson's equation for gravity,

$$\nabla^2\varphi = 4\pi G\rho \ , \tag{A.12}$$

for which φ is the gravitational potential.

Similar to the energy-momentum tensor, the Einstein tensor also has zero covariant divergence, i.e.

$$G^{\mu\nu}{}_{;\mu} = G^{\mu\nu}{}_{,\mu} + \Gamma^{\mu}{}_{\mu\alpha}G^{\alpha\nu} + \Gamma^{\nu}{}_{\mu\alpha}G^{\mu\alpha} = 0 \ . \tag{A.13}$$

An added feature to the equations of general relativity is the possibility of vacuum energy, i.e. the energy of empty space. Given that $T_{\mu\nu}$ gives the density of the constituents in the Universe, an energy-momentum tensor of vacuum can similarly be constructed as

$$T^{\rm vac}_{\mu\nu} = \rho_{\rm vac}g_{\mu\nu} \ . \tag{A.14}$$

Incorporating this energy-momentum density, the Einstein field equation becomes

$$\begin{aligned} R_{\mu\nu} - \frac{1}{2}g_{\mu\nu}R &= -8\pi G\ (T^{\rm c}_{\mu\nu} + \rho_{\rm vac}g_{\mu\nu}) \\ &= -8\pi G\ \tilde{T}_{\mu\nu} \ , \end{aligned} \tag{A.15}$$

so that the redefined energy-momentum tensor $\tilde{T}_{\mu\nu}$ is the sum of the energy-momentum tensor of the matter content, $T^{\rm c}_{\mu\nu}$, and that of the vacuum energy, $T^{\rm vac}_{\mu\nu}$. The expression for vacuum energy density can then be defined in terms of the cosmological constant, Λ, which is often attributed to the energy causing of the expansion of the Universe; the so-called dark energy $\rho_{\rm vac} = \Lambda/(8\pi G)$. As such, the Einstein equation can be written

$$R_{\mu\nu} - \frac{1}{2} g_{\mu\nu} R + \Lambda g_{\mu\nu} = -8\pi G T^{\rm c}_{\mu\nu} \ , \tag{A.16}$$

The density of the cosmological constant is therefore interchangeable with the vacuum energy density by

$$\rho_{\rm vac} = \rho_\Lambda = \frac{\Lambda}{8\pi G} \ . \tag{A.17}$$

A.2 Friedmann-Lemaître-Robertson-Walker Metric

Solutions of the Einstein field equations give rise to the non-static models of the Universe, of which the Friedmann-Lemaître-Robertson-Walker (FLRW) models form the general framework representing the Universe that is compatible with the Cosmological Principle. The FLRW metric is given by

$$ds^2 = dt^2 - R(t)^2 [dr^2 + S_k(r)^2 d\psi^2] \ , \tag{A.18}$$

where $d\psi^2 = d\theta^2 + \sin^2\theta \ d\phi^2$, and $S_k(r)$ with $k = -1$ describing a closed universe with negative spatial curvature; $k = 0$ with no spatial curvature, i.e. a flat universe; and $k = +1$ an open universe, whose spatial surface has positive curvature. However, the scale factor $R(t)$ is commonly normalised to unity in the present epoch t_0, such that

$$a(t) \equiv \frac{R(t)}{R_0} \ , \tag{A.19}$$

with $R_0 \equiv R(t_0)$, the curvature parameter $\kappa = k R_0^{-1}$, and $a(t_0)$ is set to unity. The rate of expansion of the Universe is given by the Hubble parameter, as

$$H(t) = \frac{\dot{R}(t)}{R(t)} = \frac{\dot{a}(t)}{a(t)} \ . \tag{A.20}$$

An associated Hubble parameter for the present epoch is defined as $H_0 = H(t_0)$. In terms of a dimensionless Hubble parameter h, it is

$$H_0 = 100 \ h \ \text{km s}^{-1} \ \text{Mpc}^{-1} \ . \tag{A.21}$$

	Matter[a]	Radiation[b]	Curvature	Cosmological constant
ω =	0	1/3	−1/3	−1
$\rho \propto$	a^{-3}	a^{-4}	a^{-2}	a^{0}
$a \propto$	$t^{2/3}$	$t^{1/2}$	t	e^{Ht}

Table A.1: Scaling relations of energy density and scale factor for the constituents of the Universe; matter, radiation, curvature and the cosmological constant, for a given equation of state parameter ω. *a*) includes non-relativistic matter, i.e. baryonic and cold dark matter. *b*) includes radiation and relativistic matter.

Solving the Einstein field equations gives rise to the Friedmann equations. The first Friedmann equation relates the expansion rate to the curvature and the density of the Universe:

$$\left(\frac{\dot{a}}{a}\right)^2 = \frac{8\pi G}{3}\rho - \frac{\kappa}{a^2} + \frac{\Lambda}{3} \ , \tag{A.22}$$

in natural units. Using Eqn. A.20, and introducing the density parameter Ω as the ratio of the total energy density in the Universe to a critical density,

$$\rho_c = \frac{3H^2}{8\pi G} \ , \tag{A.23}$$

the Friedmann equation can be expressed as

$$\Omega - 1 = \frac{\kappa}{H^2 a^2} \ . \tag{A.24}$$

Then, for a closed universe $\Omega > 1$, or correspondingly $\kappa > 0$; if flat $\Omega = 1$, or $\kappa = 0$; and for an open universe $\Omega < 1$, or $\kappa < 0$.

The second Friedmann equation gives the acceleration rate of the Universe, which is determined by the pressure and density,

$$\frac{\ddot{a}}{a} = -\frac{4\pi G}{3}(\rho + 3P) \ . \tag{A.25}$$

A direct consequence of the Friedmann equations is the continuity equation,

$$\frac{d\rho}{dt} + 3\frac{\dot{a}}{a}(\rho + P) = 0 \ . \tag{A.26}$$

	Ω_Λ	Ω_m	Ω_bm	Ω_cdm	H_0	t_0
WMAP	0.714	0.287	0.046	0.240	69.3	13.77
Planck	0.685	0.315	0.049	0.265	67.3	13.82

Table A.2: Measured cosmological parameters from the 9-year results of WMAP (Table 17, Bennett et al. 2013) and first results of Planck (Table 2, Planck Collaboration et al. 2014). Age of the Universe t_0 is in units of Gyr, and the Hubble constant H_0 in units of km s^{-1} Mpc^{-1}. Note that Ω_bm and Ω_cdm are calculated from the given values of $\Omega_\mathrm{bm}h^2$ and $\Omega_\mathrm{cdm}h^2$ in Planck Collaboration et al. (2014), and do not exactly add up to Ω_m, as we neglect the errors in the measured values. Ω_Λ refers to the density of the cosmological constant.

It integrates to $\rho_i(a) \propto a^{-3(1+\omega_i)}$, and thus holds information on how the constituents i of the Universe scale with the spatial evolution. Here ($i = \mathrm{m}, \mathrm{r}, \Lambda$) refers to matter, radiation, and the cosmological constant, respectively, and

$$\omega_i = \frac{P_i}{\rho_i} \tag{A.27}$$

is the equation of state. The cosmological constant is interchangeable with vacuum energy, following Eqn. A.17. Matter refers to all non-relativistic matter, hence both baryonic and cold dark matter fall within this category. Relativistic matter is included in the radiation component. Combined with the first Friedmann equation, the continuity equation yields the time evolution of the scale factor,

$$a(t) \propto t^{\frac{2}{3(1+\omega)}} \ . \tag{A.28}$$

The scaling relations for each constituent are summarised in Table A.1. Using the density parameters for each constituent, $\Omega_i = \rho_i \rho_\mathrm{c}^{-1}$, the first Friedmann equation can be expressed in terms of H_0:

$$\left(\frac{H}{H_0}\right)^2 = \left(\frac{\dot{a}}{a}\right)^2 = \Omega_\mathrm{r} a^{-4} + \Omega_\mathrm{m} a^{-3} + \Omega_\kappa a^{-2} + \Omega_\Lambda \ . \tag{A.29}$$

The consistency relation requires

$$\sum_i \Omega_i + \Omega_\kappa = 1 \ , \tag{A.30}$$

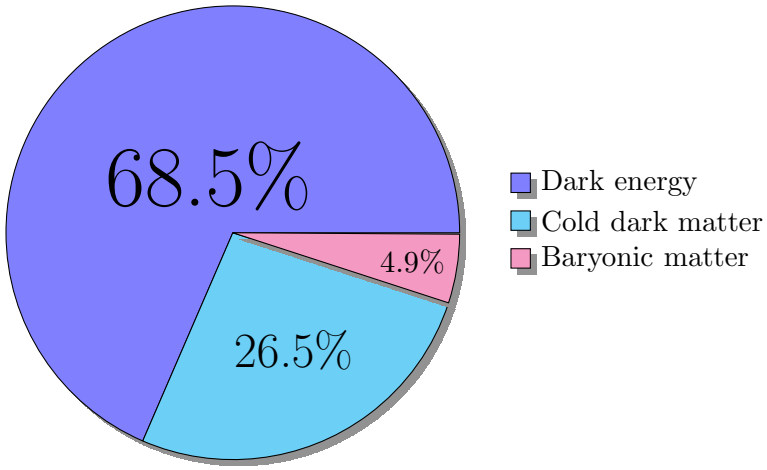

Fig. A.1: The constituents of the Universe. Dark energy dominates the total content of the Universe; cold dark matter makes up about a quarter; baryonic matter accounts for less than 5%.

with ($i = \mathrm{m}, \mathrm{r}, \Lambda$), and the contribution of curvature to the total energy density is given by the right hand side of Eqn. A.24:

$$\Omega_\kappa = \frac{\kappa}{H^2 a^2} \ . \tag{A.31}$$

The currently accepted representation of our Universe is the Lambda cold dark matter (ΛCDM) model. It assumes the flat expanding space-time given by the FLRW metric, i.e. $\Omega_\Lambda = 1 - \Omega_\mathrm{m}$. Ordinary baryonic matter and cold dark matter make up the matter content, so that $\Omega_\mathrm{m} = \Omega_\mathrm{bm} + \Omega_\mathrm{cdm}$. The cosmological constant, Λ, is commonly attributed to the accelerated expansion in the form of the unknown quantity, called dark energy. It is the simplest model of Big Bang cosmology able to explain the observations of the CMB, the large-scale distribution of galaxies, the abundance of light nuclei, and the accelerated expansion remarkably well.

Two major cosmological missions have been of utmost importance for the development of the study cosmology – the Wilkinson Microwave Anisotropy Probe (WMAP), launched in 2001 and ran for over 12 years by NASA; and the Planck observatory, launched by ESA in 2009, that ran for over 4 years. Their complimentary data have led to measurements at high precision of the early Universe, the CMB, and the fractional densities of the constituents of the Universe (Fig. A.1). They also have established the cosmo-

logical parameters to high precision (Hinshaw et al. 2013; Bennett et al. 2013; Planck Collaboration et al. 2014, see Table A.2).

A.3 Distances and Comoving Volume

Measuring distances in an expanding Universe requires a comoving set of coordinates. The comoving distance $D_\mathrm{c} = R_0 r$ remains fixed with the expansion of the Universe, and is therefore time independent. The physical distance D_p grows with expansion. Any calculations done on large scales thus require a relation between these two sets of coordinates, given by the scale factor (Eqn. A.19), so that

$$D_\mathrm{p}(t) = a(t) D_\mathrm{c} \ . \tag{A.32}$$

The expansion of the Universe can then easily be linked to Hubble's law, which links the recessional velocity $v_\mathrm{rec} = \dot{D}_\mathrm{p}$ to the physical distance. When evaluated today,

$$v_\mathrm{rec} = \dot{a} D_\mathrm{c} = \frac{\dot{a}}{a} D_\mathrm{p} = H_0 D_\mathrm{p} \ . \tag{A.33}$$

The physical manifestation of the scale factor is the consequences of the decreasing radiative energy with expansion, $E \propto a^{-1}$. This is observed in terms of a stretching of the wavelength (or similarly, a shorter observed frequency to that emitted). The ratio between observed and emitted quantities is measured as the redshift z between the source and observer,

$$1 + z \equiv \frac{\lambda(t_0)}{\lambda(t)} = \frac{a(t_0)}{a(t)} \ , \tag{A.34}$$

if the observation is made today ($t = t_0$), and the scale factor $a(t)$ corresponds to time t, when the source emitted the photon with wavelength $\lambda(t)$, and $a(t_0) \equiv 1$. Using Eqn. A.34, the first Friedmann equation may be redefined in terms of redshift, which is important when calculating distances and volumes in the expanding Universe:

$$H^2 = H_0^2 \left[\Omega_\mathrm{r} (1+z)^4 + \Omega_\mathrm{m} (1+z)^3 + \Omega_\kappa (1+z)^2 + \Omega_\Lambda \right] \ . \tag{A.35}$$

The radial null geodesic is $dt^2 - a(t)^2 R_0^2 dr^2 = 0$, given by the FLRW metric (Eqn. A.18). Using Eqn. A.34 and the Friedmann equation (Eqn. A.35), the

comoving distance is related to the redshift by

$$D_{\rm c} = \frac{1}{H_0}\int_0^z \frac{dz}{\left[\Omega_{\rm r}(1+z)^4 + \Omega_{\rm m}(1+z)^3 + \Omega_\kappa(1+z)^2 + \Omega_\Lambda\right]^{1/2}} \ . \tag{A.36}$$

For a flat, matter dominated Universe, $\Omega_{\rm m} = \Omega = 1$, and the contributions from Ω_κ and $\Omega_{\rm r}$ can be neglected. The redshift dependence of the Hubble parameter is then $H(z) = H_0(1+z)\sqrt{1+\Omega z}$ (Peacock 2007), hence the distance travelled by a photon is

$$R_0 r = \frac{1}{H_0}\int_0^z \frac{dz'}{\left[(1+z')\sqrt{1+\Omega z'}\right]} \ , \tag{A.37}$$

if measured today, recalling $D_{\rm c} = R_0 r$. Integrated, this gives the expression

$$R_0 S_k(r) = \frac{2}{H_0}\frac{\Omega z + (\Omega - 2)(\sqrt{1+\Omega z} - 1)}{\Omega^2(1+z)} \ . \tag{A.38}$$

The spatial curvature can be used to determine R_0 from the first Friedmann equation,

$$R_0 = \frac{1}{H_0\sqrt{\Omega_\kappa}} \ . \tag{A.39}$$

The luminosity distance $D_{\rm L}$ is related to the observed flux Φ of a source of luminosity L by

$$\Phi = \frac{L}{4\pi D_{\rm L}^2} \tag{A.40}$$

$$= L(1+z)^{-2}A^{-1} \ . \tag{A.41}$$

The source radiates outwards in a sphere with area given by the FLRW metric (Eqn. A.18), $A = 4\pi R_0^2 S_k^2(r)$, and radius r. The flux density will however suffer losses due to redshift and time dilation. Hence, the luminosity distance is defined by

$$D_{\rm L} = (1+z)R_0 S_k(r) \ , \tag{A.42}$$

and can be solved using Eqn. A.38.

The angular diameter distance, being the ratio between the physical transverse size to the angular size, is

$$D_{\rm A} = (1+z)^{-1}R_0 S_k(r) \ , \tag{A.43}$$

hence it is linked to the luminosity distance by $D_{\rm L} = (1+z)^2 D_{\rm A}$.

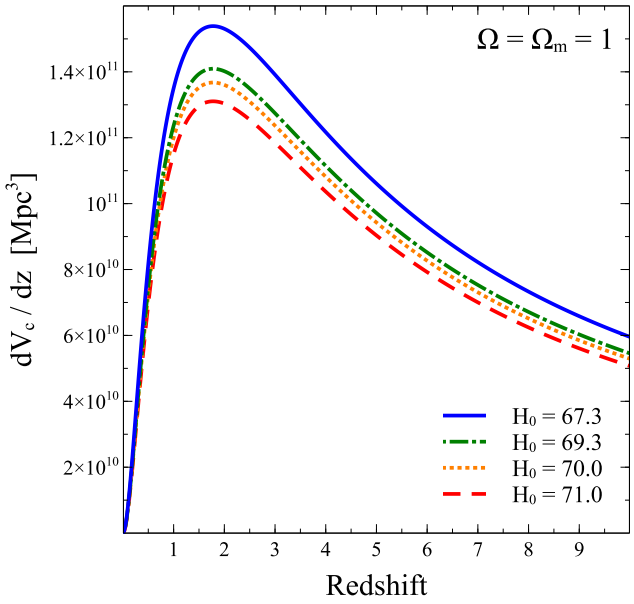

Fig. A.2: The differential comoving volume calculated for values of H_0 (in units of km s^{-1} Mpc^{-1}), using the definition for a flat, matter-dominated Universe, so that $\Omega = \Omega_m = 1$ (Eqn. A.46, see Peacock 2007). The blue solid curve gives the differential volume with $H_0 = 67.3$ and the green dash-dotted curve is the volume with $H_0 = 69.3$, as found by Planck and WMAP, respectively (see Table A.2). The orange dotted and red dashed curves represent the differential volume with cosmologies used to derive the X-ray detected ($H_0 = 70$, see Sec. 2.3.2) and γ-ray detected AGN ($H_0 = 71$, see Sec. 2.4.2), respectively.

The comoving volume element (Peacock 2007) is, for the metric of the form given in Eqn. A.18,

$$dV_c = 4\pi[R_0 S_k(r)]^2 R_0 dr \ . \tag{A.44}$$

Hence, a differential volume can be defined, using the relation between redshift and distance (Eqn. A.37) and its integrated form (Eqn. A.38). For a matter dominated Universe

$$\frac{dV_c}{dz} = \frac{16\pi}{H_0^3} \frac{[\Omega z + (\Omega - 2)(\sqrt{1+\Omega z} - 1)]^2}{\Omega^4 (1+z)^3 \sqrt{1+\Omega z}} \ . \tag{A.45}$$

For a flat Universe, where $\Omega = 1$, the differential volume is simplified to

$$\frac{dV_c}{dz} = \frac{16\pi}{H_0^3} \frac{[z - \sqrt{1+z} + 1]^2}{(1+z)^3 \sqrt{1+z}} \ . \tag{A.46}$$

Appendix B

Low-Energy Astrophysical Neutrinos

In the thesis we look at the high-energy neutrino emission in the Universe, and investigate if AGN are the source of this emission. However, the full picture of the neutrino emission in the Universe involves the lower energy emission as well, as seen in Fig. 1.9. In this Appendix we briefly outline the production of neutrinos in stellar sources; the detection of Solar neutrinos was the first step in the study of astrophysical neutrinos, followed by the discovery of neutrino emission from the supernova 1987A. The existence of the ubiquitous neutrino background is discussed as well. Even though it is currently out of the realm of observation, it holds significant information of the early Universe. The possibility of an indirect detection is nonetheless explored, such as looking for absorption lines in the spectra of neutrinos detected by *IceCube* (e.g. Ibe and Kaneta 2014; Ioka and Murase 2014).

We also give an overview in the first neutrino experiments and detectors, which led to the large-scale neutrino observatories we have today.

B.1 Solar Neutrinos

Solar neutrino astronomy was established by the Homestake solar neutrino experiment by Davis Jr. and Bahcall in 1969 which provided definite proof that the source of solar radiation was due to thermonuclear fusion processes. Through weak β-decay processes solar neutrinos are created predominantly as ν_{e} neutrinos. The MSW resonance effect (see Sec. 1.1.3) will however lead to two-thirds transitioning to ν_{μ} and ν_{τ} neutrinos as they travel from the solar core to detectors on Earth, with energies of order $\sim$MeV.

Decades of studies have confirmed the Standard Solar Model (SSM), where hydrogen is fused to helium in the solar core. This converts protons to neutrons, with the inevitable result of neutrino emission, following standard β-decay reactions. The theory of thermonuclear energy production was developed since the late 1920s (Giunti and Kim 2007), and the modern theory on stellar nucleosynthesis, describing the process dominant in the sun is called the pp-chain, and was developed by (among others) Hans Bethe in the 1930s (Bethe and Critchfield 1938; Bethe 1939).

The thermonuclear release of energy occurs because the constituent nucleons, i.e. protons and neutrons, have larger masses than combined in the nucleus, described in Sec. 1.1.4. The pp-chain, in which four protons and two electrons convert into a ^{4}He nucleus and emit two electron neutrinos, i.e.

$$4\mathrm{p} + 2\mathrm{e}^- \rightarrow {}^4\mathrm{He} + 2\nu_\mathrm{e} + Q \ , \tag{B.1}$$

the release of energy is $Q = 26.731$ MeV. The binding energy of the ^{4}He nucleus is $B(4,2) = 28.296$ MeV, so the excess energy is released as photons or kinetic energy of neutrinos.

The pp-chain consists of three main branches and two additional rare reactions, seen in Fig. B.1. Neutrinos are emitted in five of the eleven possible reactions; primarily in the initial reaction, named pp; in the rare pe$^-$p-reaction; in the ^{7}Be reaction of the pp-II branch; the ^{8}B of the pp-III branch; and in the hep-reactions.

Even though we receive an enormous amount of neutrino flux from the Sun, this detection is difficult as the majority of solar neutrinos are generated in the pp-reaction. These are of very low energy and as seen in Sec. B.4, the detector threshold energies of most observatories are far higher. The majority of detected neutrinos are from the high-energy ^{7}Be and ^{8}B reactions, falling in the energy range of the detector sensitivities, shown in Fig. B.4. Despite the pe$^-$p- and hep-neutrinos also being high-energy, such events are rare and not easily detected. Fig. B.1 shows the branching ratios of the various interactions occurring in the Sun, illustrating origins of various neutrino reactions.

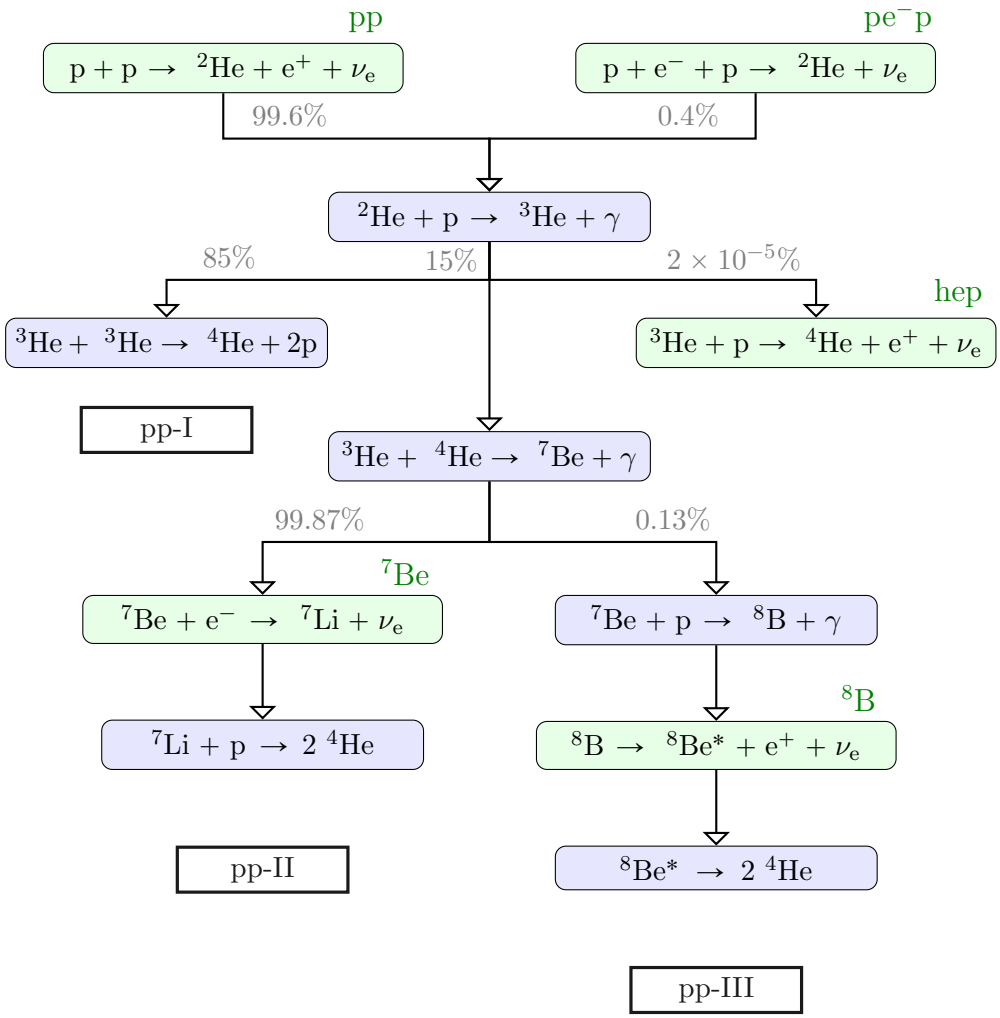

Fig. B.1: The pp-chain of thermonuclear reactions in stars. The reactions producing neutrinos are green, their name given above. In the blue boxes are the other reactions, and below each branch of the chain reactions, in black boxes is the name of the branch. The branching ratio of the reactions in the Sun are given for each level.

B.2 Stellar and Supernova Neutrinos

Due to the solar neutrino detections, this naturally means that neutrinos are also generated in all stellar sources. A full description is therefore useful in order to learn about the inner cores of stars and determine the neutrino SED at MeV energies. Combined with stellar evolution models, this may be constructed over cosmic time, and the evolution of MeV-neutrinos may be mapped. This is particularly interesting for studies of the structural formation in the Universe. Due to the detection of neutrinos from SN1987A, supernova neutrinos are another valuable source of information.

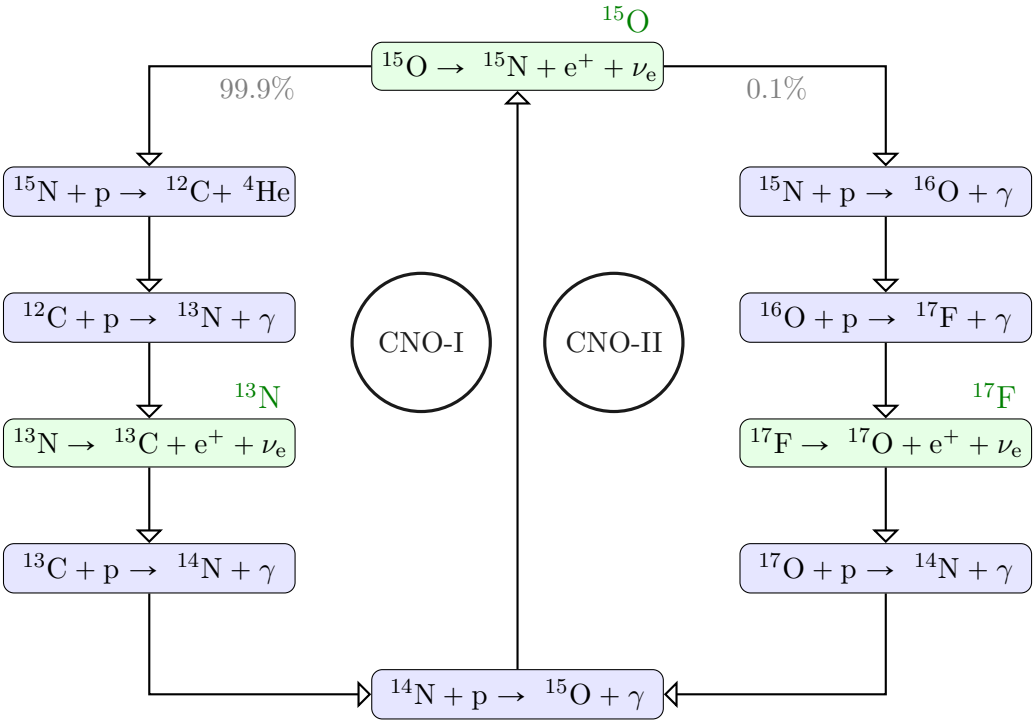

Fig. B.2: The CNO cycle of thermonuclear reactions in stars. The reactions producing neutrinos are green, and the name given to these reactions is given above the reactions. In the blue boxes are the other reactions, with the main CNO-I cycle on the left, and the CNO-II cycle on the right. The branching ratio of the reactions in the Sun are given for each level. These are important for stars of greater masses to that of the Sun, and the dominant fusion reaction for stars of about 1.3 times that of the Sun.

In addition to the pp-chain responsible for the nuclear fusion in stars, the CNO (carbon-nitrogen-oxygen) cycle is a further set of stellar thermonuclear reactions, shown in Fig. B.2. This is not important for the Sun, nor for stars of comparable or lower mass, due to temperature dependencies. Whereas the pp-chain requires temperatures of 4×10^6 K, the CNO cycle requires 1.5×10^7 K to be self-maintaining, and 1.7×10^7 K for it to be the dominant fusion process in a star. With a core temperature of 1.6×10^7 K, the Sun's ^{4}He production originating from the CNO cycle only accounts for about 1.7% of the total ^{4}He population.

The net effect of the CNO is the same as that of the pp-chain, in that four protons fuse (through carbon, nitrogen and oxygen isotopes) to ^{4}He-nuclei, neutrinos and positrons. The positrons will subsequently annihilate

with electrons to produce photons.

In addition to the CNO-I and CNO-II cycle (Fig. B.2), there are additional branches which are only important for particularly massive stars. These are produced in the CNO-III cycle, as

$$^{17}\mathrm{O} \rightarrow\ ^{18}\mathrm{F} \rightarrow\ ^{18}\mathrm{O} \rightarrow\ ^{15}\mathrm{N} \rightarrow\ ^{16}\mathrm{O} \rightarrow\ ^{17}\mathrm{F} \rightarrow\ ^{17}\mathrm{O}\ , \tag{B.2}$$

which diverges from the CNO-II branch in the ^{17}O reaction to produce ^{18}F and a neutrino, eventually joining the CNO-II branch again in the production of ^{15}N from the ^{18}O-reaction. Similarly, the CNO-IV branch (which is also only important in massive stars) diverges from the CNO-III branch in the reaction of ^{18}O, to produce the heavier ^{19}F nucleus instead of the ^{15}N nucleus in the CNO-II branch, joining it again in the production of ^{16}O, i.e.

$$^{19}\mathrm{F} \rightarrow^{16} \mathrm{O} \rightarrow^{17} \mathrm{F} \rightarrow^{17} \mathrm{O} \rightarrow^{18} \mathrm{F} \rightarrow^{18} \mathrm{O} \rightarrow^{19} \mathrm{F}\ . \tag{B.3}$$

The depletion of available hydrogen in the stellar core, driven by fusion processes, determines the life of a star. Whereas the pp-chain is slower, the CNO cycle drives massive stars to have shorter lives. Given the close link between neutrino emission and the fusion reactions in stars, knowledge of one will allow a closer study of the other. As such, stellar evolution can be examined closer by using stellar mass functions and star formation rates, and similarly the evolution of neutrino emission from stellar sources over cosmic time may also be deduced.

Neutrinos are also known to be emitted from supernovae, as was realised with the detection of neutrinos from SN1987A (e.g. Hirata et al. 1987, see Sec. B.4). Supernovae (SNe) are powerful explosions which end the lives of massive stars, and in the process eject enormous amounts of matter, along with a considerable population of neutrinos of energies between $10 - 30$ MeV. Whereas the photon signal from SNe may take hours or days to escape from the stellar envelope, neutrinos will rapidly escape the core. This means that the study of SN-neutrinos provides information about the very earliest stages of the explosion, inaccessible using photon astronomy.

SNe are classified according to the type of explosion which occurs, largely dependent on the progenitor star. A first classification is the presence of H-

lines in the spectra. If hydrogen is present, the SN is classified as a Type II; if these lines are absent, it is a Type I. Further classifications can be made across these types, depending on the mechanism of the explosion. This becomes apparent in the spectra of SNe when sufficient time has passed for the inner regions to become visible. While Type Ia SNe show Fe emission in their spectra, Types Ib, Ic, and Type II SNe are dominated by O and C emission lines.

Type Ia SNe are thought to be generated through thermonuclear mechanisms, where a carbon-oxygen white dwarf accretes mass from a close companion star. As the white dwarf depletes its source of thermonuclear fusion, the accretion of matter will allow it to reach the Chandrasekhar mass limit of $\approx 1.44\ M_{\odot}$. The white dwarf becomes unstable and begins to collapse, triggering the fusion of carbon and oxygen to heavier elements. This causes a thermonuclear explosion, and what is left is an expanding nebula without a central compact object. These SNe are however not expected to produce any significant neutrino flux.

An important source of SN neutrinos are however the remaining types of SNe. These, SNe Ib, Ic and II, are driven by more energetic mechanisms, with a progenitor star of mass $\geqslant 8M_{\odot}$. They are the end of the evolution of very massive stars, and the final explosion is caused by the shock wave produced when the stellar core collapses. It leaves behind a proto-neutron star surrounded by an ejected stellar envelope. In some cases, the ejected stellar envelope falls back onto the neutron star, hence it will collapse to a black hole. This occurs after the core-collapsing explosion.

Massive stars undergo all stages of fusion, from hydrogen through to silicon, with an inner dense iron-core. When there is no more nuclear fuel to burn, the iron core will contract and the temperature increases in the process

$$\gamma + {}^{56}\mathrm{Fe} \rightarrow 13\alpha + 4\mathrm{n}\ . \tag{B.4}$$

This reduces the pressure of the electrons aided by free electrons (in addition

to the electron capture of nuclei, with A nucleons of which are Z protons),

$$\begin{aligned} \mathrm{e}^- + N(A,Z) &\rightarrow N(A,Z-1) + \nu_\mathrm{e} \\ \mathrm{e}^- + \mathrm{p} &\rightarrow \mathrm{n} + \nu_\mathrm{e} \ . \end{aligned} \tag{B.5}$$

Neutrinos leave the core, carrying away most of the kinetic energy of the captured electrons at the onset of the collapse, with average neutrino energies around 15 MeV (Bahcall 1989). The pressure no longer supports the gravitational pull of the core initiating the collapse. With decreasing electron pressure the process of collapse accelerates. As the density in the core increases, even neutrinos are trapped in the collapsing material. With the formation of a proto-neutron star a shock develops when the stellar envelope collapses onto it. Neutrinos are crucial to subsequent steps of the process: the shock propagates through the infalling matter, with neutrinos produced en masse behind it by the transformation of most protons into neutrons through electron capture. Neutrinos pile up behind the shock and are released in a prompt electron neutrino burst, which can be distinguished from the thermal emission of neutrinos of all flavours.

These neutrinos are produced in the hot core of the proto-neutron star through pair annihilation, electron-nucleon and nucleon-nucleon bremsstrahlung, plasmon decay (e.g. Kantor and Gusakov 2007), and photo-annihilation. They free-stream out of the mantle of the newly formed neutron star, at the 'neutrinosphere'. These are energy- and flavour-dependent, thus a sphere for each neutrino flavour exists.

B.3 The Cosmic Neutrino Background

There exists a background of a relic neutrino population, similar to the photon background of the CMB. This background, the CνB, originates from the very first seconds after the Big Bang when neutrinos decoupled from matter. Though it contains information of the Universe when it was barely formed (i.e. much earlier than the CMB) its low temperature today suggests that it can never be directly observed.

In the early Universe, when the temperature of photons were $1-100$ MeV, neutrinos were in thermal equilibrium in hot plasma (mainly comprised of

electrons, positrons and photons) by the weak interactions

$$\begin{aligned} \nu + \bar{\nu} &\leftrightarrows \mathrm{e}^+ + \mathrm{e}^- \\ \nu(\bar{\nu}) + \mathrm{e}^+(\mathrm{e}^-) &\leftrightarrows \nu(\bar{\nu}) + \mathrm{e}^+(\mathrm{e}^-) \ . \end{aligned} \tag{B.6}$$

Neutrinos decoupled from the rest of the plasma when the temperature reached about $T_\gamma \sim 1$ MeV, however both neutrinos and photons remained at comparable temperatures as the Universe expanded as the neutrinos were relativistic at decoupling. As the neutrinos decoupled, only photons remained relativistic in equilibrium, whereas the electrons and positrons became non-relativistic transferring their entropy to the photons through pair annihilation. The photons therefore gained in density, as the pair production reaction became less likely to happen, which lead to an increase in temperature. Thus, the relation between the current CMB temperature, $T_{\gamma,0}^{\mathrm{CMB}}$, T_γ^{CMB} at redshift z is given by:

$$T_\gamma^{\mathrm{CMB}} = T_{\gamma,0}^{\mathrm{CMB}} \left(\frac{2}{g_s}\right)^{1/3} (1+z) \ , \tag{B.7}$$

where g_s are the degrees of freedom (equal to 2 for bosons, giving the value of the numerator fraction), which is $2 \times (7/8)$ for fermions. The temperature of the relic neutrinos today can be found by accounting for redshift losses,

$$T_{\nu,0}^{\mathrm{C}\nu\mathrm{B}} = \frac{T_\nu^{\mathrm{C}\nu\mathrm{B}}}{(1+z)} \ . \tag{B.8}$$

From measurements of the CMB temperature, $T_{\gamma,0}^{\mathrm{CMB}} = 2.725$ K$(= 2.348 \times 10^{-4}$ eV), the current temperature of the relic neutrinos can be estimated as

$$\begin{aligned} T_{\nu,0}^{\mathrm{C}\nu\mathrm{B}} &= \left(\tfrac{4}{11}\right)^{1/3} T_{\gamma,0}^{\mathrm{CMB}} \\ &= 1.945 \text{ K} (= 1.676 \times 10^{-4} \text{ eV}) \ . \end{aligned} \tag{B.9}$$

B.4 Experiments and Detectors

The first neutrino experiments were located at nuclear reactors and, later, at particle accelerators. All three neutrino flavours have been discovered through these means.

The very first neutrino detection was made by Cowan and Reines in 1956. The experiment took place at a nuclear reactor in Hanford; then Savannah River power plant in Georgia (Cowan et al. 1956; Reines and Cowan 1956). Located twelve metres underground, and eleven metres from the reactor, the

experiment was shielded from unwanted emissions. Nuclear reactors produce a constant neutrino flux of the order $10^{12} - 10^{13}$ cm^{-2}s^{-1}, and the average energy of the incoming reactor anti-neutrinos to the experiment was 3 MeV. Two tanks, containing 40 kg of cadmium chloride ($CdCl_2$) dissolved in 200 litres of water (H_2O), provided the proton target for the inverse β-decay reaction ($\bar{\nu}_e + p \rightarrow n + e^+$, see Eqn. 1.51). The water tanks were sandwiched between three liquid ($\sim$ 1400 litres) scintillator detectors, each containing 110 PMTs, as shown in Fig. B.3. Flashes of light were produced first as γ-rays, produced by the annihilation of the positron with an electron (Eqn. 1.43), reached the scintillators. Then, about 5μs later, additional flashes were produced by the emission of additional γ-rays in the absorption of a neutron by a cadmium nucleus, following

$$n + {}^{108}Cd \rightarrow {}^{109}Cd^* \rightarrow {}^{109}Cd + \gamma s \ . \tag{B.10}$$

The pair annihilation photons were each emitted with an energy of the electron rest mass, whereas the neutron capture process would release about 9 MeV of energy as γ-rays. This unique signature confirmed the existence of the neutrino, for which Reines won the 1995 Nobel Prize in Physics (as it is not awarded posthumously, Cowan did not share the prize).

The other neutrino flavours were detected in particle accelerators. Accelerators produce beams of highly energetic particles, producing a shower of secondary particles. In 1960, the Alternating Gradient Synchrotron at BNL produced a beam of protons with energies reaching 33 GeV – the highest energies achieved through man-made endeavours at the time.

L. M. Lederman, M. Schwartz and J. Steinberger used this accelerator to generate a 15-GeV proton beam, which they focussed on a beryllium target, producing a shower of pions (and kaons). These pions would subsequently decay into muons and neutrinos (see Eqns. 1.45-1.47). The beam was then passed through a 13.5 metres thick steel wall, suppressing the propagation of muons, and allowing predominantly neutrinos to pass through. Neutrinos were detected as they passed through a 10-ton spark chamber – a detector consisting of ninety aluminium plates surrounded by neon gas. The interaction

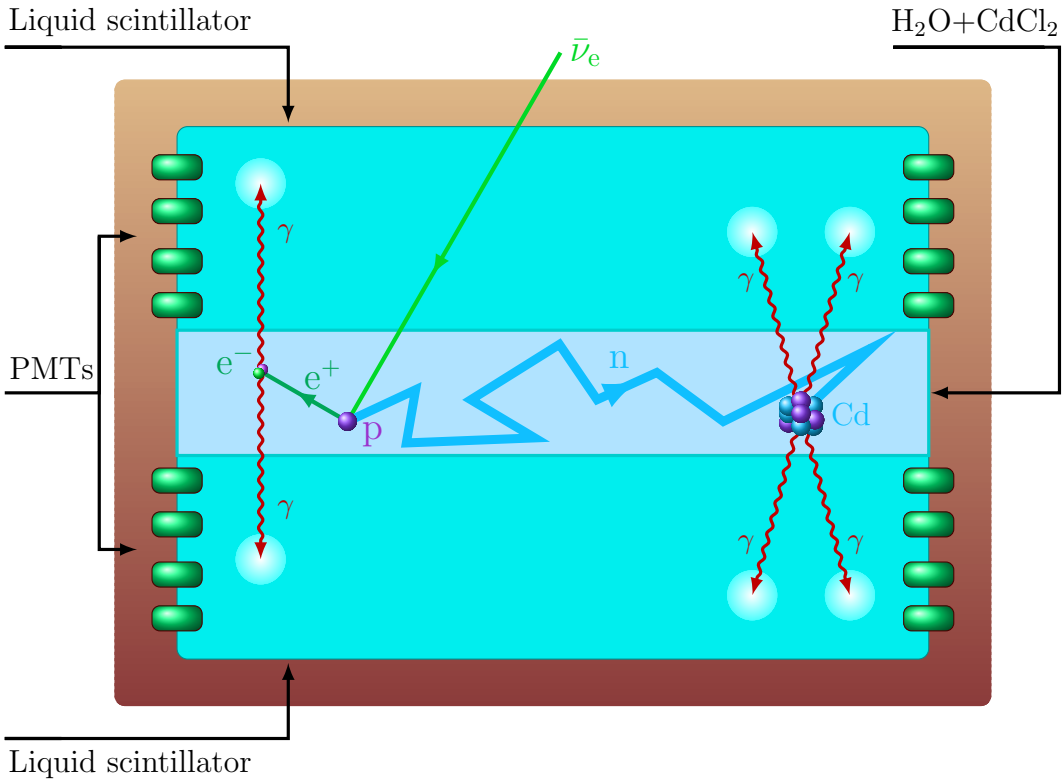

Fig. B.3: Illustration of the Cowan-Reines experiment. The tank with a water solution of cadmium chloride ($H_2O+CdCl_2$) is sandwiched between liquid scintillator detectors with PMTs connected in parallel. An anti-neutrino ($\bar{\nu}_e$) enters from the reactor, and interacts with the water solution through the inverse β-decay reaction. The positron (e^+) annihilates with an electron (e^-), producing a pair of γs. The neutron (n) diffuses, and is, after a delay, captured by a cadmium (Cd) nucleus, emitting additional γ-rays. These produce flashes in the scintillator, which is recorded by the PMTs.

between the beamed neutrinos and protons in the aluminium nuclei produced neutrons and muons (Eqn. 1.50), and the latter (charged) particle would create a spark trail as it ionised the gas. This muon trail was then photographed, and culminated in the discovery of the muon neutrino (Danby et al. 1962). Lederman, Schwartz and Steinberger won the 1988 Nobel Prize in Physics for this neutrino beam method, and for demonstrating the doublet structure of leptons through the discovery of the muon neutrino.

The third neutrino, the ν_τ, was discovered several decades later in the Fermilab DONUT (Direct Observation of the NU Tau) experiment, using the TEVatron circular particle accelerator (DONUT Collaboration et al. 2001).

Neutrinos are detected through the observation of their associated charged lepton, as seen above. The τ is, however, significantly heavier (see Fig. 1.2) than the e^- and μ, requiring the primary proton beam to be accelerated to much higher energies. Furthermore, it decays quickly, with a mean life time of $\approx 3 \times 10^{-13}$ s, and is therefore difficult to detect. The muon lifetime is, for comparison, about 2μs, and the electron is, for all intents and purposes, a stable particle (its lifetime is experimentally measured to $> 4.6 \times 10^{26}$ years – exceedingly longer than the age of the Universe).

The scientists involved in the DONUT experiment therefore used the TEVatron to generate a beam of protons to energies of 800 GeV, which was passed through a tungsten target to produce a shower of secondary mesons. Heavy mesons, such as the D_s would decay to produce a τ, which rapidly decayed to a ν_τ. The neutrino beam was then passed through magnets to deflect charged particles in the beam, and additional shielding to suppress further contamination in the beam from other particle species. The beam would then reached the hybrid emulsion spectrometer, the heart of the DONUT experiment. Here, the neutrinos interacted with nuclei in the the dense emulsion target sheets, producing τ-leptons that left identifiable trails detectable by layers of scintillation fibres (see Fig.1.13).

The most powerful particle accelerators today can reach energies of 13 TeV (the Large Hadron Collider at CERN), however, naturally occurring high-energy particle emission is observed at considerably higher energies. This implies that there are particle interactions which cannot be studied by man-made methods, however they can be indirectly studied with the construction of dedicated observatories.

The first experiment carried out with the purpose of studying astrophysical neutrinos was by Davis Jr. and Bahcall in 1969. They wanted to provide a test of thermonuclear fusion models as the source of Solar radiation, and thus designed an experiment in the Homestake Gold Mine in South Dakota, 1478 metres below the surface (Bahcall and Davis 2000). The Homestake Solar Neutrino Observatory had a threshold energy of $E_{\nu,\mathrm{th}} = 0.814$ MeV, and was sensitive to the high-energy ^{8}B flux (see Fig. B.4) – a by-product of the

pp-I and pp-II branches of the solar pp-cycle (see Fig. B.1, Sec. B.1). Bahcall calculated the predicted capture rate of neutrinos in the detector, and Davis Jr. tested this prediction in the experiment.

Using a radiochemical method, Solar neutrinos were detected as they interacted with chlorine nuclei in 380 cubic metres of cleaning fluid (predominantly chlorine) through the inverse β-decay reaction,

$$^{37}\mathrm{Cl} + \nu_{\mathrm{e}} \rightarrow ^{37}\mathrm{Ar} + \mathrm{e}^{-} \ . \tag{B.11}$$

The experiment uncovered a puzzle, as an anomaly in their data was discovered. They did indeed confirm a neutrino signal, however the detected rate was was lower by one-third of those theoretically predicted by Bahcall using the SSM. This deficiency is known as the Solar Neutrino Problem (SNP, Bahcall 1969, 1971), and led to the construction of further observatories to confirm the results (see e.g. Giunti and Kim 2007). Davis won the 2002 Nobel Prize in Physics with M. Koshiba for their cosmic neutrino detections.

In the 1990s the radiochemical Gallium experiment (GALLEX) was constructed in the Laboratori Nazionali del Gran Sasso (LNGS), Italy, with 101 tonnes of liquid gallium chloride ($\mathrm{GaCL_3}$-HCl) and 30.3 tonnes of gallium. In the late 1990s it was upgraded to the Gallium Neutrino Observatory (GNO), using the reaction

$$^{71}\mathrm{Ga} + \nu_{\mathrm{e}} \rightarrow ^{71}\mathrm{Ge} + \mathrm{e}^{-} \tag{B.12}$$

to confirm the SNP deficit of Solar neutrinos in the early 2000s. As the threshold energy of of the experiment was $E_{\nu,\mathrm{th}} = 0.233$ MeV, it was sensitive to low energy neutrinos from the fundamental pp-cycle (see Fig. B.4). It therefore detected neutrinos from all nuclear reactions in the Sun. The Soviet-American Gallium Experiment (SAGE) also reported a confirmation of the SNP. The experiment was conducted in the Russian Baksan Neutrino Observatory, and ran from the mid-1990s to the mid-2000s, about 2000 metres beneath the Caucasus mountains.

In 1983, the Kamioka Nucleon Decay Experiment (Kamiokande) began operation a kilometre underground in the Japanese Kamioka mine. It was designed to observe high-energy ^{8}B solar neutrinos through ν_e-sensitive reactions,

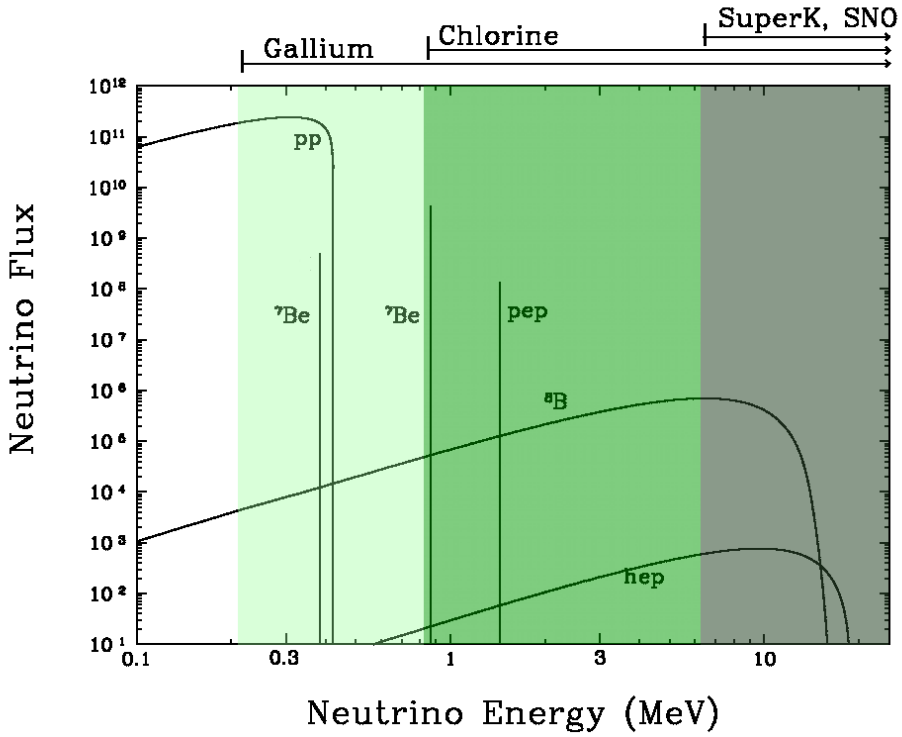

Fig. B.4: Predicted Solar neutrino energy spectrum from the Solar model of Bahcall and Pinsonneault (2004), for given by-products of the pp-I and pp-II branches. Units for neutrino fluxes from continuum sources is in $\mathrm{cm}^{-2}\mathrm{s}^{-1}\mathrm{MeV}^{-1}$, and for line sources the units are $\mathrm{cm}^{-2}\mathrm{s}^{-1}$. Above the figure are the threshold energies of various Solar experimental methods. The Homestake experiment used a chlorine target; the GALLEX/GNO experiments used a gallium target; the water Cherenkov method was used by Kamiokande/SuperK and SNO. See text for details. Adapted from figure in Bahcall and Peña-Garay (2004).

and detected neutrinos interacting with water nuclei in a Cherenkov detector. The inner structure of the detector contained 2142 tonnes of purified water and 948 PMTs to register interactions. The outer volume contained another 1500 tonnes of water, and an additional 123 PMTs.

Between 1983 and 1996, the Kamiokande experiment went through three phases, lowering the threshold energy from $E_{\nu,\mathrm{th}} = 9.3$ MeV, to $E_{\nu,\mathrm{th}} = 7.0$ MeV in the upgraded Kamiokande-III phase. The construction of a 50 kilotonne water Cherenkov detector was completed near Kamiokande in 1996. It was named Super-Kamiokande (SK), and was upgraded to Super-Kamiokande-

II (SK-II) in the early 2000s. This had an effective volume of 630 cubic metres, and a threshold energy for Solar ν_e of 5.0 MeV. The corresponding neutrino threshold energy was 4.7 MeV (see Fig. B.4). The SK experiment proved that neutrinos came from the Sun, as the Cherenkov method provided directional information, and in 1998 they announced a confirmation of the SNP, providing the first strong evidence of neutrino oscillation phenomenon as a solution to the problem (see Sec. 1.1.3).

The solution to the SNP was confirmed by the Sudbury Neutrino Observatory (SNO), located 2092 metres below ground in Creighton mine near Sudbury, Canada. Using 1000 tonnes of ultra-pure water in a 12 metre diameter container, Cherenkov light was detected by 9456 PMTs immersed in the water. SNO detected not only neutrinos through the CC reactions, but also NC and ES. Whereas the rate of ν_e-neutrinos through CC-interactions were about 35% of the predicted rate, the detection rate of neutrino through NC interactions agreed with the predictions of the SSM. This indicated that the "missing" ν_e had transitioned to ν_μ- and ν_τ-flavours on their journey from the centre of the Sun to the Earth through the MSW resonance (see e.g. Ahmad et al. 2001; Giunti and Kim 2007, see also Sec. 1.1.3). The detector was sensitive to ^{8}B Solar neutrinos, with a CC threshold energy of 1.442 MeV of the ν_e. The threshold energy for NC reactions of all flavours was $E_{\nu,\mathrm{th}} = 2.224$ MeV. Similar for all types of neutrinos, the threshold energy of the detector for ES reactions was 5.7 MeV.

The results of the SK-II and SNO experiments therefore definitively proved the neutrino oscillation phenomenon, indicating furthermore that neutrinos in fact have mass.

Kamiokande-II was also involved with the first detection of neutrinos from outside our solar system (Hirata et al. 1987, 1988), and so, along with the solar neutrino studies, marked the beginning of extra-solar neutrino astronomy. In February of 1987, a supernova explosion in the Large Magellanic Cloud (LMC) was observed. A few hours before the photonic emission reached Earth, the Kamioka observatory was one of three to detect neutrino events. The Irvine-Michigan-Brookhaven (IMB) water Cherenkov detector (in the USA,

Bionta et al. 1987; Bratton et al. 1988), the Baksan Underground Scintillation Telescope (in the former Soviet Union, Alekseev et al. 1987; Alexeyev et al. 1988), and Kamioka detectors in Japan, simultaneously registered a burst of neutrino events in the space of ten seconds (e.g. Koshiba 1992, see also Sec. B.2). The detectors recorded about 25 events in total, which corresponded to the visual detection of the SN explosion, now known as SN1987A, three hours later.

A natural extension to the confirmed Solar and SN-neutrinos would be the existence of a population of neutrinos with even higher energies. This idea was conceptualised by the DUMAND collaboration in the late 1970s, and a detector capable of observing the highest-energy neutrinos came with the cubic-kilometre sized *IceCube* observatory (see Sec. 1.3).

List of Symbols

List of Abbreviations

ΛCDM	lambda cold dark matter 221
AGN	active galactic nuclei 61
AMANDA	Antarctic Muon And Neutrino Detector Array 53
ANITA	Antarctic Impulsive Transient Antenna 59
ANTARES	Astronomy with a Neutrino Telescope and Abyss environmental REsearch 53
ARA	Askaryan Radio Array 59
AURA	Askaryan Under-ice Radio Array 60
BAT	Burst Alert Telescope 80
BLR	broad-line region 66
BLRG	broad-line radio galaxy 63
BNL	Brookhaven National Laboratory 17
CνB	cosmic neutrino background 231
CC	charged current 27
Cen A	FR-I radio galaxy Centaurus A 129
CERN	European Organisation for Nuclear Research 18
ChaMP	Chandra Multi-wavelength Project 80
Chandra	*Chandra* X-ray Observatory 79
CMB	cosmic microwave background 41
CNO	carbon-nitrogen-oxygen 228
CR	cosmic ray 38
CXRB	cosmic X-ray background 74
DONUT	Direct Observation of the NU Tau 234
DUMAND	Deep Underwater Muon and Neutrino Detection 52
EBL	extragalactic background light 35
EGB	extragalactic γ-ray background 81

ES	elastic scattering 36
ESA	European Space Agency 221
Fermi	Fermi Gamma-Ray Space Telescope 83
Fermilab	Fermi National Accelerator Laboratory 18
FR	Fanaroff-Riley 63
FLRW	Friedmann-Lemaître-Robertson-Walker 218
FSRQ	flat spectrum radio quasar 65
FWHM	full width half maximum 66
GALLEX	GALLium EXperiment 236
GNO	Gallium Neutrino Observatory 236
GRB	gamma-ray burst 39
GVD	Gigaton Volume Detector 53
GWS	Glashow-Weinberg-Salam 18
GZK	Greisen-Zatsepin-Kuzmin 43
HBL	high-energy synchrotron peaked BL Lac 68
HE	high-energy 56
HPQ	high-polarisation quasar 69
HSP	high synchrotron peaked 69
IBL	intermediate-energy synchrotron peaked BL Lac 68
IC	inverse Compton 183
IGM	intergalactic medium 39
IceCube	IceCube Neutrino Observatory 53
IMB	Irvine-Michigan-Brookhaven 238
IR	infra-red 70
ISP	intermediate synchrotron peaked 69
LAT	Large Area Telescope 83
LDDE	luminosity dependent density evolution 77
LF	luminosity function 62
LBL	low-energy synchrotron peaked BL Lac 68
LMC	Large Magellanic Cloud 238
LNGS	Laboratori Nazionali del Gran Sasso 236
LPQ	low-polarisation quasar 69

LSP	low synchrotron peaked 69
LUNASKA	Lunar Ultra-high energy Neutrino Astrophysics with the SKA 60
MPLE	modified pure luminosity evolution 76
MSW	Mikheyev-Smirnov-Wolfenstein 26
NASA	National Aeronautics and Space Administration 221
NC	neutral current 27
NEMO	Neutrino Mediterranean Observatory 57
NESTOR	Neutrino Extended Submarine Telescope with Oceanographic Research . 57
NLR	narrow-line region 66
NLRG	narrow-line radio galaxy 63
OVV	optical violent variables 65
pγ	proton-photon 32
PAO	Pierre Auger Observatory 57
PDE	pure density evolution 76
PLE	pure luminosity evolution 76
PMNS	Pontecorvo-Maki-Nakagawa-Sakata 23
PMT	photomultiplier tube 51
Planck	Planck space observatory 221
pp	proton-proton 30
QCD	Quantum Chromodynamics 19
QED	Quantum Electrodynamics 20
QSO	quasi-stellar object 63
quasar	quasi-stellar radio source 65
RICE	Radio Ice Cherenkov Experiment 59
RLQ	radio-loud quasars 65
ROSAT	Röntgensatellit 79
RQQ	radio-quiet quasars 63
SAGE	Soviet-American Gallium Experiment 236
SED	spectral energy distribution 68
SK	Super-Kamiokande 237
SMBH	super-massive black hole 49
SN(e)	supernova(e) 229

SNO	Sudbury Neutrino Observatory 238
SNP	Solar Neutrino Problem 236
SNR	supernova remnant 39
SSA	synchrotron self-absorption 185
SSC	synchrotron self-Compton 183
SSM	Standard Solar Model 226
SSRQ	steep spectrum radio quasar 65
Swift	Swift Gamma-Ray Burst Mission 80
Sy1, Sy2	Seyfert 1, Seyfert 2 63
UHE	ultrahigh-energy 61
UHECR	ultrahigh-energy cosmic ray 38
UV	ultraviolet 63
WMAP	Wilkinson Microwave Anisotropy Probe 221
XLF	X-ray luminosity function 75
XMM-Newton	X-ray Multi-Mirror Mission – Newton 79
γLF	γ-ray luminosity function 81

Bibliography

Aab, A., Abreu, P., Aglietta, M., Ahn, E. J., Al Samarai, I., et al. (2015), Improved limit to the diffuse flux of ultrahigh energy neutrinos from the Pierre Auger Observatory, *Phys. Rev. D* **91**(9), 092008.

Aad, G., Abajyan, T., Abbott, B., Abdallah, J., Abdel Khalek, S., et al. (2013), Measurements of Higgs boson production and couplings in diboson final states with the ATLAS detector at the LHC, *Physics Letters B* **726**, 88–119.

Aartsen, M. G., Abbasi, R., Abdou, Y., Ackermann, M., Adams, J., et al. (2013), First Observation of PeV-Energy Neutrinos with IceCube, *Physical Review Letters* **111**(2), 021103.

Aartsen, M. G., Abbasi, R., Ackermann, M., Adams, J., Aguilar, J. A., et al. (2014a), Search for a diffuse flux of astrophysical muon neutrinos with the IceCube 59-string configuration, *Phys. Rev. D* **89**(6), 062007.

Aartsen, M. G., Abraham, K., Ackermann, M., Adams, J., Aguilar, J. A., et al. (2015a), Evidence for Astrophysical Muon Neutrinos from the Northern Sky with IceCube, *Physical Review Letters* **115**(8), 081102.

Aartsen, M. G., Ackermann, M., Adams, J., Aguilar, J. A., Ahlers, M., et al. (2014b), Observation of High-Energy Astrophysical Neutrinos in Three Years of IceCube Data, *Physical Review Letters* **113**(10), 101101.

Aartsen, M. G., Ackermann, M., Adams, J., Aguilar, J. A., Ahlers, M., et al. (2015b), Atmospheric and astrophysical neutrinos above 1 TeV interacting in IceCube, *Phys. Rev. D* **91**(2), 022001.

Abazajian, K. N., Blanchet, S. and Harding, J. P. (2011), Contribution of blazars to the extragalactic diffuse gamma-ray background and their future spatial resolution, *Phys. Rev. D* **84**(10), 103007.

Abbasi, R., Abdou, Y., Abu-Zayyad, T., Ackermann, M., Adams, J., et al. (2012), An absence of neutrinos associated with cosmic-ray acceleration in γ-ray bursts, *Nature* **484**, 351–354.

Abbasi, R. U., Abu-Zayyad, T., Allen, M., Amman, J. F., Archbold, G., et al. (2008), First Observation of the Greisen-Zatsepin-Kuzmin Suppression, *Physical Review Letters* **100**(10), 101101.

Abdo, A. A., Ackermann, M., Agudo, I., Ajello, M., Aller, H. D., et al. (2010a), The Spectral Energy Distribution of Fermi Bright Blazars, *ApJ* **716**, 30–70.

Abdo, A. A., Ackermann, M., Ajello, M., Antolini, E., Baldini, L., et al. (2010b), The Fermi-LAT High-Latitude Survey: Source Count Distributions and the Origin of the Extragalactic Diffuse Background, *ApJ* **720**, 435–453.

Abraham, J., Abreu, P., Aglietta, M., Aguirre, C., Allard, D., et al. (2008), Observation of the Suppression of the Flux of Cosmic Rays above 4×10^{19}eV, *Physical Review Letters* **101**(6), 061101.

Abreu, P., Aglietta, M., Ahn, E. J., Albuquerque, I. F. M., Allard, D., et al. (2011), Search for ultrahigh energy neutrinos in highly inclined events at the Pierre Auger Observatory, *Phys. Rev. D* **84**(12), 122005.

Achterberg, A., Ackermann, M., Adams, J., Ahrens, J., Andeen, K., et al. (2007), Multiyear search for a diffuse flux of muon neutrinos with AMANDA-II, *Phys. Rev. D* **76**(4), 042008.

Ageron, M., Aguilar, J. A., Al Samarai, I., Albert, A., Ameli, F., André, M., Anghinolfi, M., Anton, G., Anvar, S., Ardid, M. and et al. (2011), ANTARES: The first undersea neutrino telescope, *Nuclear Instruments and Methods in Physics Research A* **656**, 11–38.

Aguilar, J. A., Samarai, I. A., Albert, A., André, M., Anghinolfi, M., et al. (2011), Search for a diffuse flux of high-energy ν with the ANTARES neutrino telescope, *Physics Letters B* **696**, 16–22.

Ahlers, M. and Halzen, F. (2012), Minimal cosmogenic neutrinos, *Phys. Rev. D* **86**(8), 083010.

Ahmad, Q. R., Allen, R. C., Andersen, T. C., Anglin, J. D., Bühler, G., et al. (2001), Measurement of the Rate of $\nu_e + \mathrm{d} \rightarrow \mathrm{p} + \mathrm{p} + \mathrm{e}^-$ Interactions Produced by ^{8}B Solar Neutrinos at the Sudbury Neutrino Observatory, *Physical Review Letters* **87**(7), 071301.

Ahrens, J., Bai, X., Barwick, S. W., Bay, R. C., Becka, T., et al. (2003), Limits on Diffuse Fluxes of High Energy Extraterrestrial Neutrinos with the AMANDA-B10 Detector, *Physical Review Letters* **90**(25), 251101.

Aird, J., Nandra, K., Laird, E. S., Georgakakis, A., Ashby, M. L. N., et al. (2010), The evolution of the hard X-ray luminosity function of AGN, *MNRAS* **401**, 2531–2551.

Ajello, M., Costamante, L., Sambruna, R. M., Gehrels, N., Chiang, J., et al. (2009), The Evolution of Swift/BAT Blazars and the Origin of the MeV Background, *ApJ* **699**, 603–625.

Ajello, M., Romani, R. W., Gasparrini, D., Shaw, M. S., Bolmer, J., et al. (2014), The Cosmic Evolution of Fermi BL Lacertae Objects, *ApJ* **780**, 73.

Ajello, M., Shaw, M. S., Romani, R. W., Dermer, C. D., Costamante, L., et al. (2012), The Luminosity Function of Fermi-detected Flat-spectrum Radio Quasars, *ApJ* **751**, 108.

Alekseev, E. N., Alekseeva, L. N., Volchenko, V. I. and Krivosheina, I. V. (1987), Possible detection of a neutrino signal on 23 February 1987 at the Baksan underground scintillation telescope of the Institute of Nuclear Research, *Soviet Journal of Experimental and Theoretical Physics Letters* **45**, 589.

Alexeyev, E. N., Alexeyeva, L. N., Krivosheina, I. V. and Volchenko, V. I. (1988), Detection of the neutrino signal from SN 1987A in the LMC using the INR Baksan underground scintillation telescope, *Physics Letters B* **205**, 209–214.

Alvarez-Muñiz, J. and Halzen, F. (2002), Possible High-Energy Neutrinos from the Cosmic Accelerator RX J1713.7-3946, *ApJL* **576**, L33–L36.

Anchordoqui, L. A., Barger, V., Cholis, I., Goldberg, H., Hooper, D., et al. (2013), Cosmic Neutrino Pevatrons: A Brand New Pathway to Astronomy, Astrophysics, and Particle Physics, *ArXiv e-prints* .

Anchordoqui, L. A., Goldberg, H., Halzen, F. and Weiler, T. J. (2004), Neutrino bursts from Fanaroff Riley I radio galaxies, *Physics Letters B* **600**, 202–207.

Anchordoqui, L. A., Goldberg, H., Hooper, D., Sarkar, S. and Taylor, A. (2007), Predictions for the cosmogenic neutrino flux in light of new data from the Pierre Auger Observatory, *Phys. Rev. D* **76**(12), 123008.

Andrés, E., Askebjer, P., Bai, X., Barouch, G., Barwick, S. W., et al. (2001), Observation of high-energy neutrinos using Čerenkov detectors embedded deep in Antarctic ice, *Nature* **410**, 441–443.

Antonucci, R. (1993), Unified models for active galactic nuclei and quasars, *ARA&A* **31**, 473–521.

Antonucci, R. R. J. and Ulvestad, J. S. (1985), Extended radio emission and the nature of blazars, *ApJ* **294**, 158–182.

Argüelles, C. A., Bustamante, M. and Gago, A. M. (2010), IceCube expectations for two high-energy neutrino production models at active galactic nuclei, *J. Cosmology Astropart. Phys.* **12**, 5.

Arnison, G., Astbury, A., Aubert, B., Bacci, C., Bauer, G., et al. (1983a), Experimental observation of isolated large transverse energy electrons with associated missing energy at $\sqrt{(}s)$=540 GeV, *Physics Letters B* **122**, 103–116.

Arnison, G., Astbury, A., Aubert, B., Bacci, C., Bauer, G., et al. (1983b), Experimental observation of lepton pairs of invariant mass around 95 GeV/c^2 at the CERN SPS collider, *Physics Letters B* **126**, 398–410.

Arteaga-Velázquez, J. C. (2012), Neutrino production from photo-hadronic interactions of the gamma flux from Active Galactic Nuclei with their gas content, *Astroparticle Physics* **37**, 40–50.

Asano, K. and Nagataki, S. (2006), Very High Energy Neutrinos Originating from Kaons in Gamma-Ray Bursts, *ApJL* **640**, L9–L12.

ATLAS Collaboration Aad, G., Abajyan, T., Abbott, B., Abdallah, J., et al. (2012), Observation of a new particle in the search for the Standard Model Higgs boson with the ATLAS detector at the LHC, *Physics Letters B* **716**, 1–29.

Atoyan, A. and Dermer, C. D. (2001), High-Energy Neutrinos from Photomeson Processes in Blazars, *Physical Review Letters* **87**(22), 221102.

Atoyan, A. M. and Dermer, C. D. (2003), Neutral Beams from Blazar Jets, *ApJ* **586**, 79–96.

Avni, Y. and Bahcall, J. N. (1980), On the simultaneous analysis of several complete samples - The V/Vmax and Ve/Va variables, with applications to quasars, *ApJ* **235**, 694–716.

Avrorin, A. V., Aynutdinov, V. M., Balkanov, V. A., Belolaptikov, I. A., Bogorodsky, D. Y., et al. (2009), Search for high-energy neutrinos in the Baikal neutrino experiment, *Astronomy Letters* **35**, 651–662.

Avrorin, A. V., Aynutdinov, V. M., Belolaptikov, I. A., Bogorodsky, D. Y., Brudanin, V. B., et al. (2013), Current status of the BAIKAL-GVD project, *Nuclear Instruments and Methods in Physics Research A* **725**, 23–26.

Aynutdinov, V., Avrorin, A., Balkanov, V., Belolaptikov, I., Bogorodsky, D., et al. (2009), Baikal neutrino telescope – An underwater laboratory for astroparticle physics and environmental studies, *Nuclear Instruments and Methods in Physics Research A* **598**, 282–288.

Aynutdinov, V., Balkanov, V., Belolaptikov, I., Bezrukov, L., Borschov, D., et al. (2006), Search for a diffuse flux of high-energy extraterrestrial neutrinos with the NT200 neutrino telescope, *Astroparticle Physics* **25**, 140–150.

Baerwald, P. and Guetta, D. (2013), Estimation of the Neutrino Flux and Resulting Constraints on Hadronic Emission Models for Cyg X-3 Using AGILE Data, *ApJ* **773**, 159.

Bagnaia, P., Banner, M., Battiston, R., Bloch, P., Bonaudi, F., et al. (1983), Evidence for $Z^0 \rightarrow e^+e^-$ at the CERN pp collider, *Physics Letters B* **129**, 130–140.

Bahcall, J. N. (1969), Neutrinos from the Sun, *Scientific American* **221**, 28–37.

Bahcall, J. N. (1971), Some Unsolved Problems in Astrophysics, *AJ* **76**, 283.

Bahcall, J. N. (1989), *Neutrino astrophysics*, Cambridge University Press.

Bahcall, J. N. and Davis, Jr., R. (2000), The Evolution of Neutrino Astronomy, *PASP* **112**, 429–433.

Bahcall, J. N. and Peña-Garay, C. (2004), Solar models and solar neutrino oscillations, *New Journal of Physics* **6**, 63.

Bahcall, J. N. and Pinsonneault, M. H. (2004), What Do We (Not) Know Theoretically about Solar Neutrino Fluxes?, *Physical Review Letters* **92**(12), 121301.

Banner, M., Battiston, R., Bloch, P., Bonaudi, F., Borer, K., et al. (1983), Observation of single isolated electrons of high transverse momentum in events with missing transverse energy at the CERN pp collider, *Physics Letters B* **122**, 476–485.

Barger, A. J. (2005), The cosmic history of the X-ray background: One contribution of 13 to a Discussion Meeting 'The impact of active galaxies on the Universe at large', *Royal Society of London Philosophical Transactions Series A* **363**, 685–694.

Barthel, P. D. (1989), Is every quasar beamed?, *ApJ* **336**, 606–611.

Beall, J. H. and Bednarek, W. (2002), Neutrinos from Early-Phase, Pulsar-driven Supernovae, *ApJ* **569**, 343–348.

Becker, J. K. (2008), High-energy neutrinos in the context of multimessenger astrophysics, *Phys. Rep.* **458**, 173–246.

Becker, J. K., Biermann, P. L. and Rhode, W. (2005), The diffuse neutrino flux from FR-II radio galaxies and blazars: A source property based estimate, *Astroparticle Physics* **23**, 355–368.

Becker, J. K. and Biermann, P. L. (2009), Neutrinos from active black holes, sources of ultra high energy cosmic rays, *Astroparticle Physics* **31**, 138–148.

Becker, J. K., Meli, A. and Biermann, P. L. (2011), Neutrinos from photo-hadronic interactions in Pks2155-304, *Nuclear Instruments and Methods in Physics Research A* **630**, 269–272.

Becker Tjus, J., Eichmann, B., Halzen, F., Kheirandish, A. and Saba, S. M. (2014), High-energy neutrinos from radio galaxies, *Phys. Rev. D* **89**(12), 123005.

Begelman, M. C., Rudak, B. and Sikora, M. (1990), Consequences of relativistic proton injection in active galactic nuclei, *ApJ* **362**, 38–51.

Bell, A. R. (1978), The acceleration of cosmic rays in shock fronts. I, *MNRAS* **182**, 147–156.

Bennett, C. L., Larson, D., Weiland, J. L., Jarosik, N., Hinshaw, G., et al. (2013), Nine-year Wilkinson Microwave Anisotropy Probe (WMAP) Observations: Final Maps and Results, *ApJS* **208**, 20.

Benvenuti, A., Cheng, D. C., Cline, D., Ford, W. T., Imlay, R., et al. (1974), Observation of Muonless Neutrino-Induced Inelastic Interactions, *Physical Review Letters* **32**, 800–803.

Berat, C. and Pierre Auger Collaboration (2013), Radio detection of extensive air showers at the Pierre Auger Observatory, *Nuclear Instruments and Methods in Physics Research A* **718**, 471–474.

Beresinsky, V. S. and Zatsepin, G. T. (1969), Cosmic rays at ultra high energies (neutrino?), *Physics Letters B* **28**, 423–424.

Berezinskii, V. S. and Ozernoi, L. M. (1981), Neutrino dating of the galaxy formation epoch, *A&A* **98**, 50–56.

Berezinskiĭ, V. S. (1981), MEETINGS AND CONFERENCES: The neutrino astronomy of high energies: sources and fluxes, *Soviet Physics Uspekhi* **24**, 242–244.

Berezinsky, V., Gazizov, A., Kachelrieß, M. and Ostapchenko, S. (2011), Restricting UHECRs and cosmogenic neutrinos with Fermi-LAT, *Physics Letters B* **695**, 13–18.

Berezinsky, V. and Dokuchaev, V. (2006), High-energy neutrino as observational signature of massive black hole formation, *A&A* **454**, 401–407.

Beringer, J., Arguin, J.-F., Barnett, R. M., Copic, K., Dahl, O., et al. (2012), Review of Particle Physics, *Phys. Rev. D* **86**(1), 010001.
(and 2013 partial update for the 2014 edition).

Best, P. N. (2009), Radio source populations: Results from SDSS, *Astronomische Nachrichten* **330**, 184–189.

Bethe, H. A. (1939), Energy Production in Stars, *Physical Review* **55**, 434–456.

Bethe, H. A. and Critchfield, C. L. (1938), The Formation of Deuterons by Proton Combination, *Physical Review* **54**, 248–254.

Biermann, P. L. and Strittmatter, P. A. (1987), Synchrotron emission from shock waves in active galactic nuclei, *ApJ* **322**, 643–649.

Bionta, R. M., Blewitt, G., Bratton, C. B., Casper, D. and Ciocio, A. (1987), Observation of a neutrino burst in coincidence with supernova 1987A in the Large Magellanic Cloud, *Physical Review Letters* **58**, 1494–1496.

Bird, D. J., Corbató, S. C., Dai, H. Y., Dawson, B. R., Elbert, J. W., et al. (1993), Evidence for correlated changes in the spectrum and composition of

cosmic rays at extremely high energies, *Physical Review Letters* **71**, 3401–3404.

Blandford, R. D. and Königl, A. (1979), Relativistic jets as compact radio sources, *ApJ* **232**, 34–48.

Blandford, R. D. and Payne, D. G. (1982), Hydromagnetic flows from accretion discs and the production of radio jets, *MNRAS* **199**, 883–903.

Blandford, R. D. and Rees, M. J. (1978), Extended and compact extragalactic radio sources - Interpretation and theory, *Phys. Scr* **17**, 265–274.

Blandford, R. D. and Znajek, R. L. (1977), Electromagnetic extraction of energy from Kerr black holes, *MNRAS* **179**, 433–456.

Blumenthal, G. R. and Gould, R. J. (1970), Bremsstrahlung, Synchrotron Radiation, and Compton Scattering of High-Energy Electrons Traversing Dilute Gases, *Reviews of Modern Physics* **42**, 237–271.

Bratton, C. B., Casper, D., Ciocio, A., Claus, R., Crouch, M., et al. (1988), Angular distribution of events from SN1987A, *Phys. Rev. D* **37**, 3361–3363.

Bray, J. D., Ekers, R. D., Protheroe, R. J., James, C. W., Phillips, C. J., et al. (2013), LUNASKA neutrino search with the Parkes and ATCA telescopes, *in* R. Lahmann, T. Eberl, K. Graf, C. James, T. Huege, T. Karg and R. Nahnhauer (eds.), *American Institute of Physics Conference Series*, Vol. 1535 of *American Institute of Physics Conference Series*, pp.21–26.

Bray, J. D., Ekers, R. D., Roberts, P., Reynolds, J. E., James, C. W., et al. (2015), A limit on the ultra-high-energy neutrino flux from lunar observations with the Parkes radio telescope, *ArXiv e-prints* .

Capone, A., Aiello, S., Aloisio, A., Ameli, F., Amore, I., et al. (2009), Recent results and perspectives of the NEMO project, *Nuclear Instruments and Methods in Physics Research A* **602**, 47–53.

Cavagnolo, K. W., McNamara, B. R., Nulsen, P. E. J., Carilli, C. L., Jones, C. and Bîrzan, L. (2010), A Relationship Between AGN Jet Power and Radio Power, *ApJ* **720**, 1066–1072.

Chadwick, J. (1932), Possible Existence of a Neutron, *Nature* **129**, 312.

Chiarusi, T. and Spurio, M. (2010), High-energy astrophysics with neutrino telescopes, *European Physical Journal C* **65**, 649–701.

Christiansen, H. R., Orellana, M. and Romero, G. E. (2006), High-energy neutrino emission from x-ray binaries, *Phys. Rev. D* **73**(6), 063012.

CMS Collaboration Chatrchyan, S., Khachatryan, V., Sirunyan, A. M., Tumasyan, A., et al. (2012), Observation of a new boson at a mass of 125 GeV with the CMS experiment at the LHC, *Physics Letters B* **716**, 30–61.

Coles, P. and Lucchin, F. (2002), *Cosmology: The Origin and Evolution of Cosmic Structure, Second Edition*, Second edition, John Wiley and Sons.

Connolly, A. (2008), The radio Cherenkov technique for ultra-high energy neutrino detection, *Nuclear Instruments and Methods in Physics Research A* **595**, 260–263.

Cowan, Jr., C. L., Reines, F., Harrison, F. B., Kruse, H. W. and McGuire, A. D. (1956), Detection of the Free Neutrino: A Confirmation, *Science* **124**, 103–104.

Cuoco, A. and Hannestad, S. (2008), Ultrahigh energy neutrinos from Centaurus A and the Auger hot spot, *Phys. Rev. D* **78**(2), 023007.

Danby, G., Gaillard, J.-M., Goulianos, K., Lederman, L. M., Mistry, N., et al. (1962), Observation of High-Energy Neutrino Reactions and the Existence of Two Kinds of Neutrinos, *Physical Review Letters* **9**, 36–44.

De Young, D. S. (1972), The Distribution of Radiation from Relativistically Expanding Radio Sources, *ApJ* **177**, 573.

Dermer, C. D., Murase, K. and Inoue, Y. (2014), Photopion production in black-hole jets and flat-spectrum radio quasars as PeV neutrino sources, *Journal of High Energy Astrophysics* **3**, 29–40.

Dermer, C. D., Murase, K. and Takami, H. (2012), Variable Gamma-Ray Emission Induced by Ultra-high Energy Neutral Beams: Application to 4C +21.35, *ApJ* **755**, 147.

Dermer, C. D., Ramirez-Ruiz, E. and Le, T. (2007), Correlation of Photon and Neutrino Fluxes in Blazars and Gamma-Ray Bursts, *ApJL* **664**, L67–L70.

Donato, D., Ghisellini, G., Tagliaferri, G. and Fossati, G. (2001), Hard X-ray properties of blazars, *A&A* **375**, 739–751.

DONUT Collaboration, Kodama, K., Ushida, N., Andreopoulos, C., Saoulidou, N., et al. (2001), Observation of tau neutrino interactions, *Physics Letters B* **504**, 218–224.

Dunlop, J. S. and Peacock, J. A. (1990), The Redshift Cut-Off in the Luminosity Function of Radio Galaxies and Quasars, *MNRAS* **247**, 19.

Eichler, D. (1979), High-energy neutrino astronomy - A probe of galactic nuclei, *ApJ* **232**, 106–112.

Eichler, D. and Schramm, D. N. (1978), High energy neutrino astronomy, *Nature* **275**, 704–706.

Ekers, R. D., James, C. W., Protheroe, R. J. and McFadden, R. A. (2009), Lunar radio Cherenkov observations of UHE neutrinos, *Nuclear Instruments and Methods in Physics Research A* **604**, 106.

Elvis, M., Wilkes, B. J., McDowell, J. C., Green, R. F., Bechtold, J., et al. (1994), Atlas of quasar energy distributions, *ApJS* **95**, 1–68.

Engel, R., Seckel, D. and Stanev, T. (2001), Neutrinos from propagation of ultrahigh energy protons, *Phys. Rev. D* **64**(9), 093010.

Englert, F. and Brout, R. (1964), Broken Symmetry and the Mass of Gauge Vector Mesons, *Physical Review Letters* **13**, 321–323.

Evans, D. A., Kraft, R. P., Worrall, D. M., Hardcastle, M. J., Jones, C., et al. (2004), Chandra and XMM-Newton Observations of the Nucleus of Centaurus A, *ApJ* **612**, 786–796.

Fabian, A. C. (2004), Obscured Active Galactic Nuclei and Obscured Accretion, *Coevolution of Black Holes and Galaxies* p.446.

Fabian, A. C. and Barcons, X. (1992), The origin of the X-ray background, *ARA&A* **30**, 429–456.

Falcke, H. and Biermann, P. L. (1995), The jet-disk symbiosis. I. Radio to X-ray emission models for quasars., *A&A* **293**, 665–682.

Falcke, H., Malkan, M. A. and Biermann, P. L. (1995), The jet-disk symbiosis. II.Interpreting the radio/UV correlations in quasars., *A&A* **298**, 375.

Fanaroff, B. L. and Riley, J. M. (1974), The morphology of extragalactic radio sources of high and low luminosity, *MNRAS* **167**, 31P–36P.

Fermi, E. (1934a), Versuch einer Theorie der β-Strahlen. I, *Zeitschrift für Physik* **88**(3-4), 161–177.

Fermi, E. (1934b), Tentativo di una Teoria Dei Raggi β, *Il Nuovo Cimento* **11**(1), 1–19.

Fossati, G., Maraschi, L., Celotti, A., Comastri, A. and Ghisellini, G. (1998), A unifying view of the spectral energy distributions of blazars, *MNRAS* **299**, 433–448.

Gaisser, T. K., Halzen, F. and Stanev, T. (1995), Particle astrophysics with high energy neutrinos, *Phys. Rep.* **258**, 173–236.

Gehrels, N. and Razzaque, S. (2013), Gamma-ray bursts in the swift-Fermi era, *Frontiers of Physics* **8**, 661–678.

Ghisellini, G., Celotti, A., Fossati, G., Maraschi, L. and Comastri, A. (1998), A theoretical unifying scheme for gamma-ray bright blazars, *MNRAS* **301**, 451–468.

Ghisellini, G., Della Ceca, R., Volonteri, M., Ghirlanda, G., Tavecchio, F., et al. (2010), Chasing the heaviest black holes of jetted active galactic nuclei, *MNRAS* **405**, 387–400.

Ghisellini, G. (ed.) (2013), *Radiative Processes in High Energy Astrophysics*, Vol. 873 of *Lecture Notes in Physics, Berlin Springer Verlag.*

Ghisellini, G. and Celotti, A. (2001), The dividing line between FR I and FR II radio-galaxies, *A&A* **379**, L1–L4.

Ghisellini, G. and Tavecchio, F. (2008), The blazar sequence: a new perspective, *MNRAS* **387**, 1669–1680.

Ginzburg, V. L. (1971), Physics of Our Days: what Problems of Physics and Astrophysics are of Special Importance and Interest at Present?, *Soviet Physics Uspekhi* **14**, 21–39.

Giunti, C. and Kim, C. W. (2007), *Fundamentals of Neutrino Physics and Astrophysics*, Oxford University Press.

Giunti, C. and Studenikin, A. (2009), Neutrino electromagnetic properties, *Physics of Atomic Nuclei* **72**, 2089–2125.

Glashow, S. L. (1961), Partial-symmetries of weak interactions, *Nucl. Phys. A* **22**, 579–588.

Gorham, P. W., Allison, P., Barwick, S. W., Beatty, J. J., Besson, D. Z., et al. (2009), New Limits on the Ultrahigh Energy Cosmic Neutrino Flux from the ANITA Experiment, *Physical Review Letters* **103**(5), 051103.

Gorham, P. W., Allison, P., Baughman, B. M., Beatty, J. J., Belov, K., et al. (2010), Observational constraints on the ultrahigh energy cosmic neutrino flux from the second flight of the ANITA experiment, *Phys. Rev. D* **82**(2), 022004.

Gorham, P. W., Allison, P., Baughman, B. M., Beatty, J. J., Belov, K., et al. (2012), Erratum: Observational constraints on the ultrahigh energy cosmic neutrino flux from the second flight of the ANITA experiment [Phys. Rev. D 82 022004 (2010)], *Phys. Rev. D* **85**(4), 049901.

Greisen, K. (1966), End to the Cosmic-Ray Spectrum?, *Physical Review Letters* **16**, 748–750.

Gribov, V. and Pontecorvo, B. (1969), Neutrino astronomy and lepton charge, *Physics Letters B* **28**, 493–496.

Guralnik, G. S., Hagen, C. R. and Kibble, T. W. (1964), Global Conservation Laws and Massless Particles, *Physical Review Letters* **13**, 585–587.

Halzen, F. (2014), The highest energy neutrinos: First evidence for cosmic origin, *Astronomische Nachrichten* **335**, 507.

Halzen, F. and ICnumu, J. G. (1988), High Energy Neutrino Detection in Deep Polar Ice, *UH-511-659-88, MAD/PH/428* .

Halzen, F. and O'Murchadha, A. (2008), Neutrinos from Auger Sources, *ArXiv e-prints* .

Halzen, F. and Zas, E. (1997), Neutrino Fluxes from Active Galaxies: A Model-Independent Estimate, *ApJ* **488**, 669–674.

Hardee, P. E. (2006), Stability and Structure in Astrophysical Jets, *in* H. R. Miller, K. Marshall, J. R. Webb and M. F. Aller (eds.), *Blazar Variability Workshop II: Entering the GLAST Era*, Vol. 350 of *Astronomical Society of the Pacific Conference Series*, p.205.

Harding, J. P. and Abazajian, K. N. (2012), Models of the contribution of blazars to the anisotropy of the extragalactic diffuse gamma-ray background, *J. Cosmology Astropart. Phys.* **11**, 26.

Hasert, F. J., Kabe, S., Krenz, W., von Krogh, J., Lanske, D., et al. (1973), Observation of neutrino-like interactions without muon or electron in the gargamelle neutrino experiment, *Physics Letters B* **46**, 138–140.

Hasert, F. J., Kabe, S., Krenz, W., Von Krogh, J., Lanske, D., et al. (1974), Observation of neutrino-like interactions without muon or electron in the Gargamelle neutrino experiment, *Nuclear Physics B* **73**, 1–22.

Hasinger, G., Miyaji, T. and Schmidt, M. (2005), Luminosity-dependent evolution of soft X-ray selected AGN. New Chandra and XMM-Newton surveys, *A&A* **441**, 417–434.

Heinz, S. and Begelman, M. C. (2000), Jet Acceleration by Tangled Magnetic Fields, *ApJ* **535**, 104–117.

Higgs, P. W. (1964), Broken Symmetries and the Masses of Gauge Bosons, *Physical Review Letters* **13**, 508–509.

Hillas, A. M. (1984), The Origin of Ultra-High-Energy Cosmic Rays, *ARA&A* **22**, 425–444.

Hillas, A. M. (2006), Cosmic Rays: Recent Progress and some Current Questions, *ArXiv Astrophysics e-prints* .

Hinshaw, G., Larson, D., Komatsu, E., Spergel, D. N., Bennett, C. L., et al. (2013), Nine-year Wilkinson Microwave Anisotropy Probe (WMAP) Observations: Cosmological Parameter Results, *ApJS* **208**, 19.

Hirata, K., Kajita, T., Koshiba, M., Nakahata, M. and Oyama, Y. (1987), Observation of a neutrino burst from the supernova SN1987A, *Physical Review Letters* **58**, 1490–1493.

Hirata, K. S., Kajita, T., Koshiba, M., Nakahata, M., Oyama, Y., et al. (1988), Observation in the Kamiokande-II detector of the neutrino burst from supernova SN1987A, *Phys. Rev. D* **38**, 448–458.

Ibe, M. and Kaneta, K. (2014), Cosmic neutrino background absorption line in the neutrino spectrum at IceCube, *Phys. Rev. D* **90**(5), 053011.

IceCube Collaboration (2013), Evidence for High-Energy Extraterrestrial Neutrinos at the IceCube Detector, *Science* **342**.

Inoue, Y. and Totani, T. (2009), The Blazar Sequence and the Cosmic Gamma-ray Background Radiation in the Fermi Era, *ApJ* **702**, 523–536.

Inoue, Y., Totani, T. and Mori, M. (2010), Prospects for a Very High-Energy Blazar Survey by the Next-Generation Cherenkov Telescopes, *PASJ* **62**, 1005–.

Iocco, F., Murase, K., Nagataki, S. and Serpico, P. D. (2008), High-Energy Neutrino Signals from the Epoch of Reionization, *ApJ* **675**, 937–945.

Ioka, K. and Murase, K. (2014), IceCube PeV-EeV neutrinos and secret interactions of neutrinos, *Progress of Theoretical and Experimental Physics* **2014**(6), 060001.

Jacobsen, I. B. and Saxton, C. J. (in prep.), Diffuse high-energy neutrino fluxes from AGN using M87 as reference source.

Jacobsen, I. B., Wu, K., On, A. Y. L. and Saxton, C. J. (2015), High-energy neutrino fluxes from AGN populations inferred from X-ray surveys, *MNRAS* **451**, 3649–3663.

Jacobsen, I. B., Younsi, Z. and Wu, K. (in prep.), A neutrino luminosity function for blazars.

James, C. W., Protheroe, R. J., Ekers, R. D., Alvarez-Muñiz, J., McFadden, R. A., et al. (2011), LUNASKA experiment observational limits on UHE neutrinos from Centaurus A and the Galactic Centre, *MNRAS* **410**, 885–889.

Jelley, J. V. (1996), The feasibility of detecting neutrinos of cosmic origin by radio frequency Cherenkov radiation in Antarctic ice, *Astroparticle Physics* **5**, 255–261.

Kachelrieß, M., Ostapchenko, S. and Tomàs, R. (2009), High energy radiation from Centaurus A, *New Journal of Physics* **11**(6), 065017.

Kantor, E. M. and Gusakov, M. E. (2007), The neutrino emission due to plasmon decay and neutrino luminosity of white dwarfs, *MNRAS* **381**, 1702–1710.

Katz, U. F. and Spiering, C. (2012), High-energy neutrino astrophysics: Status and perspectives, *Progress in Particle and Nuclear Physics* **67**, 651–704.

Kellermann, K. I., Sramek, R., Schmidt, M., Shaffer, D. B. and Green, R. (1989), VLA observations of objects in the Palomar Bright Quasar Survey, *AJ* **98**, 1195–1207.

Kelner, S. R., Aharonian, F. A. and Bugayov, V. V. (2006), Energy spectra of gamma rays, electrons, and neutrinos produced at proton-proton interactions in the very high energy regime, *Phys. Rev. D* **74**(3), 034018.

Kodama, K., Ushida, N., Andreopoulos, C., Saoulidou, N., Tzanakos, G., et al. (2008), Final tau-neutrino results from the DONuT experiment, *Phys. Rev. D* **78**(5), 052002.

Koers, H. B. J. and Tinyakov, P. (2008), Relation between the neutrino flux from Centaurus A and the associated diffuse neutrino flux, *Phys. Rev. D* **78**(8), 083009.

Koers, H. B. J., Pe'er, A. and Wijers, R. A. M. J. (2006), Parameterization of the energy and rapidity distributions of secondary pions and kaons produced in energetic proton-proton collisions, *ArXiv High Energy Physics - Phenomenology e-prints* .

Kolb, E. W., Turner, M. S. and Walker, T. P. (1985), Production and detection of high-energy neutrinos from Cygnus X-3, *Phys. Rev. D* **32**, 1145–1151.

Komissarov, S. S. (2011), Magnetic acceleration of relativistic jets., *Mem. Soc. Astron. Italiana* **82**, 95.

Koshiba, M. (1992), Observational neutrino astrophysics, *Phys. Rep.* **220**, 229–381.

Kotera, K., Allard, D. and Olinto, A. V. (2010), Cosmogenic neutrinos: parameter space and detectabilty from PeV to ZeV, *J. Cosmology Astropart. Phys.* **10**, 13.

Kotera, K. and Olinto, A. V. (2011), The Astrophysics of Ultrahigh-Energy Cosmic Rays, *ARA&A* **49**, 119–153.

Kravchenko, I., Frichter, G. M., Seckel, D., Spiczak, G. M., Adams, J., et al. (2003), Performance and simulation of the RICE detector, *Astroparticle Physics* **19**, 15–36.

Kravchenko, I., Hussain, S., Seckel, D., Besson, D., Fensholt, E., et al. (2012), Updated results from the RICE experiment and future prospects for ultra-high energy neutrino detection at the south pole, *Phys. Rev. D* **85**(6), 062004.

Lacki, B. C., Thompson, T. A., Quataert, E., Loeb, A. and Waxman, E. (2011), On the GeV and TeV Detections of the Starburst Galaxies M82 and NGC 253, *ApJ* **734**, 107.

Landsman, H. and AURA Collaboration (2007), AURA next generation neutrino detector in the South Pole, *Nuclear Physics B Proceedings Supplements* **168**, 268–270.

Landsman, H., Ruckman, L., Varner, G. S. and IceCube Collaboration (2009), AURA – A radio frequency extension to IceCube, *Nuclear Instruments and Methods in Physics Research A* **604**, 70.

Learned, J. G. and Mannheim, K. (2000), High-Energy Neutrino Astrophysics, *Annual Review of Nuclear and Particle Science* **50**, 679–749.

Learned, J. G. and Pakvasa, S. (1995), Detecting $\nu_?$ oscillations at PeV energies, *Astroparticle Physics* **3**, 267–274.

Lemoine, M. and Waxman, E. (2009), Anisotropy vs chemical composition at ultra-high energies, *J. Cosmology Astropart. Phys.* **11**, 9.

Linke, F., Font, J. A., Janka, H.-T., Müller, E. and Papadopoulos, P. (2001), Spherical collapse of supermassive stars: Neutrino emission and gamma-ray bursts, *A&A* **376**, 568–579.

Linsley, J. (1963), Evidence for a Primary Cosmic-Ray Particle with Energy 10^{20} eV, *Physical Review Letters* **10**, 146–148.

Loeb, A. and Waxman, E. (2006), The cumulative background of high energy neutrinos from starburst galaxies, *J. Cosmology Astropart. Phys.* **5**, 3.

Longair, M. S. (1994), *High energy astrophysics. Vol.2: Stars, the galaxy and the interstellar medium*, Second edition, Cambridge University Press.

Maki, Z., Nakagawa, M. and Sakata, S. (1962), Remarks on the Unified Model of Elementary Particles, *Progress of Theoretical Physics* **28**, 870–880.

Maller, J. and Pierre Auger Collaboration (2014), Radio detection of extensive air showers at the Pierre Auger Observatory, *Nuclear Instruments and Methods in Physics Research A* **742**, 232–236.

Mannheim, K. (1993), The proton blazar, *A&A* **269**, 67–76.

Mannheim, K. (1995), High-energy neutrinos from extragalactic jets, *Astroparticle Physics* **3**, 295–302.

Mannheim, K. (1999), Neutrino oscillations and blazars, *Astroparticle Physics* **11**, 49–57.

Mannheim, K., Protheroe, R. J. and Rachen, J. P. (2001), Cosmic ray bound for models of extragalactic neutrino production, *Phys. Rev. D* **63**(2), 023003.

Margolis, S. H., Schramm, D. N. and Silberberg, R. (1978), Ultrahigh-energy neutrino astronomy, *ApJ* **221**, 990–1002.

Markov, M. A. and Zheleznykh, I. M. (1986), Large-scale Cherenkov detectors in ocean, atmosphere and ice, *Nuclear Instruments and Methods in Physics Research A* **248**, 242–251.

Marscher, A. P. (2009), Jets in Active Galactic Nuclei, *ArXiv e-prints* .

Mehdipour, M., Branduardi-Raymont, G., Kaastra, J. S., Petrucci, P. O., Kriss, G. A., et al. (2011), Multiwavelength campaign on Mrk 509. IV. Optical-UV-X-ray variability and the nature of the soft X-ray excess, *A&A* **534**, A39.

Mikheev, S. P. and Smirnov, A. I. (1986), Resonant amplification of neutrino oscillations in matter and solar-neutrino spectroscopy, *Nuovo Cimento C Geophysics Space Physics C* **9**, 17–26.

Mortlock, D. J., Warren, S. J., Venemans, B. P., Patel, M., Hewett, P. C., et al. (2011), A luminous quasar at a redshift of z = 7.085, *Nature* **474**, 616–619.

Mücke, A. and Protheroe, R. J. (2001), Neutrino Emission from HBLs and LBLs, *International Cosmic Ray Conference* **3**, 1153.

Mücke, A., Protheroe, R. J., Engel, R., Rachen, J. P. and Stanev, T. (2003), BL Lac objects in the synchrotron proton blazar model, *Astroparticle Physics* **18**, 593–613.

Murase, K., Inoue, Y. and Dermer, C. D. (2014), Diffuse neutrino intensity from the inner jets of active galactic nuclei: Impacts of external photon fields and the blazar sequence, *Phys. Rev. D* **90**(2), 023007.

Mushotzky, R. (2004), How are AGN Found?, *in* A. J. Barger (ed.), *Supermassive Black Holes in the Distant Universe*, Vol. 308 of *Astrophysics and Space Science Library*, p.53.

Nagataki, S. (2004), High-Energy Neutrinos Produced by Interactions of Relativistic Protons in Shocked Pulsar Winds, *ApJ* **600**, 883–904.

Neddermeyer, S. H. and Anderson, C. D. (1937), Note on the Nature of Cosmic-Ray Particles, *Physical Review* **51**, 884–886.

Nellen, L. (1994), Neutrino production in active galaxies, **40**, 262–270.

Nellen, L., Mannheim, K. and Biermann, P. L. (1993), Neutrino production through hadronic cascades in AGN accretion disks, *Phys. Rev. D* **47**, 5270–5274.

Neronov, A. Y. and Semikoz, D. V. (2002), Which blazars are neutrino loud?, *Phys. Rev. D* **66**(12), 123003.

Novikov, I. D. and Thorne, K. S. (1973), Astrophysics of black holes., *in* C. Dewitt and B. S. Dewitt (eds.), *Black Holes (Les Astres Occlus)*, pp.343–450.

Orr, M. J. L. and Browne, I. W. A. (1982), Relativistic beaming and quasar statistics, *MNRAS* **200**, 1067–1080.

Padovani, P. and Giommi, P. (1995), The connection between x-ray- and radio-selected BL Lacertae objects, *ApJ* **444**, 567–581.

Page, M. J., Symeonidis, M., Vieira, J. D., Altieri, B., Amblard, A., et al. (2012), The suppression of star formation by powerful active galactic nuclei, *Nature* **485**, 213–216.

Peacock, J. A. (2007), *Cosmological Physics*, Seventh edition, Cambridge University Press.

Perkins, D. H. (2000), *Introduction to High Energy Physics*, fourth edition, Cambridge University Press.

Perl, M. L. (1980), The Tau Lepton, *Annual Review of Nuclear and Particle Science* **30**, 299–335.

Perl, M. L., Abrams, G. S., Boyarski, A. M., Breidenbach, M., Briggs, D. D., et al. (1975), Evidence for anomalous lepton production in e^+e^- annihilation, *Physical Review Letters* **35**, 1489–1492.

Peterson, B. M. (1997), *An Introduction to Active Galactic Nuclei*, Cambridge University Press.

Pierre Auger Collaboration, Abraham, J., Abreu, P., Aglietta, M., Aguirre, C., et al. (2007), Correlation of the Highest-Energy Cosmic Rays with Nearby Extragalactic Objects, *Science* **318**, 938–.

Pierre Auger Collaboration, Abraham, J., Abreu, P., Aglietta, M., Aguirre, C., et al. (2008), Correlation of the highest-energy cosmic rays with the positions of nearby active galactic nuclei, *Astroparticle Physics* **29**, 188–204.

Planck Collaboration, Ade, P. A. R., Aghanim, N., Armitage-Caplan, C., Arnaud, M., et al. (2014), Planck 2013 results. XVI. Cosmological parameters, *A&A* **571**, A16.

Protheroe, R. J. (1996), Gamma rays and neutrinos from AGN jets, *Adeliade preprint ADP-AT-96-4* .

Rachen, J. P. (2000), Hadronic blazar models and correlated X-ray/TeV flares, *in* B. L. Dingus, M. H. Salamon and D. B. Kieda (eds.), *American Institute of Physics Conference Series*, Vol. 515 of *American Institute of Physics Conference Series*, pp.41–52.

Rachen, J. P. and Mészáros, P. (1998), Photohadronic neutrinos from transients in astrophysical sources, *Phys. Rev. D* **58**(12), 123005.

Rapidis, P. A. and NESTOR Collaboration (2009), The NESTOR underwater neutrino telescope project, *Nuclear Instruments and Methods in Physics Research A* **602**, 54–57.

Razzaque, S., Jean, P. and Mena, O. (2010), High energy neutrinos from novae in symbiotic binaries: The case of V407 Cygni, *Phys. Rev. D* **82**(12), 123012.

Razzaque, S., Mészáros, P. and Waxman, E. (2004), Neutrino signatures of the supernova: Gamma ray burst relationship, *Phys. Rev. D* **69**(2), 023001.

Reimer, A., Böttcher, M. and Postnikov, S. (2005), Neutrino Emission in the Hadronic Synchrotron Mirror Model: The "Orphan" TeV Flare from 1ES 1959+650, *ApJ* **630**, 186–190.

Reines, F. and Cowan, C. L. (1956), The Neutrino, *Nature* **178**, 446–449.

Reynoso, M. M., Medina, M. C. and Romero, G. E. (2011), A lepto-hadronic model for high-energy emission from FR I radiogalaxies, *A&A* **531**, A30.

Reynoso, M. M., Romero, G. E. and Medina, M. C. (2012), A two-component model for the high-energy variability of blazars. Application to PKS 2155-304, *A&A* **545**, A125.

Rieger, F. M., Bosch-Ramon, V. and Duffy, P. (2007), Fermi acceleration in astrophysical jets, *Ap&SS* **309**, 119–125.

Riesselmann, K. (2007), logbook: Neutrino Invention, *Symmetry Magazine* **04**(07), 1.
http://www.symmetrymagazine.org/article/march-2007/neutrino-invention.

Romani, R. W. (2006), The Spectral Energy Distribution of the High-z Blazar Q0906+6930, *AJ* **132**, 1959–1963.

Ruffert, M. and Janka, H.-T. (1998), Colliding neutron stars. Gravitational waves, neutrino emission, and gamma-ray bursts, *A&A* **338**, 535–555.

Ruffert, M., Janka, H.-T., Takahashi, K. and Schaefer, G. (1997), Coalescing neutron stars - a step towards physical models. II. Neutrino emission, neutron tori, and gamma-ray bursts., *A&A* **319**, 122–153.

Rybicki, G. B. and Lightman, A. P. (1979), *Radiative processes in astrophysics*, John Wiley & Sons Inc.

Salam, A. and Ward, J. C. (1964), Electromagnetic and weak interactions, *Physics Letters* **13**, 168–171.

Sauty, C., Tsinganos, K. and Trussoni, E. (2002), Jet Formation and Collimation, *in* A. W. Guthmann, M. Georganopoulos, A. Marcowith and K. Manolakou (eds.), *Relativistic Flows in Astrophysics*, Vol. 589 of *Lecture Notes in Physics, Berlin Springer Verlag*, p.41.

Sbarrato, T., Padovani, P. and Ghisellini, G. (2014), The jet-disc connection in AGN, *MNRAS* **445**, 81–92.

Schmidt, M. (1963), 3C 273 : A Star-Like Object with Large Red-Shift, *Nature* **197**, 1040.

Schmidt, M. (1968), Space Distribution and Luminosity Functions of Quasi-Stellar Radio Sources, *ApJ* **151**, 393.

Schnabel, J. (2015), Search for a Diffuse Flux of Cosmic Neutrinos with ANTARES, *Physics Procedia* **61**, 627–632.

Schneider, R., Guetta, D. and Ferrara, A. (2002), Gamma-ray bursts from the first stars: neutrino signals, *MNRAS* **334**, 173–181.

Schramm, D. N. (1980), Neutrino astronomy, *in* J. Ehlers, J. J. Perry and M. Walker (eds.), *Ninth Texas Symposium on Relativistic Astrophysics*, Vol. 336 of *Annals of the New York Academy of Sciences*, pp.380–388.

Sigl, G. and van Vliet, A. (2014), PeV Neutrinos from Ultra-High-Energy Cosmic Rays, *ArXiv e-prints* .

Sikora, M., Begelman, M. C., Madejski, G. M. and Lasota, J.-P. (2005), Are Quasar Jets Dominated by Poynting Flux?, *ApJ* **625**, 72–77.

Silberberg, R. and Shapiro, M. M. (1977), High-energy cosmic neutrinos and photons from point sources, and implications for galactic confinement, *International Cosmic Ray Conference* **2**, 26–29.

Silberberg, R. and Shapiro, M. M. (1979), Neutrinos as a Probe for the Nature of and Processes in Active Galactic Nuclei, *International Cosmic Ray Conference* **10**, 357.

Silk, J. and Rees, M. J. (1998), Quasars and galaxy formation, *A&A* **331**, L1–L4.

Silverman, J. D., Green, P. J., Barkhouse, W. A., Kim, D.-W., Kim, M., et al. (2008), The Luminosity Function of X-Ray-selected Active Galactic Nuclei: Evolution of Supermassive Black Holes at High Redshift, *ApJ* **679**, 118–139.

Spruit, H. C. (2010), Theory of Magnetically Powered Jets, *in* T. Belloni (ed.), *Lecture Notes in Physics, Berlin Springer Verlag*, Vol. 794 of *Lecture Notes in Physics, Berlin Springer Verlag*, p.233.

Spruit, H. C., Foglizzo, T. and Stehle, R. (1997), Collimation of magnetically driven jets from accretion discs, *MNRAS* **288**, 333–342.

Stecker, F. W. (1973), Ultrahigh Energy Photons, Electrons, and Neutrinos, the Microwave Background, and the Universal Cosmic-Ray Hypothesis, *Ap&SS* **20**, 47–57.

Stecker, F. W. (2005), Note on high-energy neutrinos from active galactic nuclei cores, *Phys. Rev. D* **72**(10), 107301.

Stecker, F. W. (2007), Are diffuse high energy neutrinos and γ-rays from starburst galaxies observable?, *Astroparticle Physics* **26**, 398–401.

Stecker, F. W. (2013), Ice Cube Observed PeV Neutrinos from AGN Cores, *ArXiv e-prints* .

Stecker, F. W., Done, C., Salamon, M. H. and Sommers, P. (1991), High-energy neutrinos from active galactic nuclei, *Physical Review Letters* **66**, 2697–2700.

Stecker, F. W. and Salamon, M. H. (1996), High Energy Neutrinos from Quasars, *Space Sci. Rev.* **75**, 341–355.

Street, J. C. and Stevenson, E. C. (1937), New Evidence for the Existence of a Particle of Mass Intermediate Between the Proton and Electron, *Physical Review* **52**, 1003–1004.

't Hooft, G. (1971), Renormalization of massless Yang-Mills fields, *Nuclear Physics B* **33**, 173–199.

't Hooft, G. and Veltman, M. (1972), Regularization and renormalization of gauge fields, *Nuclear Physics B* **44**, 189–213.

Tadhunter, C. (2008), An introduction to active galactic nuclei: Classification and unification, *New A Rev.* **52**, 227–239.

Takami, H., Inoue, S. and Yamamoto, T. (2012), Propagation of ultra-high-energy cosmic ray nuclei in cosmic magnetic fields and implications for anisotropy measurements, *Astroparticle Physics* **35**, 767–780.

Takami, H., Murase, K. and Dermer, C. D. (2013), Disentangling Hadronic and Leptonic Cascade Scenarios from the Very-high-energy Gamma-Ray Emission of Distant Hard-spectrum Blazars, *ApJL* **771**, L32.

Tanvir, N. R., Fox, D. B., Levan, A. J., Berger, E., Wiersema, K., et al. (2009), A γ-ray burst at a redshift of z˜8.2, *Nature* **461**, 1254–1257.

Tavecchio, F., Ghisellini, G. and Guetta, D. (2014), Structured Jets in BL Lac Objects: Efficient PeV Neutrino Factories?, *ApJL* **793**, L18.

Tchernin, C., Aguilar, J. A., Neronov, A. and Montaruli, T. (2013), An exploration of hadronic interactions in blazars using IceCube, *A&A* **555**, A70.

The Pierre Auger Collaboration (2015), The Pierre Auger Cosmic Ray Observatory, *ArXiv e-prints* .

Tucker, W. (1975), *Radiation processes in astrophysics*, MIT Press.

Ueda, Y., Akiyama, M., Ohta, K. and Miyaji, T. (2003), Cosmological Evolution of the Hard X-Ray Active Galactic Nucleus Luminosity Function and the Origin of the Hard X-Ray Background, *ApJ* **598**, 886–908.

Urry, C. (2004), AGN Unification: An Update, *in* G. T. Richards and P. B. Hall (eds.), *AGN Physics with the Sloan Digital Sky Survey*, Vol. 311 of *Astronomical Society of the Pacific Conference Series*, p.49.

Urry, C. M. and Padovani, P. (1995), Unified Schemes for Radio-Loud Active Galactic Nuclei, *PASP* **107**, 803.

van der Laan, H. (1966), A Model for Variable Extragalactic Radio Sources, *Nature* **211**, 1131.

Vila, G. S. and Romero, G. E. (2010), Leptonic/hadronic models for electromagnetic emission in microquasars: the case of GX 339-4, *MNRAS* **403**, 1457–1468.

Volonteri, M., Haardt, F., Ghisellini, G. and Della Ceca, R. (2011), Blazars in the early Universe, *MNRAS* **416**, 216–224.

Watson, A. A. (2008), Highlights from the Pierre Auger Obseervatory - the birth of the hybrid era, *ArXiv e-prints* .

Waxman, E. (2011), High energy cosmic ray and neutrino astronomy, *ArXiv e-prints* .

Waxman, E. and Bahcall, J. (1997), High Energy Neutrinos from Cosmological Gamma-Ray Burst Fireballs, *Physical Review Letters* **78**, 2292–2295.

Waxman, E. and Bahcall, J. (1999), High energy neutrinos from astrophysical sources: An upper bound, *Phys. Rev. D* **59**(2), 023002.

Weinberg, S. (1967), A Model of Leptons, *Physical Review Letters* **19**, 1264–1266.

Willott, C. J., Rawlings, S., Blundell, K. M., Lacy, M. and Eales, S. A. (2001), The radio luminosity function from the low-frequency 3CRR, 6CE and 7CRS complete samples, *MNRAS* **322**, 536–552.

Wilson, F. L. (1968), Fermi's Theory of Beta Decay, *American Journal of Physics* **36**, 1150–1160.

Winter, W. (2012), Neutrino spectra and flavor composition on the Hillas plot, *Journal of Physics Conference Series* **375**(5), 052038.

Wolfenstein, L. (1978), Neutrino oscillations in matter, *Phys. Rev. D* **17**, 2369–2374.

Wright, E. L. (2006), A Cosmology Calculator for the World Wide Web, *PASP* **118**, 1711–1715.

Yoshiguchi, H., Nagataki, S., Tsubaki, S.-y. and Sato, K. (2003), Small-Scale Clustering in the Isotropic Arrival Distribution of Ultra-High-Energy Cosmic Rays and Implications for Their Source Candidates, *ApJ* **586**, 1211–1231.

Zatsepin, G. T. and Kuz'min, V. A. (1966), Upper Limit of the Spectrum of Cosmic Rays, *ZhETF Pisma Redaktsiiu* **4**, 114.

Zhang, B., Dai, Z. G., Mészáros, P., Waxman, E. and Harding, A. K. (2003), High-Energy Neutrinos from Magnetars, *ApJ* **595**, 346–351.

Zinn, P.-C., Middelberg, E. and Ibar, E. (2011), Infrared-faint radio sources: a cosmological view. AGN number counts, the cosmic X-ray background and SMBH formation, *A&A* **531**, A14.